Predictive, Adaptive, and Time-Varying Control of Spacecraft Orbits and Attitude

by

Avishai Weiss

A dissertation submitted in partial fulfillment
of the requirements for the degree of
Doctor of Philosophy
(Aerospace Engineering)
in the University of Michigan
2013

Doctoral Committee:

Professor Ilya Kolmanovsky, Chair
Professor Dennis S. Bernstein
Professor James Cutler
Professor A. Galip Ulsoy

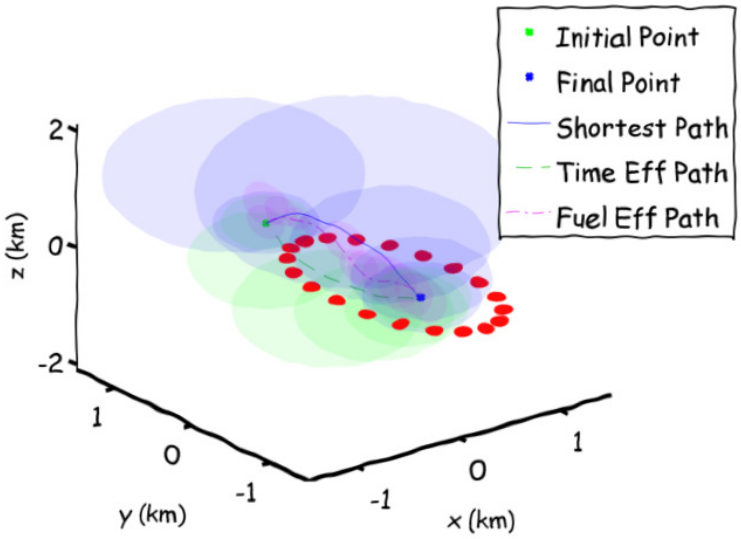
Initial Point
Final Point
Shortest Path
Time Eff Path
Fuel Eff Path
z (km)
2
0
-2
y (km)
1
0
-1
x (km)
-1
0
1

2013

To my parents.

A C K N O W L E D G M E N T S

I want to thank my advisor, Professor Ilya Kolmanovsky for his incredible guidance and inspiration. Professor Kolmanovsky has been a terrific mentor; he is a kind, caring, interesting, brilliant, and hard-working advisor who has served as an inspirational role model to me throughout my time at Michigan. He goes out of his way to help and provide assistance, and always makes time to listen to me, whether it is an off-the-wall idea unrelated to research, or a last minute nerve-calming presentation rehearsal.

Next, I'd like to thank Professor Dennis Bernstein. The endless encouragement and advice he has provided me throughout my Ph.D. studies has been invaluable. I am privileged to have had the opportunity to work with and learn from Professor Bernstein.

Special thanks to the rest of my committee, Professor James Cutler and Professor A. Galip Ulsoy, who have provided tremendous support and helpful suggestions. A special debt of gratitude goes to Professor Cutler, without whom I would not have found my way to Michigan.

Additional thanks to my collaborators and friends at the Air Force Research Lab in Albuquerque, NM, where I spent two summers: Dr. Richard S. Erwin, Dr. Morgan Baldwin, Dr. Fred Leve, and Dr. Moriba Jah.

I want to thank all my coauthors on the various conference and journal papers that have contributed to the work presented in this dissertation, and specifically, a big debt of gratitude goes to Chris Petersen for hard work on the multiple gains, cost matrices, and disturbance sets presented in Chapter 3. Thank you to Marc Camblor for generating Figure 4.1, and Kshitij Agarwal for the joint work on CMGs.

Finally, a heartfelt thanks to Cory Robinson, who has been so supportive and understanding, and has patiently managed the distance while I have been away at school.

TABLE OF CONTENTS

LIST OF FIGURES

LIST OF TABLES

LIST OF APPENDICES

LIST OF ABBREVIATIONS

CWH Clohessy-Wiltshire-Hill

FPR Forward-Propagating Riccati

MPC Model Predictive Control

CMGs control momentum gyroscopes

SGCMGs single-gimbal CMGs

LTV linear time-varying

QP quadratic program

ABSTRACT

Predictive, Adaptive, and Time-Varying Control of Spacecraft Orbits and Attitude

by

Avishai Weiss

Chair: Ilya Kolmanovsky

This dissertation contributes several control strategies that provide advanced capabilities in spacecraft applications. Specifically, we consider predictive, adaptive, and time-varying control methods, and apply them to orbital and attitude control.

First, we develop a Model Predictive Control (MPC) approach with dynamically reconfigurable constraints for orbital rendezvous and docking. The controller is designed to transition between MPC-based guidance during spacecraft rendezvous and MPC-based guidance during spacecraft docking, with each phase having distinct requirements, constraints, and sampling rates. Obstacle/debris avoidance is considered in the rendezvous phase and handled using a dynamically rotating hyperplane. A Line of Sight (LoS) cone constraint, bandwidth constraints on the spacecraft attitude control system, and exhaust plume direction constraints are addressed during the docking phase. The MPC controller is demonstrated in simulation studies using a nonlinear model of

spacecraft orbital motion. An Extended Kalman Filter (EKF) is used to estimate spacecraft states based on relative angles and relative range measurements.

Second, we consider spacecraft relative motion control based on the use of safe positively invariant sets. In this approach, a connectivity graph is constructed between a set of forced equilibria, forming a virtual net that is centered around a nominal orbital position. The connectivity between two equilibria is determined based on safe positively invariant sets in order to guarantee that transitions between equilibria can be effected while spacecraft actuator limits are adhered to and debris collisions are avoided. A graph search algorithm is implemented to find the shortest path around the debris. One of the advantages this approach has over conventional open-loop trajectory optimization, is the ability to incorporate bounded disturbances into relative motion planning, while rigorously guaranteeing constraint enforcement. Disturbances may occur due to thrust errors, delays, air drag, solar pressure, or failed or leaking components.

Third, for attitude control, we extend the continuous inertia-free control law for spacecraft attitude tracking derived in prior work to handle magnetic actuation, reaction wheels, and control momentum gyroscopes (CMGs). For magnetic actuation, the spacecraft is assumed to be in low-Earth orbit and actuated by only three orthogonal electromagnetic actuators. For reaction wheels, we assume three axisymmetric wheels. For CMGs, we assume three fixed-speed single-gimbal CMGs (SGCMGs) with spherical wheel. In all cases, the actuators are mounted in a known and linearly independent, but not necessarily orthogonal, configuration with an arbitrary and unknown orientation relative to the unknown spacecraft principal axes. We demonstrate effective attitude control capability without relying on inertia matrix characterization.

Lastly, motivated by the time-varying dynamics of magnetic attitude control and relative motion control on elliptic orbits, we develop a forward-propagating Riccati-based linear time-varying (LTV) feedback controller. We show that if the closed-loop dynamics matrix is symmetric, then the Forward-Propagating Riccati (FPR) controller is asymptotically stabilizing. We also show, using averaging theory, that, in the case of periodically time-varying systems, and under suitable assumptions, there exists a period below which the dynamics of the closed-loop system are asymptotically stable. In other words, closed-loop stability is guaranteed for systems with time-varying dynamics of sufficiently high frequency. Additionally, we show that there is a separation of estimator and FPR regulator dynamics and thus FPR control may be used in an output feedback configuration. We apply the FPR controller to a magnetically actuated spacecraft for both inertial and nadir pointing, as well as to a maneuvering spacecraft in an elliptic orbit around the Earth.

CHAPTER 1

Introduction

The unifying theme of this dissertation is the development of control methods that provide advanced capabilities for spacecraft orbital and attitude control. This chapter provides an overview and summarizes the contributions made in this dissertation.

1.1 Orbital Control

1.1.1 Rendezvous and Docking

Autonomous spacecraft rendezvous and docking maneuvers are among the most important and difficult components of modern spacecraft missions [1]. Examples include transport vehicle approach and docking to the International Space Station (ISS), capture and recovery of tumbling satellites, and avoidance or flybys of space objects (i.e. debris). Traditionally, relative motion maneuvers are performed using *open-loop* planning techniques [2]. Ad hoc maneuver corrections may be employed to compensate for errors inherent in open-loop control. Literature on spacecraft rendezvous control is extensive and includes, for instance, [2–10], and references therein.

Recently, more interest has been emerging in *closed-loop* maneuvering, especially for missions that involve formation flying or automated rendezvous, docking, and proximity operations. The XSS-11 [11] spacecraft has been developed by the Air Force Research Laboratory as a platform for demonstrating such relative motion capabilities. The robustness, fuel efficiency, speed, safety, and reliability of spacecraft relative motion maneuvers can be improved through the application of feedback control.

With this motivation, in [12–14] an approach to perform relative motion maneuvers based on the application of linear quadratic Model Predictive Control (MPC) and dynamically reconfigurable linear constraints was developed. This approach enables fuel efficient maneuvers that, in real time, can be replanned to account for unconsidered disturbances,

changing target conditions or objectives, and time-varying path constraints such as the presence of obstacles or debris. The MPC controller uses a linearized relative motion model and linear constraints that are generated online in order to compute the optimal control sequence over a finite horizon; it then applies the first element of this sequence to the spacecraft and repeats the process at the next sampling instance. For maneuvers confined to the orbital plane, References [12–14] demonstrated the capability to approach both a non-rotating and rotating, or tumbling, platform, while avoiding an obstacle along the spacecraft's path. In addition, robustness to unmeasured disturbances through the mechanism of systematic MPC feedback corrections was demonstrated. Finally, it was shown that the linear quadratic MPC approach with dynamically reconfigurable constraints reduces to an on-line solution of a quadratic programming (QP) problem, which is computationally feasible on-board a spacecraft. Furthermore, if the spacecraft approaches a non-rotating platform with a known Line of Sight (LoS) cone orientation, an explicit MPC approach that does not require on-board optimization can be used and is based on storing an offline pre-computed MPC law in the form of a piecewise affine control function (i.e., in the form of look-up tables and if-then-else conditions). The main limitation of [12–14] is that relative motion maneuvers are confined to the orbital plane of the target spacecraft.

Several other variants of the MPC framework for relative motion control have been proposed in the literature. The approach employed by [3, 15] uses a variable length horizon and requires the solution of a mixed-integer linear program at every control step. An application of MPC to spacecraft guidance in proximity of a space station is considered in [16], where an unconstrained MPC is proposed for guidance to the neighborhood of the space station, while the LoS between the station and the spacecraft sensors is maintained by a constrained spacecraft attitude controller and a control allocation scheme to operate the thrusters. In a similar context, a receding horizon controller that uses the solutions of non-convex quadratically constrained quadratic programs has been proposed in [17] for passively safe proximity operations, where a statistical model of the uncertainty is used for improving robustness with respect to position uncertainty.

1.1.2 Debris Avoidance

Orbital debris is an exponentially growing problem, with about 40% of ground-trackable objects originating from explosions that now number approximately 5 per year [18]. Spacecraft maneuver planning procedures thus have to address debris avoidance requirements. While obstacle avoidance is a standard problem in robotics [19, 20], the related spacecraft problems have several unique features. In particular, the space environment is relatively

uncluttered, thus permitting for a variety of maneuvers. Spacecraft dynamics are quite different from those of typical robots. Maneuver efficiency with respect to time and fuel consumption is a critical consideration. The states of the spacecraft and the debris can only be estimated, often with a significant estimation error. Finally, computational algorithms must be fast and optimized given moving objects and the limited computing power onboard most spacecraft. These unique features of spacecraft maneuver planning problems provide the motivation for the development of specialized algorithms.

Interest in spacecraft trajectory optimization with obstacle avoidance has increased in recent years. An optimal control problem with path constraints constructed as 'keep out' zones to avoid obstacles was formulated in [21]. The Sparse Optimal Control Software (SOCS) software was then used to solve the problem [22]. Another nonlinear optimal control formulation was used in [23] to solve for minimum-fuel rendezvous between a target and chaser, where collision avoidance requirements were incorporated as inequality constraints. The method involved solving a sequence of unconstrained optimal control problems, whose solution converges to the solution of the original problem. A 3-D static optimization over final relative position and time-of-flight such that obstacles are avoided and cost is optimized is presented in [24]. Feedback is incorporated by re-planning over either constant or variable time intervals.

Debris avoidance strategies have also been defined utilizing collision avoidance probabilities. Collision avoidance strategies based upon the number of evasive maneuvers, expected risk reduction, false alarm rate, required propellant consumption, and mass fraction for an accepted collision probability are presented in [25].

Guidance based on artificial potential function is used in [24, 26] to determine a rendezvous path free of obstacles. A potential function is developed with the intent that a minimum occurs at a desired relative position and then a dynamic control law is used to ensure the trajectory is obstacle free [26].

The spacecraft obstacle avoidance problem has also been treated using linear programming techniques [27–30]. In [27], the minimum-fuel avoidance maneuver is formulated with linear constraints and discrete dynamics modeled as an LTV system. In [28], the trajectory optimization problem is formulated as a linear programming problem with the capability of including operational constraints and the optimal number of maneuvers is determined. In [29], a mixed-integer linear program results from combining collision avoidance, trajectory optimization, and fleet assignment to obtain the optimal solution for spacecraft maneuvers. A robust linear programming technique is proposed in [30]. The maneuver can be constructed by solving a linear programming problem with no integer constraints and guaranteeing collision avoidance with respect to bounded navigation uncertainty.

1.2 Attitude Control

The development of a spacecraft attitude control system is often a labor-intensive process due to the need for an accurate characterization of the spacecraft inertia. Determining and predicting the mass properties of a spacecraft may be difficult, however, due to fuel usage, deployment, structural articulation, and docking. To alleviate this requirement, the control algorithms given in [31–33] are inertia-free in the sense that they require no prior modeling of the mass distribution. An adaptive inertia-free attitude control law is given in [34] for minimum-time maneuvers. Inertia-free control laws for motion-to-rest and tracking are given in [31, 35, 36].

Attitude control laws use various parameterizations of the rotation Lie group SO(3). Euler angles are conceptually the simplest, but cannot represent all angular velocities due to gimbal lock. A related difficulty arises in the use of Rodrigues parameters and modified Rodrigues parameters, which have singularities at 180-deg and 360-deg rotation angles, respectively. The most common attitude representation is based on quaternions, which can represent all attitudes and all angular velocities, but provide a double cover of SO(3), that is, each physical attitude is represented by two elements of the 4-dimensional sphere S^3. A continuous controller designed on the set of Euler parameters can thus inadvertently command the spacecraft to needlessly rotate as much as 360 degrees to reach the commanded attitude. This is known in the literature as the unwinding problem [37]. The inertia-free, quaternion-based control laws in [31, 38, 39] exhibit unwinding.

There are several approaches to avoid unwinding. The traditional approach is to implement a logic statement that confines the quaternions to a hemisphere of S^3 [40]. This approach introduces a discontinuous control law, which can lead to chattering in the presence of noise. This issue and associated complications are addressed in [41].

The results of [32] are based on rotation matrices, which constitute a one-to-one representation of physical attitude without attitude or angular-velocity singularities [42]. Since SO(3) is a compact manifold, every continuous vector field on it necessarily possesses more than one equilibrium, in fact, at least four. This means that global convergence on SO(3) under continuous, time-invariant control is impossible. Consequently, the objective of [32, 43, 44] is almost global stabilization, where the spurious equilibria are saddle points. Although the derivation of the inertia-free controller in ref. [32] is based on rotation matrices, the relevant attitude error given by the S-parameter (see (4.27)) can be computed from any attitude parameterization, such as quaternions or modified rodrigues parameters, and thus the continuous inertia-free controllers presented in [32] are not confined to rotation matrices.

1.2.1 Magnetic Attitude Control

Satellites in low-Earth orbit (LEO) can take advantage of the Earth's magnetic field for attitude control [45, 46]. In particular, magnetic actuation is an elegant and efficient way to change the total angular momentum of a spacecraft without using mass ejection, such as thrusters. Consequently, magnetic actuation can reduce or remove the need for fuel. For small spacecraft, the benefits of magnetic actuation include reduced cost, power, weight, and spatial efficiency.

The challenging aspect of magnetic actuation is that the torque produced on the spacecraft lies in the plane that is perpendicular to the local direction of Earth's geomagnetic field. The spacecraft is thus, at each moment in time, underactuated. Nevertheless, Earth's geomagnetic field is sufficiently varying in time and space that, for orbits not coinciding with Earth's magnetic equator (when using a nonrotating dipole model of the geomagnetic field), the spacecraft is fully controllable [47].

Magnetic attitude control has been studied [48], and various techniques have been developed for both linear and nonlinear problem formulations. Periodic approximations of the time-variation of the geomagnetic field are considered in refs. [49–51], a model predictive controller is developed in ref. [48], and Lyapunov methods are applied in ref. [52].

An additional challenge in magnetic actuation, is the fact that the magnitude and direction of the local geomagnetic field may be uncertain. Although the geomagnetic field is modeled and updated periodically [53], these models have limited accuracy, and forecasts of the geomagnetic field may be erroneous due to unmodeled effects and unpredictable disturbances [54]. Consequently, it is desirable to develop control techniques for magnetic actuation that rely solely on current, on-board measurements of the geomagnetic field.

1.3 Contributions and Outline

Contributions of this research are:

- The development of an MPC controller for three dimensional constrained rendezvous and docking maneuvers.
- The development of an on-board relative motion maneuver planning approach for debris avoidance that can handle set bounded disturbances.
- The extension of inertia-free control laws to spacecraft actuated by reaction-wheels, CMGs, and magnetic torquers.

- The development of a novel stabilization technique for linear time-varying systems and the application to both magnetically actuated spacecraft, and spacecraft rendezvous maneuvers on elliptic orbits.

The dissertation is organized by method, with each section developing control strategy and applying it to spacecraft orbital and/or attitude case studies. Derivations of the equations of motion used can be found in Appendix A, for orbital dynamics, and Appendix B, for attitude dynamics of spacecraft with momentum exchange devices, where the derivation is done carefully with clear and transparent account for all the relevant assumptions.

In Chapter 2, we present an extension of the approach developed in [12–14]. This includes the treatment of three dimensional relative motion maneuvers with three dimensional LoS cone constraints, the use of an MPC controller to prescribe Δv impulsive velocity changes rather than piecewise constant thrust profiles as in [12–14], and the demonstration of the ability to transition between MPC guidance in the spacecraft rendezvous phase and MPC guidance in the spacecraft docking phase, with requirements, constraints, and sampling rates specific to each phase. To avoid the need for a long MPC control horizon or long sampling periods in the rendezvous phase, a reference governor like approach, where the desired equilibrium set-point is replaced by a virtual set-point [55], is employed. In addition, bandwidth constraints on the spacecraft attitude control system are treated, while thrust direction constraints are handled by introducing an appropriate penalty term in the cost function and a relative-distance dependent constraint on the thrust vector. Also, three dimensional obstacle avoidance is demonstrated using a dynamically reconfigurable hyperplane constraint. The obstacle is assumed to be changing in size, which corresponds to changes in the estimates of its location. The MPC controller is validated on a full nonlinear model of spacecraft orbital motion, and it is demonstrated that the MPC feedback can be implemented with only measurements of relative angles and relative range. To accomplish the latter, an Extended Kalman Filter (EKF) is utilized to provide state estimates for the MPC controller. Simulation results based on a set of parameters representative of a small spacecraft with limited thrust capability are shown.

In Chapter 3, we describe the development of an on-board maneuver planning approach based on the use of constraint-admissible positively invariant sets [56]. The sets determine connectivity between forced and unforced spacecraft equilibria in the Clohessy-Wiltshire-Hill (CWH) relative motion frame [57]. The collection of equilibria form a *virtual net* in the vicinity of the spacecraft. Two equilibria are connected if a choice of a Linear Quadratic (LQ) feedback gain can be made that results in a transition between the equilibria which avoids collision with a potentially moving debris/obstacle while satisfying limits on thrust. A connectivity graph for all the equilibria in the net is constructed based on *fast growth dis-*

tance computation between two ellipsoidal sets, while real-time graph search algorithms are used to optimize an equilibria hopping sequence to avoid debris collisions. Unlike trajectory optimization, the method does not rely on precise assignment of spacecraft position along the trajectory, and is able to assure robustness to unmeasured (but set-bounded) disturbances and uncertainties.

The inertia-free control laws in refs. [31–33] assume that 3-axis input torques can be specified without on-board momentum storage, which implies implementation in terms of thrusters. However, attitude control laws are often implemented with momentum exchange devices, and thus the on-board stored momentum varies with time. To account for this effect, in Chapter 4, we extend [32] to handle reaction wheel and CMG based actuation. Additionally, we extend the control law to a magnetic actuation scheme. Like the inertia-free control laws in refs. [31–33], the tuning of this control law requires no knowledge of the mass properties of the spacecraft, and we specify the necessary assumptions and modeling information concerning the actuators and their placement relative to the bus.

In Chapter 5 we develop a forward-propagating Riccati-based (FPR) linear time-varying (LTV) feedback controller. FPR control is a technique for stabilizing LTV systems without the need for knowing the dynamics in advance. We apply the FPR controller to spacecraft magnetic actuation. As in ref. [49], the controller uses a linear time-varying model of the dynamics, but makes no periodicity assumptions, which are accurate only to first order. Since FPR feedback requires knowledge of only the current magnetic field, this approach obviates the need for advance knowledge of the geomagnetic field and thus does not rely on either geomagnetic approximations or forecasts. The controller given in ref. [52] also has this feature, and similarly works based on a measurement of the geomagnetic field at the current time. We show through simulations that the FPR controller is robust to realistic error sources, including the nonlinearities of attitude control that are not captured by the linearized model, actuator saturation, and noisy magnetic measurements. We consider an output feedback configuration, where angular rate measurements are not used. Additionally, we use FPR control to address a class of relative motion control problems for spacecraft on elliptic orbits, as the linearized equations of motion are time-varying. Elliptic orbits are used to deploy a variety of spacecraft for communications and planet/star observation purposes. For instance, Molniya and Tundra orbits host communication satellites launched from predominately northern latitudes [58]. Based on extensive simulations on a nonlinear model that includes perturbation forces, the FPR controller stabilizes spacecraft relative motion dynamics on elliptic orbits, and is robust to many error sources, including severe thrust magnitude and direction deviations, and even intermittent thrust availability.

Finally, in Chapter 6, we provide concluding thoughts and ideas for future work.

1.4 Relevant Publications

The following publications are related to the subject matter of this dissertation.

Predictive:

- A. Weiss, M. Baldwin, R. S. Erwin, and I. Kolmanovsky, "Spacecraft Constrained Maneuver Planning for Moving Obstacle Avoidance Using Positively Invariant Constraint Admissible Sets," *Proc. Amer. Contr. Conf.*, Washington, DC, June 2013.

- A. Weiss, M. Baldwin, R. S. Erwin, and I. Kolmanovsky, "Spacecraft Constrained Maneuver Planning Using Positively Invariant Constraint Admissible Sets," *Bar-Itzhack Memorial Symposium*, Haifa, Israel, October 2012.

- A. Weiss, I. Kolmanovsky, M. Baldwin, and R. S. Erwin, "Model Predictive Control of Three Dimensional Spacecraft Relative Motion," *Proc. Amer. Contr. Conf.*, pp. 173-178, Montreal, Canada, June 2012. [Best Presentation in Session Award].

- M. Baldwin, A. Weiss, I. Kolmanovsky, and R. S. Erwin, "Spacecraft Debris Avoidance using Positively Invariant Constraint Admissible Sets," *AAS/AIAA Space Flight Mechanics Meeting*, Charleston, SC, January 2012, AAS-12-250 .

Adaptive:

- A. Weiss, A. Sanyal, I. Kolmanovsky, and D. S. Bernstein, "Inertia-Free Spacecraft Attitude Control with Reaction-Wheel Actuation," *AIAA Journal of Guidance, Control, and Dynamics*. To Appear.

- A. Weiss, G. Cruz, K. Agarwal, Y. Rahman, M. Medikeri, A. Xie, M. Camblor, I. Kolmanovsky, and D. S. Bernstein, "Inertia-free Attitude Control Laws for Spacecraft with Torquers, Thrusters, and Wheels," *Bar-Itzhack Memorial Symposium*, pp. 322-391, Haifa, Israel, October 2012.

- K. Agarwal, A. Weiss, I. Kolmanovsky, and D. S. Bernstein, "Inertia-Free Spacecraft Attitude Control with Control-Moment-Gyro Actuation," *AIAA Guid. Nav. Contr. Conf.*, Minneapolis, MN, August 2012, AIAA-2012-5003-282.

- A. Weiss, I. Kolmanovsky, and D. S. Bernstein, "Inertia-Free Attitude Control of Spacecraft with Unknown Time-Varying Mass Distribution," *Proc. 62nd IAC*, Cape Town, South Africa, October 2011, IAC-11-C1.5.9.

- A. Weiss, X. Yang, I. Kolmanovsky, and D. S. Bernstein, "Inertia-Free Spacecraft Attitude Control with Reaction-Wheel Actuation," *AIAA Guid. Nav. Contr. Conf.*, Toronto, August 2010, AIAA-2010-8297-163.

Time-varying:

- A. Weiss, M. Baldwin, R. S. Erwin, I. Kolmanovsky, and D. S. Bernstein, "Forward-Integration Riccati-Based Feedback Control for Spacecraft Rendezvous Maneuvers on Elliptic Orbits," *Proc. Conf. Dec. Contr.*, pp. 1752-1757, Maui, HI, December 2012.

- A. Weiss, I. Kolmanovsky, and D. S. Bernstein, "Forward-Integration Riccati-Based Output-Feedback Control of Magnetically Actuated Spacecraft," *AIAA Guid. Nav. Contr. Conf.*, Minneapolis, MN, August 2012, AIAA-2012-5042-137.

- A. Weiss, I. Kolmanovsky, and D. S. Bernstein, "Forward-Integration Riccati-Based Output-Feedback Control of Linear Time-Varying Systems," *Proc. Amer. Contr. Conf.*, pp. 6708-6714, Montreal, Canada, June 2012. [Best Presentation in Session Award].

CHAPTER 2

Model Predictive Control for Spacecraft Rendezvous and Docking

This chapter develops an MPC controller for performing 3-dimensional spacecraft rendezvous and docking maneuvers. The equations of motion for spacecraft orbital dynamics are reviewed in Appendix A. Our formulation of the MPC controller is geared towards spacecraft of the XSS-11 type [11]. By applying ideas in this chapter to appropriately modified cost and constraints, other relative motion, rendezvous, and proximity maneuvering problems may be similarly handled.

2.1 Model Predictive Controller

MPC represents an attractive framework to deal with the multitude of state and control constraints in spacecraft relative motion problems. MPC generates control actions by applying a moving horizon trajectory optimization to predictions based on a system model subject to pointwise-in-time state and control constraints [59, 60]. The control is periodically recomputed with the current state estimate as an initial condition, thereby providing a feedback action that improves robustness to uncertainties and disturbances. A special formulation of the MPC optimization problem, where rendezvous is separated from docking, is necessary to avoid a long control horizon and avoid solving a highly complex online optimization problem. For instance, longer sampling periods are introduced in the rendezvous phase, when the approaching spacecraft is further away from the target, versus the docking phase, when the approaching spacecraft is closer to the target. Various other steps need to be taken to convert the maneuver requirements into an MPC problem formulation that can be handled efficiently by MPC solvers. In particular, and as in the planar case [12–14], we seek formulations that can be treated by quadratic programming (QP) solvers and have low computation overhead.

2.1.1 Penalties and Constraints

During rendezvous and docking, the space vehicle must adhere to various constraints [12–14] while executing the maneuver. See Figure 2.1 for a schematic of a docking maneuver subject to constraints. Depending on the portion of the relative motion maneuver being

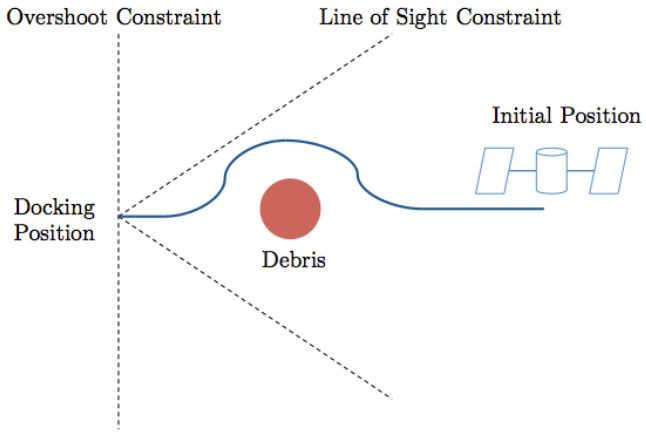

Figure 2.1: Schematic of a spacecraft docking maneuver subject to line of sight, overshoot, and debris avoidance constraints.

completed, different constraints must be addressed pertaining to the vehicle and the path it takes. For example, a space vehicle can not produce limitless thrust in any direction; therefore, thrust magnitude and direction must be limited during both rendezvous and docking. However, the orientation of the vehicle is only constrained during the docking phase and does not play a major role in the rendezvous phase. Certain constraints may be treated as 'soft' to enhance solution feasibility, and as such we implement them as penalties in the MPC cost.

We consider the discrete-time spacecraft model (A.3) with the velocity impulses $U_k = \Delta v_k = \Delta[\dot{x}_k \ \dot{y}_k \ \dot{z}_k]^{\mathrm{T}}$ as the control signals. Impulse-based control of spacecraft is often assumed in relative motion problems [4]. Maximum Δv constraints

$$|U_k|_\infty \leq u_{\max}, \tag{2.1}$$

are implemented during both rendezvous and docking to adhere to the finite thrusting capability of the vehicle, where $u_{\max} = 10$ m/sec. During the docking phase, thrust direction limits are imposed so that the spacecraft does not fire its thrusters into the target. This requirement is treated by imposing a time-varying control constraint. For example, consid-

ering an in-orbital track target with an approach from $+y$, this constraint is given by

$$\Delta \dot{y}_k \leq \mu e^{-\beta k}, \quad \mu > 0, \beta > 0, \tag{2.2}$$

that is, the thrust in the y-direction is progressively constrained as the spacecraft approaches the target. We consider a spacecraft configuration that includes only one thruster. To enable an attitude controller to keep up with commanded thrust direction changes, we augment the MPC cost function with a term

$$\sum_{k=0}^{N} (U_k - U_{k-1})^{\mathrm{T}} R^{\text{attitude}} (U_k - U_{k-1}), \tag{2.3}$$

where $R^{\text{attitude}} = R^{\mathrm{T}}{}_{\text{attitude}} > 0$. This term penalizes the rate of thrust vector changes and we found it to be effective in dealing with attitude controller bandwidth and capability limits. R^{attitude} is made to be a function of control magnitude so that it retains the same relative weight in the cost function irrespective of the magnitude of U_k. The quadratic form of (2.3) facilitates the application of QP-based MPC solvers.

Several path constraints are implemented to ensure a safe trajectory for the vehicle. During the docking phase, the target vehicle's sensors constrain the approaching space vehicle. We implement this constraint using a Line of Sight (LoS) cone that emanates from the docking port [15]. LoS cone constraints in three dimensions are quadratic. Since we subsequently formulate the MPC problem as a quadratic program (QP) with affine constraints, we reformulate these constraints using an inner polyhedral approximation given by

$$A_{\text{cone}} X \leq b_{\text{cone}}. \tag{2.4}$$

The code for calculating this approximation is given in Appendix C.1. We treat the LoS constraint as soft by imposing a penalty for deviations outside the cone and augmenting this penalty to the MPC cost function. This cost is given by

$$\sum_{k=1}^{N} \lambda \mathbf{1}^{\mathrm{T}} (A_{\text{cone}} X_k - b_{\text{cone}})_+, \tag{2.5}$$

where $(\cdot)_+$ denotes positive part ($x_+ = x$ if $x > 0$ and 0 otherwise; applied componentwise), and λ is the weight. In order to avoid missing an in-track target, an overshoot constraint

$$y_k \geq 0, \tag{2.6}$$

is implemented. Constraints used in other docking approaches may be different but will have similar functional form.

Obstacle/debris avoidance is a non-convex problem with several possible formulations (e.g. Mixed Integer Programming [29]). For this work, as limited processing power is a driving factor, obstacle/debris avoidance was formulated using linear dynamically reconfigurable constraints. A hyperplane is chosen to separate the obstacle/debris from the space vehicle. The constraint is given by

$$n_k^{\mathrm{T}} X \geq n_k^{\mathrm{T}} r_{\mathrm{c},k}, \tag{2.7}$$

where n_k is the normal vector to the hyperplane, $r_{\mathrm{c},k}$ is a point on the boundary of the uncertainty ellipsoid associated with overbounding the obstacle/debris, and X is the position of the vehicle. The hyperplane is rotated with a preselected rotation rate over the length of the maneuver by varying n_k and $r_{\mathrm{c},k}$ so that the hyperplane normal guides the target spacecraft around the obstacle. The avoidance constraint (2.7) is capable of handling a 'growing' or 'uncertain' obstacle/debris by manipulating $r_{\mathrm{c,k}}$. Note that the hyperplane rotation direction is dictated as a part of the problem formulation.

2.1.2 MPC Problem Formulation

By using linearized equations of motion, linear equality and inequality constraints, and quadratic costs on the states and control actions, the MPC problem may be formulated as a quadratic programming (QP) problem. QPs can be solved using any number of generic solvers (MATLAB's quadprog, CPLEX, PQP, etc.) [61]. Alternatively, using multiparametric programming, an explicit MPC approach that does not require on-board optimization may be used [62, 63]. The downside of explicit solutions is that they are not straightforward to apply when dynamics of constraints are time-varying, the do not scale well to large problems, and the execution times of look-up tables and logic may be longer than simply solving the QP.

In this work, we solve the QP in real time using CVXGEN, which generates very efficient custom primal-dual interior-point solvers [64]. Unlike the generic solvers which solve single problem instances, CVXGEN accepts high level descriptions (see Appendix C.2) of QP families and turns them into highly efficient flat, library-free C code that solve many problem instances. This strategy allows CVXGEN to exploit the structure (sparsity) of the specific QP family for fast run-time execution. This is especially useful in an MPC framework where the QP has structure and is repeatedly solved at each sampling instant. The generated code does not branch, which allows for predictable run times, and is orders

of magnitude faster than generic solvers [64], both highly desirable features for embedded applications with limited processing power such as on-board a spacecraft. The CVXGEN generated custom solver can handle time-varying dynamics and constraints. For instance, it is applicable to maneuvers on elliptic orbits.

Based on practical considerations, the problem is separated into distinct rendezvous and docking phases. In the rendezvous phase, the spacecraft is a significant distance away from the target. A sampling period of 120 sec is used and a Δv magnitude constraint is enforced. Since the thrust of the spacecraft is limited, to avoid the need for a long control horizon, a reference governor like approach is introduced. In this approach, the desired equilibrium set-point is dynamically modified. Instead of locating the set-point at the origin, the QP determines forced equilibria between the approaching spacecraft and the target. We found that if we do not include a reference governor, we are not able to attain closed-loop stability. The prediction horizon is not long enough for the optimization problem to 'see' the target and, thus, cannot recover from aggressive initial thrust. Introducing a dynamically modified set-point moderates the control action. The rendezvous phase QP is given by

$$\begin{aligned}
\text{minimize} \quad & \sum_{k=1}^{N-1} (X_k - X_\text{s})^T Q (X_k - X_\text{s}) \\
& \quad + \sum_{k=1}^{N-1} (U_k - U_\text{s})^T R (U_k - U_\text{s}) \\
& \quad + (X_N - X_\text{s})^T Q^\text{final} (X_N - X_\text{s}) + X_\text{s}^T P X_\text{s} \\
\text{subject to} \quad & X_{k+1} = A X_k + B U_k \\
& X_\text{s} = A X_\text{s} + B U_\text{s} \\
& |U_k|_\infty \leq u_\text{max} \\
& n_k^\text{T} r_{c,k} - n_k^\text{T} X_k \leq 0
\end{aligned} \tag{2.8}$$

where N is the control and prediction horizon, X_k and U_k are the state and control variables to be determined, X_s and U_s are the forced equilibrium state and control determined as part of the solution, Q and R are the weighting matrices, P is the weighting on the forced equilibrium states, and Q^final is the terminal state weighting matrix determined from the solution of the Riccati equation for the unconstrained infinite horizon problem. The equality constraint $X_{k+1} = AX_k + BU_k$ comes from the discrete CWH model (Appendix A), and $|U_k|_\infty \leq u_\text{max}$ is the maximum Δv constraint (2.1). If obstacle/debris avoidance is not part of the problem formulation, the constraint $n_k^\text{T} r_{c,k} - n_k^\text{T} X_k \leq 0$ is omitted.

When the approaching spacecraft enters a specified box around the target, the docking phase begins. During this phase the reference governor type action is removed as it is no

longer necessary; the origin, that is the true desired equilibrium can be reached over the optimization horizon under the problem constraints. The sampling period is reduced to 20 sec to facilitate faster control updates. A LoS cone constraint is imposed and is treated as soft via a polyhedral cost penalty. A thrust direction constraint (2.2) and an in-track target overshoot constraint (2.6) are also imposed. Additionally, the rotation that the approaching spacecraft must perform between thrust impulses is approximately penalized by imposing a cost on change in control policy (2.3). The docking phase QP for constraints that are configured for an in-track V-bar approach, is given by

$$\begin{aligned}
\text{minimize} \quad & \sum_{k=1}^{N-1} X_k^{\mathrm{T}} Q X_k + U_k^{\mathrm{T}} R U_k + X_N^{\mathrm{T}} Q^{\text{final}} X_N \\
& + \sum_{k=1}^{N} \lambda \mathbf{1}^{\mathrm{T}} (A_{\text{cone}} X_k - b_{\text{cone}})_+ \\
& + \sum_{k=0}^{N} (U_k - U_{k-1})^{\mathrm{T}} R^{\text{attitude}} (U_k - U_{k-1}) \qquad (2.9) \\
\text{subject to} \quad & X_{k+1} = A X_k + B U_k \\
& |U_k|_\infty \leq u_{\max} \\
& \Delta \dot{y}_k \leq \mu e^{-\beta k} \\
& y_k \geq 0
\end{aligned}$$

where X_k and U_k are the state and control variables to be determined, Q and R are the weighting matrices, and Q^{final} is the terminal state weighting matrix determined from the solution of the Riccati equation. The LoS cone constraint and rotation rate constraint are implemented as soft constraints in the cost function using A_{cone} and b_{cone} for LoS and the weighting matrix R^{attitude} for the rotation rate. The equality constraint and the thrust constraint are the same as the rendezvous phase.

2.1.3 Implementation using State Estimates

The MPC controller may be implemented using only the output measurements of relative range and relative angles, given by

$$Y_1 = \sqrt{x^2 + y^2 + z^2} + \nu_1,$$

$$Y_2 = \text{atan2}\,(x, y) + \nu_2,$$

$$Y_3 = \text{atan2}\left(z, \sqrt{x^2 + y^2}\right) + \nu_3,$$

where x, y and z are the relative x-position, y-position and z-position, respectively, atan2 denotes the four quadrant arc-tangent, and ν_1, ν_2, and ν_3 are the measurement noise in each output channel. An Extended Kalman Filter (EKF) based on the CWH equations is used to estimate the spacecraft states given the measurements [65]. The output measurement equations are nonlinear and hence the convergence of the EKF estimates is only expected when the state estimate is initialized sufficiently close to the true state.

2.2 Stability Analysis

In the preceding section we presented an MPC problem formulation that we found to be effective in completing spacecraft rendezvous and docking maneuvers. In this section we discuss additional steps we have considered beyond numerical simulations in ensuring closed-loop stability.

2.2.1 Terminal State Constraint

In the classical MPC formulation, MPC stability is guaranteed when imposing a terminal state constraint i.e. $x_N = 0$, as it requires the state to be equal to the equilibrium at the end of the horizon [59]. Imposing this constraint renders the MPC value function a Lyapunov function.

A downside of the terminal state constraint is that it requires the horizon to be long enough so that, subject to all the problem constraints, a maneuver is feasible. The domain of attraction of the controller under this architecture is all states steerable to the equilibrium in N steps, where N is the horizon. The terminal state constraint can be relaxed to a terminal set constraint.

2.2.2 Terminal Penalty Based on LQR

Setting $Q^{\text{final}} = P$, where P is the solution to the Discrete Algebraic Riccati Equation (DARE), then, near the origin where constraints are inactive, the solution to the QP is

an LQ controller. The maximum positively invariant set O_∞ of the LQ controller under constraints is a guaranteed domain of attraction for the MPC controller [59].

2.2.3 Simulation Study and Discussion

In our problem formulations we use the terminal penalty based on LQR. We compare the difference in fuel consumption with and without a terminal state constraint for a rendezvous phase simulation without reference governor action or obstacle avoidance constraints. Figure 2.2 provides maneuver comparisons for 2 initial conditions. Total Δv for (a) 0.9051 m/s, (b) 0.9174 m/s, (c) 27.3419, (d) 31.6235.

The results suggest that when the horizon is long enough so that the optimization problem drives the spacecraft towards the desired equilibrium, as it is in our case, adding a terminal penalty leads to a performance degradation in fuel without much trajectory perturbation. We subsequently rely on only a terminal penalty based on LQR, which guarantees local stability.

2.3 Case Studies

In subsections 2.3.1-2.3.4 we provide case studies that highlight various unique features of our MPC solution. Subsection 2.3.5 provides three complete rendezvous and docking maneuvers using only relative range and relative angle measurements.

2.3.1 Attitude Control Penalty

The effects of including the attitude control penalty $R^{\text{attitude}} \neq 0$ are apparent in Figure 2.3. The average angle between consecutive velocity changes is smaller on average when including the penalty, reducing the effort of the attitude control system to change the orientation before the next thrust event.

2.3.2 Debris Avoidance

Fig. 2.4 shows the effect of hyperplane rotation rate on maneuvers for a growing obstacle. The growing obstacle reflects the increasing amount of uncertainty about its relative position.

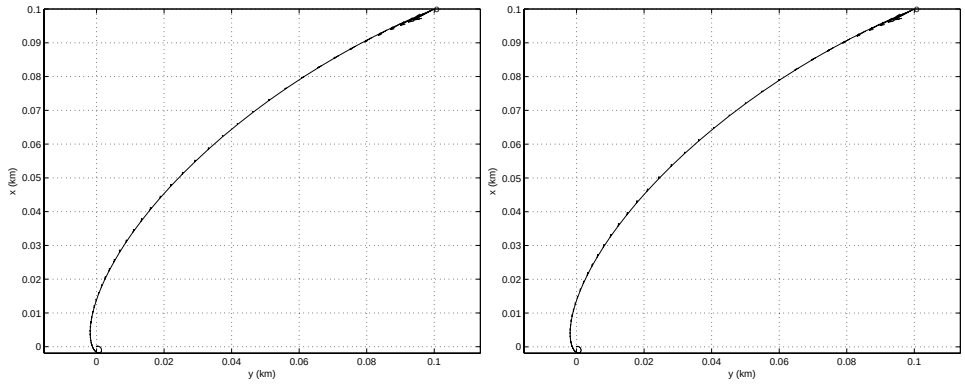

(a) No Terminal State Constraint (b) $x_N = 0$

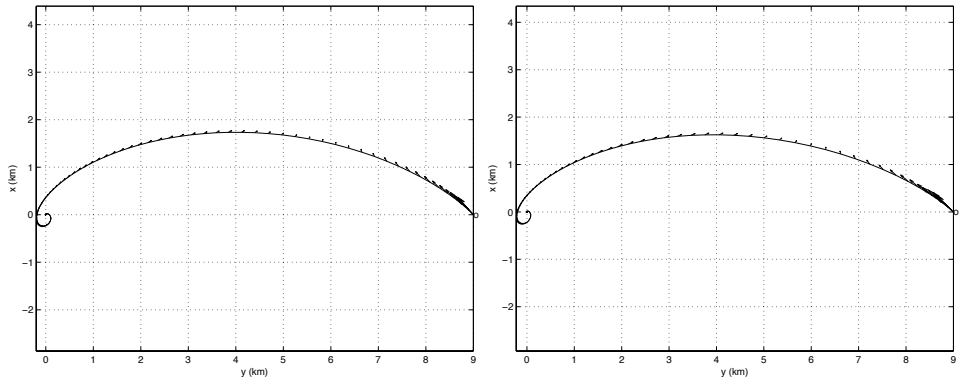

(c) No Terminal State Constraint (d) $x_N = 0$

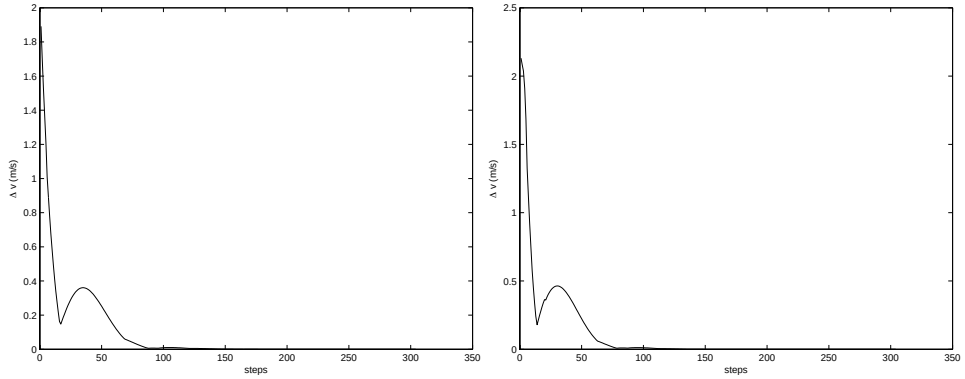

(e) No Terminal State Constraint (f) $x_N = 0$

Figure 2.2: (a): No terminal state constraint. $x_0 = [0.1\ 0.1\ 0.1\ 0\ 0\ 0]^{\mathrm{T}}$. (b): $x_N = 0$, $x_0 = [0.1\ 0.1\ 0.1\ 0\ 0\ 0]^{\mathrm{T}}$. (c),(d): The same as (a),(b) but with $x_0 = [0\ 10\ 0\ 0\ 0\ 0]^{\mathrm{T}}$ and the weighting on fuel R increased 1000 fold. (e),(f): The Δv comparison for (c),(d).

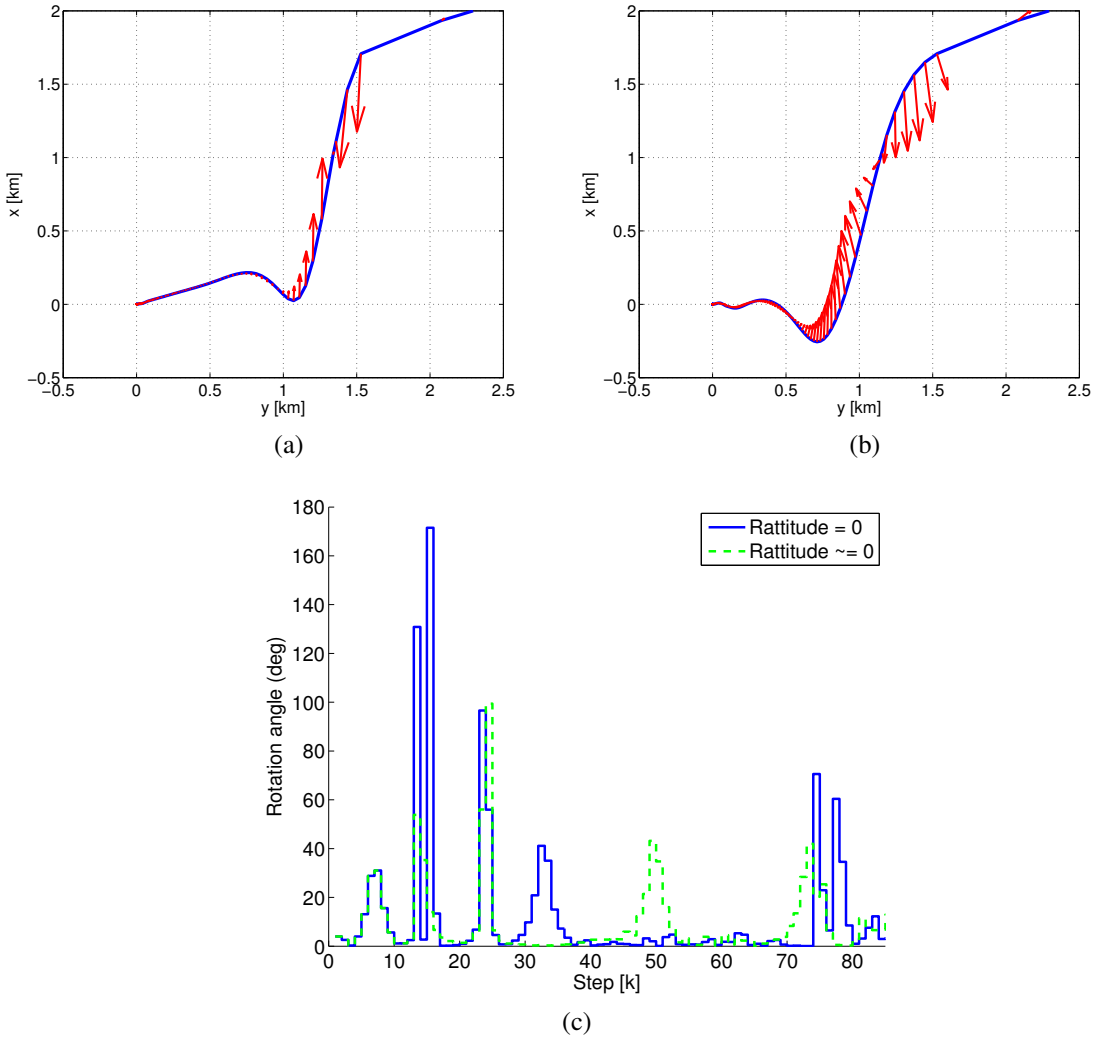

Figure 2.3: Spacecraft trajectory on x-y plane. Arrows indicate the direction and scaled magnitude of Δv's induced by thrusting. (a) With $R^{\text{attitude}} > 0$; (b) With $R^{\text{attitude}} = 0$; (c) Comparison of the angles between two consecutive velocity changes for the cases (a) and (b).

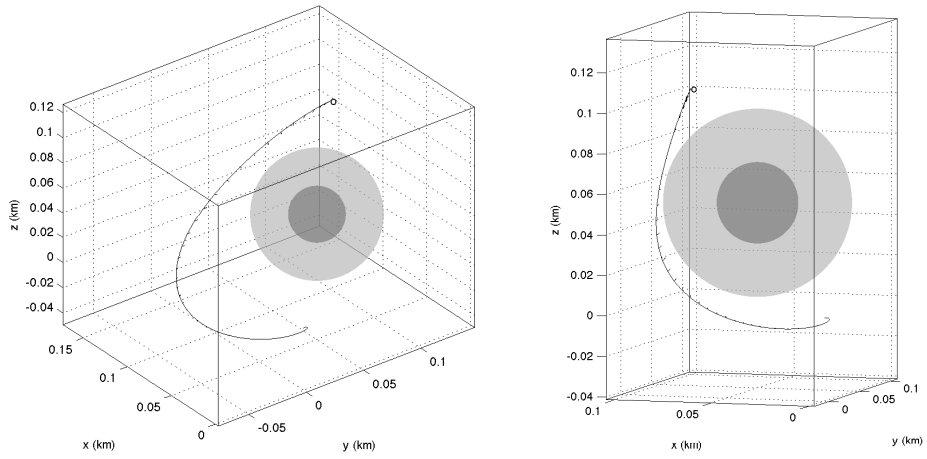

(a) Slower rotation rate (b) Faster rotation rate

Figure 2.4: Debris avoidance maneuvers using a rotating hyperplane constraint for two different rotation rates. The obstacle is growing, reflecting increasing levels of uncertainty.

2.3.3 Robustness to Nonlinearity

Fig. 2.5 illustrates the robustness of the Model Predictive Control (MPC) controller compared to that of an open-loop trajectory. Here, a 100 km in-track MPC maneuver that is successfully completed in a linear simulation is simulated open-loop using the nonlinear equations of motion (A.1) and compared to an MPC solution where the feedback is based on the true state given by the nonlinear model. Due to the nonlinearities that the linearized model does not capture, the open-loop maneuver does not result in successful rendezvous with the target, whereas the maneuver that uses systematic feedback corrections based on the true state does.

2.3.4 Domains of Attraction

The range of initial, non-zero velocity for which the MPC controller, under the specified thrust constraints, successfully brings the approaching spacecraft to the origin is shown in Fig. 2.6. The initial position of the spacecraft is $[0\ 2\ 0]^{\mathrm{T}}$ km. For initial velocity in the radial x direction of -10 to 20 m/s, the vehicle successfully reaches the target. Similarly, the z direction ranged between -10 and 10 m/s. A variation twice that of the z direction was successfully implemented in the y direction, which is expected given the natural stability of the crosstrack axis.

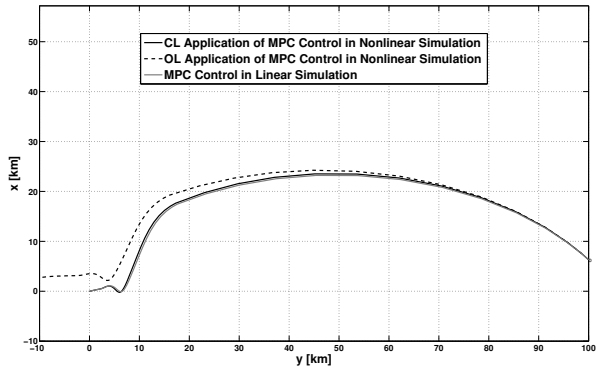

Figure 2.5: Spacecraft trajectories on x-y plane for MPC based on a linear simulation, with MPC based on nonlinear simulation, and with open-loop control based on a linear simulation.

2.3.5 Rendezvous and Docking Maneuvers

Three complete maneuvers are now considered:

Case 1

A phasing maneuver with the approaching spacecraft in the same orbit but at a different true anomaly than the target. The LoS cone is oriented along the orbital track. This maneuver is also known as as V-bar docking with initial spacecraft position along V-bar. The initial position is $[0.63\ 10\ 0]^{\mathrm{T}}$ km, and initial velocity is $[0\ 0\ 0]^{\mathrm{T}}$ km/s.

Case 2

The approaching spacecraft is in a lower orbit than the target. The LoS cone is positioned for V-bar docking. This maneuver is also known as V-bar docking with an initial spacecraft position along R-bar. The initial position is $[-2\ 0.126\ 0]^{\mathrm{T}}$ km, and initial velocity is $[0\ 0\ 0]^{\mathrm{T}}$ km/s.

Case 3

Same as Case 2 but with the LoS cone positioned for R-bar docking, i.e., oriented along the radial line.

The control horizon and the prediction horizon N is fixed at 30 steps. The sampling period in the rendezvous phase is 2 min and is 20 sec in the docking phase. The switch between the rendezvous and docking phases occurs when the estimated spacecraft position enters a 2 km box around the target. The spacecraft is in a nominal circular orbit at an

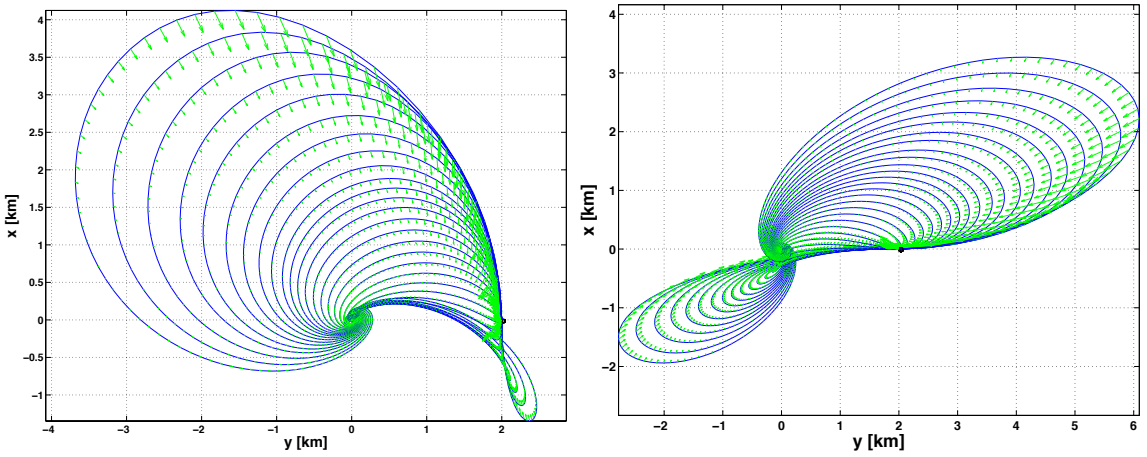

(a)

(b)

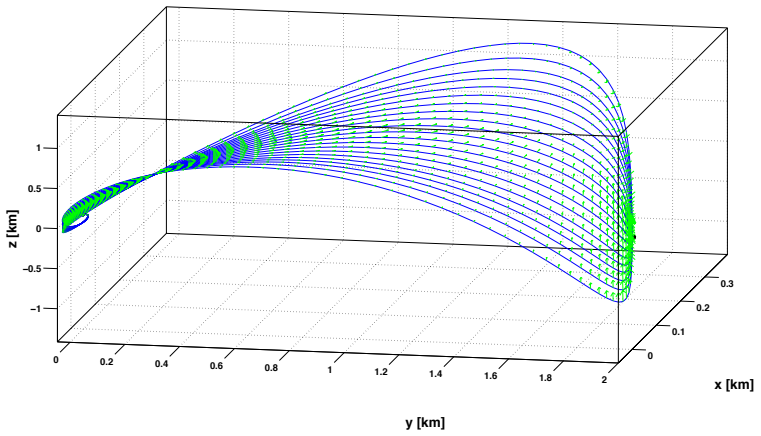

(c)

Figure 2.6: Spacecraft trajectories with varying nonzero initial velocities. Arrows indicate the direction and scaled magnitude of Δv's induced by thrusting: (a) With nonzero initial velocities from -10 m/s to 20 m/s in the x direction; (b) With nonzero initial velocities from -20 m/s to 20 m/s is the y direction; (b) With nonzero initial velocities from -10 m/s to 10 m/s is the z direction.

altitude of 850 km above the Earth. The fuel expenditure for all cases is summarized in Table 2.1.

2.3.5.1 Case 1: V-bar docking with initial spacecraft position along V-bar

The simulated MPC maneuver trajectories for V-bar docking with an initial spacecraft position along V-bar are shown in Figure 2.7. The simulation results are obtained based on the *nonlinear* relative motion model (A.1). The MPC controller uses an EKF with the linearized CWH model for prediction in order to estimate the spacecraft states based on relative range and angle measurements. The initial estimated state is $[-0.5\ 7\ 1.0\ 0\ 0\ 0]^{\mathrm{T}}$. The EKF estimates converge rapidly to the actual states. Note that the spacecraft motion is three dimensional even though the starting position is in the orbital plane. The out of orbital plane motion is excited since there is a non-zero initial estimation error of the spacecraft position in the z-direction that the MPC controller is trying to correct. Once the docking phase is started, the LoS cone constraint is activated. The trajectory enters into the LoS cone and proceeds towards the origin while satisfying the constraint. Large velocity changes are applied initially and become smaller and more gradual as the spacecraft approaches the origin; control activity increases immediately after entering the docking phase and then decays. The time history of the velocity change direction indicates that the thrust in the direction of the target is minimized as the spacecraft approaches the target.

A debris is introduced during the rendezvous phase at $[-0.5\ 7\ 1.0]^{\mathrm{T}}$ km. Fig. 2.8 shows the modified maneuver trajectories for a clockwise hyperplane rotation (Fig. 2.8b) and a counterclockwise hyperplane rotation (Fig. 2.8c). The obstacle 'grows' or becomes more uncertain as time progresses. The counterclockwise rotation of the hyperplane forces the spacecraft radially outward, thus increasing the fuel expenditure (see Table 2.1).

2.3.5.2 Case 2: V-bar docking with initial spacecraft position along R-bar

Figure 2.9 demonstrates a typical maneuver with the LoS cone constraint positioned for a V-bar approach [2]. The spacecraft, with initial position coordinates $[-2 \quad 0.126 \quad 0]^{\mathrm{T}}$ and initial position coordinate estimates $[-2.8 \quad -0.01 \quad 0.1]^{\mathrm{T}}$ starts the motion as in the R-bar approach. Once the docking phase is activated, the trajectory enters into the LoS cone positioned for a V-bar approach and proceeds towards the origin while satisfying the LoS cone constraint. The vehicle must use greater fuel at the beginning of the rendezvous phase to thrust the vehicle to enter the docking phase under the required conditions. The same increase in thrust demonstrated in the V-bar approach during the entry into the docking phase is evident in this case as well. This increase in thrust is necessary to meet the required

constraints of the docking phase.

2.3.5.3 Case 3: R-bar docking with initial spacecraft position along R-bar

Figure 2.10 demonstrates a maneuver similar to Case 2 but with the LoS cone constraint positioned for an R-bar approach. The behavior is qualitatively similar to the one in Figure 2.9. The constraints and maneuver requirements are satisfied using the proposed MPC approach.

Table 2.1: Total Δv for all maneuvers.

Test case	1			2	3
	No obstacle	CW	CCW		
MPC	.0368 km/s	.0369 km/s	.0414 km/s	.0073 km/s	.0145 km/s

2.3.6 Total Δv vs Time to Rendezvous

To study fuel usage (measured in terms of total Δv) relative to maneuver time, the relative weights Q and R are varied, generating a trade-off curve. This curve, shown in Fig. 2.11, demonstrates that shorter maneuver times may be achieved at the cost of increased fuel consumption.

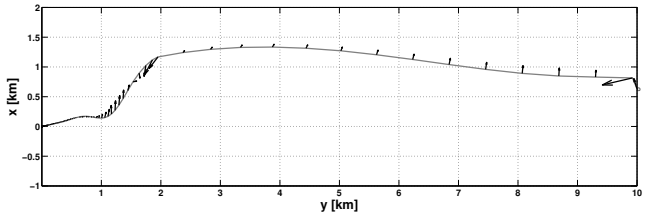

(a)

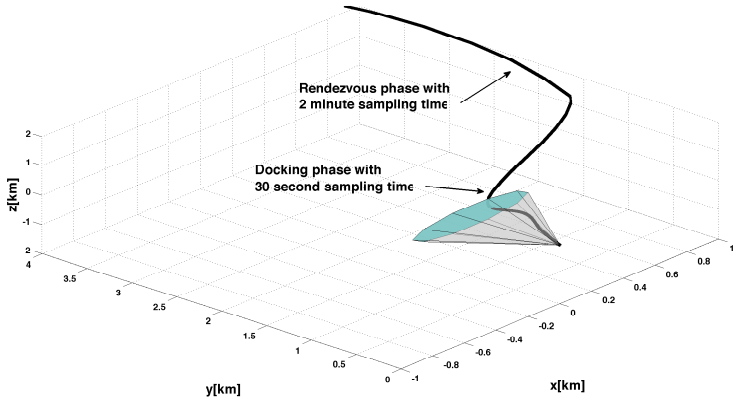

(b)

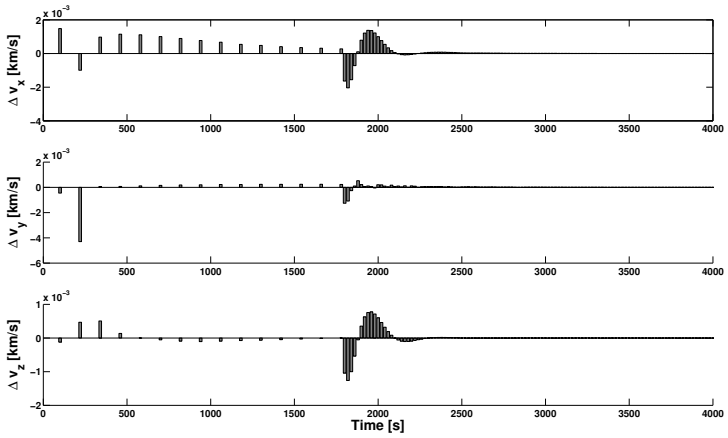

(c)

Figure 2.7: Case 1. (a) Spacecraft trajectory on *x*-*y* plane with constraints configured for V-bar docking. (b) Trajectory in 3D with rendezvous and docking phases and LoS cone constraints shown. (c) The three components of Δv showing control history through the rendezvous and docking phases.

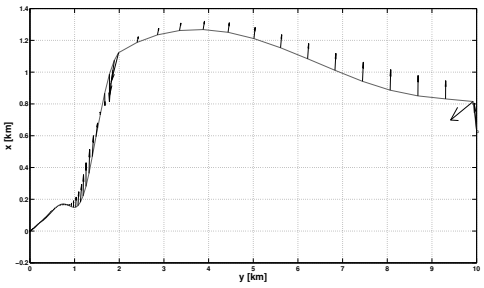

(a)

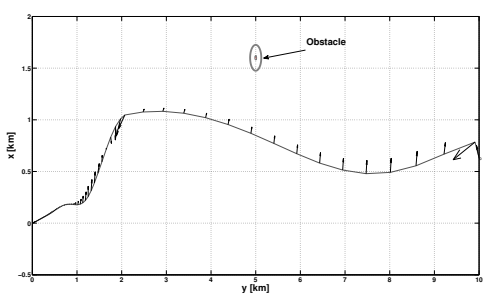

(b)

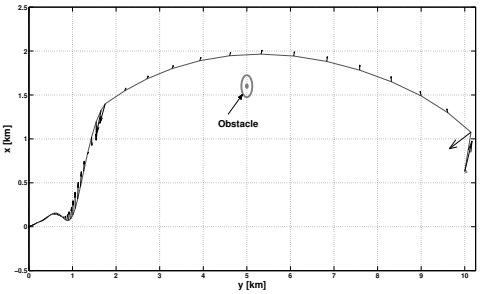

(c)

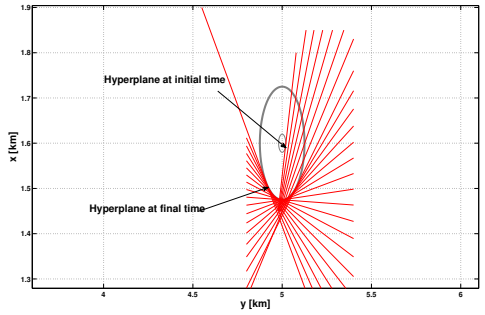

(d)

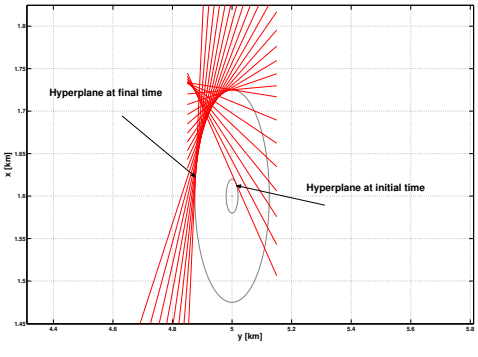

(e)

Figure 2.8: Case 1. (a) Spacecraft trajectory on *x*-*y* plane without an obstacle. Initial position is $[0.63\ 10\ 0]^{\mathrm{T}}$ (b) Trajectory in *x*-*y* plane with obstacle located at $[1.6\ 5\ 0]^{\mathrm{T}}$ and a clockwise rotation of the hyperplane. (c) Trajectory in *x*-*y* plane with obstacle located at $[1.6\ 5\ 0]^{\mathrm{T}}$ and a counterclockwise rotation of the hyperplane (d) Clockwise rotation of hyperplane. (e) Counterclockwise rotation of hyperplane.

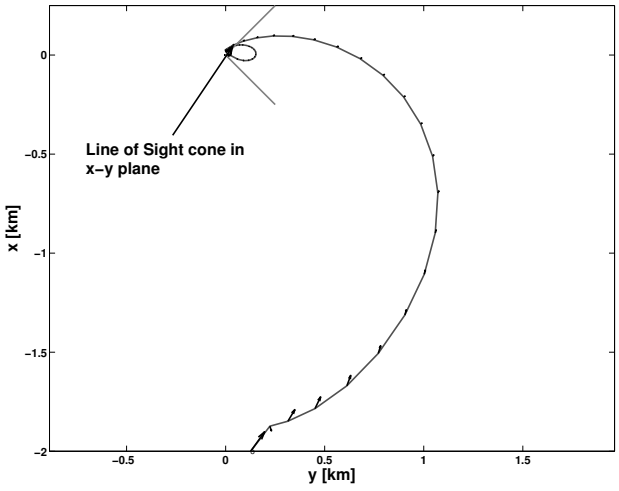

(a)

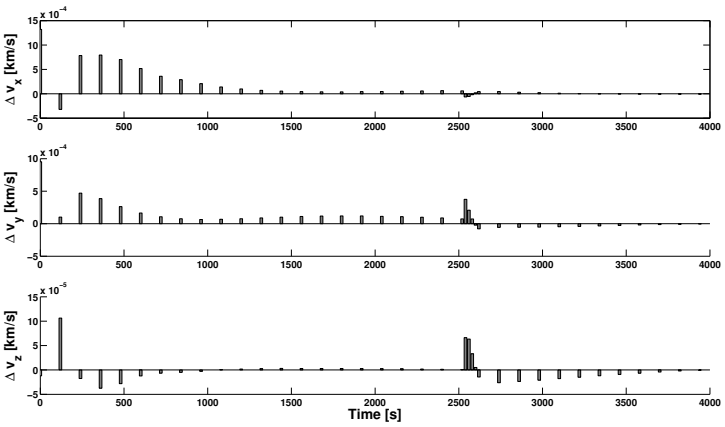

(b)

Figure 2.9: Case 2. (a) Spacecraft trajectory on *x*-*y* plane with initial position $[-2,\ 0.126,\ 0]^{\mathrm{T}}$ and the LoS cone pointed in the V-bar direction. (b) The three components of Δv.

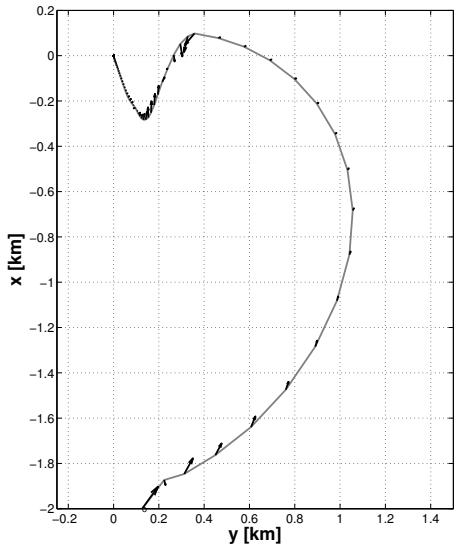

(a)

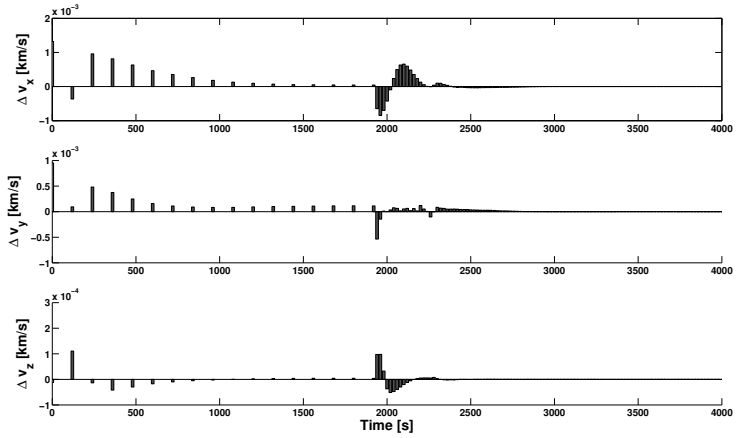

(b)

Figure 2.10: Case 3. (a) Spacecraft trajectory on x-y plane with initial position $[-2,\ 0.126,\ 0]^{\mathrm{T}}$ and the LoS cone pointed in the R-bar direction. (b) The three components of Δv.

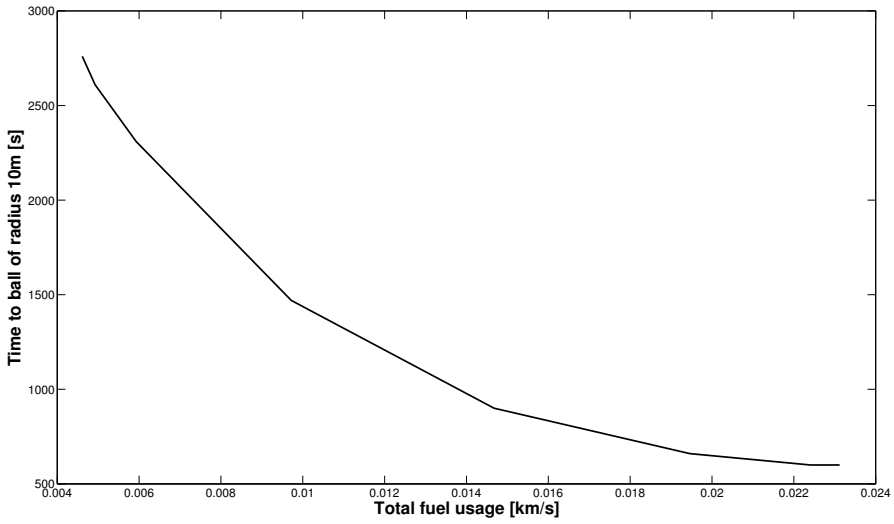

Figure 2.11: Trade-off curve demonstrating fuel usage of MPC controller with varying weight on fuel. Total fuel usage is determined by taking the sum of the two-norm of the control across time.

CHAPTER 3

Safe Positively Invariant Sets for Spacecraft Debris Avoidance

This chapter develops a chained invariant set method to avoid both static and moving debris during spacecraft relative motion maneuvers. The equations of motion for spacecraft orbital dynamics are reviewed in Appendix A. We use linearized equations of motion (A.3), where continuous thrust actuation $U_k = [F_{x,k},\ F_{y,k},\ F_{z,k}]^{\mathrm{T}}$ is assumed.

Our approach to debris avoidance is based on utilizing constraint-admissible positively invariant sets [56, 66–68] centered around spacecraft forced and unforced equilibria. A finite set of these equilibria used for constructing debris avoidance maneuvers is referred to as a *virtual net.* Given an estimate of the debris position, we build a connectivity graph that identifies the equilibria in the virtual net between which the spacecraft can move, with guaranteed collision-free motion and within the available thrust authority. We then employ graph search to determine an efficient path between the equilibria that ensures debris avoidance. One of the main reasons this framework is attractive compared to alternatives such as open-loop trajectory planning, is the ability to incorporate bounded disturbances such as thrust errors, air drag, and solar pressure.

3.1 Virtual Net

The virtual net comprises a finite set of equilibria, $X_e(r)$, corresponding to a finite set of prescribed spacecraft positions $r \in \mathcal{N} = \{r_1, r_2, \ldots, r_n\} \subset R^3$,

$$X_e(r_k) = \begin{bmatrix} r_k & 0 \end{bmatrix}^{\mathrm{T}} = \begin{bmatrix} r_{x,k} & r_{y,k} & r_{z,k} & 0 & 0 & 0 \end{bmatrix}^{\mathrm{T}},\ k = 1, \cdots, n, \tag{3.1}$$

whose velocity states are zero, and where n is the number of equilibria in the virtual net. See Figure 3.1. We assume that for all $r \in \mathcal{N}$, the corresponding values of control necessary to support the specified equilibria in steady-state satisfy the imposed thrust limits.

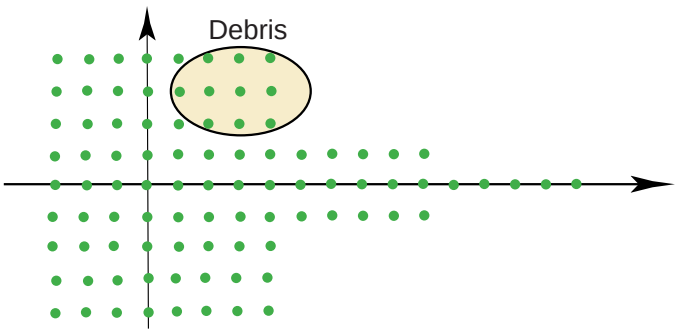

Figure 3.1: The virtual net for debris avoidance. Dots correspond to positions at equilibria, $X_e(r)$, on a virtual net. The ellipsoid represents the debris position and uncertainty.

3.2 LQ Controller with Gain Switching

A conventional Linear-Quadratic (LQ) feedback

$$U = K(X - X_e(r)) + \Gamma r = KX + H(K)r, \tag{3.2}$$

is used to control the spacecraft thrust to arrive at a commanded equilibrium (3.1), where

$$\Gamma = \begin{bmatrix} -3n^2 m_c & 0 & 0 \\ 0 & 0 & 0 \\ 0 & 0 & n^2 m_c \end{bmatrix},$$

$$H(K) = \Gamma - K \begin{bmatrix} I_3 \\ 0_3 \end{bmatrix},$$

and where I_3 denotes the 3×3 identity matrix while 0_3 denotes the 3×3 zero matrix. The LQ controller provides an asymptotically stable closed-loop system but does not enforce debris avoidance constraints.

To provide greater flexibility in handling constraints, a multimode controller architecture is employed [66]. Specifically, we assume that a finite set of LQ gains $K \in \mathcal{K} = \{K_1, \cdots, K_m\}$ is available to control the spacecraft. By using a large control weight in the LQ cost functional, motions with low fuel consumption yet large excursions can be generated; using a large control weight in the LQ cost, motions with short transition time can be generated [69]. We assume that a preference ordering has been defined and the gains are arranged in the order of descending preference, from K_1 being the highest preference gain to K_m being the lowest preference gain.

3.3 Positively Invariant Sets

The ellipsoidal set

$$\bar{C}(r,K) = \{X \in R^6 : \frac{1}{2}(X - X_e(r))^T P(K)(X - X_e(r)) \leq 1\} \subset R^6, \tag{3.3}$$

where

$$\bar{A}(K)^{\mathrm{T}} P \bar{A}(K) - P < 0, \tag{3.4}$$

$\bar{A}(K) = (A + BK)$, and $P = P(K) > 0$ is positively invariant for the closed-loop dynamics. Positive invariance implies that any trajectory of the closed-loop system that starts in $\bar{C}(r,K)$ is guaranteed to stay in $\bar{C}(r,K)$ as long as the same LQ gain K is used and the set-point command r is maintained. To achieve the positive invariance, the matrix P can be obtained as the solution of the discrete-time Riccati equation in the LQ problem or as the solution of the above Lyapunov equation for the closed-loop asymptotically stable system. We note that, because the system is linear, the positive invariance of $\bar{C}(r,K)$ implies the positive invariance of the scaled set

$$C(r,K,\rho) = \{X \in R^6 : \frac{1}{2}(X - X_e(r))^T P(K)(X - X_e(r)) \leq \rho^2\}, \quad \rho \geq 0.$$

Geometrically, the set $C(r,K,\rho)$ corresponds to an ellipsoid scaled by the value of ρ and centered around $X_e(r)$, $r \in \mathcal{N}$.

3.4 Debris Representation

We use a set, $O(z,Q)$, centered around the position $z \in R^3$, to over-bound the position of the debris, i.e.,

$$O(z,Q) = \{X \in R^6 : (SX - z)^T Q(SX - z) \leq 1\}, \tag{3.5}$$

where $Q = Q^{\mathrm{T}} > 0$ and

$$S = \begin{bmatrix} 1 & 0 & 0 & 0 & 0 & 0 \\ 0 & 1 & 0 & 0 & 0 & 0 \\ 0 & 0 & 1 & 0 & 0 & 0 \end{bmatrix}. \tag{3.6}$$

The set $O(z,Q)$ can account for the debris and spacecraft physical sizes and also for the uncertainties in the estimation of the debris/spacecraft position. Note that the set $O(z,Q)$ has an ellipsoidal shape in the position directions and it is unbounded in the velocity direc-

tions. Ellipsoidal sets, rather than polyhedral sets, are used here to over-bound the debris, since ellipsoidal bounds are typically produced by position estimation algorithms, such as the Extended Kalman Filter (EKF).

3.5 Static Debris Avoidance Approach

Consider now $r_i \in \mathcal{N}$, representing a possible position on the net that the spacecraft can move to as a part of the debris avoidance maneuver. Suppose that the current state of the spacecraft is $X(t_0)$ at the time instant $t_0 \in Z^+$. If there exists a $\rho \geq 0$ and $K_j \in \mathcal{K}$ such that

$$X(t_0) \in C(r_i, K_j, \rho) \text{ and } O(z, Q) \cap C(r_i, K_j, \rho) = \emptyset, \tag{3.7}$$

the spacecraft can move to the position $r_i \in \mathcal{N}$ by engaging the control law with $r(t) = r_i$ and $K(t) = K_j$, $t \geq t_0$, and without hitting the debris confined to $O(z, Q)$. This idea underlies our subsequent approach to debris avoidance, where we maintain the spacecraft within a tube formed by positively invariant sets that do not intersect with debris.

3.5.1 Growth Distances

The minimum value of $\rho \geq 0$ for which $O(z, Q) \bigcap C(r, K, \rho) \neq \emptyset$ is referred to as the *growth distance* [70]. This growth distance can also be viewed as the least upper bound on the values of ρ for which $O(z, Q)$ and $C(r, K, \rho)$ do not intersect. See Figure 3.2. We use the notation $\rho_g(r, K, Q, z)$ to reflect the dependence of the growth distance on the set-point $r \in \mathcal{N}$, the control gain $K \in \mathcal{K}$ and the obstacle parameters Q and z.

Note that the growth distance depends on the position of the debris which may be unknown in advance. Consequently, growth distance computations have to be performed online.

Since spacecraft have limited thrust, we additionally define a maximum value of $\rho = \rho_u(r, K)$ for which $X \in C(r, K, \rho_u(r, K))$ implies that the thrust $U = KX + H(K)r$ satisfies the imposed thrust limits. We refer to ρ_u as the *thrust limit on growth distance.* Unlike ρ_g, the value of ρ_u does not depend on the position or shape of the debris and can be pre-computed off-line.

Finally, we define *the thrust limited growth distance*

$$\rho^*(r, K, Q, z) = \min\{\rho_g(r, K, Q, z), \rho_u(r, K)\}. \tag{3.8}$$

Note that $X(t_0) \in C(r_i, K_j, \rho^*(r_i, K_j, z))$ implies that the ensuing closed-loop spacecraft tra-

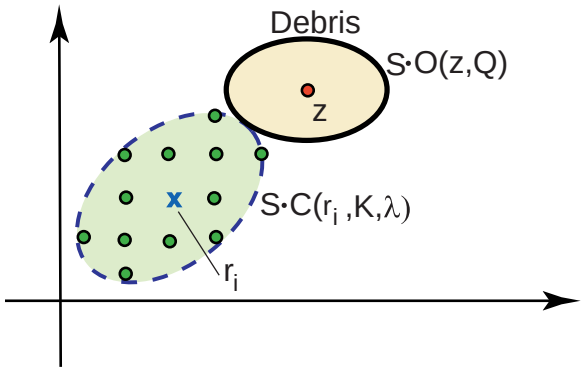

Figure 3.2: The positively invariant set is grown till touching the debris. The spacecraft can move from any of the equilibria on the virtual net inside the positively invariant set $C(r,K,\rho)$ to $X_e(r_i)$ marked by 'x' without colliding with the debris.

jectory under the control (3.2), where $r(t) = r_i$ and $K(t) = K_j$ for $t \geq t_0$, satisfies the thrust limits and avoids collisions with a debris confined to $O(z,Q)$.

The above definitions were given for the case of a single stationary debris, $O(z,Q)$. In the case of multiple debris, the growth distance is replaced by the *multi-growth distance*, which is the minimum growth distance to each of $O(z_l,Q_l)$, $l = 1,\cdots,n_d$.

3.5.2 Growth Distance Computations

Define $\bar{X} = X - X_e(r)$ and $\alpha = 2\rho^2$. The problem of determining the growth distance $\rho_g(r,K,Q,z)$, reduces to the following constrained optimization problem:

$$\begin{aligned} \min_{\alpha,\bar{X}} \quad & \alpha \\ \text{subject to} \quad & \bar{X}^{\mathrm{T}} P \bar{X} \leq \alpha \\ & ((S(\bar{X} + X_e(r)) - z)^{\mathrm{T}} Q((S(\bar{X} + X_e(r)) - z) \leq 1 \end{aligned} \tag{3.9}$$

To solve this optimization problem, we use the Karush-Kuhn-Tucker (KKT) conditions [71, 72]. Note that standard linear independence constraint qualification conditions hold given that $P > 0$. We define

$$\mathcal{L} = \alpha + \lambda_1(\bar{X}^{\mathrm{T}} P \bar{X} - \alpha) + \lambda_2((S(\bar{X} + X_e(r)) - z)^{\mathrm{T}} Q(S(\bar{X} + X_e(r)) - z) - 1),$$

where λ_1 and λ_2 are Lagrange multipliers. The stationarity of the Lagrangian (setting partial derivative equal to zero) with respect to α yields $\lambda_1 = 1$. The stationarity of the

Lagrangian with respect to $\bar{X}$ yields

$$\bar{X} = \bar{X}(\lambda_2, r, z) = -(P + \lambda_2 S^{\mathrm{T}} Q S)^{-1} S^{\mathrm{T}} Q (S X_e(r) - z)\lambda_2, \tag{3.10}$$

where the scalar $\lambda_2 \geq 0$ is to be determined. Note that $P > 0$, $S^{\mathrm{T}} Q S \geq 0$, $\lambda_2 \geq 0$ (as the Lagrange multiplier corresponding to an inequality constraint) imply that $(P + \lambda_2 S^{\mathrm{T}} Q S)$ is invertible. The problem reduces to finding a nonnegative scalar λ_2, which is the root of

$$F(\lambda_2, r, z) = ((S X - z)^{\mathrm{T}} Q (S X - z) - 1 = 0, \tag{3.11}$$

where

$$X = \bar{X}(\lambda_2, r, z) + X_e(r).$$

The scalar root finding problem (3.11) has to be solved online multiple times for different $r \in \mathcal{N}$, and in the case of avoiding a predicted debris path also for different z's. To solve this problem fast, while reusing previously found solutions as approximations, a dynamic Newton-Raphson's algorithm is used [72–74]. This algorithm uses predictor-corrector updates to track the root as a function of z and r, and is given by

$$\begin{aligned}
\lambda_2^{k+1,+} &= \lambda_2^k + \{\frac{\partial F}{\partial \lambda_2}(\lambda_2^k, z^k, r^k)\}^{-1}\{-F(\lambda_2^k, z^k, r^k) - \frac{\partial F}{\partial z}(\lambda_2^k, z^k, r^k)(z^{k+1} - z^k) \\
&\quad - \frac{\partial F}{\partial r}(\lambda_2^k, z^k, r^k)(r^{k+1} - r^k)\}, \\
\lambda_2^{k+1} &= max\{0, \lambda_2^{k+1,+}\}.
\end{aligned}$$

To implement the algorithm, we take advantage of the known functional form for F and explicitly compute the partial derivatives,

$$\begin{aligned}
\frac{\partial \bar{X}}{\partial \lambda_2} &= (P + \lambda_2 S^{\mathrm{T}} Q S)^{-1}\left\{-S^{\mathrm{T}} Q (S X_e(r) - z) - S^{\mathrm{T}} Q S \bar{X}\right\}, \\
\frac{\partial F}{\partial \lambda_2} &= 2(S X - z)^{\mathrm{T}} Q (S \frac{\partial \bar{X}}{\partial \lambda_2}), \\
\frac{\partial \bar{X}}{\partial r} &= (P + \lambda_2 S^{\mathrm{T}} Q S)^{-1}\left\{-S^{\mathrm{T}} Q S \Omega\right\}\lambda_2, \\
\frac{\partial F}{\partial r} &= 2(S \bar{X} - z + r)^{\mathrm{T}} Q (S \frac{\partial \bar{X}}{\partial r} + I_3), \\
\frac{\partial \bar{X}}{\partial z} &= (P + \lambda_2 S^{\mathrm{T}} Q S)^{-1} S^{\mathrm{T}} Q S \Omega \lambda_2, \\
\frac{\partial F}{\partial z} &= 2(S \bar{X} - z + r)^{\mathrm{T}} Q (S \frac{\partial \bar{X}}{\partial z} - I_3),
\end{aligned} \tag{3.12}$$

where, $X_e(r) = \Omega r$,

$$\Omega = \begin{bmatrix} I_3 \\ 0 \end{bmatrix},$$

and I_3 denotes the 3×3 identity matrix. Note that $S\,\Omega = I_3$.

Figure 3.3 illustrates growth distance tracking. For the first 20 iterations, r^k is held constant to enable initial convergence of the algorithm. Then, r^k varies through the virtual net. One iteration of the Newton-Raphson algorithm per value of r^k is used to update the root, λ_2^{k+1}. Figure 3.3b demonstrates that the growth distance tracking is accurate. The growth distance is occasionally zero indicating an overlap between several r^k and the debris. Figure 3.3c illustrates the trajectory of r^k in three dimensions.

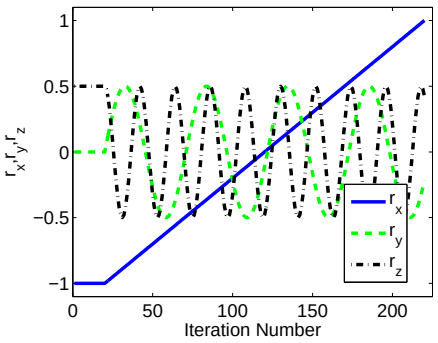

(a)

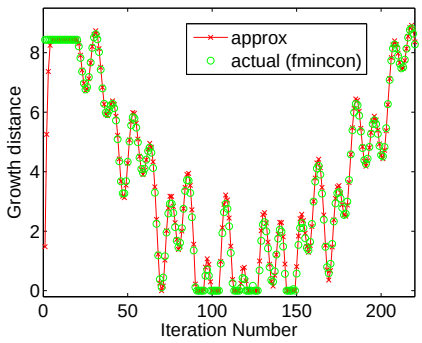

(b)

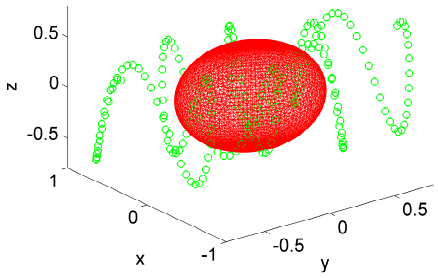

(c)

Figure 3.3: (a) Components of r, r_x, r_y and r_z varying versus the iteration number. (b) Growth distance versus iteration number computed by dynamic Newton-Raphson algorithm. (c) The trajectory of r and the debris.

3.5.3 Thrust Limit on Growth Distance Computations

Suppose that the thrust limits are expressed in the form $\|LU\| \leq 1$ for an appropriately defined matrix L and norm $\|\cdot\|$. The computational procedures to determine $\rho_u(r, K)$ involve solving a bilevel optimization problem where $\|L(KX + H(K)r)\|$ is maximized subject to the constraint $X \in C(r, K, \alpha)$, and bisections are performed on the value of α so that the maximum value is driven to 1. As we demonstrate in this section, in special cases this computation can be greatly simplified.

Suppose that the thrust constraints are prescribed in terms of polyhedral norm bounds, specifically

$$e_i^{\mathrm{T}}(KX + Hr) \leq u_{\max}, \quad i = 1, 2, \cdots, m, \tag{3.13}$$

where e_i are the vertices of the unit norm polytope, and $u_{\max}$ is the norm bound. The infinity norm, for instance, has $m = 6$, and

$$\begin{aligned} e_1 &= \begin{bmatrix} 1 \\ 0 \\ 0 \end{bmatrix} \quad e_2 = \begin{bmatrix} -1 \\ 0 \\ 0 \end{bmatrix} \quad e_3 = \begin{bmatrix} 0 \\ 1 \\ 0 \end{bmatrix} \\ e_4 &= \begin{bmatrix} 0 \\ -1 \\ 0 \end{bmatrix} \quad e_5 = \begin{bmatrix} 0 \\ 0 \\ 1 \end{bmatrix} \quad e_6 = \begin{bmatrix} 0 \\ 0 \\ -1 \end{bmatrix}. \end{aligned} \tag{3.14}$$

In the case of non-polyhedral norm bounds, such as the 2-norm, an approximation by a polyhedral norm bound may be employed.

The thrust limit on the growth distance is then determined based on solving, for $i = 1, \cdots, n$, the optimization problems

$$\begin{array}{ll} \text{maximize} & e_i^{\mathrm{T}}(KX + Hr) \\ \text{subject to} & \frac{1}{2}(X - X_e(r))^{\mathrm{T}} P (X - X_e(r)) \leq c. \end{array} \tag{3.15}$$

If the value of c is found for which the solutions X_i^* of (3.15) satisfy $\max_i\{e_i^{\mathrm{T}}(KX_i^* + Hr)\} = u_{\max}$, then $\rho_u(r, K) = \sqrt{c}$.

The problem (3.15) can be solved by diagonalizing P, using an orthogonal matrix, V,

$$P = V^{\mathrm{T}} \Lambda V, \ \Lambda = \mathrm{diag}[\lambda_1^2, \cdots, \lambda_6^2], \lambda_i > 0.$$

By defining, $z = X - X_e(r)$, and ζ so that

$$z = V^{\mathrm{T}} \Lambda^{-\frac{1}{2}} \zeta,$$

it follows that

$$\begin{aligned} z^{\mathrm{T}} P z &= \zeta^{\mathrm{T}} \Lambda^{-\frac{1}{2}} V P V^{\mathrm{T}} \Lambda^{-\frac{1}{2}} \zeta \\ &= \zeta^{\mathrm{T}} \zeta. \end{aligned}$$

The problem (3.15) can now be re-written as

$$\begin{array}{ll} \text{maximize} & h_i^{\mathrm{T}} \zeta + e_i^{\mathrm{T}} \Gamma r \\ \text{subject to} & \frac{1}{2} \zeta^{\mathrm{T}} \zeta \leq c, \end{array} \tag{3.16}$$

where

$$h_i^{\mathrm{T}} = e_i^{\mathrm{T}} K V^{\mathrm{T}} \Lambda^{-\frac{1}{2}}.$$

The solution to the constrained maximization problem (3.16) of maximizing the inner-product of two vectors over a unit 2-norm ball is given by

$$\zeta_i = \frac{h_i}{\|h_i\|} \sqrt{2c}, \tag{3.17}$$

where $\|\cdot\|$ denotes the vector 2-norm. The maximum value of the objective function in (3.15) is given by

$$\|h_i\| \sqrt{2c} + e_i^{\mathrm{T}} \Gamma r.$$

Consequently, to satisfy (3.13), we let

$$c = \begin{cases} 0, & \text{if } \exists\, i : u_{\max} \leq e_i^{\mathrm{T}} \Gamma r, \\ \min\limits_i \dfrac{1}{2} \left(\dfrac{u_{\max} - e_i^{\mathrm{T}} \Gamma r}{\|h_i\|} \right)^2, & \text{otherwise.} \end{cases} \tag{3.18}$$

Thus, the problem of finding the thrust limit on the growth distance for polyhedral norm bounds has an explicit solution given by (3.18). Even though the computation of thrust limits on the growth distance can be performed offline for the nominal operating conditions, fast computational procedures are beneficial in case of thruster failures, degradations, and restrictions on thrust directions (e.g., caused by the presence of other spacecraft nearby), all of which can lead to changing constraints on thrust during spacecraft missions.

We note that the condition $u_{\max} \geq \max_i \{e_i^{\mathrm{T}} \Gamma r\}$ is satisfied if the available thrust can maintain the equilibrium $X_e(r)$ in steady-state. We also note, that, based on the form of Γ, c is independent of r_y, the in-track component of the equilibrium in the virtual net. Hence the computations of $\rho_u(r, K)$ need only be performed with $r_y = 0$.

When a spacecraft does not have independent thrusters in x, y and z directions, a 2-norm

thrust limit is more practical. Unfortunately, (3.15) is, in general, a non-convex problem. In this case, the 2-norm bound can be approximated by a polyhedral norm bound (3.13), with the vertices e_i selected on the unit 2-norm ball in R^3. We note that higher accuracy of this approximation requires a higher number of vertices in (3.13), which thus, complicates (3.18).

Finally, we note that when Δv's are treated as control inputs, the thrust limit on growth distance is induced by the available Δv. In this case, computing the thrust limited growth distance is completely analogous to computing it in the case when the control input is the thrust force or thrust acceleration.

3.5.4 Connectivity Graph and Graph Search

We now introduce a notion of *connectivity* between two vertices of the virtual net, $r_i \in \mathcal{N}$ and $r_j \in \mathcal{N}$. The vertex r_i is connected to the vertex r_j if there exists a gain $K \in \mathcal{K}$ such that

$$X_e(r_i) \in int\, C(r_j, K, \rho^*(r_j, K, z)), \tag{3.19}$$

where *int* denotes the interior of a set. The connectivity implies that a spacecraft located close to an equilibrium corresponding to r_i can transition to an equilibrium $X_e(r_j)$ by using limited thrust and avoiding collision with the debris. We note that if r_i is connected to r_j this does not imply that, in turn, r_j is connected to r_i. We also note that connectivity depends on the existence of an appropriate control gain from the set of gains $\mathcal{K}$ but the condition (3.19) does not need to hold for all gains.

The on-line motion planning with debris avoidance is performed according to the following procedure (for simplicity, described here for the case of a single debris):

Step 1: Determine the debris location and shape (i.e., z and Q).

Step 2: By using fast growth distance computations, determine the thrust limited growth distance based on (3.8), with ρ_g computed online and ρ_u precomputed offline.

Step 3: Construct a graph connectivity matrix between all $r_i, r_j \in \mathcal{N}$. In the graph connectivity matrix, if two vertices are not connected, the corresponding matrix element is zero; if they are connected the corresponding matrix element is 1. In parallel, build the control gain selectivity matrix, which identifies the index of the highest preference gain K for which r_i and r_j are connected. This gain will be applied if the edge connecting r_i and r_j is traversed.

Step 4: Perform graph search to determine a sequence of connected vertices $r[k] \in \mathcal{N}$ and control gains $K[k] \in \mathcal{K}$, $k = 1, \cdots, l_p$, such that $r[1]$ satisfies the initial constraints, $r[l_p]$ satisfies the final constraints, and the path length l_p is minimized.

Per the above algorithm, graph search is utilized to determine the minimum number of equilibrium hops around a piece of debris. After the path has been determined as a sequence of the set-points and the corresponding control gains, the execution of the path proceeds by checking if the current state, $X(t)$ is in the safe positively invariant set corresponding to the next reference r^+ and next control gain K^+ in the sequence; if it is, then the controller switches to this reference and control gain:

$$X(t) \in C(r^+, K^+, \rho^*(r^+, K^+, z)) \rightarrow r(t) = r^+,\ K(t) = K^+. \tag{3.20}$$

3.6 Cost Matrices

As described in the previous section, the connectivity graph matrix is comprised of ones and zeros, and thus, graph search results in a minimum length path between desired $r_i, r_j \in \mathcal{N}$.

In order to produce time efficient and thrust efficient paths, offline we simulate transitions between all $r_i, r_j \in \mathcal{N}$ for each $K \in \mathcal{K}$ and record the time and fuel consumption to reach a box of 1m around the target vertex. The results are merged into time and fuel matrices that store the respective minimum value, while in parallel, the control selectivity matrix identifies which gain K produced said minimum.

Step 3 in the motion planning procedure is augmented so that the graph connectivity matrix is multiplied elementwise with a desired cost matrix. Vertices that are not connected retain a corresponding matrix element of zero, while vertices that are connected now contain a matrix element of time or fuel cost.

3.7 Moving Debris Avoidance Approach

To avoid a non-stationary debris, its path can be covered by a union of a finite number of ellipsoidal sets,

$$\mathcal{D} = \bigcup_{l=1}^{l=n_d} O(z_l, Q_l), \tag{3.21}$$

where the center of the lth set is denoted by $z_l \in R^3$, and the lth set shape is defined by $Q_l = Q_l^{\mathrm{T}} > 0$. Then, the debris avoidance condition for the closed-loop trajectory that emanates

from $X(0)$ with the set-point r_i and gain K_j is given by

$$X(0) \in C(r_i, K_j, \rho) \text{ and } O(z_l, Q_l) \cap C(r_i, K_j, \rho) = \emptyset, \quad \text{for all } l = 1, \cdots, n_d. \tag{3.22}$$

The same approach, with larger n_d, can be used to handle *multiple* non-stationary debris. Note, however, that this approach is conservative as it does not account for the debris progressions along their paths versus time.

Hence, we introduce the notion of time into the problem; whereas a transition between r_i and r_j might not be feasible at time t_1, based on the motion of a debris, it might become feasible at time t_2. To accommodate moving debris, we introduce sets $C_k(r, K, \rho)$, $0 \leq k \leq N$, defined by the following relation,

$$\bar{A}(K)^k \Big(C_k(r, K, \rho) - \{X_e(r)\} \Big) \subseteq \Big(C(r, K, \rho) - \{X_e(r)\} \Big), \tag{3.23}$$

Note that if $X(0) \in C_k(r, K, \rho)$, then $X(1) \in C_{k-1}(r, K, \rho)$, $X(2) \in C_{k-2}(r, K, \rho), \cdots, X(k) \in C_0(r, K, \rho) = C(r, K, \rho)$. The set $C_k(r, K, \rho)$ can be much larger than $C(r, K, \rho)$; any states in $C_k(r, K, \rho)$ contract to $C(r, K, \rho)$ in k steps.

3.7.1 Connectivity Graph and Graph Search

We now define *connectivity* between two vertices of the virtual net, $r_i \in \mathcal{N}$ and $r_j \in \mathcal{N}$ at a specified time t_0. This notion is based on the fact that the time to transition from any state in $C_N(r, K, \rho)$ to $C(r, K, \rho)$ is less or equal than N steps. Suppose that the debris path $D(t_0 : t_0 + N \cdot H)$ has been predicted over the $N \cdot H$ discrete steps from the time instant t_0, where

$$D(t_k : t_r) = \bigcup_{t=t_k}^{t=t_r} O(z(t), Q(t)).$$

The node $r_i \in \mathcal{N}$ is connected to $r_i \in \mathcal{N}$ at the time instant $t_k = t_0 + kN$ if there exists $K \in \mathcal{K}$ such that

$$D(t_k : t_k + N) \cap C(r_i, K, \rho) = \emptyset. \tag{3.24}$$

The node $r_i \in \mathcal{N}$ is connected to node $r_j \in \mathcal{N}$ at time t_k if there exists $K \in \mathcal{K}$ such that

$$D(t_k : t_k + N) \cap C_N(r_j, K, \rho) = \emptyset \tag{3.25}$$

and

$$C(r_i, K, \rho) \subset C_N(r_j, K, \rho). \tag{3.26}$$

The connectivity implies that a spacecraft located close to an equilibrium corresponding to r_i, $X_e(r_i)$, can transition close to an equilibrium $X_e(r_j)$ between the time instants t_k and $t_k + N$ while avoiding collision with the debris. We note that if r_i is connected to r_j this does not imply that, in turn, r_j is connected to r_i. We also note that connectivity depends on the existence of an appropriate control gain from the set of gains $\mathcal{K}$ but does not need to hold for all gains. Furthermore, since connectivity depends on the predicted motion of the debris, connectivity/non-connectivity can depend on time.

The on-line motion planning with debris avoidance is performed according to the following procedure:

Step 1: Determine the debris location, shape and predict the debris path $D(t_0 : t_0 + N \cdot H)$

Step 2: Construct graph connectivity matrices corresponding to $t_k, k = 0, 1, \cdots, H$. In the graph connectivity matrix, if two vertices, r_i and r_j, are not connected at t_k, the corresponding matrix element is zero; if they are connected the corresponding matrix element is 1. In parallel, build the control gain selectivity matrix, which identifies the index of the highest preference gain K for which r_i and r_j are connected. This gain will be applied if the edge connecting r_i and r_j is traversed.

Step 3: Perform graph search to determine a sequence $r[t_k] \in \mathcal{N}$ and control gains $K[k] \in \mathcal{K}$, $k = 1, \cdots, l_p$, such that $r[t_1]$ satisfies the initial constraints, $r[l_p]$ satisfies the final constraints, and the path length l_p (or another cost function such as the expected fuel consumption or expected maneuver time) is minimized.

Per the above algorithm, a graph search is utilized to determine the minimum number of equilibrium hops around a debris starting at t_0.

Remark 1: The condition (3.25) is conservative. It can be replaced by a less conservative condition,

$$D(t_k : t_k + m) \cap C_{N-m}(r_j, K, \rho) = \{\emptyset\},$$

$$m = 0, 1, \cdots, N,$$

at a price of more demanding computations.

Remark 2: The condition (3.25) is checked computationally using the fast growth distance algorithm described in Section 3.5.3. The intersection is empty if C_N can be grown before it touches $D(t_k : t_k + N)$. This fast growth distance algorithm is essential to be able to rapidly construct the connectivity matrices.

Remark 3: In our simulations, the path search is performed using the standard Dijkstra's algorithm. It is applied to a lifted graph with vertices being the pairs (r_i, t_k).

3.8 Bounded Disturbances

We now discuss how the debris avoidance approach can be extended to handle bounded disturbances. For simplicity, we consider the case of multiple stationary debris. Consider the system

$$X_{k+1} = AX_k + BU_k + Bw, \tag{3.27}$$

where $w \in W$, W is the convex hull of w^i for $i = 1, \ldots, n_w$, w^i are the vertices of a disturbance set, and n_w is the number of vertices. Note that W is a compact set.

The positive invariance of $C(r, K, \gamma)$, $\gamma > 0$, for $W = \{0\}$ has already been established. When $W \neq \{0\}$, it can be shown that there exists $\gamma_{\min}$ such that the set is positively invariant for $\gamma > \gamma_{\min}$. Note that $\gamma_{\min} = \gamma_{\min}(K)$.

Since $C(r, K, \gamma_{\min}(K))$ is disturbance invariant, it contains the minimum invariant set that is an attractor for closed-loop trajectories, as long as r and K are maintained at constant values. Hence, in the case of bounded disturbances, connectivity can be redefined by replacing $X_e(r_i)$ in (3.19) with $C(r_i, K, \gamma_{\min}(K))$. Specifically, the vertex $r_i \in \mathcal{N}$ is connected to the vertex $r_j \in \mathcal{N}$ if there exists $K \in \mathcal{K}$ such that

$$C(r_i, K, \gamma_{\min}(K)) \subset int\, C(r_j, K, \rho^*(r_j, K, z)), \quad \text{for all } l = 1, \ldots, m. \tag{3.28}$$

The condition (3.28) ensures that a switch from r_i to r_j may occur and that subsequent dynamics will not lead to collision with the debris once $X(t) \in C(r_i, K, \gamma_{\min}(K))$.

3.8.1 Disturbance Set Calculations

To compute $\gamma_{\min}$ under all possible $w \in W$, it is sufficient to examine the flow at the vertices w^i of the disturbance set and demonstrate that if $X_k \in C(r, K, \gamma(K))$ and $w \in \{w^i, i = 1, \ldots, n_w\}$, then $X_{k+1} \in C(r, K, \gamma(K))$. The value $\gamma_{\min}$ is the minimum γ for which this condition holds.

To find $\gamma_{\min}$ we use a bilevel optimization strategy where the inner loop solves n_w optimization problems numerically with respect to X,

$$\begin{aligned} &\text{maximize} \quad F_i(X) = \tfrac{1}{2}(AX + BU + Bw^i)^{\mathrm{T}} \frac{P(K)}{\gamma_i^2}(AX + BU + Bw^i), \\ &\text{subject to} \quad \tfrac{1}{2}(X - X_e(r))^T P(K)(X - X_e(r)) \leq \gamma_i^2, \end{aligned} \tag{3.29}$$

and the outer loop performs bisections on each γ_i, so that all $F_i(X^*(\gamma_i))$, where $X^*(\gamma_i)$ denotes the inner-loop solution, are driven to 1. Thus, $\gamma_{\min} = \min(\gamma_i)$ for $i = 1, \ldots, n_w$. Note that $\gamma_{\min}$ is independent of equilibrium r, and so this calculation may be done once offline for each $K \in \mathcal{K}$ and stored onboard for real time implementation.

3.9 Simulation Results

Simulations are now provided that illustrate the debris avoidance approach. We consider a nominal circular orbit of 850 km and discretize the HCW equations with a sampling period, ΔT, of 30 seconds. We construct an approximately 2 km cubed virtual net. We let $\mathcal{K} = \{K_1, K_2, K_3\}$, where K_1, K_2, K_3 are the LQ gains associated with weight matrices $Q = \text{diag}(100, 100, 100, 10^7, 10^7, 10^7)$, and $R_1 = 2\times10^5 I_3$, $R_2 = 2\times10^7 I_3$, and $R_3 = 2\times10^9 I_3$. These gains are chosen to represent preferences for fuel considerations, maneuver time considerations, and a compromise between them. We impose a maximum thrust constraint of 10 N in each axis. In all simulations, Dijkstra's algorithm is used to find the shortest cost path from initial node to final node.

3.9.1 Static Debris

We consider an ellipsoidal set $O(z_1, Q_1)$ over-bounding a debris centered at $z_1 = [0.3\ 0.4\ 0.5]^{\mathrm{T}}$ km, where $Q_1 = 100 I_3$. We use the technique of [75] where bisections are applied to (3.11) to determine the growth distance to the debris from each node in the net. The spacecraft's initial condition is $X(0) = X_e(r_0)$, where $r_0 = [0.32\ 0\ 1.61]^{\mathrm{T}}$ km. The target equilibrium node is $X_e(0)$.

Figure 3.4 shows the path the spacecraft takes under closed-loop control in order to avoid the debris. The spacecraft is able to complete the desired maneuver well within maximum thrust constraints while successfully avoiding the debris. In Figure 3.5 we rerun the simulation for a grid of initial conditions. The figure clearly demonstrates the initial conditions for which the maneuver path is perturbed from that which the spacecraft would have taken had there been no debris.

Next, we add a second debris $O(z_2, Q_2)$ centered at $z_2 = [0.3\ -0.4\ 0.5]^{\mathrm{T}}$, where $Q_2 = 100 I_3$. In calculating the growth distance, we take the minimum distance to each of $O(z_i, Q_i)$, $i = 1, 2$. Figure 3.6 shows the path the spacecraft takes under closed-loop control in order to avoid both debris.

3.9.2 Moving Debris

We consider the case of a non-stationary debris where we treat its motion as the union of static debris along the path (3.21). A union of ellipsoidal sets over-bounds the debris' motion, where the debris positions z_i are generated by sampling the relative motion of the debris with the initial condition $[0\ 0.5\ 0\ 0\ 0.0006\ 0]^{\mathrm{T}}$, and where $Q_i = 200 I_3, i = 1 \ldots n_d$. The spacecraft's initial condition is $X(0) = X_e(r_0)$, where $r_0 = [0\ 1\ 0]^{\mathrm{T}}$ km. The target

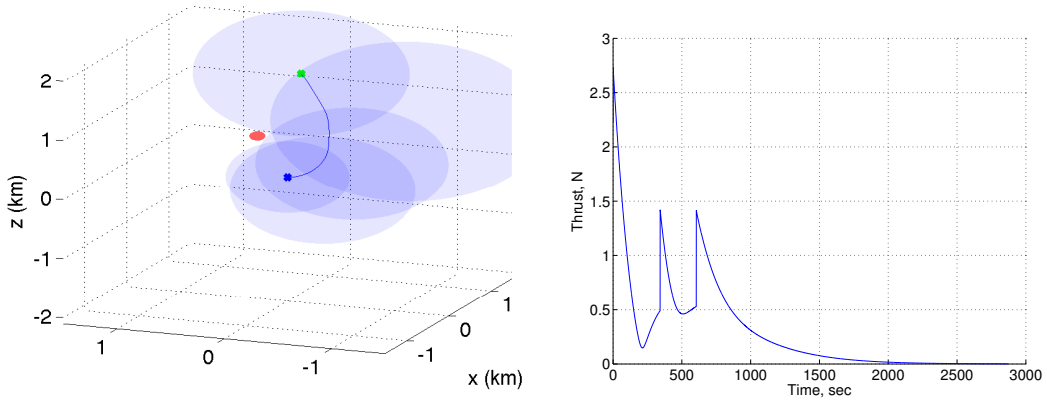

(a) Debris Avoidance Path. (b) Norm of Thrust Profile.

Figure 3.4: (a) Debris avoidance path for a single debris. The green x marks the initial node. The blue x marks the final node. The red ellipsoid represents the debris. The blue line is the path the spacecraft takes in order to avoid the debris. The blue ellipsoids represent the invariant sets along the path. (b) The time history of thrust magnitude.

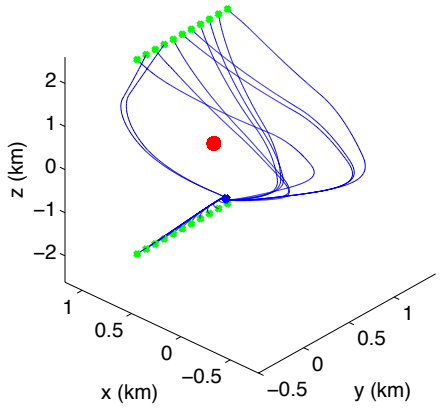

Figure 3.5: Debris avoidance paths for many initial conditions. Each green x marks an intial condition. The blue x marks the final node. The red ellipsoid represents the debris. The blue lines are the paths that the spacecraft takes from each initial condition in order to avoid the debris. We do not show the invariant set ellipsoids for visual clarity.

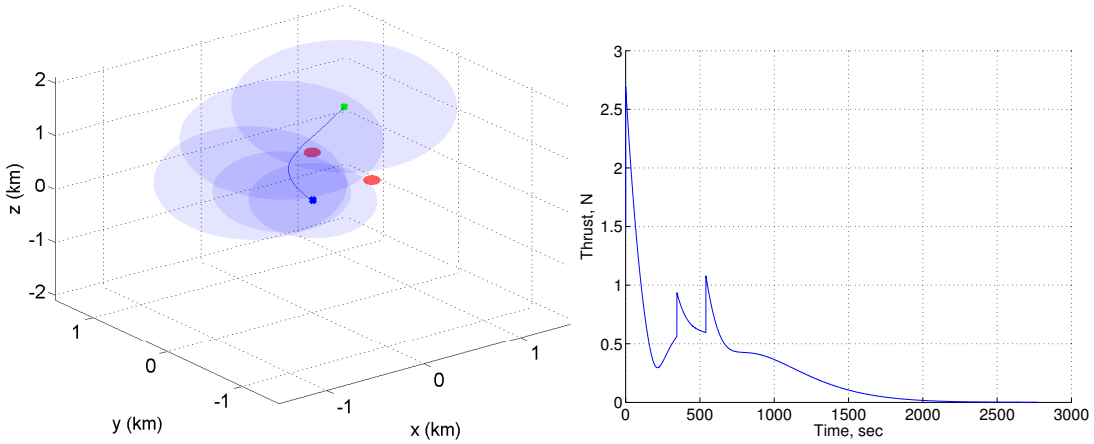

(a) Debris Avoidance Path.

(b) Norm of Thrust Profile.

Figure 3.6: (a) Debris avoidance path for 2 pieces of debris. The green x marks the initial node. The blue x marks the final node. The red ellipsoids represents the 2 pieces of debris. The blue line is the path the spacecraft takes in order to avoid the debris. The blue ellipsoids represent the invariant sets along the path. (b) The time history of thrust magnitude.

equilibrium node is $X_e(r_d)$, where $r_0 = [0\ -1\ 0]^{\mathrm{T}}$ km. We use the single gain K_2 and do not include fuel or time cost matrices in the simulation, searching for a minimum length path. Figure 3.7 demonstrates that the spacecraft is able to avoid the closed debris path by 'hopping' under it.

In Figure 3.8, we repeat the simulation for time efficient and thrust efficient paths and allow all $K \in \mathcal{K}$. Table 3.1 summarizes the total time, thrust and nodes traversed for the three paths. Note that the minimum length path now 'hops' over the debris path instead of under it, as now that it has access to K_1 it finds a shorter path. Also note that the time efficient path takes longer to complete than the minimum length path. While the cost matrices described in Section 3.6 calculate time and thrust to travel between all vertices in the virtual net, the execution of the path does not require the spacecraft to reach intermediate vertices, rather, switching to the next reference once the current state enters the next reference's invariant set (3.20). As such, the cost matrices only provide a heuristic for selecting efficient paths. In Figure 3.9 we require the paths to travel through intermediate vertices to show that, in this case, the cost matrices accurately determine efficient paths. The results are summarized in Table 3.2.

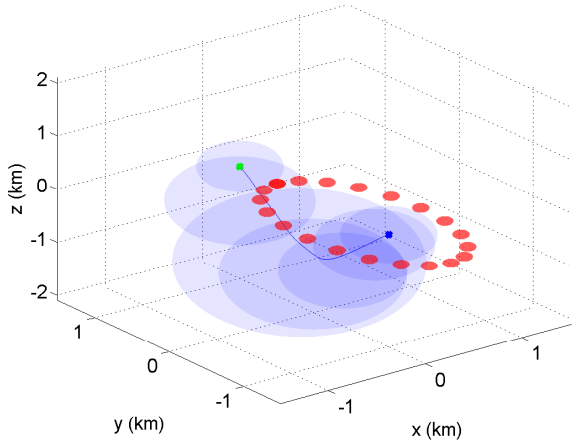

(a) Debris Avoidance Path.

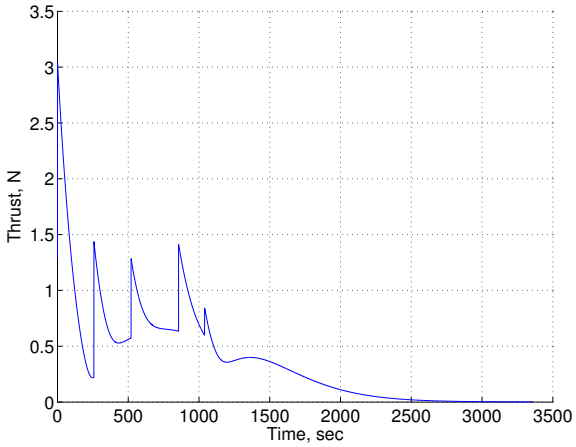

(b) Norm of Thrust Profile.

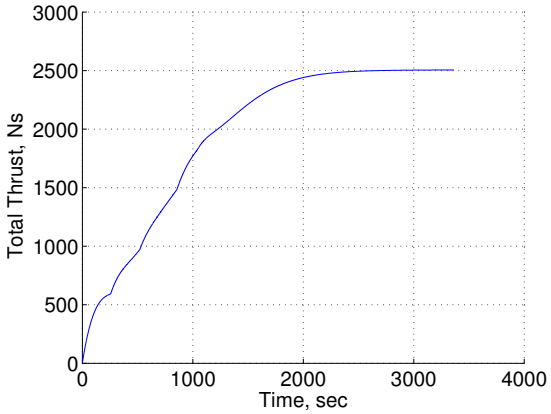

(c) Cumulative Thrust.

Figure 3.7: (a) Debris avoidance path for a non-stationary debris using the union method. The green x marks the initial node. The blue x marks the final node. The red ellipsoids represent the debris path. The blue line is the path the spacecraft takes in order to avoid the debris. The blue ellipsoids represent the maximally grown invariant sets, C, along the path. (b) The time history of thrust magnitude. (c) Cumulative thrust vs time.

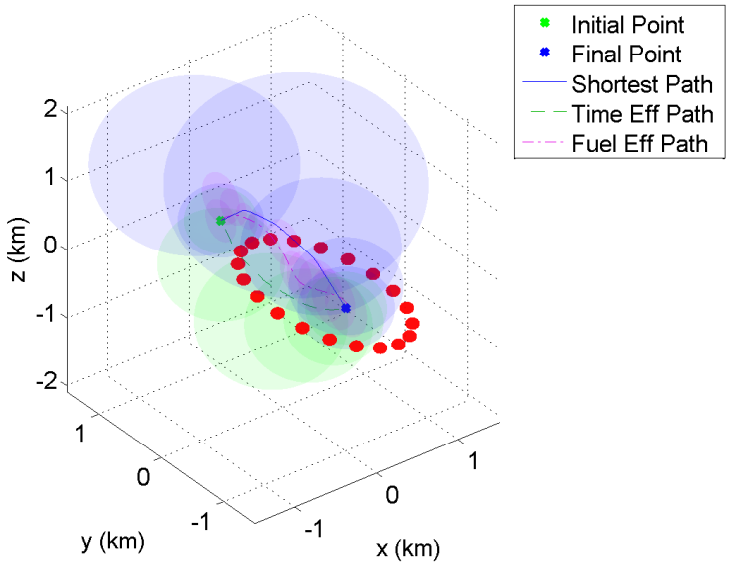

(a) Debris Avoidance Path.

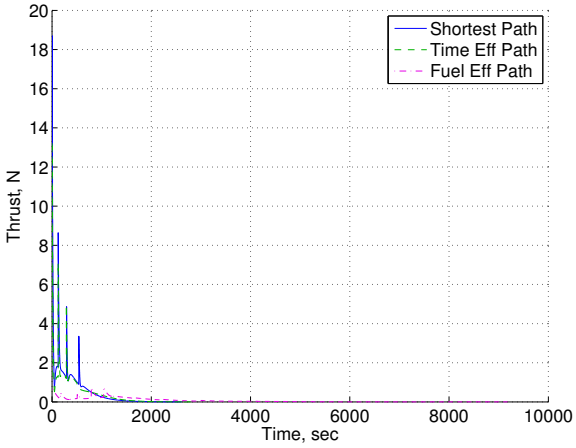

(b) Norm of Thrust Profile.

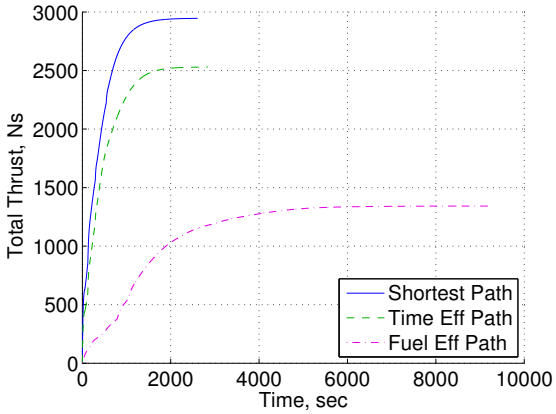

(c) Cumulative Thrust.

Figure 3.8: (a) Multiple debris avoidance paths for a non-stationary debris using the union method. (b) The time history of thrust magnitude. (c) Cumulative thrust vs time.

Table 3.1: Total Time, Thrust, and Nodes Traversed for all Maneuver Paths for a Union of Static Debris.

	Total Time	Total Thrust	Total # of Nodes	Gains used
Minimum Length Path	2611.5 s	1472.85 N·s	6	K_1
Time Efficient Path	2841 s	1264.95 N·s	6	K_1, K_2
Thrust Efficient Path	9177 s	671.297 N·s	11	K_2, K_3

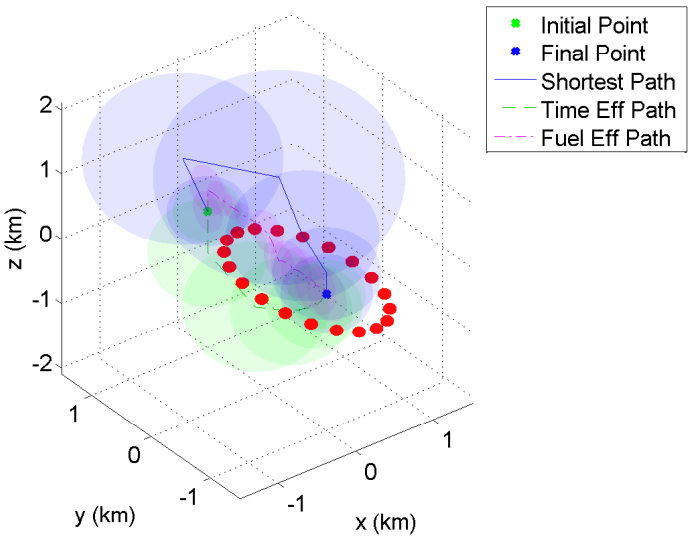

(a) Debris Avoidance Path.

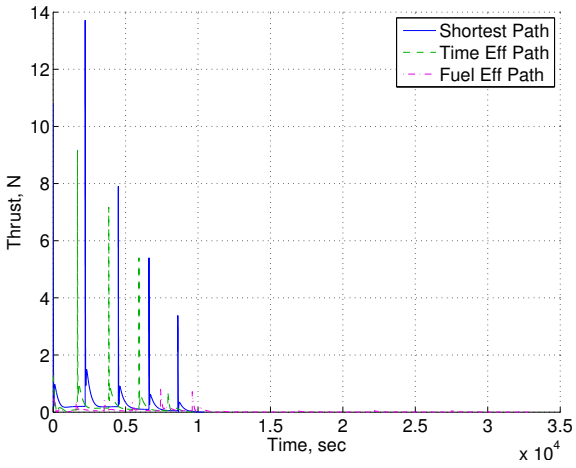

(b) Norm of Thrust Profile.

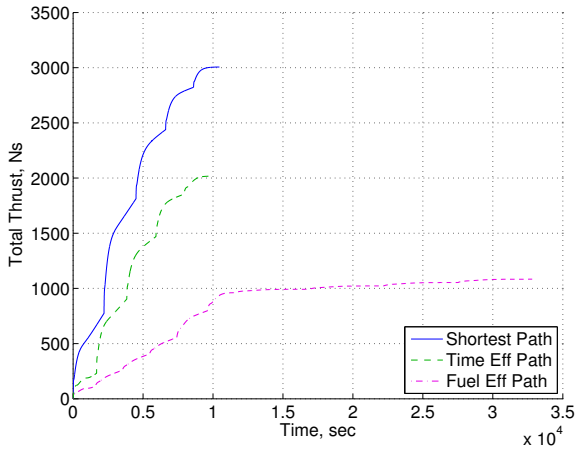

(c) Cumulative Thrust.

Figure 3.9: (a) Multiple debris avoidance paths that travel through intermediate nodes for a non-stationary debris using the union method. (b) The time history of thrust magnitude. (c) Cumulative thrust vs time.

Table 3.2: Total Time, Thrust, and Nodes Traversed for all Maneuver Paths that Travel Through Intermediate Nodes for a Union of Static Debris.

	Total Time	Total Thrust	Total # of Nodes	Gains used
Minimum Length Path	10457.5 s	3006.13 N·s	6	K_1
Time Efficient Path	9862 s	2017.11 N·s	6	K_1, K_2
Thrust Efficient Path	32812.5 s	1083.58 N·s	11	K_2, K_3

We now repeat the simulations taking into account the debris' motion as a function of time. We use the single gain K_2 and do not include fuel or time cost matrices in the simulation, searching for a minimum length path. Figure 3.10 shows that the graph search algorithm is able to find a path which passes through the debris' path but avoids collision due to the debris' location elsewhere at the specific time instant at which the spacecraft path crosses the debris' path. In Figure 3.11, we repeat the simulation for a thrust efficient path. Table 3.3 summarizes the total time, thrust and nodes traversed for the two paths. Note that the thrust efficient path uses more thrust than the minimum length path. In Figure 3.12 we require the paths to travel through intermediate vertices to show that, in this case, the thrust cost matrix accurately determines an efficient path. The results are summarized in Table 3.4.

Table 3.3: Total Time, Thrust, and Nodes Traversed for all Maneuver Paths using the Contractive Set Approach.

	Total Time	Total Thrust	Total # of Nodes
Minimum Length Path	4635.5 s	4635.5 N·s	7
Thrust Efficient Path	4703.5 s	781.407 N·s	7

Table 3.4: Total Time, Thrust, and Nodes Traversed for all Maneuver Paths that Travel Through Intermediate Nodes using the Contractive Set Approach.

	Total Time	Total Thrust	Total # of Nodes
Minimum Length Path	13388.5 s	2060.14 N·s	7
Thrust Efficient Path	12657.5 s	957.116 N·s	7

Finally, we run the simulation for the case of bounded disturbances. We consider $W = \{w : \|w\|_\infty \leq \varepsilon\}$ for which $n_w = 8$, that is, disturbances that fit in a box of magnitude ε. In Figure 3.13 we consider a uniform distribution of disturbances, for $\varepsilon = 0.1$ N and $\varepsilon = 0.2$ N. The spacecraft is able to safely avoid the debris' path despite being subjected to disturbances.

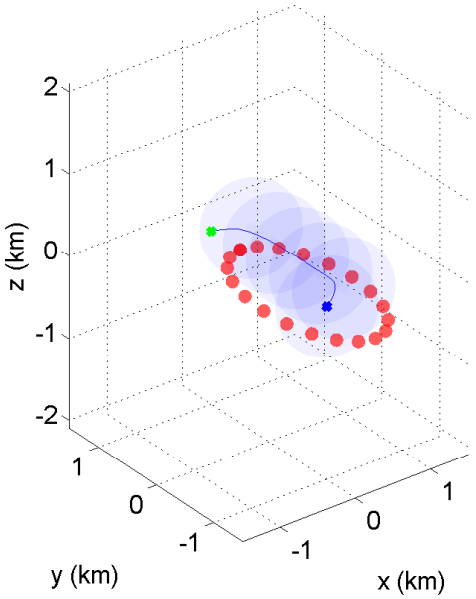

(a) Debris Avoidance Path.

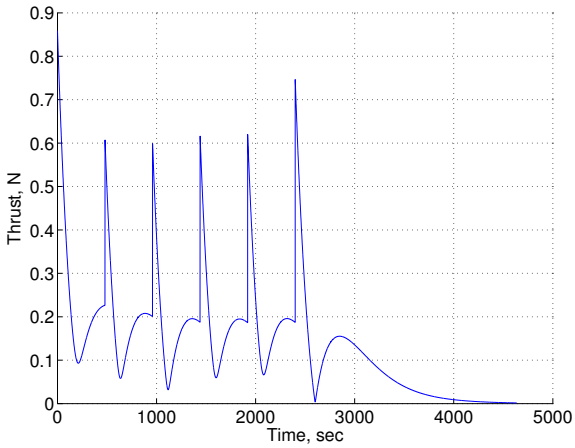

(b) Norm of Thrust Profile.

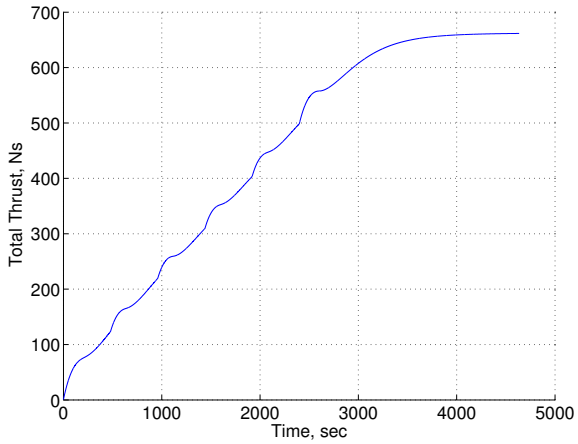

(c) Cumulative Thrust.

Figure 3.10: (a) Debris avoidance path for a non-stationary debris using the contractive set approach. The green x marks the initial node. The blue x marks the final node. The red ellipsoids represent the debris path. The blue line is the path the spacecraft takes in order to avoid the debris. The blue ellipsoids represent the invariant sets, C_N, along the path. (b) The time history of thrust magnitude.

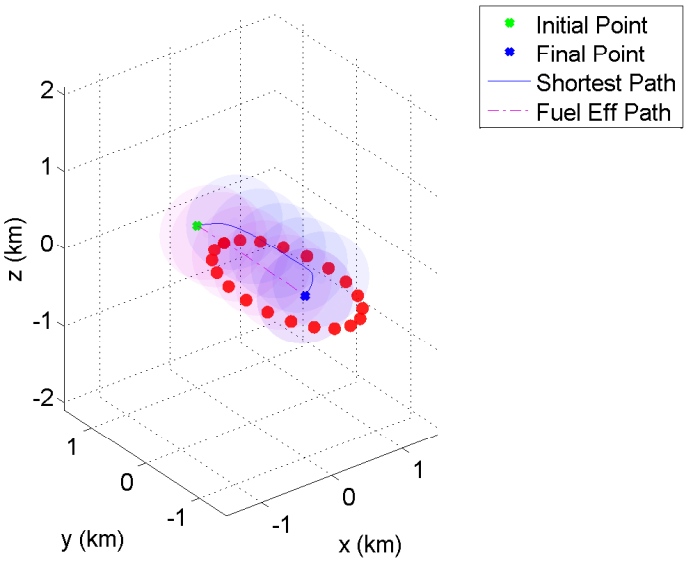

(a) Debris Avoidance Path.

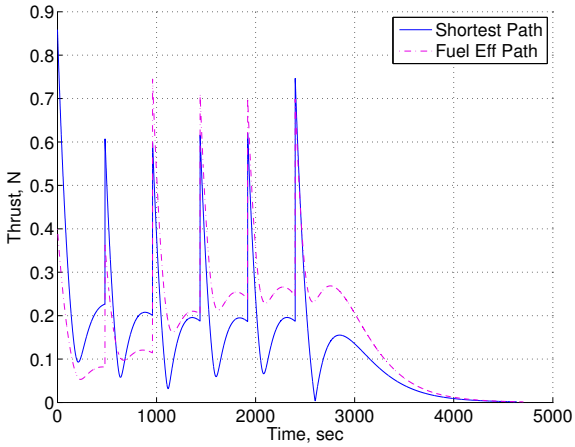

(b) Norm of Thrust Profile.

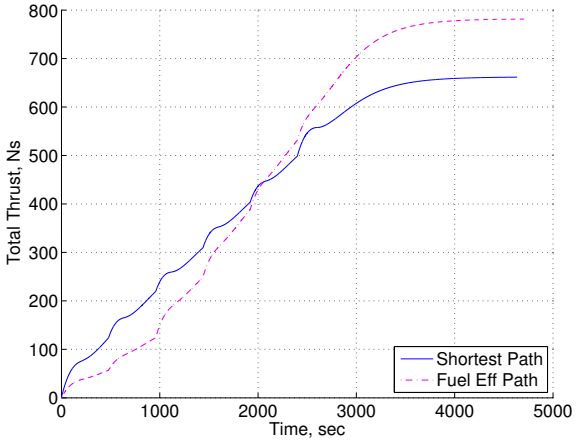

(c) Cumulative Thrust.

Figure 3.11: (a) Multiple debris avoidance paths for a non-stationary debris using the contractive set approach. The green x marks the initial node. The blue x marks the final node. The red ellipsoids represent the debris path. The blue and pink lines are the path the spacecraft takes in order to avoid the debris for minimum length path and fuel efficient path, respectively. The blue and pink ellipsoids represent the invariant sets, C_N, along the paths. (b) The time history of thrust magnitude. (c) Cumulative thrust vs time.

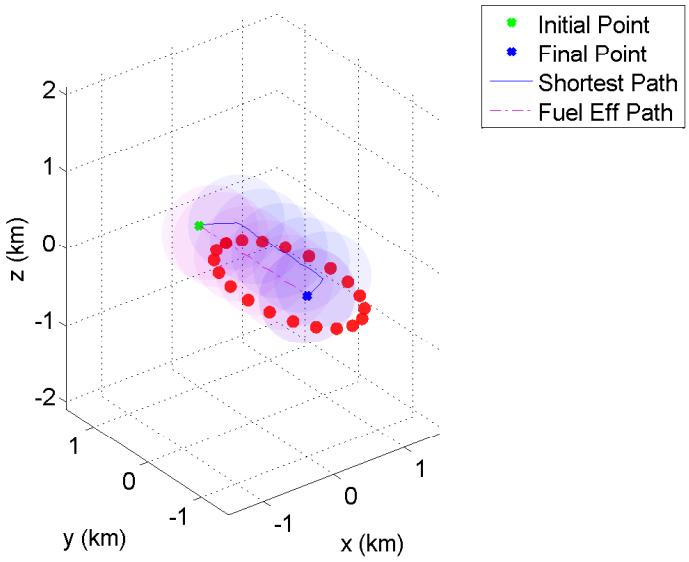

(a) Debris Avoidance Path.

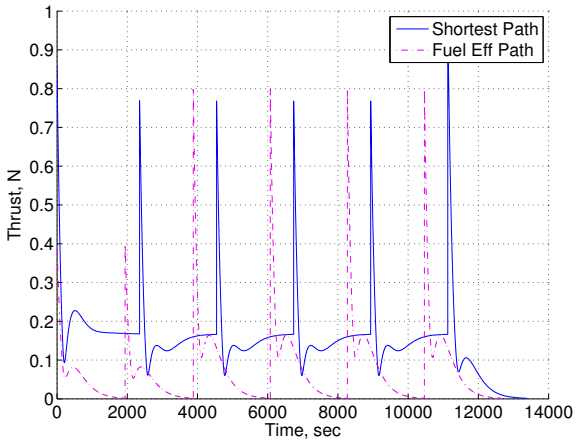

(b) Norm of Thrust Profile.

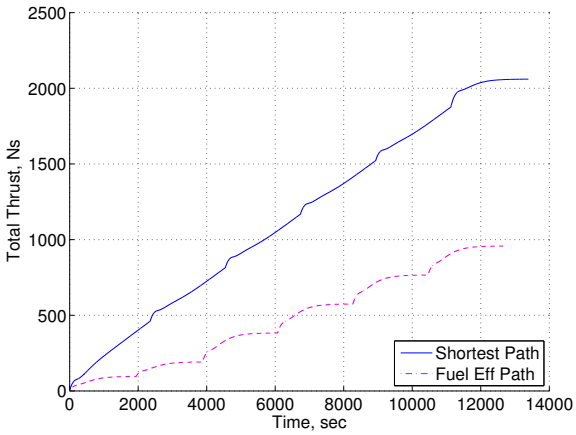

(c) Cumulative Thrust.

Figure 3.12: (a) Multiple debris avoidance paths that travel through intermediate nodes for a non-stationary debris using the contractive set approach. The green x marks the initial node. The blue x marks the final node. The red ellipsoids represent the debris path. The blue and pink lines are the path the spacecraft takes in order to avoid the debris for minimum length path and fuel efficient path, respectively. The blue and pink ellipsoids represent the invariant sets, C_N, along the paths. (b) The time history of thrust magnitude. (c) Cumulative thrust vs time.

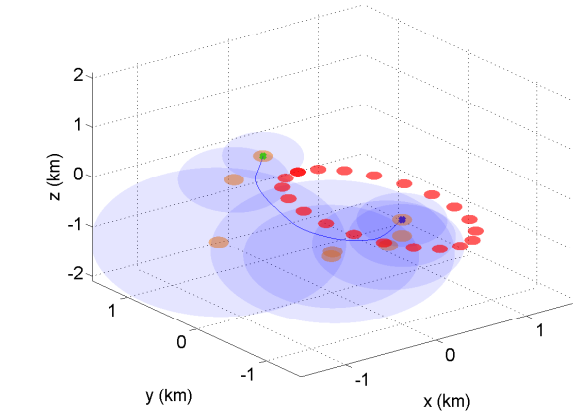

(a) Debris Avoidance Path.

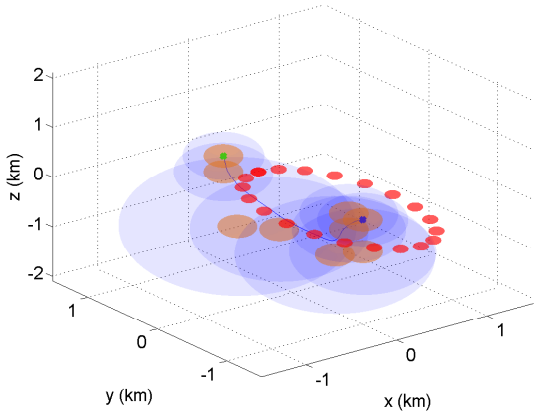

(b) Debris Avoidance Path.

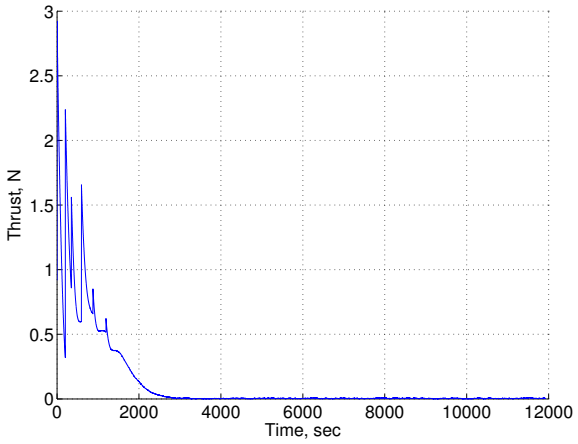

(c) Norm of Thrust Profile.

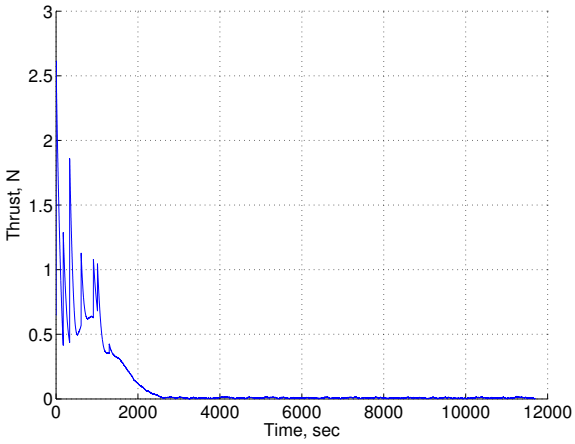

(d) Norm of Thrust Profile.

Figure 3.13: (a) Debris avoidance path for a non-stationary debris under uniform random disturbance with $\varepsilon = 0.1$ N. The green x marks the initial node. The blue x marks the final node. The red ellipsoids represent the debris path. The blue line is the path the spacecraft takes in order to avoid the debris. The blue ellipsoids represent the maximally grown invariant sets $C(r,K,\rho^*(r,K,z))$ along the path. The orange ellipsoids represent the disturbance invariant sets $C(r,K,\gamma_{\min}(K))$, along the path. (b) Debris avoidance path for a non-stationary debris under uniform random disturbance with $\varepsilon = 0.2$ N. (c), (d) Time histories of thrust magnitude.

CHAPTER 4

Inertia-Free Attitude Control

This chapter presents the extension of the inertia-free attitude controllers based on rotation matrices developed in [32] to the cases of magnetic actuation, reaction wheels, and fixed-speed SGCMGs.

The control laws that we consider are of two types. The first type comprises *fixed-gain attitude control laws* (FGAC). These control laws take the form of PD control laws tailored to the nonlinear characteristics of spacecraft dynamics. The second type of controller is an extension of fixed-gain attitude control laws to include an on-line estimate of the spacecraft inertia. This type of control law, called *estimation-based attitude control* (EBAC), is considered in [31] using quaternions and in [32] using rotation matrices.

To illustrate the control laws, we consider two basic scenarios, namely, motion-to-rest (M2R) maneuvers and motion-to-spin (M2S) maneuvers, where "rest" and "spin" refer to motion relative to an inertial frame. An M2R maneuver may begin from either rest or an arbitrary angular velocity. Hence, M2R includes maneuvers commonly referred to as slews, detumbling, and stabilization. The goal is to have the spacecraft come to rest with a specified attitude in the sense that a specified body axis is pointing in a specified inertial direction. If the M2R and M2S maneuvers begin from zero angular velocity, then we use the terminology rest-to-rest (R2R) and rest-to-spin (R2S), respectively.

An M2S maneuver aims to bring the spacecraft from an arbitrary initial angular velocity and attitude to a constant angular velocity relative to an inertial frame. Consequently, the goal is to have the spacecraft rotate at a constant rate about a body-fixed axis whose inertial direction is fixed. Specified spin maneuvers can be used, for example, to provide momentum bias to the spacecraft, or to achieve nadir pointing along a circular orbit.

The equations of motion used in this chapter for spacecraft attitude dynamics with reaction wheels is derived in Appendix B.

4.1 Spacecraft Model, Assumptions, and Control Objectives

As a spacecraft model, we consider a single rigid spacecraft bus controlled by magnetic torquers, reaction wheels, or SGCMGs. The spacecraft's angular momentum H, relative to its center of mass with respect to the inertial frame resolved in the spacecraft frame, depends on the type of torque actuation used and is detailed below for the aforementioned cases. We consider only the rotational motion of the spacecraft and not the translational motion of the spacecraft's center of mass; therefore we consider only the torque τ_{actuator} applied by the force or torque actuators. We assume that a body-fixed frame is defined for the spacecraft, whose origin is chosen to be the center of mass, and that an inertial frame is specified for determining the attitude of the spacecraft. The spacecraft equations of motion are given by Euler's equation and Poisson's equation

$$J_{\text{sc}}\dot{\omega} = H \times \omega + \tau_{\text{actuator}} + z_{\text{dist}}, \tag{4.1}$$

$$\dot{R} = R\omega^{\times}, \tag{4.2}$$

where $\omega \in \mathbb{R}^3$ is the angular velocity of the spacecraft frame with respect to the inertial frame resolved in the spacecraft frame, $\omega^{\times}$ is the cross-product matrix of ω, $J_{\text{sc}} \in \mathbb{R}^{3\times3}$ is the constant, positive-definite inertia matrix of the spacecraft including wheels if present, that is, the inertia tensor of the spacecraft relative to the spacecraft center of mass resolved in the spacecraft frame, and $R = \mathcal{O}_{\text{In/SC}} \in \mathbb{R}^{3\times3}$ is the rotation tensor that transforms the inertial frame into the spacecraft frame resolved in the spacecraft frame, and where $\mathcal{O}_{\text{In/SC}}$ is the orientation (direction cosine) matrix that transforms components of a vector resolved in spacecraft frame into the components of the same vector resolved in inertial frame.

The components of the vector τ_{actuator} represent the torque inputs about each axis of the spacecraft frame, which depends on the chosen torque actuation as detailed below. The vector z_{dist} represents disturbance torques, that is, all internal and external torques applied to the spacecraft aside from control torques, which may be due to onboard components, gravity gradients, solar pressure, atmospheric drag, or the ambient magnetic field. For convenience in (4.1), (4.2) we omit the argument t, recognizing that ω, R, u, and z_{dist} are time-varying quantities.

4.1.1 Measurement Sensors

Both rate (inertial) and attitude (noninertial) measurements are assumed to be available. For simplicity, we assume that gyro measurements are available without noise and without bias. In practice, bias can be corrected by using attitude measurements. Attitude is measured indirectly through direction measurements using sensors such as star trackers. Attitude estimation on SO(3) is considered in [76–78].

The objective of the attitude control problem is to determine control inputs such that the spacecraft attitude given by R follows a commanded attitude trajectory given by the possibly time-varying C^1 rotation matrix $R_d(t)$. For $t \geq 0$, $R_d(t)$ is given by

$$\dot{R}_d(t) = R_d(t)\omega_d(t)^\times, \tag{4.3}$$

$$R_d(0) = R_{d0}, \tag{4.4}$$

where ω_d is the desired possibly time-varying angular velocity. The error between $R(t)$ and $R_d(t)$ is given in terms of the attitude-error rotation matrix

$$\tilde{R} \triangleq R_d^T R, \tag{4.5}$$

which satisfies the differential equation

$$\dot{\tilde{R}} = \tilde{R}\tilde{\omega}^\times, \tag{4.6}$$

where the angular-velocity error $\tilde{\omega}$ is defined by

$$\tilde{\omega} \triangleq \omega - \tilde{R}^T\omega_d.$$

4.1.2 Attitude Error

A scalar measure of attitude error is given by the eigenaxis attitude error, which is the rotation angle $\theta(t)$ about the eigenaxis needed to rotate the spacecraft from its attitude $R(t)$ to the desired attitude $R_d(t)$. This angle is given by [79]

$$\theta(t) = \cos^{-1}(\tfrac{1}{2}[\mathrm{tr}\,\tilde{R}(t) - 1]). \tag{4.7}$$

4.1.3 Spacecraft Inertia

Since the control laws in this chapter require no inertia modeling, examples that span a range of possible inertia matrices are considered. The inertia of a rigid body is determined

by its principal moments of inertia, that is, the diagonal entries of the inertia tensor resolved in a principal body-fixed frame, in which case the inertia matrix is a diagonal matrix. If the inertia tensor is resolved in a non-principal body-fixed frame, then the diagonal entries are the moments of inertia and the off-diagonal entries are the products of inertia. The off-diagonal entries of the inertia matrix are thus a consequence of an unknown rotation between a principal body-fixed frame and the chosen body-fixed frame.

Figure 4.1 shows the triangular region of feasible principal moments of inertia of a rigid body. There are five cases that are highlighted for the principal moments of inertia $\lambda_1 \geq \lambda_2 \geq \lambda_3 > 0$, where $\lambda_1, \lambda_2, \lambda_3$ satisfy the triangle inequality $\lambda_1 < \lambda_2 + \lambda_3$. Let m denote the mass of the rigid body. The point $\lambda_1 = \lambda_2 = \lambda_3$ corresponds to a sphere of radius

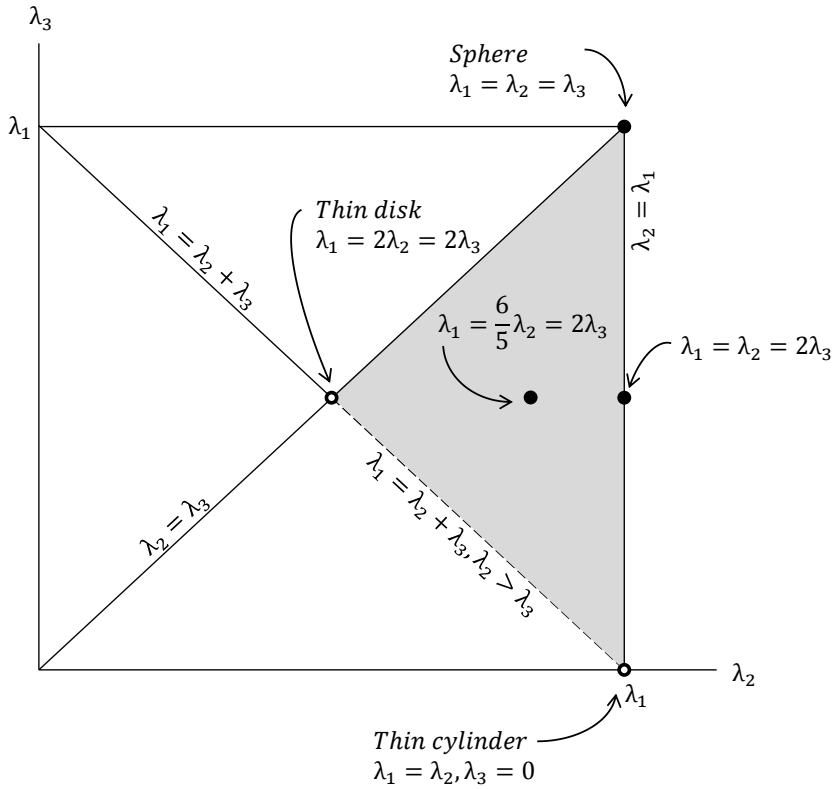

Figure 4.1: Feasible region of the principal moments of inertia $\lambda_1, \lambda_2, \lambda_3$ of a rigid body satisfying $0 < \lambda_3 \leq \lambda_2 \leq \lambda_1$, where $\lambda_1 < \lambda_2 + \lambda_3$. The shaded region shows all feasible values of λ_2 and λ_3 in terms of the largest principal moment of inertia λ_1. The open dots and dashed line segment indicate nonphysical, limiting cases.

$r = \sqrt{\frac{5\lambda_1}{2m}}$, a cube whose sides have length $l = \sqrt{\frac{6\lambda_1}{m}}$, and a cylinder of length l and radius r, where $l/r = \sqrt{3}$ and $r = \sqrt{\frac{2\lambda_1}{m}}$. The point $\lambda_1 = \lambda_2 = 2\lambda_3$ corresponds to a cylinder of

length l and radius r, where $l/r = 3$ and $r = \sqrt{\frac{2\lambda_1}{m}}$. The point $\lambda_1 = \frac{6}{5}\lambda_2 = 2\lambda_3$, located at the centroid of the triangular region, corresponds to a solid rectangular body with sides $l_1 = \sqrt{\frac{8\lambda_1}{m}} > l_2 = \sqrt{\frac{4\lambda_1}{m}} > l_3 = \sqrt{\frac{2\lambda_1}{m}}$.

The remaining cases in Figure 4.1 are nonphysical, limiting cases. The point $\lambda_1 = 2\lambda_2 = 2\lambda_3$ corresponds to a thin disk of radius $r = \sqrt{\frac{2\lambda_1}{m}}$ and length $l = 0$. The point $\lambda_1 = \lambda_2$ and $\lambda_3 = 0$ corresponds to a thin cylinder of radius $r = 0$ and length $l = \sqrt{\frac{12\lambda_1}{m}}$. Finally, each point along the line segment $\lambda_1 = \lambda_2 + \lambda_3$, where $\lambda_2 > \lambda_3$, corresponds to a thin rectangular plate with sides of length $l_1 = \sqrt{\frac{12\lambda_2}{m}} > l_2 = \sqrt{\frac{12\lambda_3}{m}}$.

For all simulations of the inertia-free control laws, the principal axes are viewed as the nominal body-fixed axes, and thus the nominal inertia matrix is a diagonal matrix whose diagonal entries are the principal moments of inertia. To demonstrate robustness, the principal moments as well as the orientation of the body-fixed frame relative to the principal axes is varied. For convenience, λ_1 is normalized to 10 kg-m^2, and the inertia matrices J_1, J_2, J_3, J_4, J_5 are chosen to correspond to the points noted in Figure 4.1. These matrices, which correspond to the sphere, cylinder with $l/r = 3$, centroid, thin disk, and thin cylinder, respectively, are defined as

$$J_1 = \text{diag}(10, 10, 10), \quad J_2 = \text{diag}(10, 10, 5), \quad J_3 = \text{diag}(10, 25/3, 5),$$
$$J_4 = \text{diag}(10, 5, 5), \quad J_5 = \text{diag}(10, 10, 0.1). \tag{4.8}$$

The inertia matrix J_3 corresponding to the centroid of the inertia region serves as the nominal inertia matrix, while the inertia matrices J_1, J_2, J_4, J_5 are used as perturbations to demonstrate robustness of the control laws. A perturbation $J(\lambda)$ of J_i in the direction of J_j thus has the form

$$J(\lambda) = (1 - \lambda)J_i + \lambda J_j, \tag{4.9}$$

where $\lambda \in [0, 1]$. Finally, in order to facilitate numerical integration of Euler's equation, note that J_5 is chosen to be a nonsingular approximation of the limiting inertia of a thin cylinder.

4.1.4 Magnetic Torquers

For a rigid spacecraft actuated by three magnetic torque devices, and without on-board momentum storage, it follows that $H = J\omega$, which, when substituted into (4.1), yields the equations of motion for a spacecraft with magnetic torquers. For the case of M2R, these

equations have the form

$$J_{\text{sc}}\dot{\omega} = (J_{\text{sc}}\omega)\times\omega + \tau_{\text{mag}} + z_{\text{dist}}, \tag{4.10}$$

where the vector $\tau_{\text{mag}} \in \mathbb{R}^3$ represents the torque on the spacecraft generated by the magnetic actuators. The vector can be written as [80]

$$\tau_{\text{mag}}(t) = u(t)\times b(t) = -b(t)^{\times}u(t), \tag{4.11}$$

where $u(t)$ is the magnetic dipole moment generated by the currents in the magnetic actuators measured in ampere-square meters (A-m^2), and where $b(t) = [b_x(t) \quad b_y(t) \quad b_z(t)]^{\text{T}}$ is Earth's geomagnetic field measured in teslas (T) and resolved in the body-fixed frame. For a discussion on generating magnetic dipole moments from magnetic torquer rods, see [81]. Defining

$$B(t) \triangleq -b(t)^{\times}, \tag{4.12}$$

we can rewrite (4.10) as,

$$J_{\text{sc}}\dot{\omega} = (J_{\text{sc}}\omega)\times\omega + Bu + z_{\text{dist}}. \tag{4.13}$$

Note that we have dropped the argument t for convenience.

4.1.5 Reaction Wheels

The dynamics of a spacecraft actuated by three axisymmetric wheels which are presented below are dervied in detail in Appendix B. The assumptions presented in Section B.1.2 are not invoked.

The angular momentum of the spacecraft relative to its center of mass with respect to the inertial frame is given by

$$H = J_{\text{sc}}\omega + J_{\alpha}\nu, \tag{4.14}$$

where $J_{\alpha}\nu$ represents the angular momentum of the reaction wheel assembly. Therefore, (4.1) has the form

$$J_{\text{sc}}\dot{\omega} = (J_{\text{sc}}\omega + J_{\alpha}\nu)\times\omega + \tau_{\text{RW}} + \tau_{\text{dist}}, \tag{4.15}$$

$$\dot{\nu} = u, \tag{4.16}$$

where (4.20) is a kinematic relation describing the angular acceleration of the reaction wheels. In practice, a servo loop is closed around each reaction wheel in order to produce the desired angular acceleration. The reaction-wheel torque has the form

$$\tau_{\mathrm{RW}} = -J_\alpha u. \tag{4.17}$$

Therefore, defining

$$B \triangleq -J_\alpha, \tag{4.18}$$

the equations of motion for a spacecraft with reaction wheels have the form

$$J_{\mathrm{sc}}\dot{\omega} = (J_{\mathrm{sc}}\omega + J_\alpha \nu) \times \omega + Bu + \tau_{\mathrm{dist}}, \tag{4.19}$$

$$\dot{\nu} = u. \tag{4.20}$$

Compared to the case of thrusters treated in ref. [32], reaction-wheel actuation complicates the dynamic equations due to the term $J_\alpha \nu$ in (4.19), as well as the integrators (4.20) augmented to the system. The torque inputs applied to each reaction wheel are constrained by current limitations on the electric motors and amplifiers as well as angular-velocity constraints on the wheels. These constraints are addressed indirectly in Section 4.3.2.

4.1.6 CMG's

The dynamics of a spacecraft actuated by three fixed-speed SGCMGs which are presented below are derived in detail in [82]. We provide a summary below.

Consider a spacecraft actuated by three orthogonal single-gimbal CMG's with spherical gyro wheels attached to a rigid bus. Each CMG is mounted so that its gimbal is free to rotate about an axis passing through the center of mass of the gyro wheel. For simplicity, the gimbals are assumed to be massless. However, we do not assume that each gimbal's axis of rotation passes through the center of mass of the bus, nor do we assume that the CMG's are balanced with respect to the bus in order to preserve the location of its center of mass. Thus the center of mass of the spacecraft and the center of mass of the bus may be distinct points.

Let the spacecraft be denoted by sc, and let c denote its center of mass. Although the spacecraft is not a rigid body, the spherical symmetry of the gyro wheels implies that c is fixed in both the bus and the spacecraft. Let c_i denote the center of mass of the ith gyro wheel. We assume a bus-fixed frame $\mathrm{F_B}$, three gimbal-fixed frames $\mathrm{F_{G_i}}$ whose y-axes are

aligned with the rotation axes of their respective gimbals, three gyro-wheel-fixed frames $\mathrm{F}_{\mathrm{W}_i}$ whose x-axes are aligned with the rotation axes of their respective gyro wheels, and an Earth-centered inertial frame F_{E}. The angular momentum of the spacecraft relative to its center of mass with respect to the inertial frame is given by

$$H = J_{\mathrm{sc}}\omega + \sum_{i=1}^{3} \beta_i \omega_{\mathrm{W}_i}. \tag{4.21}$$

In this case (4.1) becomes

$$J_{\mathrm{sc}}\dot{\omega} = \left(J_{\mathrm{sc}}\omega + \sum_{i=1}^{3} \beta_i \omega_{\mathrm{W}_i} \right) \times \omega - J_\beta \dot{u} + \tau_{\mathrm{CMG}} + z_{\mathrm{dist}}, \tag{4.22}$$

where

$$J_\beta \triangleq \begin{bmatrix} \beta_1 & 0 & 0 \\ 0 & \beta_2 & 0 \\ 0 & 0 & \beta_3 \end{bmatrix}, \qquad u \triangleq \begin{bmatrix} u_1 \\ u_2 \\ u_3 \end{bmatrix},$$

and the scalar control u_i is the angular velocity of the ith gimbal. Furthermore, the CMG actuator torque τ_{CMG} has the form

$$\tau_{\mathrm{CMG}} = Bu, \tag{4.23}$$

where

$$B \triangleq \begin{bmatrix} \beta_1 \left(\omega_{\mathrm{W}_1}^{\times} - \omega^{\times} \right) e_1 & \beta_2 \left(\omega_{\mathrm{W}_2}^{\times} - \omega^{\times} \right) e_2 & \beta_3 \left(\omega_{\mathrm{W}_3}^{\times} - \omega^{\times} \right) e_3 \end{bmatrix}. \tag{4.24}$$

Note that the actuator matrix B given by (4.24) is state-dependent and thus time-varying.

Substituting (4.23) and (4.24) into (4.22) yields Euler's equation for a spacecraft with CMG's given by

$$J_{\mathrm{sc}}\dot{\omega} = \left(J_{\mathrm{sc}}\omega + \sum_{i=1}^{3} \beta_i \omega_{\mathrm{W}_i} \right) \times \omega + Bu + z'_{\mathrm{dist}}, \tag{4.25}$$

where

$$z'_{\mathrm{dist}} \triangleq z_{\mathrm{dist}} - J_\beta \dot{u}. \tag{4.26}$$

Note that we consider $\dot{u}$ as a component of the disturbance. This approach provides direct control of the gimbal rates without an intermediary steering law as in [83].

4.2 Fixed-Gain Attitude Control (FGAC)

In this section we describe the FGAC control laws for each type of actuation. These control laws involve gains that are, in most cases, constant, and must be chosen by the user based on considerations of control authority and desired closed-loop response. Although the response of the spacecraft depends on the actual inertia of the spacecraft, convergence properties are guaranteed regardless of the spacecraft inertia, which need not be known.

The following preliminary results concerning rotation matrices are needed. Let I denote the 3×3 identity matrix, and let M_{ij} denote the i,j entry of the matrix M. The following result provides some properties of a function of rotation matrices that is used to construct a Lyapunov function.

Lemma 1. [32] Let $A \in \mathbb{R}^{3\times 3}$ be a diagonal positive-definite matrix and let R be a rotation matrix. Then the following statements hold:

i) For all $i, j = 1,2,3$, $R_{ij} \in [-1,1]$.

ii) $\mathrm{tr}\,(A - AR) \geq 0$.

iii) $\mathrm{tr}\,(A - AR) = 0$ if and only if $R = I$.

Given $a_1, a_2, a_3 \in \mathbb{R}$, define the vector measure of attitude error

$$S \triangleq \sum_{i=1}^{3} a_i(\tilde{R}^{\mathrm{T}} e_i) \times e_i, \tag{4.27}$$

where, for $i = 1,2,3$, e_i denotes the ith column of the 3×3 identity matrix. When attitude measurements are given in terms of an alternative representation, such as quaternions, the corresponding attitude-error $\tilde{R}$ defined by (4.5) can be computed, and thus (4.27) can be evaluated and used by the controller given in Theorem 2 below. Consequently, S can be computed from any attitude parameterization.

An inertia-free control law for a rigid spacecraft with three torque inputs is given by the proportional-derivative-(PD)-type SO(3)/0 control law [32]

$$u = -B^{-1}(K_{\mathrm{p}} S + K_{\mathrm{v}}\omega), \tag{4.28}$$

where B is the torque-input matrix, and K_p and K_v are proportional (attitude) and derivative (angular velocity) gains, respectively. When no disturbances are present, the this controller achieves almost global stabilization of a constant desired attitude R_d, that is, a slew maneuver that brings the spacecraft to rest. The initial conditions of the slew maneuver may be arbitrary, that is, the spacecraft may have nonzero initial velocity. This controller is inertia-free since knowledge of the spacecraft inertia J is not needed for implementation. Consequently, this controller can be implemented for stabilization and slew maneuvers without knowledge of the spacecraft's mass distribution.

We now extend (4.28) to the cases of magnetic actuation, reaction wheels, and fixed-speed SGCMGs.

4.2.1 FGAC for Magnetic Torquers

For magnetic torquing, a quaternion-based FGAC control law that relies solely on current, on-board measurements of the geomagnetic field and requires knowledge of the spacecraft inertia matrix is given by (13) of [84]. The proof of stability is based on averaging theory. We modify this control law to use rotation matrices rather than quaternions and, inspired by [85], to be inertia free. The proportional-derivative-(PD)-type control law is thus given by

$$u = -\frac{b^\times(t)}{\|b(t)\|^2}\bar{\Gamma}^{-1}(\varepsilon^2 K_\mathrm{p} S + \varepsilon K_\mathrm{v}\omega), \tag{4.29}$$

where

$$\bar{\Gamma} \triangleq \lim_{T\to\infty}\int_0^T \Gamma(t)\mathrm{d}t = \lim_{T\to\infty}\int_0^T -\frac{b^\times(t)b^\times(t)}{\|b(t)\|^2},$$

and $0 < \varepsilon < \varepsilon^*$ is a scaling of the proportional and derivative gains K_p and K_v, where ε^* is the maximum scaling. As mentioned in [84], this condition guarantees that the control action changes on the order of the natural time variation of Earth's magnetic field.

4.2.2 FGAC for Reaction Wheels

Theorem 1. *Let K_p be a positive number and let $A = \mathrm{diag}(a_1, a_2, a_3)$ be a diagonal positive-definite matrix. Then the function*

$$V(\omega, \tilde{R}) \triangleq \tfrac{1}{2}\omega^\mathrm{T} J_\mathrm{sc}\omega + K_\mathrm{p}\mathrm{tr}(A - A\tilde{R}), \tag{4.30}$$

is positive definite, that is, V is nonnegative, and $V = 0$ if and only if $\omega = 0$ and $\tilde{R} = I$.

Proof. It follows from statement 2 of Lemma 1 that $\mathrm{tr}(A - A\tilde{R})$ is nonnegative. Hence V is nonnegative. Now suppose that $V = 0$. Then, $\omega = 0$, and it follows from *iii*) of Lemma 1 that $\tilde{R} = I$. □

Theorem 2. *Let K_p be a positive number, let $K_\mathrm{v} \in \mathbb{R}^{3\times 3}$ be a positive-definite matrix, let $A = \mathrm{diag}(a_1, a_2, a_3)$ be a diagonal positive-definite matrix with distinct diagonal entries, let R_d be constant, define S as in (4.27), and define V as in Theorem 1. Consider the control law*

$$u = J_\alpha^{-1}(K_\mathrm{p} S + K_\mathrm{v}\omega). \tag{4.31}$$

Then,

$$\dot{V}(\omega, \tilde{R}) = -\omega^\mathrm{T} K_\mathrm{v} \omega \tag{4.32}$$

is negative semidefinite. Furthermore, the closed-loop system consisting of (4.19), (4.20), (4.6), and (4.31) is almost globally asymptotically stable [86], and for all initial conditions not in an embedded submanifold of $\mathbb{R}^3 \times \mathrm{SO}(3) \times \mathbb{R}^6 \times \mathbb{R}^3$ (see ref. [32]), $\omega \to 0$ and $\tilde{R} \to I$ as $t \to \infty$.

Proof. Noting that

$$\begin{aligned}
\frac{\mathrm{d}}{\mathrm{d}t}\mathrm{tr}\,(A - A\tilde{R}) &= -\mathrm{tr}\,A\dot{\tilde{R}} \\
&= -\mathrm{tr}\,A(\tilde{R}\omega^{\times} - \omega_{\mathrm{d}}^{\times}\tilde{R}) \\
&= -\sum_{i=1}^{3} a_i e_i^{\mathrm{T}}(\tilde{R}\omega^{\times} - \omega_{\mathrm{d}}^{\times}\tilde{R})e_i \\
&= -\sum_{i=1}^{3} a_i e_i^{\mathrm{T}}\tilde{R}(\omega^{\times} - \tilde{R}^{\mathrm{T}}\omega_{\mathrm{d}}^{\times}\tilde{R})e_i \\
&= -\sum_{i=1}^{3} a_i e_i^{\mathrm{T}}\tilde{R}(\omega - \tilde{R}^{\mathrm{T}}\omega_{\mathrm{d}})^{\times}e_i \\
&= \sum_{i=1}^{3} a_i e_i^{\mathrm{T}}\tilde{R}e_i^{\times}\tilde{\omega} \\
&= \left[-\sum_{i=1}^{3} a_i e_i \times \tilde{R}^{\mathrm{T}}e_i\right]^{\mathrm{T}}\tilde{\omega} \\
&= \left[\sum_{i=1}^{3} a_i (\tilde{R}^{\mathrm{T}}e_i) \times e_i\right]^{\mathrm{T}}\tilde{\omega} \\
&= \tilde{\omega}^{\mathrm{T}}S,
\end{aligned}$$

then

$$\begin{aligned}
\dot{V}(\omega, \tilde{R}) &= \omega^{\mathrm{T}}J_{\mathrm{sc}}\dot{\omega} + K_{\mathrm{p}}\omega^{\mathrm{T}}S \\
&= \omega^{\mathrm{T}}\left[(J_{\mathrm{sc}}\omega + J_{\alpha}\nu) \times \omega - J_{\alpha}u\right] + K_{\mathrm{p}}\omega^{\mathrm{T}}S \\
&= \omega^{\mathrm{T}}\left(-K_{\mathrm{p}}S - K_{\mathrm{v}}\omega\right) + K_{\mathrm{p}}\omega^{\mathrm{T}}S \\
&= -\omega^{\mathrm{T}}K_{\mathrm{v}}\omega.
\end{aligned}$$

The proof of the final statement follows from invariant set arguments that are similar to those used in ref. [32]. □

Note that $-J_{\alpha}$ is substituted for the input matrix B used in the inertia-free control law (38) of ref. [32], but otherwise the controller requires no modification for the case of reaction-wheel actuation in order to achieve almost global stabilization of a constant desired attitude R_{d}.

4.2.3 FGAC for CMG's

For the following development we assume that J_β is constant, nonsingular, and known. That is, the spacecraft has three orthogonal CMG's with spherical gyro wheels with known moments of inertia about their spin axes.

In addition, we assume that the gimbal accelerations $\dot{u}$ are negligible. We thus ignore the effect of $\dot{u}$ in the derivation of the control law by considering it a part of the disturbance z_d. This treatment of $\dot{u}$ is consistent with [87–89]. We do, however, include this effect in simulations and show through numerical examples that this is a reasonable assumption.

A difficulty encountered with CMG's is that the torque they can generate may be confined to a plane perpendicular to the requested torque. When this condition occurs, the CMG's are considered to be in a singular state, and gimbal angular velocities that synthesize the requested torque do not exist. Much of the work on CMG's has thus focused on the development of steering laws that modify the requested torque to either avoid these singular states or steer the controller through them [90–94].

While we do not use an explicit steering law to synthesize the desired torque, the matrix B in the CMG case is state-dependent and sometimes singular. Borrowing ideas from the steering-law literature, in the subsequent examples we employ practical, albeit approximate, methods for inverting B. For example, the singularity-robust (SR) inverse [95, 96] trades off between introducing torque errors in the vicinity of a singularity and the feasibility of the solution, where feasibility indicates that the gimbal angular velocities remain bounded, unlike the case of the Moore-Penrose inverse.

The SR inverse is derived from the optimization problem

$$\text{minimize} \quad e^{\mathrm{T}} W e, \tag{4.33}$$

where $e = [\tau - Yu \;\; u]^{\mathrm{T}}$, τ is the desired torque in a steering-law formulation of the CMG problem, and $W = \mathrm{diag}(W_1, W_2)$ is a block-diagonal weight matrix.

The SR inverse is thus given by

$$Y^{\#} = W_2^{-1} Y^{\mathrm{T}} \left(Y W_2 Y^{\mathrm{T}} + W_1^{-1} \right). \tag{4.34}$$

Note that different values of W_1 and W_2 yield different SR inverses, and that selecting $W_1 = 0$ and $W_2 = I$ yields the Moore-Penrose inverse.

We use the SR inverse in place of the inverse of B in a PD control law for CMG's. Since the SR inverse introduces error into the inversion, we test the ability of the control law to compensate for this disturbance. The inertia-free control law for CMG's is thus given by

the PD-type control law

$$u = -Y^{\#}(K_{\mathrm{p}}S + K_{\mathrm{v}}\omega). \tag{4.35}$$

In the simulations below we do not modify the weight matrices W_1 and W_2 based on the distance of Y from singularity. Alternative methods, such as the singular-direction avoidance (SDA) inverse [88], can also be applied.

4.3 FGAC Examples

4.3.1 FGAC Example Using Magnetic Torquers

We consider a spacecraft in a 450-km circular orbit above the Earth with an inclination of 87 deg. The International Geomagnetic Reference Field (IGRF) model is used to simulate Earth's geomagnetic field as a function of orbital position [53]. The spacecraft inertia matrix J is given by J_3, with the body-fixed frame assumed to be a principal frame.

We use the SO(3)/0 FGAC controller (4.29) for a M2R maneuver, where the objective is to bring the spacecraft from the initial attitude $R(0) = I_3$, with initial angular velocity $\omega(0) = [0.025\ 0.025\ -0.03]^{\mathrm{T}}$ rad/sec, to rest at the desired final orientation $R_{\mathrm{d}} = I_3$.

Let $K_{\mathrm{p}} = 75$, $K_{\mathrm{v}} = 75$, and $\varepsilon = 0.0004$. These values are chosen to give nominal magnetic dipole moments around 5 A-m^2, and a settling time of around 8 orbits. We test the controller in a nonlinear simulation of (4.1)-(4.2).

Figure 5.17 shows the eigenaxis attitude error, angular velocity, and magnetic dipole moment for the simulation described above. The spacecraft comes to rest at the commanded attitude within 8 orbits. The maximum magnetic dipole moment generated is less than 6 A-m^2. This quantity can be further tuned by modifying the gains K_{p} and K_{v}.

4.3.2 FGAC Example Using Reaction Wheels

We now illustrate the effectiveness of the FGAC control law (4.31) for regulating the spacecraft attitude and angular velocity using reaction-wheel actuators. The following spacecraft parameters are assumed. The bus inertia matrix J_{b} is nominally given by J_3, which corresponds to the centroid of the inertia region shown in Figure 4.1 with the body-fixed frame assumed to be a principal body-fixed frame. The quantity J_b is unknown to the controller. The axes of rotation of the reaction wheels are aligned with the spacecraft body-fixed frame unit vectors, and the wheel inertias are given by $J_{\mathrm{w}_1} = \mathrm{diag}(\alpha_1,\beta_1,\beta_1)$ kg-m^2,

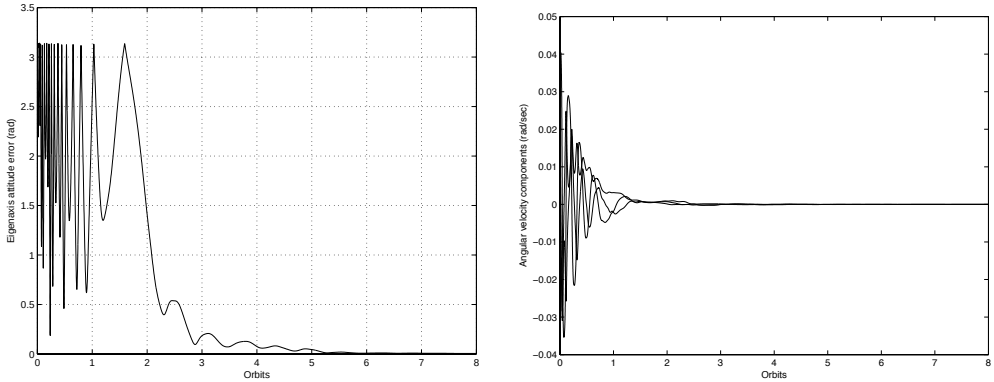

(a) (b)

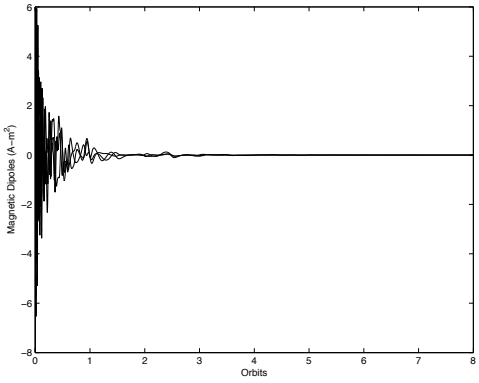

(c)

Figure 4.2: M2R maneuver for the FGAC control law (4.29) using magnetic torquers. (a) Eigenaxis attitude error, (b) angular velocity components, and (c) magnetic dipole moments. The spacecraft comes to rest at the commanded attitude within 7 orbits, and the maximum magnetic dipole moment required by the controller is less than 6 A-m^2.

$J_{w_2} = \text{diag}(\beta_2, \alpha_2, \beta_2)$ kg-m^2, and $J_{w_3} = \text{diag}(\beta_3, \beta_3, \alpha_3)$ kg-m^2, where $\alpha_1 = \alpha_2 = \alpha_3 = 0.5$ and $\beta_1 = \beta_2 = \beta_3 = 0.375$. The values of β_i are unknown to the controller.

Let K_p be given by

$$K_p = \frac{\gamma}{\text{tr}\, A}, \tag{4.36}$$

and, as in ref. [32], let $K_v = K_v(\omega)$ be given by

$$K_v = \eta \begin{bmatrix} \frac{1}{1+|\omega_1|} & 0 & 0 \\ 0 & \frac{1}{1+|\omega_2|} & 0 \\ 0 & 0 & \frac{1}{1+|\omega_3|} \end{bmatrix}. \tag{4.37}$$

Alternative choices of K_v are given in ref. [97].

Controller (4.31) is used for an aggressive slew maneuver, where the objective is to bring the spacecraft from the initial attitude $R_0 = I_3$ and initial angular velocity

$$\omega(0) = \begin{bmatrix} 1 & -1 & 0.5 \end{bmatrix}^{\mathrm{T}} \text{ rad/sec}$$

to rest ($\omega_d = 0$) at the desired final orientation $R_d = \mathrm{diag}(1, -1, -1)$, which represents a rotation of 180 deg about the x-axis. The reaction wheels are initially not spinning relative to the spacecraft, that is,

$$\nu(0) = \begin{bmatrix} 0 & 0 & 0 \end{bmatrix}^{\mathrm{T}} \text{ rad/sec.}$$

No disturbance is present, and the parameters $\gamma = \eta = 5$ are used in (4.36) and (4.37).

Figures 4.3(a)-(d) show, respectively, the attitude error, angular-velocity components, angular rates of the wheels, and the control inputs, which are the angular accelerations of the wheels. The spacecraft attitude and angular-velocity components reach the commanded values in about 100 sec. The angular rates of the wheels approach constant values that are consistent with the initial, nonzero angular momentum.

In practice, reaction wheels have a maximum instantaneous acceleration. Angular-acceleration saturation is enforced in Figures 4.4 and 4.5, where convergence is slower than in Figure 4.3, although stability is maintained.

Additionally, reaction wheels have a maximum rotational rate. Figure 4.6 shows the effect of wheel-rate saturation at 25 rad/sec, corresponding to about 240 rpm. The reaction-wheel rates are saturated for up to 25 seconds, although this does not impact the control objective. Figure 4.7 shows plots for wheel-rate saturation at 20 rad/sec, or about 190 rpm. Although this constraint on the rotation rate is too stringent to obtain zero steady-state error for the desired maneuver, the performance of the controller degrades gracefully by achieving zero spacecraft angular velocity at an offset attitude.

4.3.2.1 Inertia Robustness

To evaluate performance for slew maneuvers, define the settling-time metric

$$k_0 \triangleq \min_{k>100} \{k : \text{ for all } i \in \{1, \ldots, 100\}, \theta((k-i)T_s) < 0.05\,\text{rad}\}, \tag{4.38}$$

where k is the simulation step, T_s is the integration step size, and $\theta(kT_s)$ is the eigenaxis attitude error (4.7) at the kth simulation step. The metric k_0 is thus the minimum time such that the eigenaxis attitude error is less than 0.05 rad during the 100 most recent simulation steps.

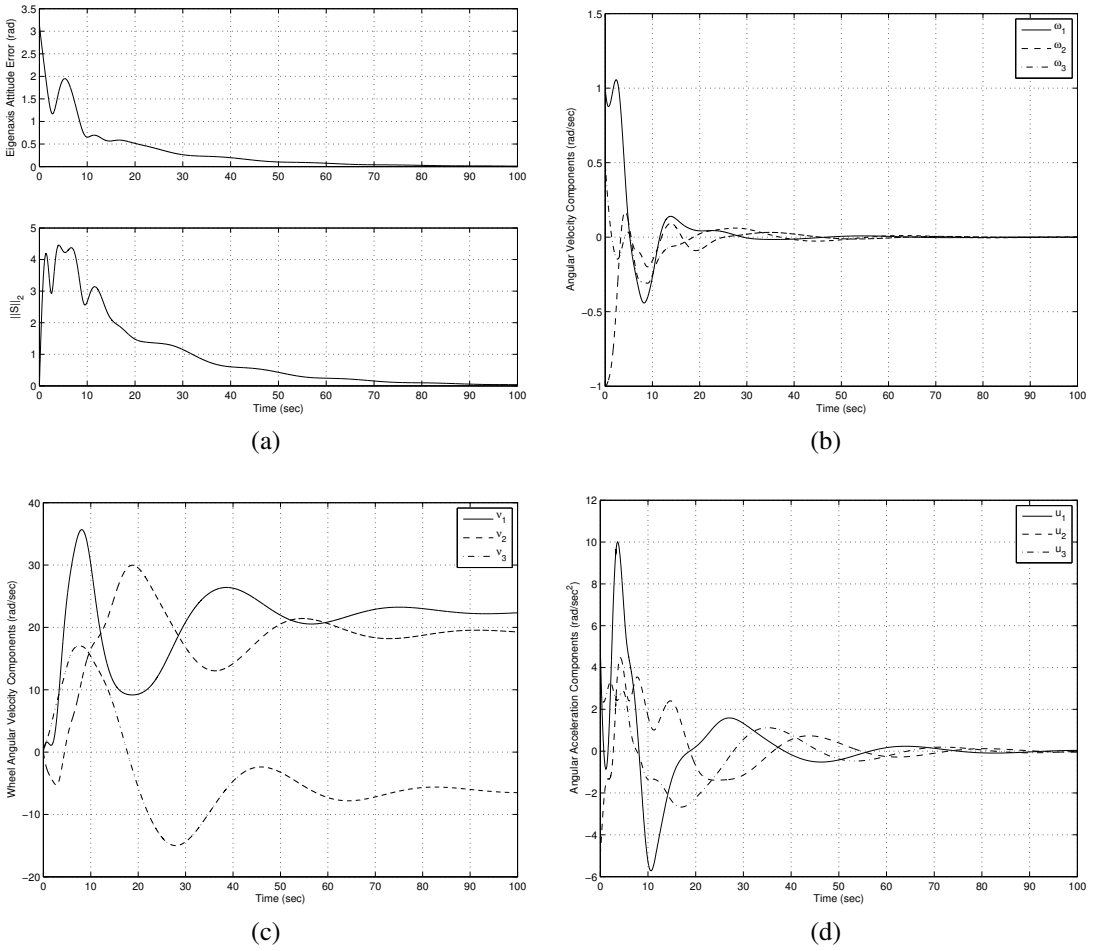

Figure 4.3: M2S maneuver for the FGAC control law (4.31) using reaction wheels and without disturbance. (a) Top: Eigenaxis attitude error. Bottom: Norm of the S parameter, (b) spacecraft angular velocity components, and (c) angular rates of the reaction wheels, (d) angular accelerations of the reaction wheels.

To illustrate the inertia-free property of the control laws (4.31) and (4.51), the inertia of the spacecraft is varied using

$$J_{\mathrm{b}}(\lambda) = (1-\lambda)J_3 + \lambda J_i, \tag{4.39}$$

where $\lambda \in [0,1]$ and $i = 1,4,5$. Figure 4.8 shows how the settling time depends on λ.

Next, the robustness to misalignment of the reaction wheels relative to the principal axes is investigated. Here, the inertia matrix is rotated by an angle ϕ about one of the axes of frame $\mathrm{F_b}$. For a rotation about the x axis of $\mathrm{F_b}$, the inertia of the spacecraft is varied using

$$J_{\mathrm{b}}(\phi) = \mathcal{O}_1(\phi) J_3 \mathcal{O}_1^{\mathrm{T}}(\phi), \tag{4.40}$$

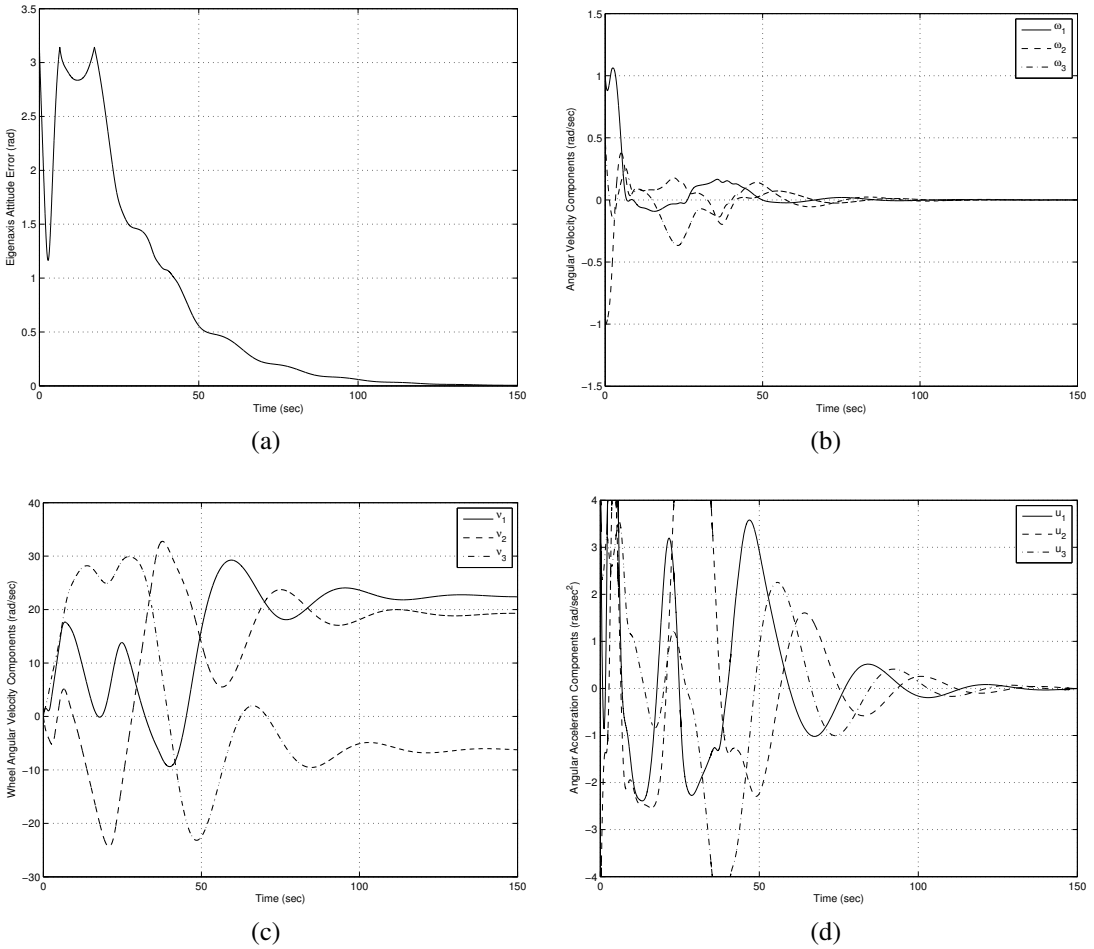

Figure 4.4: M2S maneuver for the FGAC control law (4.31) using reaction wheels and without disturbance. The acceleration of the reaction wheels is saturated at 4 rad/sec^2. (a) Eigenaxis attitude error, (b) spacecraft angular velocity components, and (c) angular rates of the reaction wheels, (d) angular accelerations of the reaction wheels.

where the proper orthogonal matrix $\mathcal{O}_1(\phi)$ rotates vectors about the x axis by the angle ϕ. Similar relations exist for rotations about the y and z axes. Figure 4.9 shows how a thruster misalignment angle ϕ affects the settling time, where ϕ is varied from -180 deg to $+180$ deg.

4.3.3 FGAC Example Using CMG's

We now illustrate the FGAC control law (4.35) using CMG's. The following spacecraft parameters are assumed. The bus inertia matrix $J_{\rm b}$ is given by J_3, which is unknown to the controller. The axes of rotation of the CMG gimbals are aligned with the spacecraft body-fixed frame unit vectors, and the wheel inertias are given by $J_{\rm w_1} = \text{diag}(\beta_1,\beta_1,\beta_1)$ kg-m^2,

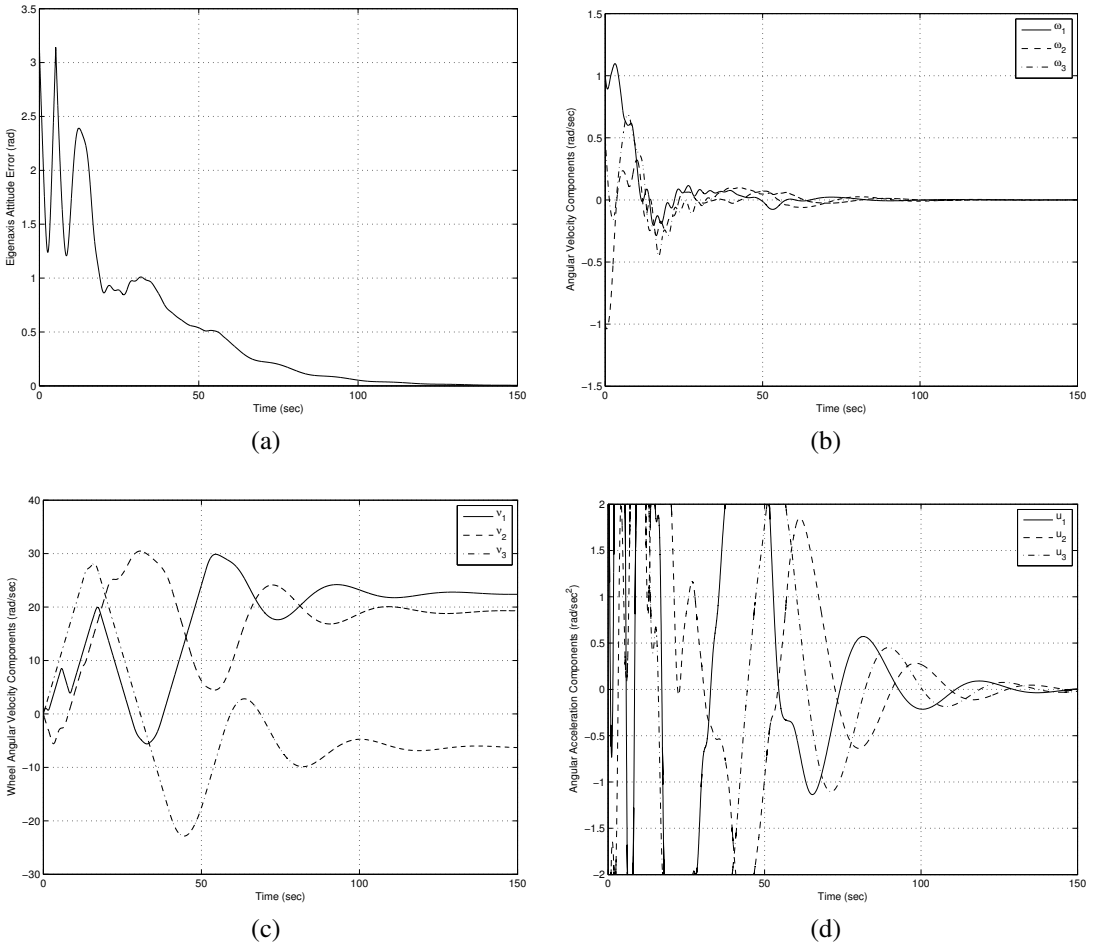

Figure 4.5: M2S maneuver for the FGAC control law (4.31) using reaction wheels and without disturbance. The acceleration of the reaction wheels is saturated at 2 rad/sec^2. (a) Eigenaxis attitude error, (b) spacecraft angular velocity components, and (c) angular rates of the reaction wheels, (d) angular accelerations of the reaction wheels.

$J_{w_2} = \text{diag}(\beta_2,\beta_2,\beta_2)$ kg-m^2, and $J_{w_3} = \text{diag}(\beta_3,\beta_3,\beta_3)$ kg-m^2, where $\beta_1 = \beta_2 = \beta_3 = 0.3$.

Let K_p be given by

$$K_p = 100\frac{\gamma}{\text{tr}A}, \tag{4.41}$$

and let K_v be given by

$$K_v = \text{diag}(100, 100, 100), \tag{4.42}$$

where $A = \text{diag}(1,2,3)$.

Controller (4.35) is used for an aggressive slew maneuver, where the objective is to

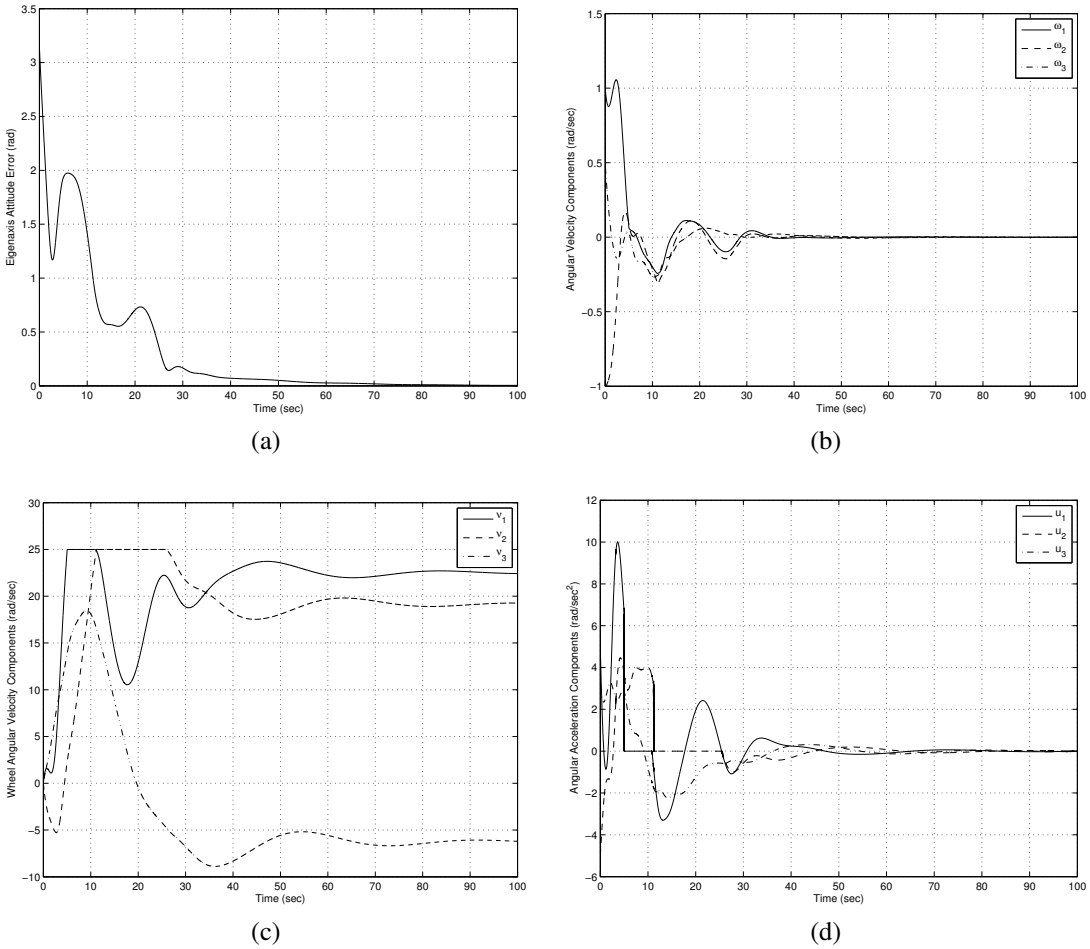

Figure 4.6: M2S maneuver for the FGAC control law (4.31) using reaction wheels and without disturbance. The maximum rotation rate of each wheel is saturated at 25 rad/sec. (a) Eigenaxis attitude error, (b) spacecraft angular velocity components, and (c) angular rates of the reaction wheels, (d) angular accelerations of the reaction wheels.

bring the spacecraft from the initial attitude $R_0 = I_3$ and initial angular velocity $\omega(0) = [1\ -1\ 0.5]^{\mathrm{T}}$ rad/sec to rest at the desired final orientation $R_{\mathrm{d}} = \mathrm{diag}(1, -1, -1)$, which represents a rotation of 180 degrees about the x-axis. The reaction wheels are initially not spinning relative to the spacecraft, that is, $\nu(0) = [0\ 0\ 0]^{\mathrm{T}}$ rad/sec. No disturbance is present.

Figure 4.10 shows the attitude error, angular-velocity components, gimbal angles, and singular values of B. The spacecraft attitude and angular-velocity components reach the commanded values in about 10 sec. The relative angular-velocity components of the reaction wheels settle down to constant values that are consistent with the initial, nonzero angular momentum.

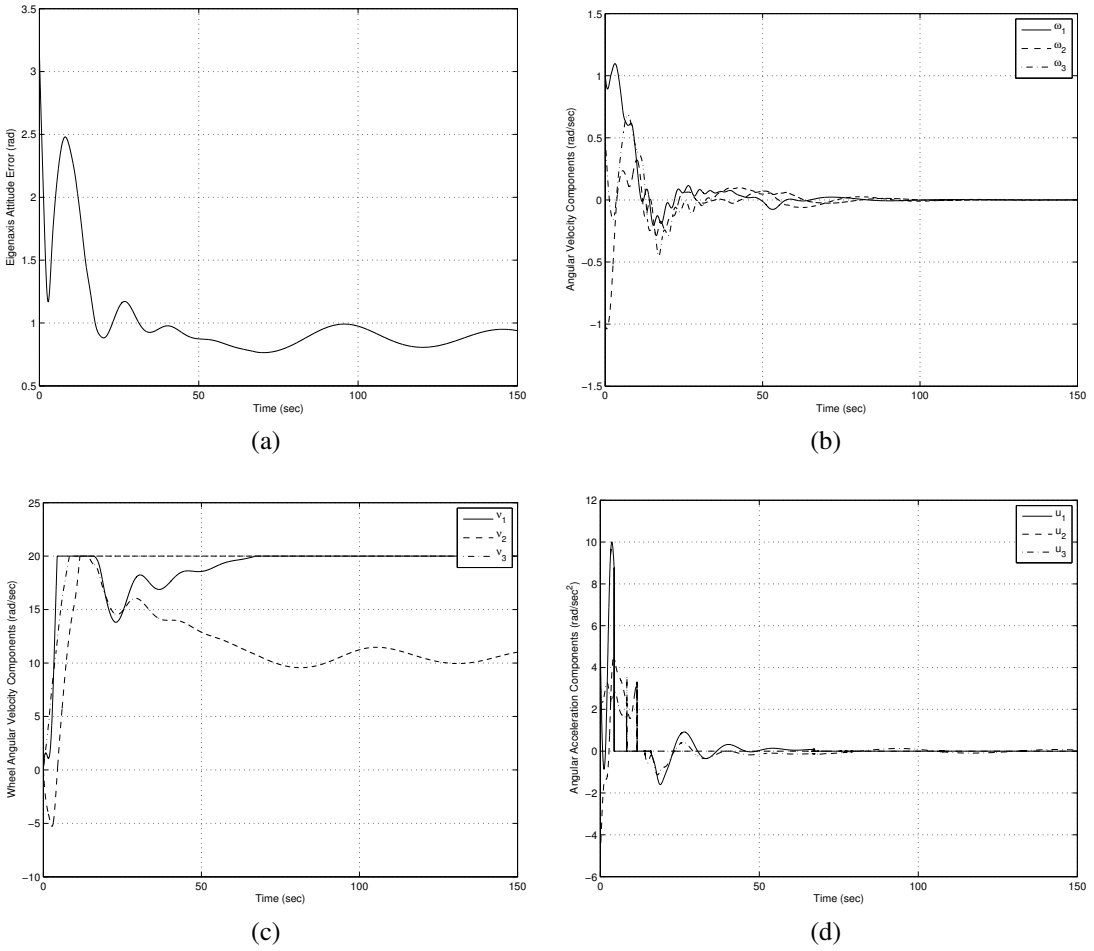

Figure 4.7: M2S maneuver for the FGAC control law (4.31) using reaction wheels and without disturbance. The maximum rotation rate of each wheel is saturated at 20 rad/sec. (a) Eigenaxis attitude error, (b) spacecraft angular velocity components, and (c) angular rates of the reaction wheels, (d) angular accelerations of the reaction wheels.

4.4 Estimator-Based Attitude Control (EBAC)

The main difference between the EBAC control laws and the FGAC control laws is that the latter exploit an estimate of the inertia matrix. These control laws are based on Lyapunov analysis, which also provides disturbance rejection for harmonic disturbances with known spectrum.

To develop an estimate of the spacecraft inertia, we introduce the notation

$$J_{\rm sc}\omega = L(\omega)\gamma,$$

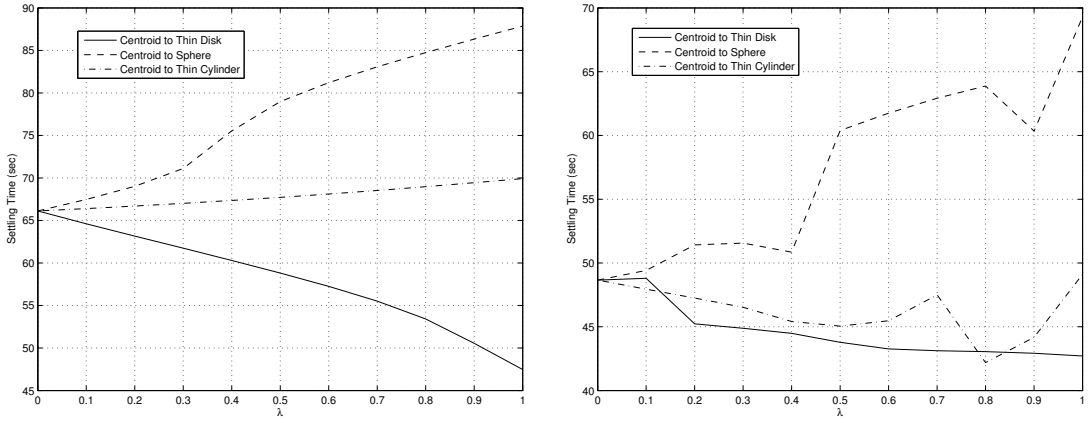

(a) (b)

Figure 4.8: Settling time as a function of λ for various combinations (4.9) of inertia matrices resolved in principal frames. Convergence is achieved for (a) control law (4.31), and (b) control law (4.51). Each controller is implemented in all cases with a single tuning. In all cases, the bus inertia J_3 is unknown.

where $\gamma \in \mathbb{R}^6$ is defined by

$$\gamma \triangleq \begin{bmatrix} J_{11} & J_{22} & J_{33} & J_{23} & J_{13} & J_{12} \end{bmatrix}^{\mathrm{T}}$$

and

$$L(\omega) \triangleq \begin{bmatrix} \omega_1 & 0 & 0 & 0 & \omega_3 & \omega_2 \\ 0 & \omega_2 & 0 & \omega_3 & 0 & \omega_1 \\ 0 & 0 & \omega_3 & \omega_2 & \omega_1 & 0 \end{bmatrix}.$$

Next, let $\hat{J}_{\mathrm{sc}} \in \mathbb{R}^{3\times 3}$ denote an estimate of J_{sc}, and define the inertia-estimation error

$$\tilde{J}_{\mathrm{sc}} \triangleq J_{\mathrm{sc}} - \hat{J}_{\mathrm{sc}}.$$

Letting $\hat{\gamma}, \tilde{\gamma} \in \mathbb{R}^6$ represent $\hat{J}_{\mathrm{sc}}, \tilde{J}_{\mathrm{sc}}$, respectively, it follows that

$$\tilde{\gamma} = \gamma - \hat{\gamma}.$$

Likewise, let $\hat{z}_{\mathrm{dist}} \in \mathbb{R}^3$ denote an estimate of z_{dist}, and define the disturbance-estimation error

$$\tilde{z}_{\mathrm{dist}} \triangleq z_{\mathrm{dist}} - \hat{z}_{\mathrm{dist}}.$$

Assuming that the disturbance is harmonic, it follows that z_{dist} can be modeled as the

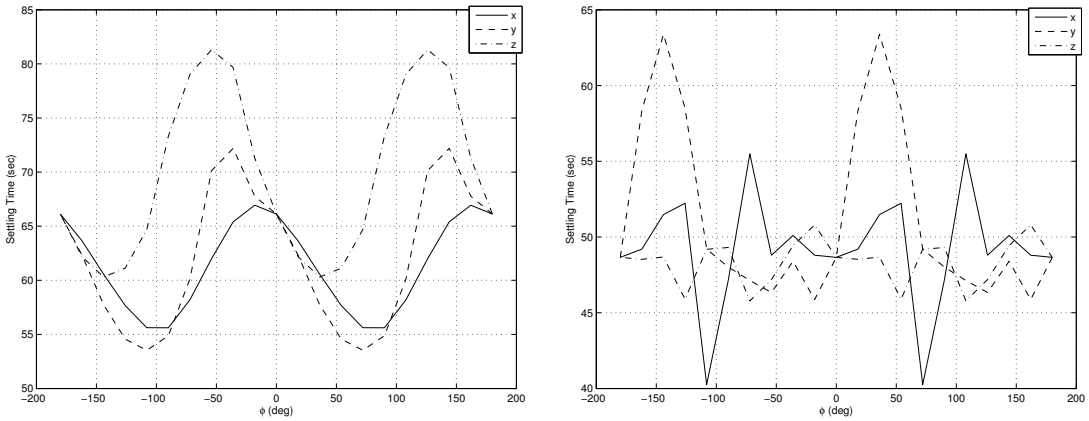

(a) (b)

Figure 4.9: Settling time as a function of principal-frame/body-frame rotation angle ϕ for rotations about each of the three principal axes of J_3. Convergence is achieved for (a) control law (4.31), and (b) control law (4.51).

output of an autonomous system of the form

$$\dot{d} = A_d d, \tag{4.43}$$

$$z_{\text{dist}} = C_d d, \tag{4.44}$$

where $A_d \in \mathbb{R}^{n_d \times n_d}$ and $C_d \in \mathbb{R}^{3 \times n_d}$ are known matrices and A_d is a Lyapunov-stable matrix. In this model, $d(0)$ is unknown, which is equivalent to the assumption that the amplitude and phase of all harmonic components in the disturbance are unknown. The matrix A_d is chosen to include eigenvalues of all frequency components that may be present in the disturbance signal, where the zero eigenvalue corresponds to constant disturbances. In effect, the controller provides infinite gain at the disturbance frequency, which results in asymptotic rejection of harmonic disturbance components. In particular, an integral controller provides infinite gain at DC in order to reject constant disturbances. In the case of orbit-dependent disturbances, the frequencies can be estimated from the orbital parameters. Likewise, in the case of disturbances originating from on-board devices, the spectral content of the disturbances may be known. In other cases, it may be possible to estimate the spectrum of the disturbances through signal processing. Since z_{d} is harmonic, A_d can be chosen to be skew symmetric, which we do henceforth. Let $\hat{d} \in \mathbb{R}^{n_d}$ denote an estimate of d, and define the disturbance-state estimation error

$$\tilde{d} \triangleq d - \hat{d}.$$

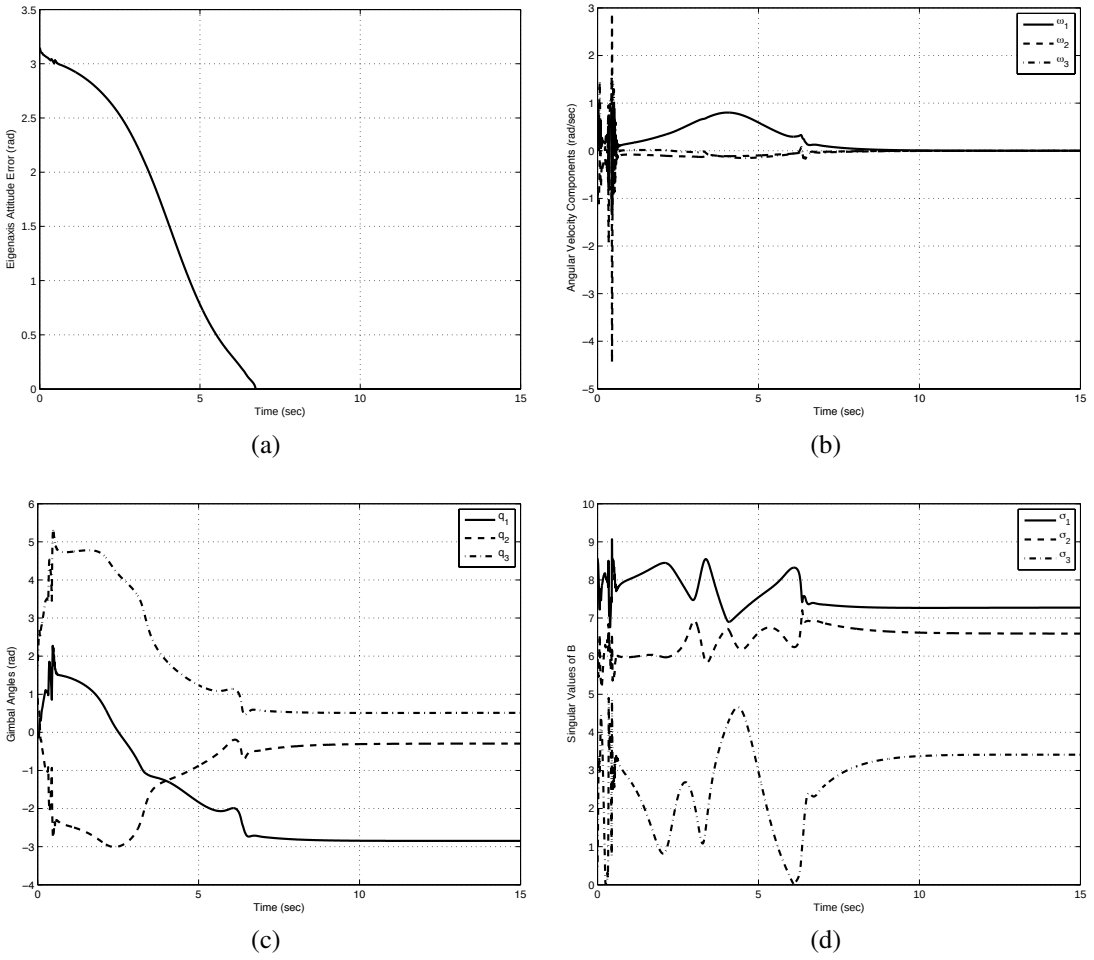

Figure 4.10: M2R maneuver for the FGAC control law (4.35) using CMGs and without disturbance. (a) Eigenaxis error, (b) spacecraft angular velocity components, (c) gimbal angles, and (d) singular values of B. the objective is to bring the spacecraft from the initial attitude $R(0) = I_3$ and initial angular velocity $\omega(0) = [1 \;\; -1 \;\; 0.5]^{\mathrm{T}}$ rad/sec to rest at the desired final orientation $R_{\mathrm{d}} = \mathrm{diag}(1, -1, -1)$, which represents a rotation of 180 degrees about the x-axis.

4.4.1 EBAC for Reaction Wheels

Rewrite (4.19) in terms of $\tilde{\omega}$ as

$$J_{\mathrm{sc}}\dot{\tilde{\omega}} = [J_{\mathrm{sc}}(\tilde{\omega} + \tilde{R}^{\mathrm{T}}\omega_{\mathrm{d}}) + J_\alpha v] \times (\tilde{\omega} + \tilde{R}^{\mathrm{T}}\omega_{\mathrm{d}}) + J_{\mathrm{sc}}(\tilde{\omega} \times \tilde{R}^{\mathrm{T}}\omega_{\mathrm{d}} - \tilde{R}^{\mathrm{T}}\dot{\omega}_{\mathrm{d}}) - J_\alpha u + \tau_{\mathrm{dist}}. \quad (4.45)$$

The assumptions upon which the following development is based are now stated.

Assumption 1. J_{sc} is constant but unknown.

Assumption 2. J_α defined by (B.18) is constant, nonsingular, and known. That is, the

spacecraft has three linearly independent, axisymmetric wheels, with known moments of inertia about their spin axes and known configuration relative to the bus.

Assumption 3. Each component of τ_{dist} is a linear combination of constant and harmonic signals, whose frequencies are known but whose amplitudes and phases are unknown.

The attitude tracking controller in the presence of disturbances given in ref. [32] is modified below for reaction-wheel actuators.

Theorem 3. *Let K_{p} be a positive number, let $K_1 \in \mathbb{R}^{3\times 3}$, let $Q \in \mathbb{R}^{6\times 6}$ and $D \in \mathbb{R}^{n_d \times n_d}$ be positive-definite matrices, let $A = \text{diag}(a_1, a_2, a_3)$ be a diagonal positive-definite matrix, and define S as in (4.27). Then the function*

$$V(\tilde{\omega}, \tilde{R}, \tilde{\gamma}, \tilde{d}) \triangleq \tfrac{1}{2}(\tilde{\omega} + K_1 S)^{\text{T}} J_{\text{sc}}(\tilde{\omega} + K_1 S) + K_{\text{p}} \text{tr}\,(A - A\tilde{R}) + \tfrac{1}{2}\tilde{\gamma}^{\text{T}} Q \tilde{\gamma} + \tfrac{1}{2}\tilde{d}^{\text{T}} D \tilde{d} \tag{4.46}$$

is positive definite, that is, V is nonnegative, and $V = 0$ if and only if $\tilde{\omega} = 0$, $\tilde{R} = I$, $\tilde{\gamma} = 0$, and $\tilde{d} = 0$.

Proof. It follows from statement 2 of Lemma 1 that $\text{tr}\,(A - A\tilde{R})$ is nonnegative. Hence V is nonnegative. Now suppose that $V = 0$. Then, $\tilde{\omega} + K_1 S = 0$, $\tilde{\gamma} = 0$, and $\tilde{d} = 0$, and it follows from *iii*) of Lemma 1 that $\tilde{R} = I$, and thus $S = 0$. Therefore, $\tilde{\omega} = 0$. □

The following result concerns attitude tracking without knowledge of the spacecraft inertia. This control law does not regulate the speed of the wheels. Consequently, the function V defined by (4.46), which is used as a Lyapunov function in the proof of Theorem 4 below, is not a positive-definite function of the angular rates of the wheels relative to the bus.

Theorem 4. *Let K_{p} be a positive number, let $K_{\text{v}} \in \mathbb{R}^{3\times 3}$, $K_1 \in \mathbb{R}^{3\times 3}$, $Q \in \mathbb{R}^{6\times 6}$, and $D \in \mathbb{R}^{n_d \times n_d}$ be positive-definite matrices, assume that $A_d^{\text{T}} D + D A_d$ is negative semidefinite, let $A = \text{diag}(a_1, a_2, a_3)$ be a diagonal positive-definite matrix with distinct diagonal entries, define S and V as in Theorem 3, and let $\hat{\gamma}$ and $\hat{d}$ satisfy*

$$\dot{\hat{\gamma}} = Q^{-1}[L^{\text{T}}(\omega)\omega^{\times} + L^{\text{T}}(K_1 \dot{S} + \tilde{\omega} \times \omega - \tilde{R}^{\text{T}} \dot{\omega}_{\text{d}})](\tilde{\omega} + K_1 S), \tag{4.47}$$

where

$$\dot{S} = \sum_{i=1}^{3} a_i [(\tilde{R}^{\text{T}} e_i) \times \tilde{\omega}] \times e_i \tag{4.48}$$

and

$$\dot{\hat{d}} = A_d\hat{d} + D^{-1}C_d^{\mathrm{T}}(\tilde{\omega} + K_1 S), \tag{4.49}$$

$$\hat{\tau}_{\mathrm{dist}} = C_d\hat{d}, \tag{4.50}$$

so that $\hat{\tau}_{\mathrm{dist}}$ *is the disturbance-torque estimate. Consider the control law*

$$u = -J_\alpha^{-1}(v_1 + v_2 + v_3), \tag{4.51}$$

where

$$v_1 \triangleq -(\hat{J}_{\mathrm{sc}}\omega + J_\alpha\nu)\times\omega - \hat{J}_{\mathrm{sc}}(K_1\dot{S} + \tilde{\omega}\times\omega - \tilde{R}^{\mathrm{T}}\dot{\omega}_{\mathrm{d}}), \tag{4.52}$$

$$v_2 \triangleq -\hat{\tau}_{\mathrm{dist}}, \tag{4.53}$$

and

$$v_3 \triangleq -K_{\mathrm{v}}(\tilde{\omega} + K_1 S) - K_{\mathrm{p}}S. \tag{4.54}$$

Then,

$$\dot{V}(\tilde{\omega}, \tilde{R}, \tilde{\gamma}, \tilde{d}) = -(\tilde{\omega} + K_1 S)^{\mathrm{T}}K_{\mathrm{v}}(\tilde{\omega} + K_1 S) - K_{\mathrm{p}}S^{\mathrm{T}}K_1 S + \tfrac{1}{2}\tilde{d}^{\mathrm{T}}(A_d^{\mathrm{T}}D + DA_d)\tilde{d} \tag{4.55}$$

is negative semidefinite. Furthermore, the closed-loop system consisting of Eqs. (4.20), (4.6), (4.45), and (4.51) is almost globally asymptotically stable, and for all initial conditions not in an embedded submanifold of $\mathbb{R}^3 \times \mathrm{SO}(3) \times \mathbb{R}^6 \times \mathbb{R}^3$ *(see ref. [32]),* $\tilde{\omega} \to 0$ *and* $\tilde{R} \to I$ *as* $t \to \infty$.

Proof.

$$
\begin{aligned}
\dot{V}(\tilde{\omega},\tilde{R},\tilde{\gamma},\tilde{d}) &= (\tilde{\omega}+K_1S)^{\mathrm{T}}(J_{\mathrm{sc}}\dot{\tilde{\omega}}+J_{\mathrm{sc}}K_1\dot{S})-K_{\mathrm{p}}\mathrm{tr}A\dot{\tilde{R}}-\tilde{\gamma}^{\mathrm{T}}Q\dot{\tilde{\gamma}}+\tilde{d}^{\mathrm{T}}D\dot{\tilde{d}}\\
&= (\tilde{\omega}+K_1S)^{\mathrm{T}}[(J_{\mathrm{sc}}\omega+J_\alpha\nu)\times\omega+J_{\mathrm{sc}}(\tilde{\omega}\times\omega-\tilde{R}^{\mathrm{T}}\dot{\omega}_{\mathrm{d}})-J_\alpha u+\tau_{\mathrm{dist}}+J_{\mathrm{sc}}K_1\dot{S}]\\
&\quad+K_{\mathrm{p}}\tilde{\omega}^{\mathrm{T}}S-\tilde{\gamma}^{\mathrm{T}}Q\dot{\tilde{\gamma}}+\tilde{d}^{\mathrm{T}}D\dot{\tilde{d}}\\
&= (\tilde{\omega}+K_1S)^{\mathrm{T}}[(J_{\mathrm{sc}}\omega+J_\alpha\nu)\times\omega+J_{\mathrm{sc}}(K_1\dot{S}+\tilde{\omega}\times\omega-\tilde{R}^{\mathrm{T}}\dot{\omega}_{\mathrm{d}})\\
&\quad+\nu_1+\nu_2+\nu_3+\tau_{\mathrm{dist}}]+K_{\mathrm{p}}\tilde{\omega}^{\mathrm{T}}S-\tilde{\gamma}^{\mathrm{T}}Q\dot{\tilde{\gamma}}+\tilde{d}^{\mathrm{T}}D\dot{\tilde{d}}\\
&= (\tilde{\omega}+K_1S)^{\mathrm{T}}[(\tilde{J}_{\mathrm{sc}}\omega)\times\omega+\tilde{J}_{\mathrm{sc}}(K_1\dot{S}+\tilde{\omega}\times\omega-\tilde{R}^{\mathrm{T}}\dot{\omega}_{\mathrm{d}})]\\
&\quad+(\tilde{\omega}+K_1S)^{\mathrm{T}}\tilde{\tau}_{\mathrm{dist}}-(\tilde{\omega}+K_1S)^{\mathrm{T}}K_{\mathrm{v}}(\tilde{\omega}+K_1S)-K_{\mathrm{p}}(\tilde{\omega}+K_1S)^{\mathrm{T}}S\\
&\quad+K_{\mathrm{p}}\tilde{\omega}^{\mathrm{T}}S-\tilde{\gamma}^{\mathrm{T}}Q\dot{\tilde{\gamma}}+\tilde{d}^{\mathrm{T}}D\dot{\tilde{d}}\\
&= (\tilde{\omega}+K_1S)^{\mathrm{T}}[L(\omega)\tilde{\gamma}\times\omega+L(K_1\dot{S}+\tilde{\omega}\times\omega-\tilde{R}^{\mathrm{T}}\dot{\omega}_{\mathrm{d}})\tilde{\gamma}]\\
&\quad-(\tilde{\omega}+K_1S)^{\mathrm{T}}K_{\mathrm{v}}(\tilde{\omega}+K_1S)-K_{\mathrm{p}}S^{\mathrm{T}}K_1S-\tilde{\gamma}^{\mathrm{T}}Q\dot{\tilde{\gamma}}\\
&\quad+\tilde{d}^{\mathrm{T}}C_d^{\mathrm{T}}(\tilde{\omega}+K_1S)+\tilde{d}^{\mathrm{T}}D[A_d\tilde{d}-D^{-1}C_d^{\mathrm{T}}(\tilde{\omega}+K_1S)]\\
&= -(\tilde{\omega}+K_1S)^{\mathrm{T}}K_{\mathrm{v}}(\tilde{\omega}+K_1S)-K_{\mathrm{p}}S^{\mathrm{T}}K_1S-\tilde{\gamma}^{\mathrm{T}}Q\dot{\tilde{\gamma}}\\
&\quad+(\tilde{\omega}+K_1S)^{\mathrm{T}}[-\omega^{\times}L(\omega)+L(K_1\dot{S}+\tilde{\omega}\times\omega-\tilde{R}^{\mathrm{T}}\dot{\omega}_{\mathrm{d}})]\tilde{\gamma}\\
&\quad+\tfrac{1}{2}\tilde{d}^{\mathrm{T}}(A_d^{\mathrm{T}}D+DA_d)\tilde{d}\\
&= -(\tilde{\omega}+K_1S)^{\mathrm{T}}K_{\mathrm{v}}(\tilde{\omega}+K_1S)-K_{\mathrm{p}}S^{\mathrm{T}}K_1S\\
&\quad+\tilde{\gamma}^{\mathrm{T}}[-Q\dot{\tilde{\gamma}}+(L^{\mathrm{T}}(\omega)\omega^{\times}+L^{\mathrm{T}}(K_1\dot{S}+\tilde{\omega}\times\omega-\tilde{R}^{\mathrm{T}}\dot{\omega}_{\mathrm{d}}))(\tilde{\omega}+K_1S)]\\
&\quad+\tfrac{1}{2}\tilde{d}^{\mathrm{T}}(A_d^{\mathrm{T}}D+DA_d)\tilde{d}\\
&= -(\tilde{\omega}+K_1S)^{\mathrm{T}}K_{\mathrm{v}}(\tilde{\omega}+K_1S)-K_{\mathrm{p}}S^{\mathrm{T}}K_1S+\tfrac{1}{2}\tilde{d}^{\mathrm{T}}(A_d^{\mathrm{T}}D+DA_d)\tilde{d}.
\end{aligned}
$$

The closed-loop spacecraft attitude dynamics (4.45) and the control law (4.51)-(4.54) can be expressed as

$$
J\dot{\tilde{\omega}} = [L(\omega)\tilde{\gamma}]^{\times}\omega+L(\tilde{\omega}\times\tilde{R}^{\mathrm{T}}\omega_{\mathrm{d}}-R^{\mathrm{T}}\dot{\omega}_{\mathrm{d}})\tilde{\gamma}-L(K_1\dot{S})\hat{\gamma}+\tilde{z}_d-K_{\mathrm{v}}(\tilde{\omega}+K_1S)-K_{\mathrm{p}}S. \tag{4.56}
$$

From Lemma 3 and Lemma 4 of ref. [32], the closed-loop system consisting of (4.47)-(4.50) and (4.56) has four disjoint equilibrium manifolds. These equilibrium manifolds in $\mathbb{R}^3\times\mathrm{SO}(3)\times\mathbb{R}^6\times\mathbb{R}^3$ are given by

$$
\mathcal{E}_i = \left\{(\tilde{\omega},\tilde{R},\tilde{\gamma},\tilde{d})\in\mathbb{R}^3\times\mathrm{SO}(3)\times\mathbb{R}^6\times\mathbb{R}^3 : \tilde{R}=\mathcal{R}_i,\ \tilde{\omega}\equiv 0,\ (\tilde{\gamma},\tilde{d})\in\mathcal{Q}_i\right\}, \tag{4.57}
$$

where, for all $i \in \{0,1,2,3\}$, $\mathcal{Q}_i$ is the closed subset of $\mathbb{R}^6 \times \mathbb{R}^3$ defined by

$$\mathcal{Q}_i \triangleq \{(\tilde{\gamma}, \tilde{d}) \in \mathbb{R}^6 \times \mathbb{R}^3 : [L(\mathcal{R}_i^{\mathrm{T}}\omega_{\mathrm{d}})\tilde{\gamma}]^{\times}(\mathcal{R}_i^{\mathrm{T}}\omega_{\mathrm{d}}) - L(\mathcal{R}_i^{\mathrm{T}}\dot{\omega}_{\mathrm{d}})\tilde{\gamma} + C_d\tilde{d} = 0,\ \dot{\tilde{\gamma}} = 0,\ \dot{\tilde{d}} = A_d\tilde{d}\}.$$

Furthermore, the equilibrium manifold $(\tilde{\omega}, \tilde{R}, (\tilde{\gamma}, \tilde{d})) = (0, I, \mathcal{Q}_0)$ of the closed-loop system given by (4.47)-(4.50) and (4.56) is locally asymptotically stable, and the remaining equilibrium manifolds given by $(0, \mathcal{R}_i, \mathcal{Q}_i)$ for $i \in \{1,2,3\}$ are unstable. Finally, the set of all initial conditions converging to these equilibrium manifolds forms a lower dimensional submanifold of $\mathbb{R}^3 \times \mathrm{SO}(3) \times \mathbb{R}^6 \times \mathbb{R}^3$. □

4.4.2 EBAC for CMG's

As in the reaction-wheel case, we invoke the assumptions presented in Section 4.2.3. The EBAC controller for CMG's is given by [82]

$$u = B^{\#}(v_1 + v_2 + v_3), \tag{4.58}$$

where $B^{\#}$ is the SR-inverse of B,

$$v_1 \triangleq -(\hat{J}_{\mathrm{sc}}\omega + \sum_{i=1}^{3}\beta_i\omega_{\mathrm{W}_i}) \times \omega - \hat{J}_{\mathrm{sc}}(K_1\dot{S} + \tilde{\omega} \times \omega - \tilde{R}^{\mathrm{T}}\dot{\omega}_{\mathrm{d}}), \tag{4.59}$$

and v_2, v_3 remain unchanged and are given by (4.53)-(4.54).

4.5 EBAC Examples

4.5.1 EBAC Examples Using Reaction Wheels

Consider the maneuver presented in Section 4.3.2 in the presence of an unknown constant nonzero disturbance torque $\tau_{\mathrm{dist}} = [0.7 \ \ -0.3 \ \ 0]^{\mathrm{T}}$ N-m. The EBAC controller (4.51) is used in place of the FGAC controller (4.31) since (4.31) lacks an integrator and thus has a constant steady-state error bias due to the persistent disturbance. The parameters of the controller (4.51) are chosen to be $K_1 = I_3$, $A = \mathrm{diag}(1,2,3)$, $\gamma = \eta = 1$, $D = I_3$, and $Q = I_6$.

Figures 4.11(a)-(f) show, respectively, the attitude error, angular velocity components, angular rates of the wheels, angular momentum, disturbance-estimate errors, and inertia-estimate errors. The spacecraft attitude and angular velocity components reach the commanded values in about 80 sec. Figure 4.11c indicates that the reaction-wheel rotational speed grows unbounded. Figure 4.11d shows that the total angular momentum of the space-

craft increases, which is consistent with the constant disturbance torque acting on the spacecraft. In practice, the spacecraft needs a method to dump the stored angular momentum so that the reaction wheel rates do not grow unbounded.

Figure 4.12 repeats the maneuver with maximum wheel saturation at 100 rad/sec, corresponding to roughly 1000 rpm. The controller brings the spacecraft to the desired orientation in about 60 sec at which time one of the angular rates of the reaction wheels reaches 100 rad/sec, disturbance and inertia estimates diverge, and the system is destabilized.

Consider a spin maneuver with the spacecraft initially at rest and $R(0) = I_3$. The desired attitude is determined by $R_d(0) = I_3$, and the commanded constant angular velocity is

$$\omega_d = \begin{bmatrix} 0.5 & -0.5 & -0.3 \end{bmatrix}^T \text{ rad/sec.}$$

Assume no disturbance. Figures 4.13(a)-(f) show, respectively, the attitude errors, angular-velocity components, angular rates of the wheels, the control inputs, which are the angular accelerations of the wheels, angular momentum, and inertia-estimate errors. For this maneuver, the spin command consists of a specified time history of rotation about a specified body axis aligned in a specified inertial direction. The controller achieves the commanded spin within about 100 sec.

4.5.2 EBAC Examples Using CMG's

Consider the maneuver presented in Section 4.3.3 in the presence of an unknown constant nonzero disturbance torque $\tau_{dist} = [0.35 \ -0.015 \ 0]^T$ N-m. Note that the EBAC controller (4.58) is used in place of the FGAC controller (4.35) since (4.35) lacks an integrator and thus has a constant steady-state error bias due to the persistent disturbance. The parameters of the controller (4.58) are chosen to be $K_1 = I_3$, $A = \text{diag}(1, 2, 3)$, $D = I_3$, and $Q = I_6$.

Figures 4.14(a)-(e) show, respectively, the attitude error, angular-velocity components, gimbal angles, inertia-estimate errors, and singular values of B. The spacecraft attitude and angular velocity components reach the commanded values in about 35 sec. Figure 4.14c indicates that the CMG gimbal angles grow unbounded.

Consider a spin maneuver with the spacecraft initially at rest and $R(0) = I_3$. The desired attitude is determined by $R_d(0) = I_3$, and the commanded angular velocity is $\omega_d = [0.005 \ -0.005 \ -0.003]^T$ rad/sec. We assume that no disturbance is present. Figures 4.15(a)-(e) show, respectively, the attitude error, angular-velocity components, gimbal angles, inertia-estimate errors, and singular values of B. For this maneuver, the spin command consists of a specified time history of rotation about a specified body axis aligned in a specified inertial direction. The controller achieves the commanded motion within about 20 sec.

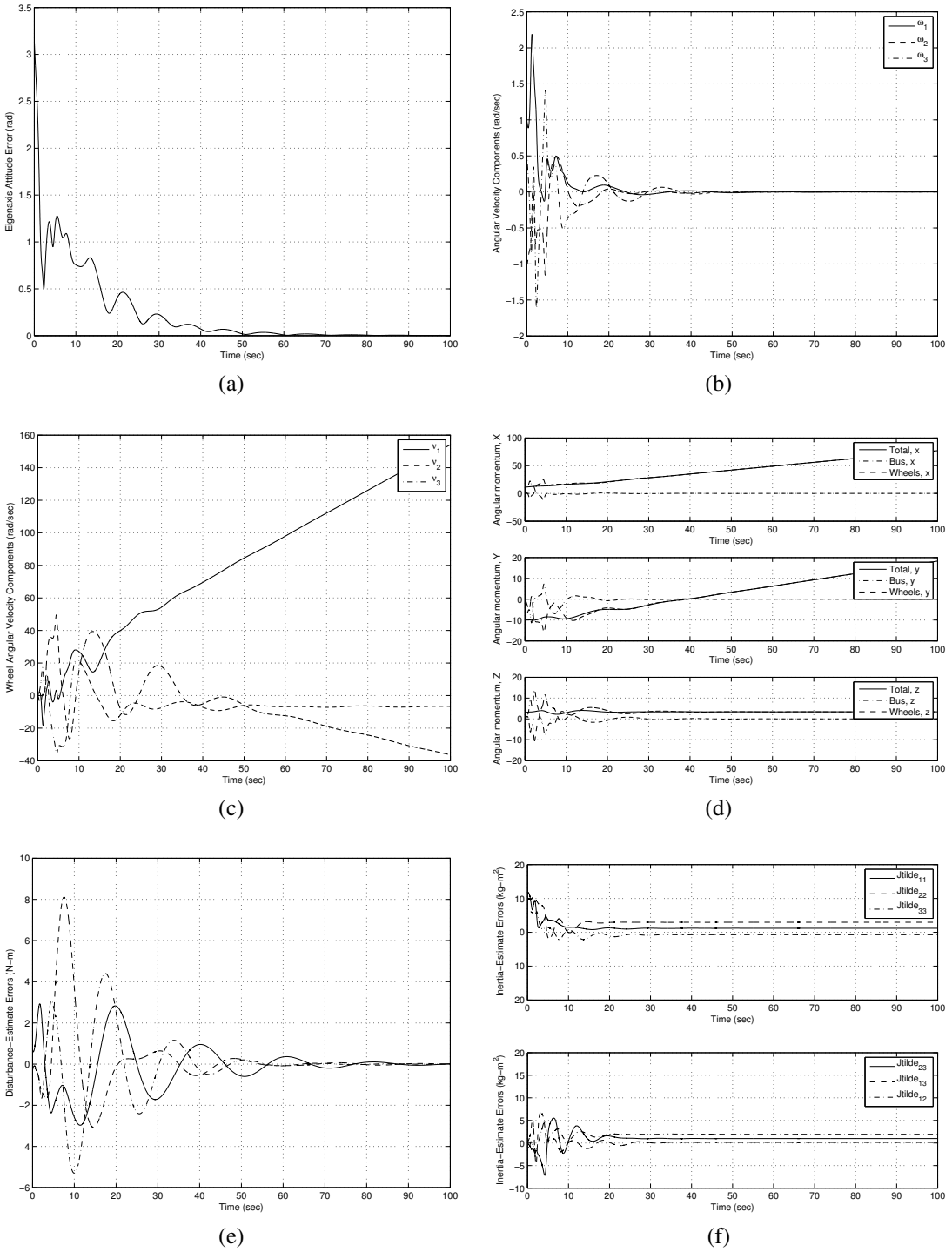

Figure 4.11: M2R maneuver for the EBAC control law (4.51) using reaction wheels with the unknown constant disturbance torque with respect to the bus-fixed frame $\tau_{\text{dist}} = [0.7 \; -0.3 \; 0]^{\text{T}}$ N-m. (a) Eigenaxis attitude error, (b) spacecraft angular velocity components, (c) wheel angular velocity components, (d) spacecraft angular momentum relative to its center of mass with respect to the inertial frame resolved in the inertial frame, (e) disturbance estimate errors, and (f) inertia estimate errors. The spin rate of the reaction wheels grows unbounded, and the total angular momentum of the spacecraft is not conserved due to the constant disturbance torque.

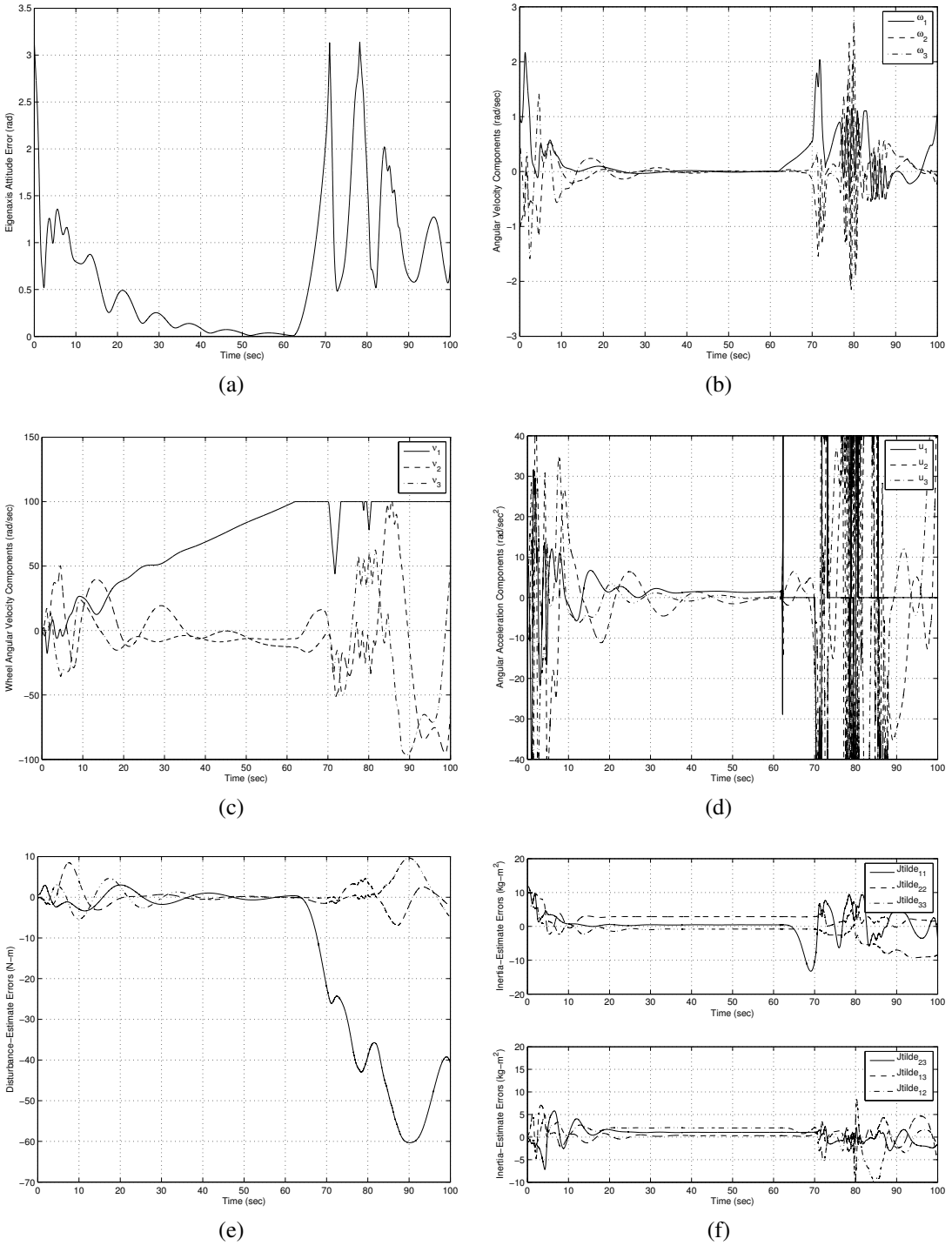

Figure 4.12: M2R maneuver for the EBAC control law (4.51) using reaction wheels with the unknown constant disturbance torque with respect to the bus-fixed frame $\tau_{\text{dist}} = [0.7 \; -0.3 \; 0]^{\text{T}}$ N-m. The maximum rotation rate of each wheel is saturated at 100 rad/sec. (a) Eigenaxis attitude error, (b) spacecraft angular velocity components, (c) wheel angular velocity components, (d) wheel angular acceleration components, (e) disturbance estimate errors, and (f) inertia estimate errors. The spacecraft achieves the desired orientation in about 60 sec. Due to the constant disturbance, the angular rates of the reaction wheels saturate and and the system is destabilized.

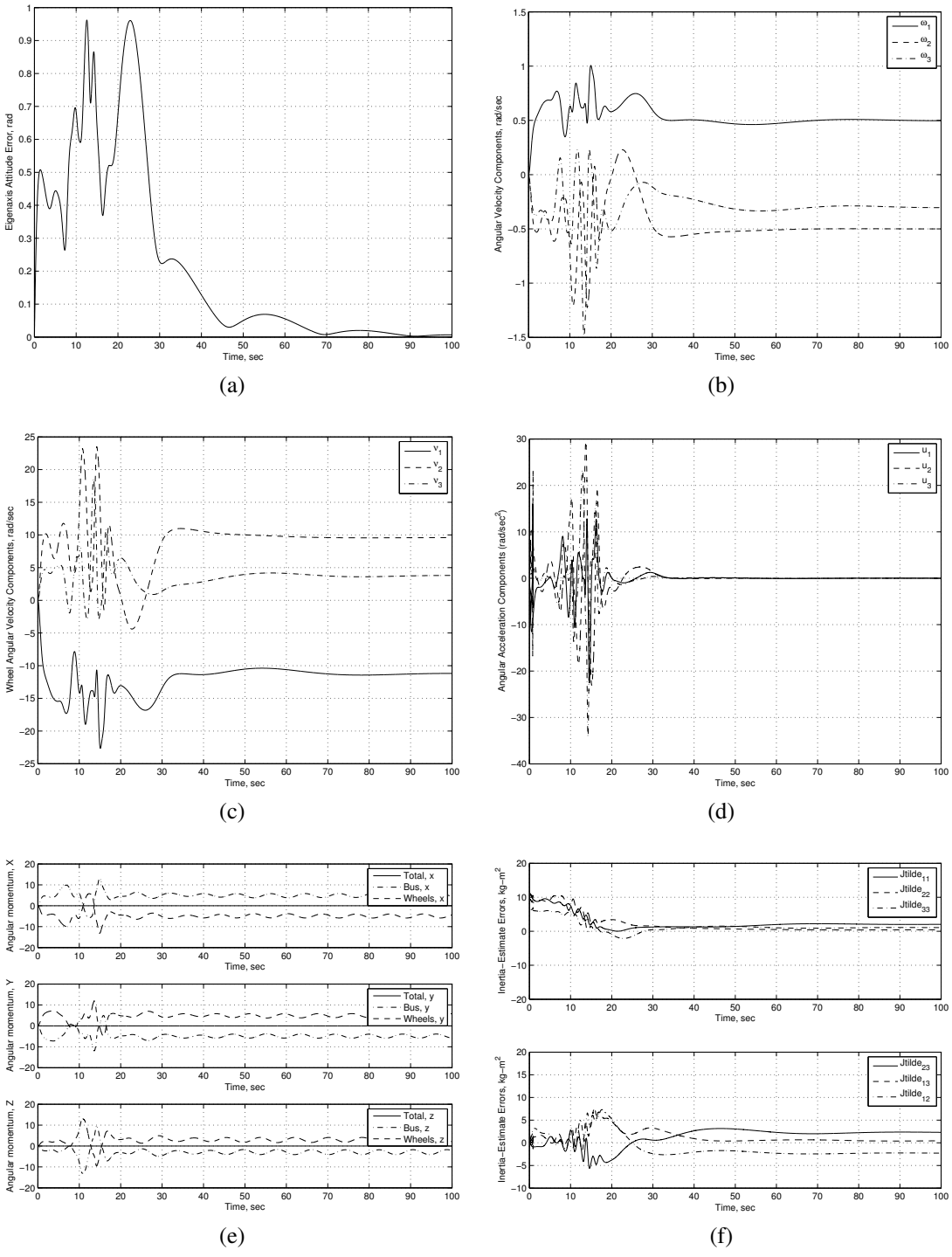

Figure 4.13: M2S maneuver for the EBAC control law (4.51) using reaction wheels. The desired attitude is $R_{\rm d}(0) = I_3$, and the commanded angular velocity is $\omega_{\rm d} = [0.5 \ -0.5 \ -0.3]^{\rm T}$ rad/sec. (a) Eigenaxis attitude error, (b) spacecraft angular velocity components, (c) wheel angular velocity components, (d) wheel angular acceleration components, (e) spacecraft angular momentum relative to its center of mass with respect to the inertial frame resolved in the inertial frame, and (f) inertia estimate errors. No disturbance is present.

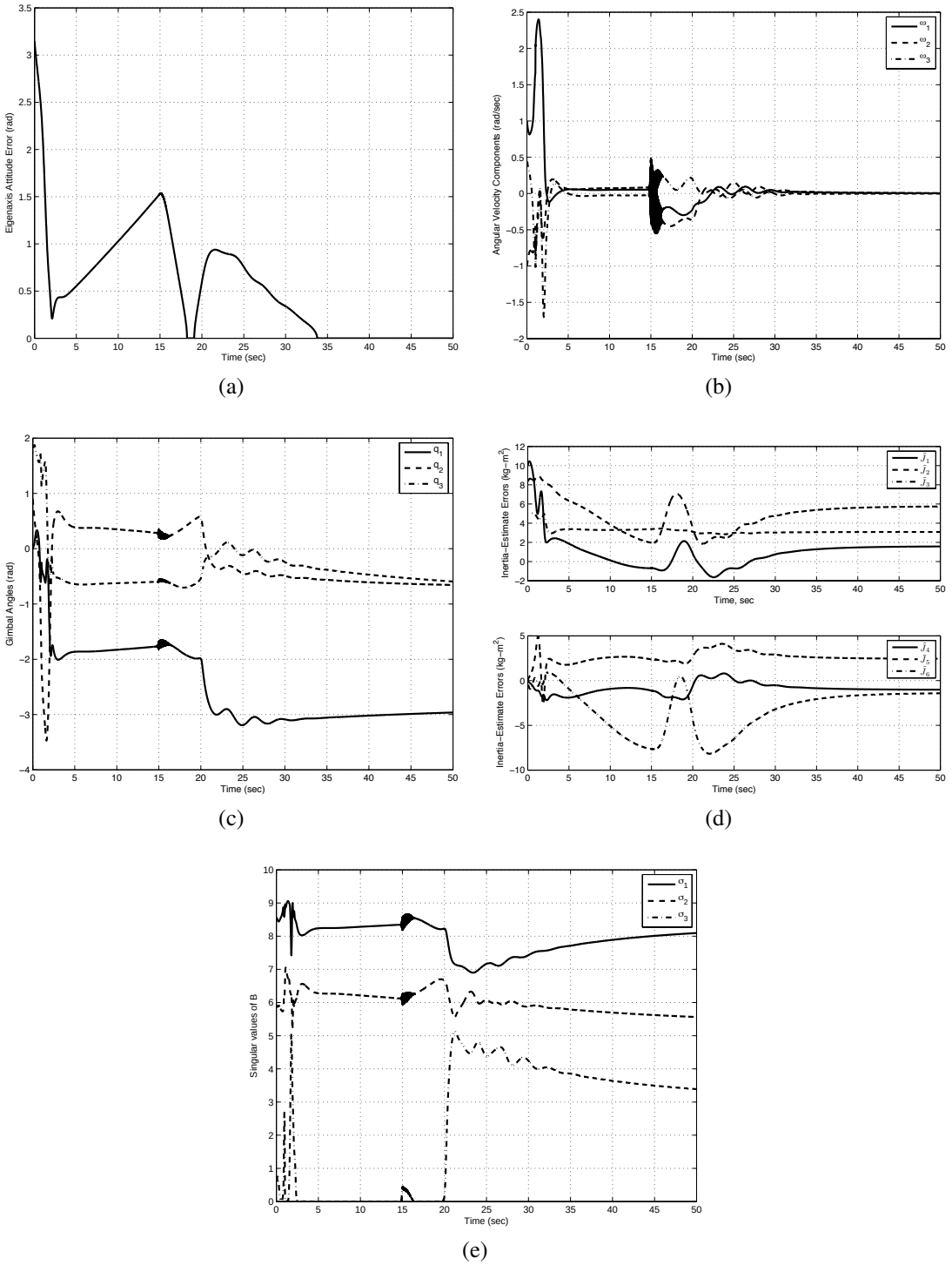

Figure 4.14: M2R maneuver for the EBAC control law (4.58) using CMG's with the unknown constant disturbance torque $\tau_{\text{dist}} = [0.35 \;\; -0.015 \;\; 0]^{\text{T}}$ N-m. (a) Eigenaxis attitude error, (b) spacecraft angular velocity components, (c) gimbal angles, (d) inertia estimate errors, and (e) singular values of B.

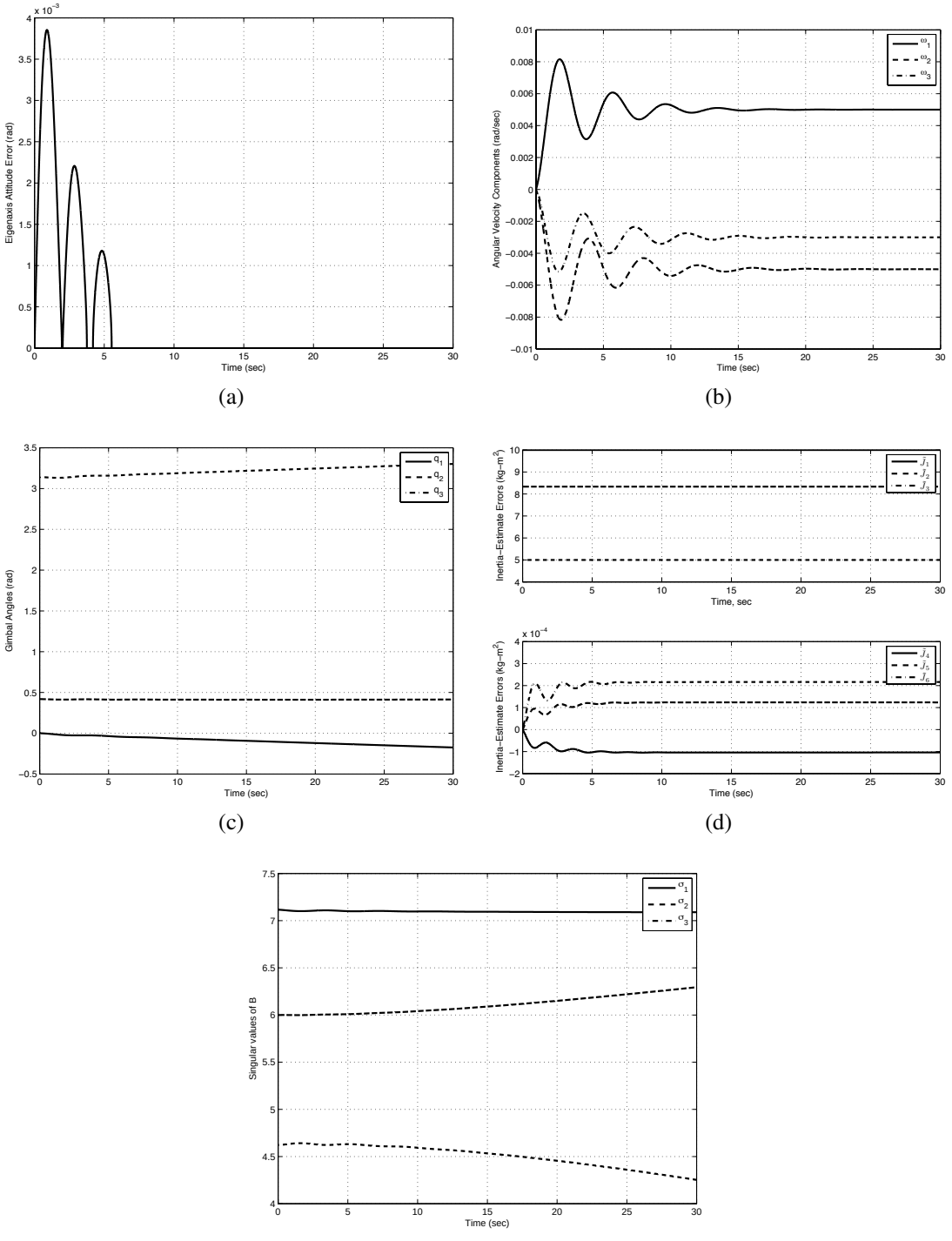

Figure 4.15: M2S maneuver for the EBAC control law (4.58) using CMG's. The desired attitude is determined by $R_{\rm d}(0) = I_3$, and the commanded angular velocity is $\omega_{\rm d} = [0.005 \;\; -0.005 \;\; -0.003]^{\rm T}$ rad/sec. (a) Eigenaxis attitude error, (b) spacecraft angular velocity components, (c) gimbal angles, (d) inertia estimate errors, and (e) singular values of B. No disturbance is present.

CHAPTER 5

Forward-Propagating Riccati-Based Feedback Control

In applications involving time-varying systems, the state dynamics matrix is often not known in advance. To address this problem, this chapter investigates the effectiveness of a forward-in-time Riccati-based control law.

5.1 Forward-Propagating Riccati Theory

A fundamental property of dynamic programming is that the optimal policies and paths are determined by a *backwards-in-time* procedure. This procedure gives rise to the Bellman equation, which in turn is related to the Hamilton-Jacobi-Bellman partial differential equation [98]. Within the context of optimal control, the Bellman equation provides optimal control time histories over a specified control horizon. In the special case of the linear system

$$\dot{x}(t) = A(t)x(t) + B(t)u(t) \tag{5.1}$$

with the quadratic cost

$$J(u) = \int_0^{t_\mathrm{f}} x^\mathrm{T}(t)R_1 x(t) + u^\mathrm{T}(t)R_2 u(t)\,\mathrm{d}t, \tag{5.2}$$

the backwards nature of the optimal control law

$$u(t) = -R_2^{-1}B^\mathrm{T}(t)P_\mathrm{b}(t)x(t) \tag{5.3}$$

is evident from the fact that the solution $P_{\mathrm{b}}(t)$ of the control Riccati equation

$$-\dot{P}_{\mathrm{b}}(t) = A^{\mathrm{T}}(t)P_{\mathrm{b}}(t) + P_{\mathrm{b}}(t)A(t) - P_{\mathrm{b}}(t)B(t)R_2^{-1}B^{\mathrm{T}}(t)P_{\mathrm{b}}(t) + R_1 \tag{5.4}$$

is obtained by integrating backwards from the boundary condition $P_{\mathrm{b}}(t_{\mathrm{f}}) \geq 0$ specified at the final time t_{f}. This procedure yields the closed-loop dynamics

$$\dot{x}(t) = A_{\mathrm{c,b}}(t)x(t), \tag{5.5}$$

where $A_{\mathrm{c,b}}(t) \triangleq A(t) - B(t)R_2^{-1}B^{\mathrm{T}}(t)P_{\mathrm{b}}(t)$.

In practice, a backwards-in-time solution procedure has the significant drawback that the dynamics of the system, that is, the matrices $A(t)$ and $B(t)$, must be known in advance. However, in many applications, the system trajectory, and thus the linearized dynamics, are not known in advance. Consequently, there is interest in forward-in-time solution procedures, in particular, for applications of model predictive and receding horizon control [99–101].

The dual of the control problem is the state estimation problem involving the observed dynamics

$$\dot{x}(t) = A(t)x(t) + w_1(t), \tag{5.6}$$

$$y(t) = C(t)x(t) + w_2(t). \tag{5.7}$$

For this problem, the estimator Riccati equation

$$\dot{Q}(t) = A(t)Q(t) + Q(t)A^{\mathrm{T}}(t) - Q(t)C^{\mathrm{T}}(t)V_2^{-1}C(t)Q(t) + V_1 \tag{5.8}$$

is solved *forward in time* with the initial-time boundary condition $Q(t_0) \geq 0$ and is guaranteed to minimize the state estimation cost. The matrices V_1 and V_2 represent the covariances of the process noise w_1 and sensor noise w_2, respectively. Under uniform complete reconstructability conditions, the resulting closed-loop error system

$$\dot{e}(t) = A_{\mathrm{e}}(t)e(t), \tag{5.9}$$

where $A_{\mathrm{e}}(t) \triangleq A(t) - Q(t)C^{\mathrm{T}}(t)V_2^{-1}C(t)$, is exponentially stable [98]. Note that, unlike the case of the control Riccati equation (5.4), implementation of the optimal state estimator in terms of the estimator Riccati equation (5.8) does *not* require advance knowledge of the dynamics matrices $A(t)$ and $C(t)$.

It is, therefore, natural to ask whether a dual version of the forward-in-time estimator Riccati equation (5.8) can provide a suboptimal, forward-in-time control law. In particular, we consider the control law

$$u(t) = -R_2^{-1} B^{\mathrm{T}}(t) P_{\mathrm{f}}(t) x(t), \tag{5.10}$$

where $P_{\mathrm{f}}(t)$ is the solution to the *forward-in-time* control Riccati equation

$$\dot{P}_{\mathrm{f}}(t) = A^{\mathrm{T}}(t) P_{\mathrm{f}}(t) + P_{\mathrm{f}}(t) A(t) - P_{\mathrm{f}}(t) B(t) R_2^{-1} B^{\mathrm{T}}(t) P_{\mathrm{f}}(t) + R_1, \tag{5.11}$$

with the *initial-time* boundary condition $P_{\mathrm{f}}(t_0) \geq 0$. Using this control law, the closed-loop dynamics are given by

$$\dot{x}(t) = A_{\mathrm{c,f}}(t) x(t), \tag{5.12}$$

where $A_{\mathrm{c,f}}(t) \triangleq A(t) - B(t) R_2^{-1} B^{\mathrm{T}}(t) P_{\mathrm{f}}(t)$. Note that (5.11) differs from the standard backwards-in-time Riccati equation (5.4) by the absence of the minus sign on the left-hand side; this feature along with the specification of an initial-time boundary condition in place of a final-time boundary condition, render it closer in spirit to the estimator Riccati equation (5.8) than the backwards-in-time Riccati equation (5.4). In fact, (5.11) is equivalent to the estimator Riccati equation with $A(t)$, $C(t)$, V_1, and V_2 replaced by the dual variables $A^{\mathrm{T}}(t)$, $B^{\mathrm{T}}(t)$, R_1, and R_2. Furthermore, $A_{\mathrm{c,f}}(t) = A_{\mathrm{e}}^{\mathrm{T}}(t)$ with the appropriate substitutions.

Thus, assuming that (5.9) is asymptotically stable, it remains to be determined whether the transposed system

$$\dot{e}(t) = A_{\mathrm{e}}^{\mathrm{T}}(t) e(t) \tag{5.13}$$

is also asymptotically stable. We call (5.13) the *quasi-dual* of (5.9) to distinguish it from the "true" dual (5.5) of (5.9). Variations of the backwards-in-time Riccati equation are discussed in [102], although that paper does not consider the use of quasi-dual dynamics.

The above discussion reflects the development in [103, 104] of forward-Riccati-based full-state-feedback control laws for time-varying systems. The approach taken in [103, 104] involves the definition of a state $z(t)$ whose magnitude is inversely proportional to the magnitude of $x(t)$ and whose dynamics are obtained by a time-dependent similarity transformation of the dynamics of $x(t)$. Consequently, the forward-Riccati-based controller for the system with state $z(t)$ anti-stabilizes the dynamics of $z(t)$; consequently, the original dynamics involving $x(t)$ are stabilized. This approach has the advantage over the backwards

Riccati solution mentioned above, namely, the time-varying matrices $A(t)$ and $B(t)$ need not be known in advance.

Since the dynamics for $z(t)$ depend on a state-dependent transformation of the dynamics of the state $x(t)$, the controller derived in [103, 104] is confined to full-state feedback. The development of our feedback law (5.10), (5.11) maintains a linear form without resorting to nonlinear transformations. Therefore, one of the main contributions of this work is to develop a forward-Riccati-based control law that does not require knowledge of the full state and thus is applicable to output feedback. In particular, by removing the requirement that the full state be known, we construct an observer-based compensator that uses the (forward) Riccati equation of the full-state estimator (5.8), and use a separation principle type result to guarantee closed-loop stability. In this way, we construct an output-feedback control law for time-varying systems whose dynamics matrices are not known in advance. This output feedback controller is described in Section 5.1.4.

Our goal is thus to investigate the applicability of the forward-in-time Riccati equation (5.11) to time-varying systems in which $A(t)$ and $B(t)$ are not known in advance. Clearly, the forward-in-time controller is stabilizing if the quasi-dual system (5.13) is asymptotically stable. In the time-invariant case, a matrix A is Hurwitz if and only if its transpose A^{T} is Hurwitz. Perhaps somewhat surprisingly, the same cannot be concluded in the time-*varying* case. In other words, stability of a time-varying system does not guarantee stability of the system with the transposed dynamics. As an illustrative example, consider

$$A(t) = \begin{bmatrix} -1 & \sin(t) - 1 \\ \sin(t) + 1 & \cos(t) \end{bmatrix},$$

and its transpose

$$A^{\mathrm{T}}(t) = \begin{bmatrix} -1 & \sin(t) + 1 \\ \sin(t) - 1 & \cos(t) \end{bmatrix}.$$

Since $A(t)$ is periodic, stability depends on the characteristic multipliers, that is, the eigenvalues of the monodromy matrix $\Phi(T, 0)$, where Φ denotes the state transition matrix. Figure 5.1 shows that while $A(t)$ is stable as seen by its state trajectories and characteristic multipliers, its transpose is not.

The main contribution of the present chapter is a collection of results under which the forward Riccati-based controller (5.10), (5.11) is stabilizing. In particular, we demonstrate that symmetry of the closed-loop dynamics is a sufficient condition for closed-loop stability. This property is using demonstrated by the quasi-duality between the state estimator

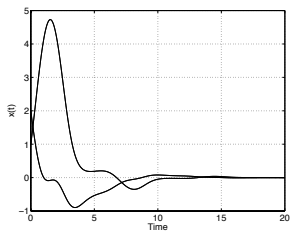

(a) State trajectories for $A(t)$

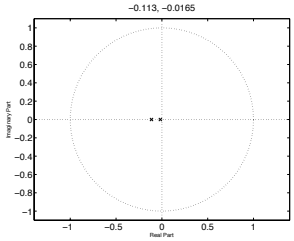

(b) Characteristic Multipliers

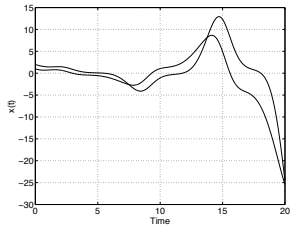

(c) State trajectory for $A^{\mathrm{T}}(t)$

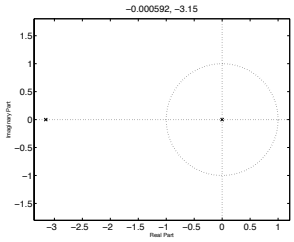

(d) Characteristic Multipliers

Figure 5.1: (a), (b): State trajectories and characteristic multipliers for $A(t)$. (c), (d): State trajectories and characteristic multipliers for $A^{\mathrm{T}}(t)$.

and the forward-Riccati-based controller, and is also brought out through Lyapunov analysis. In addition, we show that some plants are stabilizable only when the time-varying dynamics are of sufficiently high frequency. This property is demonstrated numerical examples and analysis using averaging theory. We also demonstrate using a separation principle type result for linear time-varying systems, that stability is retained in the output feedback case. Finally, experience with numerous numerical examples suggests that the forward Riccati output feedback approach is stabilizing in a much broader set of situations.

The chapter is organized as follows. Section 5.1.1 uses Lyapunov analysis to show stability with the forward-in-time controller when the closed-loop system has certain symmetric properties. In Section 5.1.2 we examine the properties of the state transition matrix and present additional conditions under which the forward-in-time controller is stabilizing. In Section 5.1.3 we demonstrate that the forward-in-time controller is stabilizing when the frequency of the time variation is sufficiently high. In Section 5.1.4 we show that we have separation of the regulator and estimator dynamics under output feedback. In Section 5.1.5 we provide illustrative numerical examples that highlight the effectiveness and desirability of the forward-in-time control law. Section 5.1.6 presents an alternate forward-in-time Riccati equation which results in a stabilizing controller for scarlar systems, and, in special cases, for non-scalar systems.

5.1.1 Lyapunov Analysis

We determine sufficient conditions for stability of the forward-in-time controller. We use Lyapunov analysis to examine the stability of the closed-loop system (5.12).

However, since (5.12) is the quasi-dual of (5.9), we first look at the closed-loop estimation system (5.9) to gain insight. Let $\bar{\Sigma}(t) = C^{\mathrm{T}}(t)V_2^{-1}C(t)$, $Q(t_0) > 0$, and rewrite (5.8) as

$$\dot{Q}(t) = A_{\mathrm{e}}(t)Q(t) + Q(t)A_{\mathrm{e}}^{\mathrm{T}}(t) + Q(t)\bar{\Sigma}(t)Q(t) + V_1.$$

Let $V(e,t) = e^{\mathrm{T}}Q^{-1}(t)e$ as in [105]. Then,

$$\begin{aligned}\dot{V} &= \dot{e}^T Q^{-1}(t)e + e^T Q^{-1}(t)\dot{e} + e^T \dot{Q}^{-1}(t)e \\ &= -e^{\mathrm{T}}\left(\bar{\Sigma}(t) + Q^{-1}(t)V_1 Q^{-1}(t)\right)e < 0. \end{aligned} \tag{5.14}$$

Similarly, we let $\Sigma(t) = B(t)R_2^{-1}B^{\mathrm{T}}(t)$, $P_{\mathrm{f}}(t_0) > 0$ and rewrite (5.11) as

$$\dot{P}_{\mathrm{f}}(t) = A_{\mathrm{c,f}}^{\mathrm{T}}(t)P_{\mathrm{f}}(t) + P_{\mathrm{f}}(t)A_{\mathrm{c,f}}(t) + P_{\mathrm{f}}(t)\Sigma(t)P_{\mathrm{f}}(t) + R_1.$$

Let $V(x,t) = x^{\mathrm{T}}P_{\mathrm{f}}^{-1}(t)x$. Then,

$$\begin{aligned}\dot{V} &= \dot{x}^T P_{\mathrm{f}}^{-1}(t)x + x^T P_{\mathrm{f}}^{-1}(t)\dot{x} + x^T \dot{P}_{\mathrm{f}}^{-1}(t)x \\ &= -x^{\mathrm{T}}\left(\Sigma(t) + P_{\mathrm{f}}^{-1}(t)R_1 P_{\mathrm{f}}^{-1}(t)\right)x + x^{\mathrm{T}}\Big(P_{\mathrm{f}}^{-1}(t)\left(A_{\mathrm{c,f}}(t) - A_{\mathrm{c,f}}^{\mathrm{T}}(t)\right) + \left(A_{\mathrm{c,f}}^{\mathrm{T}}(t) - A_{\mathrm{c,f}}(t)\right)P_{\mathrm{f}}^{-1}(t)\Big)x.\end{aligned}$$

Note the extra term in this expression versus (14). Thus, a sufficient condition for asymptotic stability of (5.12) is that $A_{\mathrm{c,f}}(t)$ is symmetric. As an example, this condition holds if $A(t)$ is symmetric, $B(t) = G(t)D(t)$, where $G(t)$ is an orthogonal matrix, $D(t) = f(t)I$ is a constant matrix, and $R_1 = R_2 = \rho I$.

5.1.2 State Transition Matrix Analysis

The state transition formula for the closed-loop system (5.12) is given by the Peano-Baker series

$$\Phi(t,t_0) = I + \int_{t_0}^{t} A_{\mathrm{c,f}}(\sigma_1)d\sigma_1 + \int_{t_0}^{t} A_{\mathrm{c,f}}(\sigma_1)\int_{t_0}^{\sigma_1} A_{\mathrm{c,f}}(\sigma_2)d\sigma_2 d\sigma_1 \ldots \tag{5.15}$$

It follows from (5.15) that, if $A_{\mathrm{c,f}}(t)$ is symmetric, then the state transition matrix for $A_{\mathrm{c,f}}(t)$ is equal to the state transition matrix for $A_{\mathrm{c,f}}^{\mathrm{T}}(t)$.

Suppose next that $A_{\mathrm{c,f}}(t)$ and its integral commute, that is,

$$A_{\mathrm{c,f}}(t)\int_{t_0}^{t} A_{\mathrm{c,f}}(\sigma)d\sigma = \int_{t_0}^{t} A_{\mathrm{c,f}}(\sigma)d\sigma A_{\mathrm{c,f}}(t) \quad \forall t, \tag{5.16}$$

or equivalently [106], if

$$A_{\mathrm{c,f}}(t_1)A_{\mathrm{c,f}}(t_2) = A_{\mathrm{c,f}}(t_2)A_{\mathrm{c,f}}(t_1) \quad \forall t_1, t_2. \tag{5.17}$$

Then, the Peano-Baker series simplifies to

$$\Phi(t, t_0) = \exp\left[\int_{t_0}^{t} A_{\mathrm{c,f}}(\sigma)d\sigma\right], \tag{5.18}$$

while

$$\Phi^{\mathrm{T}}(t, t_0) = \exp\left[\int_{t_0}^{t} A_{\mathrm{c,f}}^{\mathrm{T}}(\sigma)d\sigma\right] \tag{5.19}$$

is the state transition matrix for $A_{\mathrm{c,f}}^{\mathrm{T}}(t)$. In this case, stability of $A_{\mathrm{c,f}}(t)$ is equivalent to stability of $A_{\mathrm{c,f}}^{\mathrm{T}}(t)$.

It thus follows that if either $A_{\mathrm{c,f}}(t)$ is symmetric for all t, or if $A_{\mathrm{c,f}}(t_1)$ and $A_{\mathrm{c,f}}(t_2)$ commute for all t_1 and t_2, then, the stability of the closed-loop regulator sytem (5.12) is equivalent to the stability of the closed-loop estimator error system (5.9). Therefore, in either of these cases it follows that the forward-in-time controller (5.10) is guaranteed to stabilize (5.1).

5.1.3 Averaging Analysis

We now analyze the stability of the closed-loop system with the forward-in-time controller (5.10) at high frequencies. Specifically, we demonstrate that the forward-in-time controller is stabilizing under sufficiently fast time variation in the closed-loop dynamics.

Define the time-invariant matrices $\bar{A}$ and $\bar{B}$ by

$$\bar{A} \triangleq \frac{1}{T}\int_{0}^{\mathrm{T}} A(\omega t)dt, \tag{5.20}$$

$$\bar{B}\bar{B}^{\mathrm{T}} \triangleq \frac{1}{T}\int_{0}^{\mathrm{T}} B(\omega t)R_2^{-1}B^{\mathrm{T}}(\omega t)dt. \tag{5.21}$$

Theorem 1. *Replace $A(t)$ and $B(t)$ in (5.1) by time-periodic $A(\omega t)$ and $B(\omega t)$ with period $T = 2\pi/\omega$, where ω is a frequency parameter. Apply the forward-in-time control (5.10)*

with $P_{\mathrm{f}}(t)$ as given in (5.11). Suppose $(\bar{A},\bar{B})$ is stabilizable, $(\bar{A},R_1)$ is detectable, and let $P_{\mathrm{f}}(0) \geq 0$. Then, there exists a frequency ω^* such that, for all $\omega > \omega^*$, $P_{\mathrm{f}}(t)$ has an exponentially stable periodic solution of period T in an $O(\epsilon)$ neighborhood of P^*, where P^* is a positive-semidefinite solution of the algebraic Riccati equation,

$$0 = \bar{A}^{\mathrm{T}}P^* + P^*\bar{A} - P^*\bar{B}R_2^{-1}\bar{B}^{\mathrm{T}}P^* + R_1, \tag{5.22}$$

and $x(t) \to 0$ as $t \to \infty$.

Proof. Define the scaled time $\tau \triangleq \omega t$, and small parameter $\epsilon \triangleq \frac{1}{\omega}$. Rewrite (5.11) and (5.12) as

$$\frac{d}{d\tau}P_{\mathrm{f}}(\tau) = \epsilon\Big(A^{\mathrm{T}}(\tau)P_{\mathrm{f}}(\tau) + P_{\mathrm{f}}(\tau)A(\tau) - P_{\mathrm{f}}(\tau)B(\tau)R_2^{-1}B^{\mathrm{T}}(\tau)P_{\mathrm{f}}(\tau) + R_1\Big), \tag{5.23}$$

$$\frac{d}{d\tau}x(\tau) = \epsilon(A(\tau) - B(\tau)R_2^{-1}B^{\mathrm{T}}(\tau)P_{\mathrm{f}}(\tau))x(\tau). \tag{5.24}$$

Then, averaging equations (5.23) and (5.24), we obtain the time-invariant averaged system

$$\dot{\bar{P}}(t) = \bar{A}^{\mathrm{T}}\bar{P}(t) + \bar{P}(t)\bar{A} - \bar{P}(t)\bar{B}\bar{B}^{\mathrm{T}}\bar{P}(t) + R_1, \tag{5.25}$$

$$\dot{\bar{x}}(t) = (\bar{A} - \bar{B}\bar{B}^{\mathrm{T}}\bar{P}(t))\bar{x}(t). \tag{5.26}$$

Applying Theorems 4.11 and 3.7 in [98] to (5.25) and (5.26) with the appropriate dual substitutions yields $\bar{P}(t) \to P^*$ and $\bar{x}(t) \to 0$ as $t \to \infty$. Furthermore, under the assumption that the Hamiltonian matrix

$$H = \begin{bmatrix} \bar{A} & -\bar{B}\bar{B}^{\mathrm{T}} \\ -R_1 & -\bar{A}^{\mathrm{T}} \end{bmatrix}$$

has no eigenvalues on the imaginary axis, the convergence is exponential [107].

Then, applying Theorem 8.3 in [108] for $\omega > \omega^*$, where ω^* is sufficiently large, renders the solution of the time-varying Riccati equation (5.11) exponentially convergent to a periodic solution in an $O(\epsilon)$ neighborhood of P^*.

We complete the proof by noting that stability of (5.26) implies that there exists a positive-definite matrix M such that

$$(\bar{A} - \bar{B}\bar{B}^{\mathrm{T}}P^*)^{\mathrm{T}}M + M(\bar{A} - \bar{B}\bar{B}^{\mathrm{T}}P^*) = -\epsilon I < 0.$$

For the original closed-loop system (5.12), assuming ω^* sufficiently large, the same matrix

M yields

$$(A(t) - B(t)R_2^{-1}B^{\mathrm{T}}(t)P_{\mathrm{f}}(t))^{\mathrm{T}}M + M(A(t) - B(t)R_2^{-1}B^{\mathrm{T}}(t)P_{\mathrm{f}}(t)) = -\frac{\epsilon}{2}I < 0.$$

Therefore $x(t) \to 0$ as $t \to \infty$. □

5.1.4 Output Feedback

We now consider the situation where the full-state measurement is not available. We propose the observer-based dynamic compensator

$$\dot{\hat{x}}(t) = A(t)\hat{x}(t) + B(t)u(t) + F(t)\Big(y(t) - C(t)\hat{x}(t)\Big), \tag{5.27}$$

$$u(t) = -R_2^{-1}B^{\mathrm{T}}(t)P_{\mathrm{f}}(t)\hat{x}(t), \tag{5.28}$$

where $F(t) = Q(t)C^{\mathrm{T}}(t)V_2^{-1}$ is produced using the estimator Riccati equation (5.8). Note that, unlike the standard LQG problem, the entire system of differential equations is solved forward-in-time, and therefore (5.27), (5.28) can be implemented on a time-varying system without full-state feedback and without knowing the dynamics $A(t)$, $B(t)$, and $C(t)$ in advance.

The closed loop system consisting of the observer-based dynamic compensator (5.28) interconnected with the linear system (5.1) can be described by the linear system of dimension $2n$

$$\begin{bmatrix} \dot{x}(t) \\ \dot{\hat{x}}(t) \end{bmatrix} = A_{\mathrm{cl}}(t) \begin{bmatrix} x(t) \\ \hat{x}(t) \end{bmatrix}, \tag{5.29}$$

where n is the dimension of the state $x(t)$ and where

$$A_{\mathrm{cl}}(t) \triangleq \begin{bmatrix} A(t) & B(t)K(t) \\ F(t)C(t) & A(t) - F(t)C(t) + B(t)K(t) \end{bmatrix},$$

where $K(t) = -R_2^{-1}B^{\mathrm{T}}(t)P_f(t)$ and the Kalman gain $F(t)$ is given in (5.27).

We now show, under appropriate assumptions, the closed-loop system (5.29) is uniformly exponentially stable if both the regulator and estimator dynamics are uniformly exponentially stable.

First, we restate Theorem 4.9 of [98]. Suppose that $A(t)$ is continuous and bounded, $B(t)$ is piecewise continuous and bounded, and that $R_1, R_2 \geq \alpha I$ for $\alpha > 0$. Let $P_f(t)$ be a solution of the Riccati equation (5.11) with initial condition $P_f(t_0) \geq 0$. Then, if the pair

$\left(A^{\mathrm{T}}(t), B^{\mathrm{T}}(t)\right)$ is uniformly completely reconstructable, there exists a solution of the Riccati equation (5.11) $\bar{P}_f(t)$ such that for any $P_f(t_0) \geq 0$, $P_f(t) - \bar{P}_f(t) \to 0$ as $t \to \infty$. Furthermore, $\bar{P}_f(t)$ has an upper bound, and is nonnegative-definite for all t.

Now, the following mirrors Theorem 15.5 of [106].

Theorem 2. *Let the assumptions of Theorem 4.9 of [98] as stated above hold, let the pair* $(A(t), C(t))$ *be uniformly completely reconstructable, and define* $\delta \triangleq \|R_2^{-1}\|$. *Additionally, suppose there exist positive constants* $\varepsilon_1, \varepsilon_2, \beta_1$, *and* β_2 *such that*

$$\varepsilon_1 I \leq P_f(t) \leq \varepsilon_2 I,$$

and

$$\int_\tau^t \|B(\sigma)\|^2 d\sigma \leq \beta_1 + \beta_2(t-\tau).$$

Finally, assume that the forward-in-time controller (5.10) is exponentially stabilizing. Then, the closed-loop system (5.29) is uniformly exponentially stable.

Proof. Applying the state transformation

$$\begin{bmatrix} x(t) \\ e(t) \end{bmatrix} = \begin{bmatrix} I_n & 0_n \\ I_n & -I_n \end{bmatrix} \begin{bmatrix} x(t) \\ \hat{x}(t) \end{bmatrix} \tag{5.30}$$

yields

$$\begin{bmatrix} \dot{x}(t) \\ \dot{e}(t) \end{bmatrix} = \tilde{A}_{\mathrm{cl}} \begin{bmatrix} x(t) \\ e(t) \end{bmatrix}, \tag{5.31}$$

where

$$\tilde{A}_{\mathrm{cl}} = \begin{bmatrix} A(t) + B(t)K(t) & -B(t)K(t) \\ 0_n & A(t) - F(t)C(t) \end{bmatrix}.$$

Hence (5.29) is uniformly exponentially stable if and only if (5.31) is uniformly exponentially stable. Let $\phi(t, \tau)$ denote the transition matrix corresponding to (5.31), and let $\phi_x(t, \tau)$ and $\phi_e(t, \tau)$ denote the $n \times n$ transition matrices for $A(t) + B(t)K(t)$ and $A(t) - F(t)C(t)$, respectively. Then

$$\phi(t, \tau) = \begin{bmatrix} \phi_x(t, \tau) & -\int_\tau^t \phi_x(t, \sigma) B(\sigma) K(\sigma) \phi_x(\sigma, \tau) d\sigma \\ 0_n & \phi_e(t, \tau) \end{bmatrix}.$$

Therefore,

$$\|\phi(t,\tau)\| \leq \|\phi_x(t,\tau)\| + \|\phi_e(t,\tau)\| + \| \int_\tau^t \phi_x(t,\sigma)B(\sigma)K(\sigma)\phi_x(\sigma,\tau)d\sigma\|. \tag{5.32}$$

Let $\alpha > 0$ and $\eta > 0$. Then there exists $\gamma > 0$ such that

$$\|\phi_x(t,\tau)\|, \|\phi_e(t,\tau)\| \leq \gamma e^{-(\alpha+\eta)(t-\tau),}$$

for all t, τ with $t \geq \tau$, based on the assumption that the forward-in-time controller (5.10) is exponentially stabilizing and Theorem 4.10 of [98], respectively. Then,

$$\begin{aligned} &\| \int_\tau^t \phi_x(t,\sigma)B(\sigma)K(\sigma)\phi_x(\sigma,\tau)d\sigma\| \\ &\quad \leq \gamma^2 e^{-(\alpha+\eta)(t-\tau)} \int_\tau^t \|B(\sigma)\|\,\|K(\sigma)\|d\sigma \\ &\quad \leq \delta\varepsilon_2\gamma^2 e^{-(\alpha+\eta)(t-\tau)} \int_\tau^t \|B(\sigma)\|^2 d\sigma \\ &\quad \leq \delta\varepsilon_2\gamma^2 e^{-(\alpha+\eta)(t-\tau)} \left(\beta_1 + \beta_2(t-\tau)\right). \end{aligned} \tag{5.33}$$

Using the bound

$$te^{-\eta t} \leq \frac{1}{\eta e}, \quad t \geq 0$$

in (5.33) it follows from (5.32) that

$$\|\phi(t,\tau)\| \leq \left(2\gamma + \delta\varepsilon_2\gamma^2\left(\beta_1 + \frac{\beta_2}{\eta e}\right)\right)e^{-\alpha(t-\tau)}, \tag{5.34}$$

for all t, τ with $t \geq \tau$. □

This result implies that we obtain separation of the regulator and estimator dynamics in the sense that that if both the regulator and estimator dynamics are uniformly exponentially stable, the closed-loop system (5.29) is uniformly exponentially stable.

5.1.5 Illustrative Examples

Consider a mass attached to a wall via a spring with variable stiffness $k(t)$, as shown in Fig. 5.2.

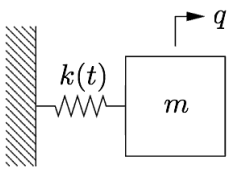

Figure 5.2: A mass constrained by a spring with time-varying stiffness.

The open-loop system is described by

$$x(t) = \begin{bmatrix} q \\ \dot{q} \end{bmatrix}, \quad A(t) = \begin{bmatrix} 0 & 1 \\ \frac{-k(t)}{m} & 0 \end{bmatrix}, \qquad B(t) = \begin{bmatrix} 0 \\ \frac{1}{m} \end{bmatrix},$$

where $k(t)$ is a time-varying stiffness that may assume positive or negative values. Let $k(t) = \sin(t)$, $m = 1$ $q(0) = 2$, and $\dot{q}(0) = 1$. Fig. 5.3 shows the open-loop response, which is unstable. We wish to stabilize this system.

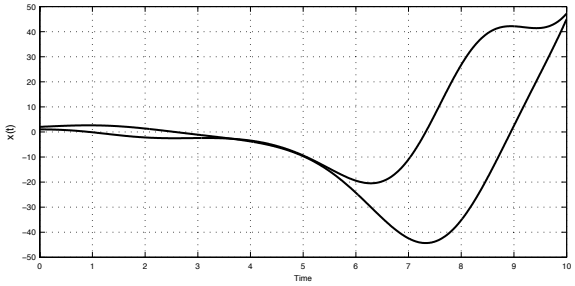

Figure 5.3: Open-loop response.

First we assume that $k(t)$ is known in advance. We apply the backwards-in-time optimal control (5.3) over a finite interval of 10 seconds. Let $R_1 = R_2 = I$ and $P_{\mathrm{b}}(10) = 0$. Fig. 5.4a shows the state trajectories and control action.

Next we assume that $k(t)$ is not known ahead of time. Instead, a perfect measurement of $k(t)$ is available at time t. We let $R_1 = R_2 = I$, $P_{\mathrm{f}}(0) = 0$, and apply the forward-in-time control (5.10). Fig. 5.4b shows the state trajectories and control action. Both backwards-in-time and forward-in-time control laws stabilize the system to the origin within 10 seconds.

Next we consider the case where the full-state measurement is not available. In this case, we use dynamic output feedback (5.27), (5.28) to stabilize the system. Suppose that

$$C(t) = \begin{bmatrix} 1 & 0 \end{bmatrix},$$

so that only the position of the mass is measured. Let $\hat{x}(t) = 0$, $V_1 = V_2 = I$, and $Q(0) = 0$. Fig. 5.5 shows that the state estimates converge to the true values, and that the origin is

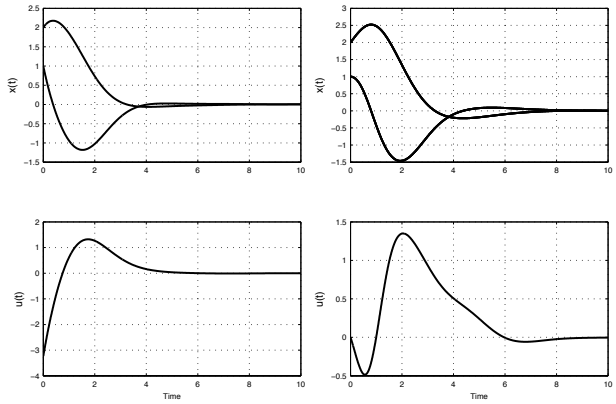

(a) *Backwards-in-time* control (b) *Forward-in-time* control

Figure 5.4: Full-state feedback for the mass-spring example.

stabilized using time-varying output feedback.

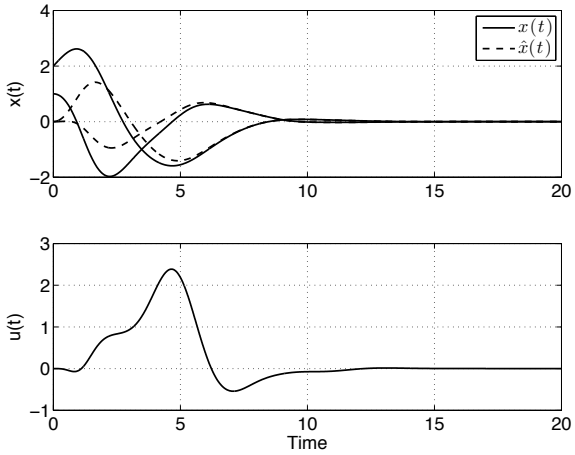

Figure 5.5: Output feedback for the mass-spring example using the forward-in-time controller. Top: State trajectories and estimates. Bottom: Control action.

We now consider an example in which the forward-in-time controller with full state measurement fails to achieve stabilization. Let

$$A = \begin{bmatrix} 1 & 0 \\ 0 & 1 \end{bmatrix}, \qquad B = \begin{bmatrix} \sin(\omega t) \\ \cos(\omega t) \end{bmatrix},$$

and $\omega = 1$. As before, we first assume that $B(t)$ is known in advance and we apply the backwards-in-time optimal control (5.3) over a finite interval of 10 seconds. Let $R_1 = R_2 = I$ and $P_b(10) = 0$. Fig. 5.6a shows the state trajectories and control time history.

Next we assume that $B(t)$ is not known by the controller ahead of time. Instead, a perfect measurement of $B(t)$ is available at time t. We let $R_1 = R_2 = I$, $P_f(0) = 0$, and apply the forward-in-time control (5.10). Fig. 5.6b shows the state trajectories and control action.

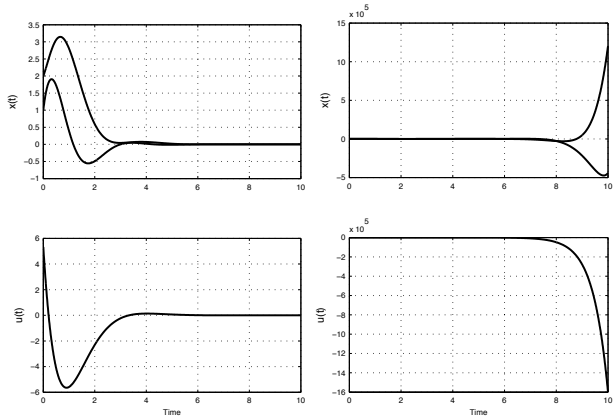

(a) *Backwards-in-time* con- (b) *Forward-in-time* control trol

Figure 5.6: Full-state feedback for $\omega = 1$ rad/sec.

We note that, although the system is controllable and thus stabilized by the backward-in-time optimal controller, the forward-in-time controller fails. However, if we increase ω to 2π rad/sec and rerun the simulation, the forward-in-time control becomes stabilizing as seen in Fig. 5.7. This phenomenon of stabilization via fast time variation is considered in Section 5.1.3.

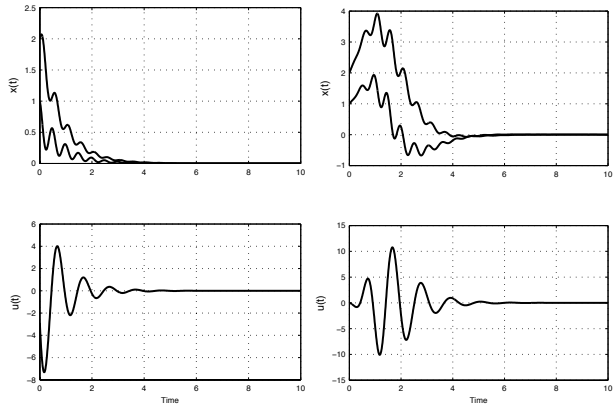

(a) *Backwards-in-time* con- (b) *Forward-in-time* control trol

Figure 5.7: Full-state feedback for $\omega = 2\pi$ rad/sec.

Finally, we consider simultaneous stabilization of two uncoupled harmonic oscillators given by

$$A = \begin{bmatrix} 0 & 1 & 0 & 0 \\ -1 & 0 & 0 & 0 \\ 0 & 0 & 0 & 1 \\ 0 & 0 & -1 & 0 \end{bmatrix}, \qquad B = \begin{bmatrix} 0 \\ \sin(\omega t) \\ 0 \\ \cos(\omega t) \end{bmatrix},$$

where $\omega = 2\pi$ rad/sec. We apply the forward-in-time control (5.10). Fig. 5.8 shows the state trajectories and control action.

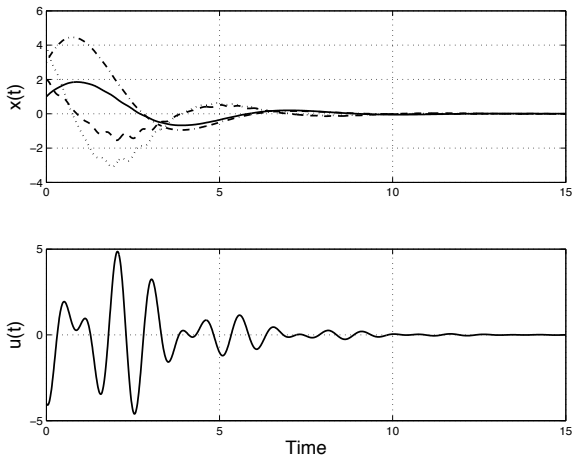

Figure 5.8: Full-state feedback for the uncoupled harmonic oscillators using the forward-in-time controller. Top: State trajectories. Bottom: Control action.

5.1.6 Nonstandard Riccati Equation

We analyze the scalar form of (5.1) in detail. Consider the system

$$\dot{x}(t) = a(t)x(t) + b(t)u(t), \tag{5.35}$$

where $a(t)$ and $b(t)$ are bounded continuous scalar functions on $[0, \infty)$. Under these assumptions, the scalar version of forward-in-time control law (5.10) is asymptotically stabilizing because the closed-loop scalar system is symmetric.

We now provide a self-contained, alternative proof of this result motivated by adaptive

control with a slight modification and an explicit controllability condition. Define

$$\beta \triangleq \sup_{t\geq 0} |b(t)|. \tag{5.36}$$

We assume that $b(t)$ is persistently exciting, that is, there exists $T_0 > 0$ and $\varepsilon > 0$ such that, for all $t \geq 0$,

$$\int_t^{t+T_0} b^2(\tau)d\tau > \varepsilon. \tag{5.37}$$

Theorem 3. *Let $\kappa > 0$, let $\alpha_0 > \max\{0, a(t)\}$ for all t, let p satisfy*

$$\dot{p}(t) = 2\alpha_0 p(t) - 2b^2(t)\kappa p^2(t),$$

let $p(0) > 0$, and let $T \geq \max\left\{T_0, \frac{1}{2\alpha_0}\ln(2\kappa\varepsilon p(0))\right\}$. Then, $p(t)$ exists on $[0,\infty)$ and satisfies

$$0 < p(t) \leq p_{\max}, \quad t \geq 0,$$

where

$$p_{\max} \triangleq \frac{1}{2\kappa\varepsilon e^{-2\alpha_0 T}}.$$

Proof. Let $[0, t_{\max})$ denote the maximal interval of existence of $p(t)$. Suppose that $t_1 \leq t_{\max}$ is the first instance where $p(t) = 0$. Then, by continuity, there exists $\delta > 0$ such that

$$0 < p(t) < \frac{\alpha_0}{\beta^2\kappa}, \quad t \in [t_1 - \delta, t_1).$$

Note that for $t \in [t_1 - \delta, t_1)$,

$$p(t)b^2(t)\kappa < p(t)\beta^2\kappa < \alpha_0,$$

which gives

$$p^2(t)b^2(t)\kappa < \alpha_0 p(t),$$

to yield

$$\dot{p}(t) = 2\alpha_0 p(t) - 2p^2(t)b^2(t)\kappa > 0.$$

Hence,

$$\begin{aligned} p(t_1) &= p(t_1-\delta) + \int_{t_1-\delta}^{t_1} \dot{p}(\tau)d\tau \\ &> p(t_1-\delta) > 0, \end{aligned}$$

contradicting the assumption $p(t_1) = 0$. Therefore t_1 does not exist, that is, $p(t) > 0$ on $[0, t_{\max})$.

Now define

$$\gamma(t) \triangleq \frac{1}{p(t)}, \quad t \in [0, t_{\max}).$$

Differentiating yields

$$\begin{aligned} \dot{\gamma}(t) &= -\frac{1}{p^2(t)}\dot{p}(t) \\ &= -\gamma^2(t)\left(2\alpha_0\frac{1}{\gamma(t)} - 2b^2(t)\kappa\frac{1}{\gamma^2(t)}\right) \\ &= -2\alpha_0\gamma(t) + 2b^2(t)\kappa, \end{aligned}$$

Thus

$$\begin{aligned} \gamma(t) &= e^{-2\alpha_0 t}\gamma(0) + \int_0^t e^{-2\alpha_0(t-\tau)}2\kappa b^2(\tau)\delta\tau \\ &\geq \int_{t-T}^t e^{-2\alpha_0(t-\tau)}2\kappa b^2(\tau)\delta\tau \\ &\geq e^{-2\alpha_0 T}\int_{t-T}^t 2\kappa b^2(\tau)\delta\tau \\ &\geq 2e^{-2\alpha_0 T}\kappa\varepsilon. \end{aligned}$$

Therefore

$$p(t) \leq \frac{1}{2\kappa\varepsilon e^{-2\alpha_0 T}}, \quad t \in [0, t_{\max}).$$

Thus the maximal interval of existence is $[0, \infty)$. □

Theorem 4. *Let the assumptions of Theorem 3 hold. Then*

$$V(x,t) \triangleq \frac{1}{2p(t)}x^2 \tag{5.38}$$

is positive definite; that is, V is nonnegative, and $V = 0$ if and only if $x = 0$.

Proof. Since $p(t)$ is bounded away from zero as shown in Theorem 3, (5.38) is positive definite. □

Theorem 5. *Let the assumptions of Theorems 3 and 4 hold and let*

$$u(t) = -\kappa p(t) b(t) x(t).$$

Then, $x(t) \to 0$ *exponentially as* $t \to \infty$.

Proof. Taking the derivative of (5.38) yields

$$\begin{aligned}
\dot{V} &= \dot{x}x\frac{1}{p} - \frac{1}{2}\frac{x^2}{p^2}\dot{p} \\
&= (a - b^2(t)\kappa p)\frac{x^2}{p} - \frac{1}{2}\frac{x^2}{p^2}\dot{p} \\
&= (a - \alpha_0)\frac{x^2}{p} = -2(\alpha_0 - a)V,
\end{aligned}$$

which is negative definite and therefore $V(x(t), t) \to 0$ exponentially as $t \to \infty$. Since p is bounded away from zero as shown in Theorem 3, and given (5.38), we conclude that $x(t) \to 0$ exponentially as $t \to \infty$. □

We now present a numerical example that is related to control over an unreliable communication channel. Let $a = \kappa = p(0) = x(0) = 1$, $\alpha_0 = 2$, $b(t) = \max\{\sin(10t), 0\}$. Note that the dynamics are unstable when $b(t) = 0$. Fig. 5.9 shows the state trajectory and control action. The state of the closed-loop system converges to the origin exponentially.

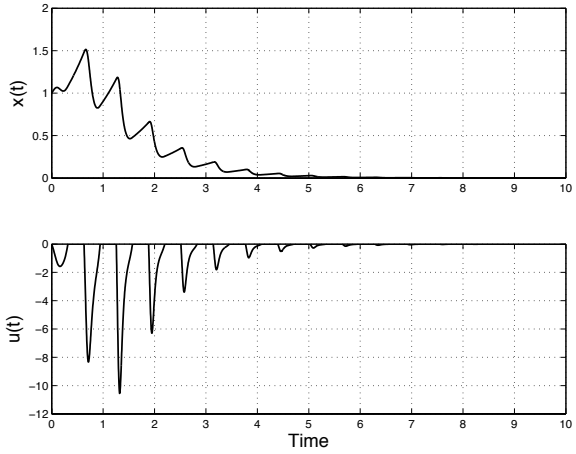

Figure 5.9: Scalar Simulation

The scalar controller can be generalized, under appropriate assumptions, to non-scalar systems. This generalization leads to a nonstandard Riccati equation.

Theorem 6. *Let $\alpha > 0$, let $P(0) > 0$, and let P satisfy*

$$\dot{P}(t) = (A(t) + \alpha I)\, P(t) + P(t)\,(A(t) + \alpha I)^{\mathrm{T}} - \Sigma(t)P^2(t) - P^2(t)\Sigma(t), \tag{5.39}$$

where

$$\Sigma(t) = B(t)B^T(t).$$

Suppose that $P(t)$ exists on $[0, \infty)$ and satisfies

$$0 < \epsilon I \leq P(t) \leq P_{\max}, \quad t \geq 0.$$

Define the Lyapunov candidate

$$V(x(t), t) = x^T(t)P^{-1}(t)x(t)$$

and let

$$u(t) = -B(t)^T P(t)x(t). \tag{5.40}$$

Then $x(t) \to 0$ exponentially as $t \to \infty$.

Proof. Computing the time derivative of V, we obtain

$$\begin{aligned}
\dot{V} &= \dot{x}^{\mathrm{T}} P^{-1} x + x^{\mathrm{T}} P^{-1} \dot{x} + x^{\mathrm{T}} \dot{P}^{-1} x \\
&= x^{\mathrm{T}} \left[(A - \Sigma P)^{\mathrm{T}} P^{-1} + P^{-1} (A - \Sigma P) - P^{-1} (A + \alpha I) - (A + \alpha I)^{\mathrm{T}} P^{-1} + P^{-1} \Sigma P + P \Sigma P^{-1} \right] x \\
&= -2\alpha x^T P^{-1} x = -2\alpha V
\end{aligned}$$

and therefore $V(x(t), t) \to 0$ exponentially as $t \to \infty$. Since $P(t)$ is positive definite and bounded, we conclude that $x(t) \to 0$ exponentially as $t \to \infty$. □

Remark 1. *We note that in all of the above cases stability is uniform with respect to the initial time.*

In presenting the scalar controller and the controller for the multi-input/multi-state case based on the nonstandard Riccati equation, we addressed the stabilizability of systems with persistently exciting input matrices. Consider the system

$$\dot{x} = Ax + B(t)u, \tag{5.41}$$

where $A \in \mathbb{R}^{n\times n}$ is a constant unstable matrix, $B(t) \in \mathbb{R}^{n\times m}$ is a bounded continuous function (and perhaps rank deficient). $B(t)$ is assumed persistently exciting, that is, there exists $T > 0$, and $\epsilon > 0$, such that for all $t \geq 0$,

$$\int_t^{t+T} B(\tau)B^{\mathrm{T}}(\tau)\delta\tau > \epsilon I. \tag{5.42}$$

As discussed in [109], stabilizability of this system is an open problem. We answer this question positively in the special cases defined by our assumptions for multi-input systems. We note that [110] addresses the case of single-input systems using a 'persistence filter' that takes an equivalent form to the scalar Riccati equation presented here.

5.2 FPR Control of Magnetically Actuated Spacecraft

We apply the FPR controller (5.10)-(5.11) to a magnetically actuated spacecraft for the cases of both inertial and nadir pointing. The spacecraft is assumed to be in low-Earth orbit and actuated by only three orthogonal electromagnetic actuators. The system model is time-varying due to the time-varying nature of the magnetic field that the spacecraft experiences as it moves through an orbit. We assume no advance knowledge of the magnetic field, and thus make no periodicity assumptions, instead relying only on measurements that are available at the current time. Even though the spacecraft model may not satisfy the sufficient conditions presented in the previous section, we show through numerical experiments that the controller is stabilizing and provides good performance. We simulate the spacecraft attitude with actuator saturation, noisy magnetic measurements, and without rate feedback. The simulations are based on the International Geomagnetic Reference Field model of the magnetic field.

5.2.1 Linearized Spacecraft Model

In order to use the FPR controller we linearize the equations of motion (4.2) and (4.10) about an equilibrium that, depending on the control objective, corresponds to either inertial pointing or Earth (nadir) pointing. These linearizations yield the system

$$\dot{x}(t) = Ax(t) + B(t)u(t), \tag{5.43}$$

where $x(t) = \begin{bmatrix} \zeta^{\mathrm{T}}(t) & \delta\omega^{\mathrm{T}}(t) \end{bmatrix}^{\mathrm{T}}$, $\zeta = \begin{bmatrix} \phi & \theta & \psi \end{bmatrix}^{\mathrm{T}} \in \mathbb{R}^3$ represents the spacecraft's 3-2-1 Euler angles relative to the inertial frame for inertial pointing and relative to the LVLH

frame for nadir pointing; $\delta\omega \in \mathbb{R}^3$ is the angular velocity of the spacecraft relative to the inertial frame for inertial pointing and relative to the LVLH frame for nadir pointing, that is, for the inertial pointing linearization, $\delta\omega = \omega$ since the equilibrium point has zero angular velocity, and, for the nadir pointing linearization, $\delta\omega$ is a perturbation about the nominal Earth-pointing angular velocity. Furthermore,

$$B(t) = \begin{bmatrix} 0 \\ -J^{-1}b^{\times}(t) \end{bmatrix} \in \mathbb{R}^{6\times 3},$$

$A = A_{\text{inertial}}$ for the inertial pointing linearization, and is given by the upper block-triangular matrix

$$A_{\text{inertial}} = \begin{bmatrix} 0 & I_3 \\ 0 & 0 \end{bmatrix} \in \mathbb{R}^{6\times 6},$$

$A = A_{\text{nadir}}$ for the nadir pointing linearization, and is given by

$$A_{\text{nadir}} = \begin{bmatrix} 0 & I_3 \\ 0 & N_v \end{bmatrix} \in \mathbb{R}^{6\times 6},$$

where

$$N_v = \begin{bmatrix} 0 & 0 & n\frac{J_2-J_3}{J_1} \\ 0 & 0 & 0 \\ n\frac{J_1-J_2}{J_3} & 0 & 0 \end{bmatrix} \in \mathbb{R}^{3\times 3},$$

n is the mean motion, that is, the angular rate of the circular orbit, and $J = \text{diag}(J_1, J_2, J_3)$. Note that for inertial pointing we do not assume that the body frame is aligned with the spacecraft principal axes, that is, J is not necessarily diagonal; this is done in nadir pointing only for simplicity.

5.2.2 Euler Angles from a Rotation Matrix

In order to implement the FPR controller in a nonlinear simulation of (4.2), (4.10) , we convert the attitude-error rotation matrix $\tilde{R}$ into Euler angles. Algorithm 1 is a method to resolve the singularities that arise from this mapping, and is adapted from ref. [111] for the case of 3-2-1 Euler angles.

Note that there exist multiple solutions for the sequence of Euler angle rotations that

Algorithm 1 Pseudocode for calculating 3-2-1 Euler angles from the attitude-error rotation matrix.

if $\tilde{R}_{13} \neq \pm 1$ **then**
  $\theta_1 = -\arcsin(\tilde{R}_{13})$
  $\psi_1 = \text{atan2}(\frac{\tilde{R}_{12}}{\cos(\theta_1)}, \frac{\tilde{R}_{11}}{\cos(\theta_1)})$
  $\phi_1 = \text{atan2}(\frac{\tilde{R}_{23}}{\cos(\theta_1)}, \frac{\tilde{R}_{33}}{\cos(\theta_1)})$

  # Comment: second set of Euler angles
  $\theta_2 = \pi - \theta_1$
  $\psi_2 = \text{atan2}(\frac{\tilde{R}_{12}}{\cos(\theta_2)}, \frac{\tilde{R}_{11}}{\cos(\theta_2)})$
  $\phi_2 = \text{atan2}(\frac{\tilde{R}_{23}}{\cos(\theta_2)}, \frac{\tilde{R}_{33}}{\cos(\theta_2)})$
else
  ϕ = anything; can set to 0
  if $\tilde{R}_{13} = -1$ **then**
    $\theta = \frac{\pi}{2}$
    $\psi = \phi + \text{atan2}(\tilde{R}_{32}, \tilde{R}_{31})$
  else
    $\theta = -\frac{\pi}{2}$
    $\psi = -\phi + \text{atan2}(-\tilde{R}_{32}, -\tilde{R}_{31})$
  end if
end if

represent a given attitude orientation. In our simulations we set $\zeta(t) = \begin{bmatrix} \phi_1 & \theta_1 & \psi_1 \end{bmatrix}^{\mathrm{T}}$ if $\tilde{R}_{13}(t) \neq \pm 1$; otherwise we set $\phi = 0$ and proceed according to Algorithm 1.

5.2.3 Numerical Studies

We consider a spacecraft in a 450-km circular orbit above the Earth with an inclination of 87 degrees. The International Geomagnetic Reference Field (IGRF) model is used to simulate Earth's geomagnetic field as a function of orbital position [53]. The spacecraft inertia matrix J is given by

$$J = \begin{bmatrix} 5 & -0.1 & -0.5 \\ -0.1 & 2 & 1 \\ -0.5 & 1 & 3.5 \end{bmatrix} \text{kg-m}^2, \tag{5.44}$$

with principal moments of inertia equal to 1.4947, 3.7997, and 5.2056 kg-m^2. We stress that, although the FPR controller uses a linearized model, all closed-loop simulations are

fully nonlinear.

5.2.4 Rest-to-Rest Maneuver

We use the FPR controller for a rest-to-rest (slew) maneuver, where the objective is to bring the spacecraft from the initial attitude

$$R(0) = \begin{bmatrix} 0.097 & 0.349 & -0.932 \\ 0.973 & -0.230 & 0.015 \\ -0.209 & -0.908 & -0.362 \end{bmatrix}, \tag{5.45}$$

which corresponds to the 3-2-1 Euler angles

$$\zeta(0) = \begin{bmatrix} 0.1 & 0.2 & 0.3 \end{bmatrix}^{\mathrm{T}} \text{rad},$$

with zero initial angular velocity $\omega(0) = \delta\omega(0) = 0$, to rest at the desired final orientation $R_{\mathrm{d}} = I_3$, $\zeta = 0$. Let the parameters of the FPR controller (5.10)-(5.11) be given by $R_1 = I_6$, $R_2^{-1} = 0.0001$, and $P_f(0) = I_6$. These values were tuned to give nominal magnetic dipole moments around 2×10^{-3} A-m^2, which is about an order of magnitude larger than the residual dipole moment of a typical nanosatellite [112], and a settling time of around 8 orbits. We test the controller in a nonlinear simulation of (4.1)-(4.2).

Figure 5.17 shows the eigenaxis attitude error, Euler angles, angular velocity, and magnetic dipole moment for the simulation described above. The spacecraft comes to rest at the commanded attitude within 7 orbits. The maximum magnetic dipole moment generated is less than 3×10^{-3} A-m^2. This quantity can be further tuned by modifying the weights R_1 and R_2.

5.2.4.1 Actuator Saturation

We now illustrate actuator-saturation handling. Let $u_{\max} = 2\times10^{-4}$ A-m^2 be the saturation limit on the magnetic dipole moments, which is about an order of magnitude less than the nominal controller tuning. If the controller specifies a magnetic dipole moment larger than $u_{\max}$, we apply the saturation as the vector scaling

$$u_{\mathrm{sat}}(t) = u_{\max}\frac{u(t)}{||u(t)||}. \tag{5.46}$$

Figure 5.18 shows the eigenaxis attitude error, Euler angles, angular velocity, and magnetic dipole moment. The spacecraft comes to rest at the commanded attitude within 12

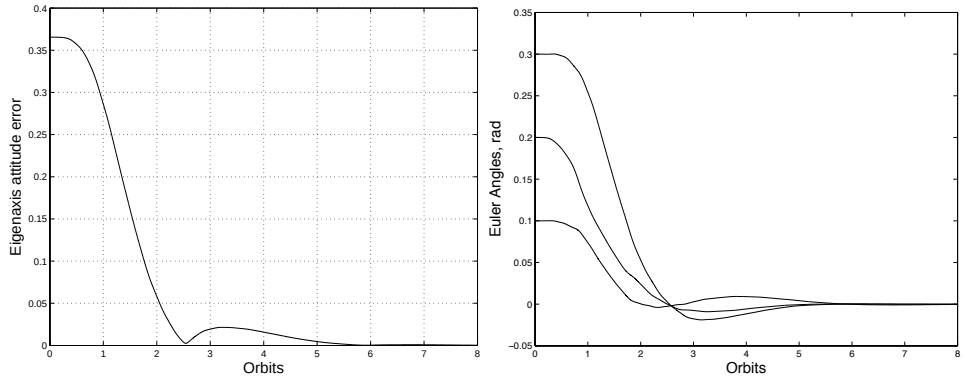

(a) Eigenaxis Attitude Error (b) Euler Angles

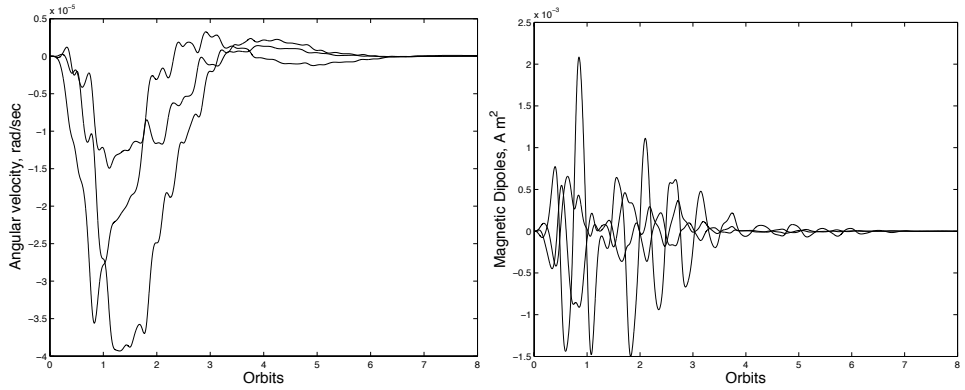

(c) Angular Velocity (d) Magnetic Dipole Moments

Figure 5.10: Full-state feedback for the rest-to-rest maneuver. (a) Eigenaxis Attitude Error, (b) Euler Angles, (c) Angular Velocity, (d) Magnetic Dipole Moments. The spacecraft comes to rest at the commanded attitude within 7 orbits, and the maximum magnetic dipole moment required by the controller is less than 3×10^{-3} A-m^2.

orbits. The magnetic dipole moment is saturated at 2×10^{-4} A-m^2.

5.2.4.2 Noisy Magnetic Field Measurement

We now consider the effects of noisy and biased magnetometer measurements. In the controller (5.10)-(5.11), we replace $-b^{\times}(t)$ with $-(R_n(\alpha)b(t)+m)^{\times}$, where $R_n(\alpha)=e^{\alpha n^{\times}}$ is a rotation matrix that rotates the magnetic field measurement by an angle α around axis n, and m is random additive noise. Let $\alpha=45°$, let $n=[-0.868 \quad 0.420 \quad 0.266]^{\mathrm{T}}$, and let m be normally distributed with zero mean and standard deviation 10^{-5} T, which is roughly one order of magnitude less than the nominal magnetic field strength. For a detailed discussion on magnetometer bias determination and calibration see ref. [113].

Figure 5.19 shows the eigenaxis attitude error, Euler angles, angular velocity, and mag-

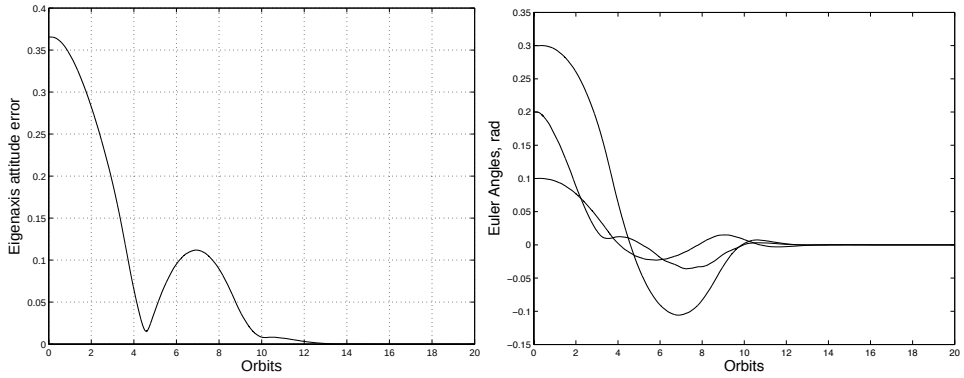

(a) Eigenaxis Attitude Error

(b) Euler Angles

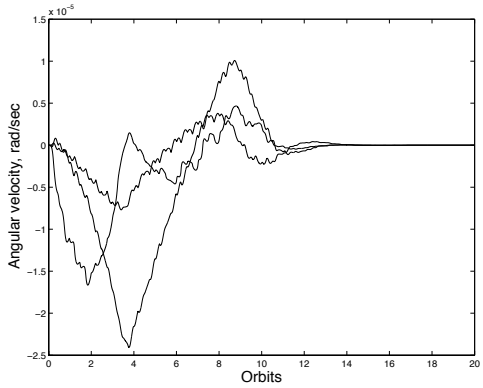

(c) Angular Velocity

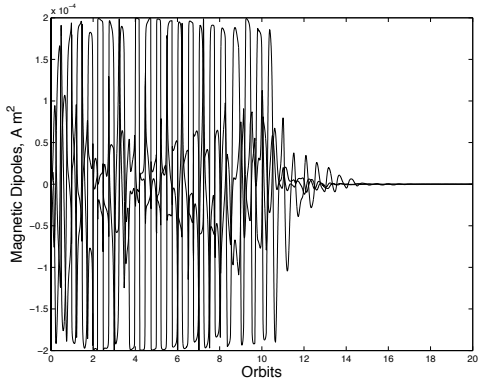

(d) Magnetic Dipole Moments

Figure 5.11: Full-state feedback with magnetic dipole moment saturation of 2×10^{-4} A-m^2 for the rest-to-rest maneuver. (a) Eigenaxis Attitude Error (b) Euler Angles, (c) Angular Velocity, (d) Magnetic Dipole Moments. The spacecraft comes to rest at the commanded attitude within 16 orbits, and the maximum magnetic dipole moment is less than 2×10^{-4} A-m^2.

netic dipole moment. The spacecraft comes to rest at the commanded attitude within 9 orbits, demonstrating that the controller is forgiving to large errors in the magnetic-field measurement.

5.2.4.3 Output Feedback

We now consider the situation where the full-state measurement is not available. In particular, we assume that we have measurements of only the attitude, that is,

$$C(t) = \begin{bmatrix} I_3 & 0 \end{bmatrix} \in \mathbb{R}^{3\times6}.$$

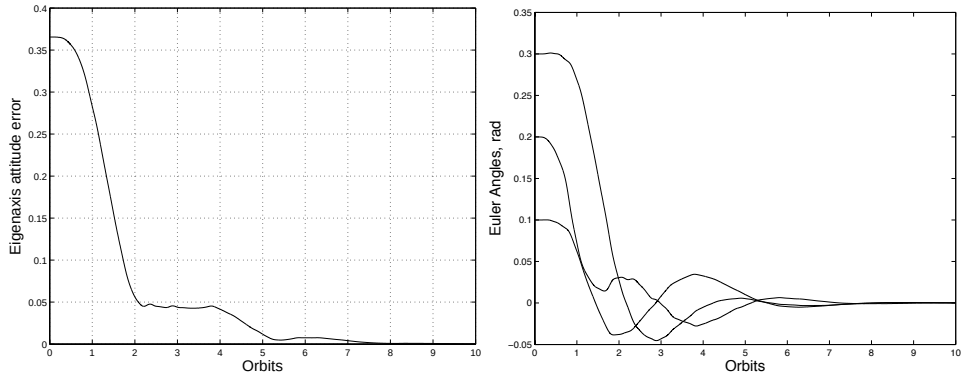

(a) Eigenaxis Attitude Error (b) Euler Angles

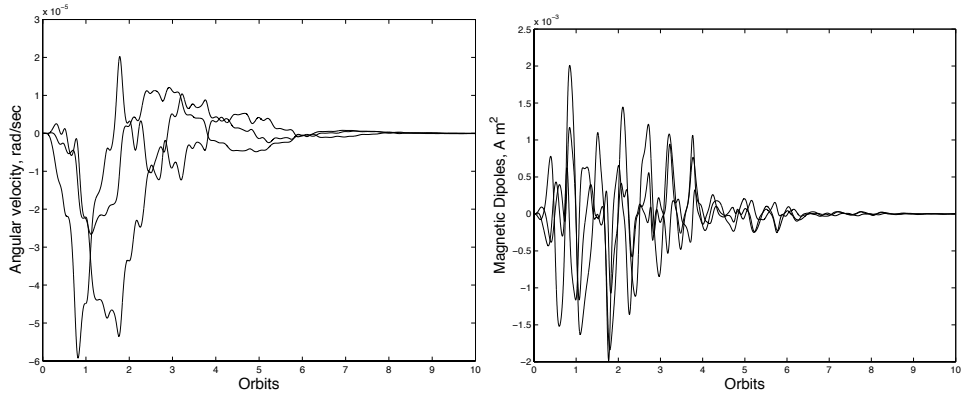

(c) Angular Velocity (d) Magnetic Dipole Moments

Figure 5.12: Full-state feedback with noisy magnetic field measurements for the rest-to-rest maneuver. The measurements are off by 45° and corrupted by gaussian noise. (a) Eigenaxis Attitude Error (b) Euler Angles, (c) Angular Velocity, (d) Magnetic Dipole Moments. The spacecraft comes to rest at the commanded attitude within 9 orbits, and the maximum magnetic dipole moment is less than 3×10^{-3} A-m^2.

In this case, we use dynamic output feedback (5.27), (5.28) to stabilize the system. We let $V_1 = I_6$, and $V_2^{-1} = 10^{-14}$ in order to slow down the convergence of the estimated states so that they are visible in the simulation.

Figure 5.20 shows the eigenaxis attitude error, Euler angles, angular velocity, and magnetic dipole moment. The estimated states converge to the true state values, and the spacecraft comes to rest at the commanded attitude within 8 orbits. Note that if the convergence of the estimated states is not slowed down, the spacecraft comes to rest faster.

5.2.4.4 Large-Angle Maneuver

We use the FPR controller (5.10)-(5.11) for a large slew maneuver, rotating 180 degrees about the x-axis. The objective is to bring the spacecraft from the initial attitude $R(0) =$

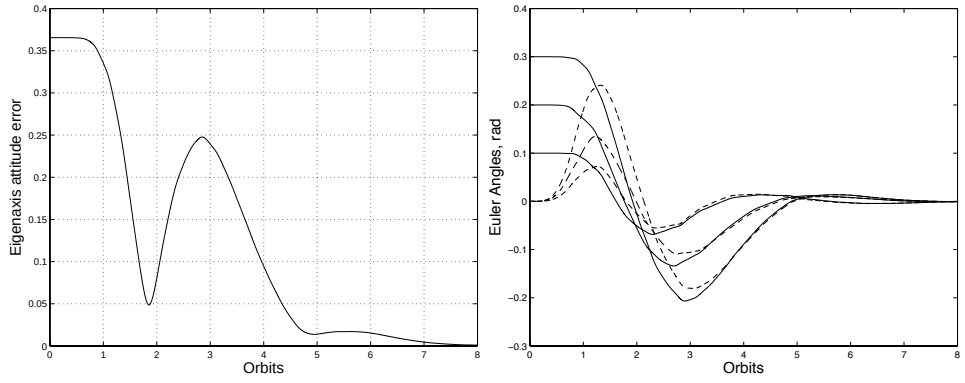

(a) Eigenaxis Attitude Error

(b) Euler Angles

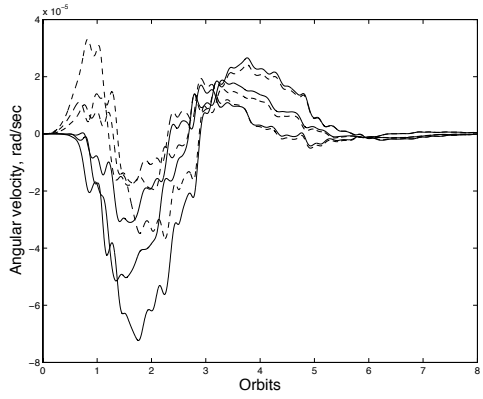

(c) Angular Velocity

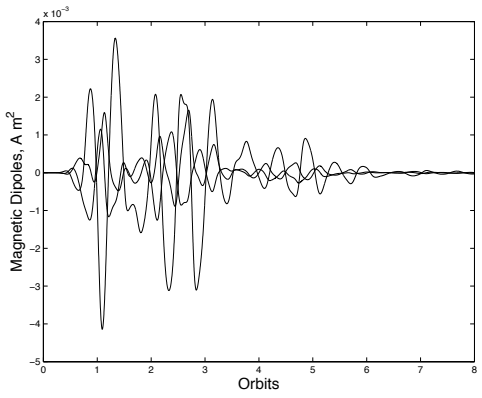

(d) Magnetic Dipole Moments

Figure 5.13: Output feedback without angular velocity measurements for the rest-to-rest maneuver. (a) Eigenaxis Attitude Error (b) Euler Angles, solid, and estimates, dashed, (c) Angular Velocity, solid, and estimates, dashed, (c) Magnetic Dipole Moments. The estimated states converge to the true values, the spacecraft comes to rest at the commanded attitude within 8 orbits, and the maximum magnetic dipole moment is less than 4×10^{-3} A-m^2.

$\mathrm{diag}(1,-1,-1)$, which corresponds to the 3-2-1 Euler angles

$$\zeta(0) = \begin{bmatrix} \pi & 0 & 0 \end{bmatrix}^{\mathrm{T}} \text{rad},$$

with zero initial angular velocity, $\omega(0) = \delta\omega(0) = 0$, to rest at the desired final orientation, $R_{\mathrm{d}} = I_3$, $\zeta = 0$.

Figure 5.14 shows the eigenaxis attitude error, Euler angles, angular velocity, and magnetic dipole moment for the simulation described above. The spacecraft comes to rest at the commanded attitude within 10 orbits. The maximum magnetic dipole moment generated is less than 2×10^{-2} A-m^2.

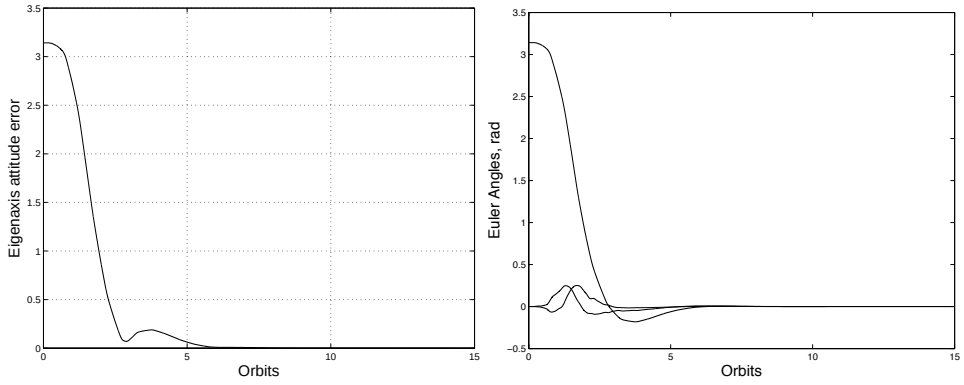

(a) Eigenaxis Attitude Error (b) Euler Angles

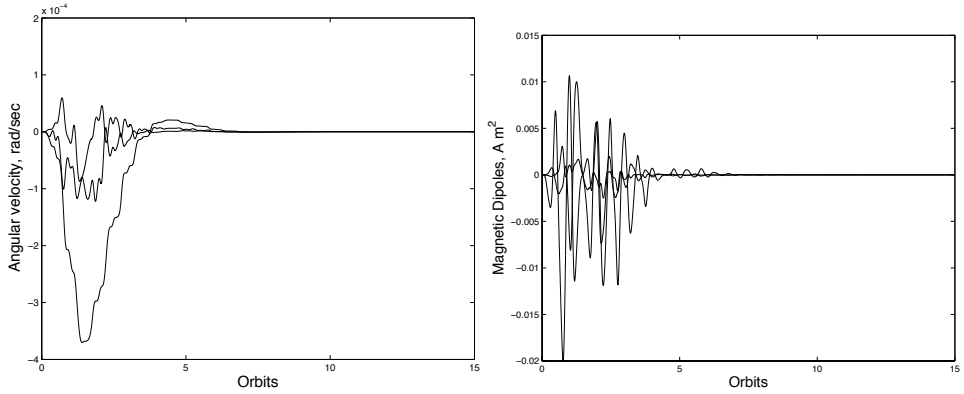

(c) Angular Velocity (d) Magnetic Dipole Moments

Figure 5.14: Full-state feedback for the large-angle maneuver. (a) Eigenaxis Attitude Error (b) Euler Angles, (c) Angular Velocity, (d) Magnetic Dipole Moments. The spacecraft comes to rest at the commanded attitude within 10 orbits, and the maximum magnetic dipole moment is less than 2×10^{-2} A-m^2.

5.2.5 Motion-to-Rest Maneuver

We now give the spacecraft the non-zero initial angular velocity

$$\omega(0) = \delta\omega(0) = \begin{bmatrix} 0.025 & 0.025 & -0.03 \end{bmatrix}^{\mathrm{T}} \text{rad/sec.}$$

The parameters of the FPR controller are as given in the previous section.

Figure 5.15 shows the eigenaxis attitude error, Euler angles, angular velocity, and magnetic dipole moment for the motion-to-rest maneuver. The spacecraft now tumbles before the magnetic actuators are able to regulate the attitude. Note that, as in the previous simulation, the controller is stabilizing for maneuvers outside the expected region of validity of the linearized model. The spacecraft comes to rest at the commanded attitude within 10

orbits. The maximum magnetic dipole moment generated is less than 1.5 A-m^2.

Note that the parameters of the controller were tuned for a small rest-to-rest maneuver and are now being applied to a motion-to-rest maneuver. If the spacecraft cannot generate the requested magnetic dipole moments, they could either be saturated, or one could retune the weight matrices R_1 and R_2 for the motion-to-rest maneuver. Also note that, since Algorithm 1 maps the Euler angles to the range $(-\pi, \pi)$, there are discontinuous jumps in Figure 5.15b.

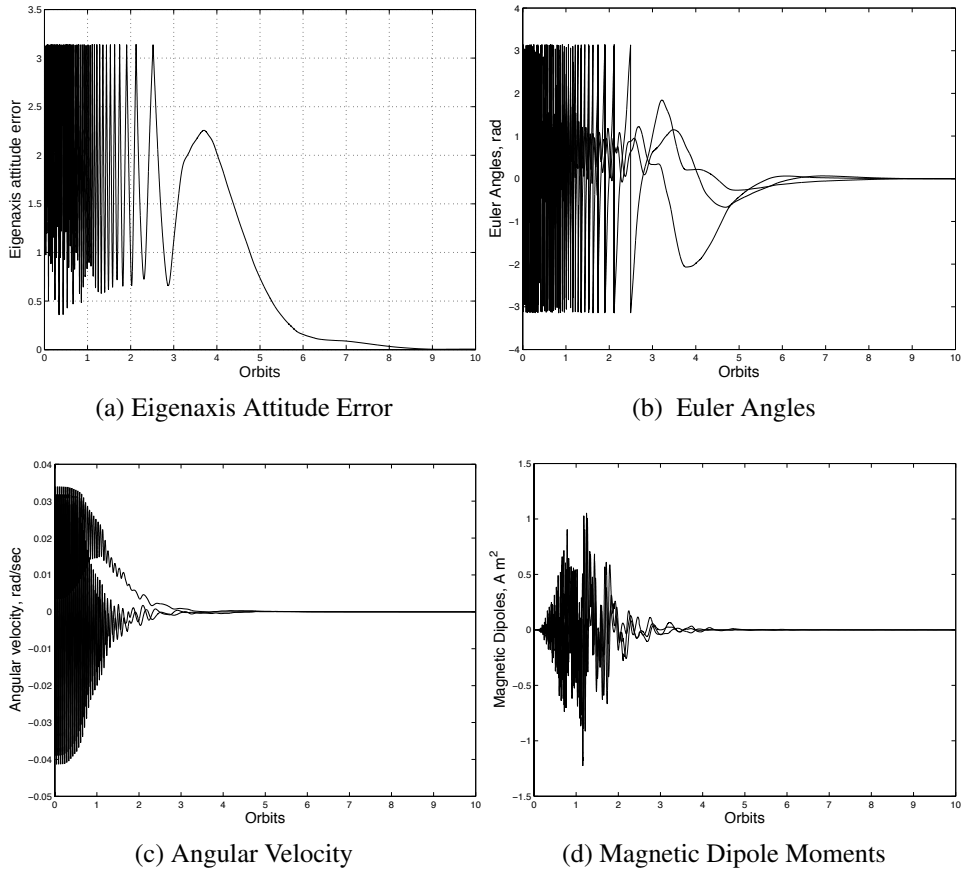

(a) Eigenaxis Attitude Error (b) Euler Angles

(c) Angular Velocity (d) Magnetic Dipole Moments

Figure 5.15: Full-state feedback for the motion-to-rest maneuver. (a) Eigenaxis Attitude Error (b) Euler Angles, (c) Angular Velocity, (d) Magnetic Dipole Moments. The spacecraft comes to rest at the commanded attitude within 10 orbits, and the maximum magnetic dipole moment is less than 1.5 A-m^2.

5.2.6 Rest-to-Spin Maneuver (Nadir Pointing)

We now use the FPR controller (5.10)-(5.11) for a rest-to-spin maneuver, where the objective is to bring the spacecraft from rest, with initial attitude $R(0) = I_3$, which corresponds

to the 3-2-1 Euler angles $\zeta(0) = 0$, and zero initial angular velocity $\omega(0) = 0$, which corresponds to $\delta\omega(0) = \begin{bmatrix} 0 & n & 0 \end{bmatrix}^{\mathrm{T}}$ rad/sec, to a nadir pointing configuration, with

$$\omega_{\mathrm{d}} = \begin{bmatrix} 0 & -n & 0 \end{bmatrix}^{\mathrm{T}} \text{ rad/sec}, \quad (\delta\omega_{\mathrm{d}} = 0)$$

where $n = 0.0011$, and $R_{\mathrm{d}}(0) = I_3$.

We rotate the spacecraft frame so that the inertia matrix J is now given by $J = \mathrm{diag}(1.4947, 5.2056, 3.7997)$ kg-m^2. This choice ensures that the spacecraft spins about its major axis as it points at the Earth. Alternatively, we could have specified ω_{d} to align with the spacecraft's major axis in the original coordinates. Note that we use $A = A_{\mathrm{nadir}}$.

Figure 5.16 shows the eigenaxis attitude error, Euler angles, angular velocity, and magnetic dipole moment for the nadir pointing maneuver. The spacecraft comes to rest at the commanded attitude within 8 orbits. The maximum magnetic dipole moment generated is less than 0.2 A-m^2.

5.3 FPR Control for Spacecraft Rendezvous Maneuvers on Elliptic Orbits

We apply the FPR controller to a maneuvering spacecraft in an elliptic orbit around the Earth. The linearized equations of motion for a spacecraft on an elliptic orbit are time-varying (Appendix A), thus impeding their treatment using most existing feedback control techniques that assume time-invariant plant models. We simulate rendezvous maneuvers on Molniya and Tundra orbits using a nonlinear model with perturbation forces. We demonstrate that the controller performs well and is robust to many error sources including severe thrust magnitude and direction deviations, and even intermittent thrust availability.

5.3.1 Numerical Studies

In the following simulations we consider spacecraft in both Molniya and Tundra orbits. See Fig. 5.17 for a plot of a Molniya orbit. The orbital elements [57] used for the Molniya orbit are given by

$$(a, e, i, \Omega, \omega, \nu) = (26559\,\mathrm{km}, 0.704482, 63.170^\circ, 206.346^\circ, 281.646^\circ, 0^\circ),$$

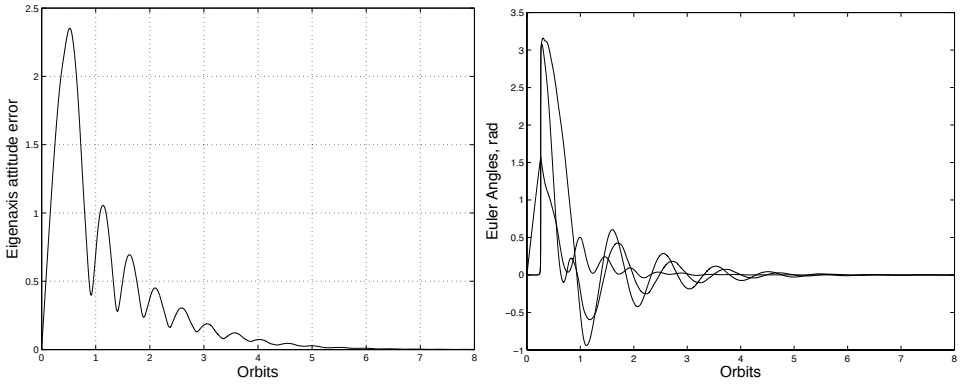

(a) Eigenaxis Attitude Error (b) Euler Angles

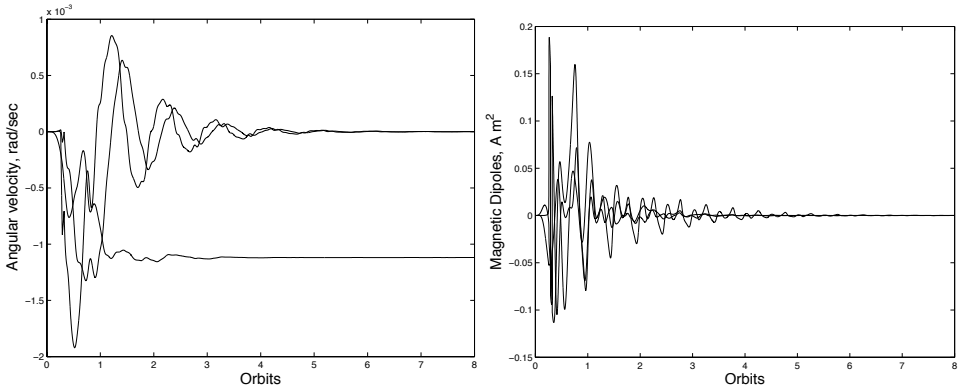

(c) Angular Velocity (d) Magnetic Dipole Moments

Figure 5.16: Full-state feedback for the nadir-pointing maneuver. (a) Eigenaxis Attitude Error (b) Euler Angles, (c) Angular Velocity, (d) Magnetic Dipole Moments. The spacecraft converges to the commanded spin within 8 orbits, and the maximum magnetic dipole moment is less than 0.2 A-m^2.

and for the Tundra orbit we use

$$(a, e, i, \Omega, \omega, \nu) = (42164\,\text{km}, 0.3, 63.170^\circ, 206.346^\circ, 281.646^\circ, 0^\circ),$$

These orbital elements give an initial position $R_0(0)$ and velocity $v_0(t)$ for the target spacecraft with which we wish to rendezvous. Note that since we let $\nu = 0$, we start at orbital perigee.

The mass of the chaser spacecraft is $m_c = 140$ kg, and the parameters of the FPR controller (5.10)-(5.11) are $R_1 = 0.001 I_6$, $R_2 = 100000$, and $P_f(0) = I_6$. These values were tuned to give appropriate nominal response time and reasonable thrust usage over a set of typical maneuvers that the spacecraft is expected to execute.

We test the controller in a high fidelity nonlinear simulation that includes both J_2 and

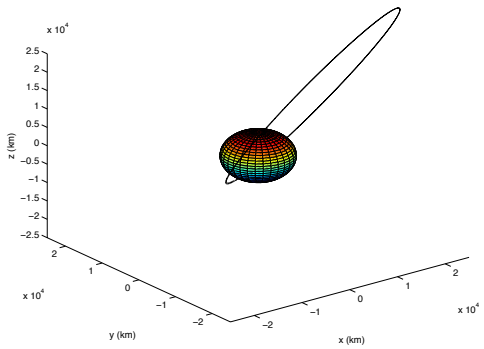

Figure 5.17: Molniya Orbit. The sphere represents the Earth.

air drag perturbations based on the Harris-Priester model [114]. The controller has no knowledge of these perturbations although we assume that accurate position and velocity information are available at the current time instant.

5.3.2 Multiple Initial Conditions

We use the FPR controller (5.10)-(5.11) for various chaser spacecraft initial conditions on the Molniya orbit, where the objective is to rendezvous the chaser spacecraft with the target spacecraft. Fig. 5.18a shows a 3D plot for initial conditions

$$[\delta x(0) \quad \delta y(0) \quad \delta z(0)] = \pm[500 \quad 500 \quad 500]\,\text{km},$$

while Fig. 5.18b shows a projection onto the orbital plane for various other initial conditions in both v-bar and r-bar approaches.

These simulation results are based on a *nonlinear model* with J_2 and air drag effects; they demonstrate that the controller is stabilizing even for large deviations in the initial conditions. Note that for open-loop maneuver planning, the applicability of (A.2) is generally limited to 50 km maneuvers. Excellent maneuvers were also obtained when the nominal orbital position is not at the perigee; the perigee location is most challenging on an elliptic orbit due to faster motion and larger influence of disturbances such as air drag. All subsequent simulations are performed at perigee.

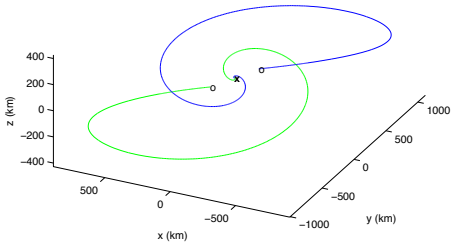

(a) 3D relative motion plot.

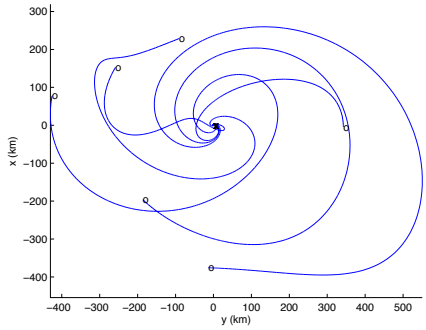

(b) Orbital plane projection.

Figure 5.18: (a) 3D relative motion plot for initial conditions near perigee on a Molniya orbit; (b) Orbital plane projection for multiple initial conditions near perigee on a Molniya orbit.

5.3.3 Thrust Saturation

Let $u_{\max} = 10$ N be the maximum thrust magnitude. If the controller specifies a thrust command with norm greater than $u_{\max}$, we let

$$u_{\text{sat}}(t) = u_{\max} \frac{u(t)}{||u(t)||}. \tag{5.47}$$

We use the FPR controller (5.10)-(5.11) for the rendezvous maneuver, where the objective is to bring the chaser spacecraft from the initial position

$$[\delta x(0) \quad \delta y(0) \quad \delta z(0)] = [250 \quad 250 \quad 250]\,\text{km},$$

with zero initial relative velocity, to rest at the desired final position, $[\delta x \quad \delta y \quad \delta z] = [0 \quad 0 \quad 0]$.

Fig. 5.19a shows the maneuver projected onto the orbital plane for the Molniya orbit. Fig. 5.19b gives the components of the thrust vector. Note that the thrust is saturated to 10 N. The spacecraft rendezvous with the target within 1.5 orbits. Fig. 5.20 shows the same plots for the Tundra orbit.

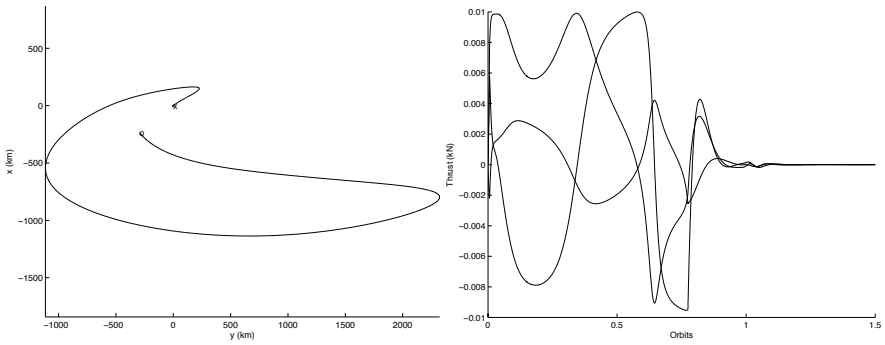

(a) Orbital plane projection (b) Thrust vector components

Figure 5.19: Rendezvous maneuver performed at perigee on a Molniya orbit with 10 N saturated thrust. (a) Orbital plane projection; (b) Thrust vector components.

All subsequent simulations are performed with thrust saturation.

5.3.4 Thrust Aligned with the Ram Direction

We now consider the case where the spacecraft only thrusts in the tangential (ram) direction ($\pm y$ axis in Hill's frame). This case is practically relevant if the spacecraft orientation cannot be changed in order to point its thruster.

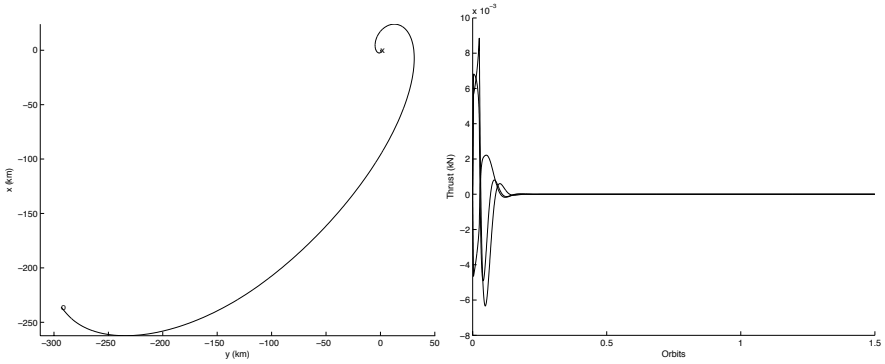

(a) Orbital plane projection (b) Thrust vector components

Figure 5.20: Rendezvous maneuver performed at perigee on a Tundra orbit with 10 N saturated thrust. (a) Orbital plane projection; (b) Thrust vector components.

We use the FPR controller (5.10)-(5.11) for the rendezvous maneuver, where the objective is to bring the chaser spacecraft from the initial position

$$[\delta x(0) \quad \delta y(0) \quad \delta z(0)] = [250 \quad 250 \quad 0]\,\text{km},$$

with zero initial relative velocity, to rest at the desired final position, $[\delta x \quad \delta y \quad \delta z] = [0 \quad 0 \quad 0]$. Let $u_{\max} = 10$ N.

Fig. 5.21a shows the maneuver projected onto the orbital plane for the Molniya orbit. Fig. 5.21b gives the components of the thrust vector. Note that only the tangential thrust is used and that it is saturated to 10 N. The spacecraft rendezvous with the target within 1.5 orbits. Fig. 5.22 shows the same plots for the Tundra orbit.

Finally, we note that we do not similarly consider radial-only thrust since the spacecraft dynamics are uncontrollable in this case, even for circular orbits.

5.3.5 Intermittent Thrust Availability and Thrust Direction Errors

We now highlight the robustness of the FPR controller to intermittent thrust availability and thrust direction errors. We assume that the thrusters are able to operate for 10 minutes every 30 minutes in order to simulate the situation where occasional burns are used to rendezvous with the target. Additionally, we assume that the attitude controller is not capable of correctly pointing the thruster in the desired direction, so that the requested thrust vector is rotated by 20° around a random body fixed vector.

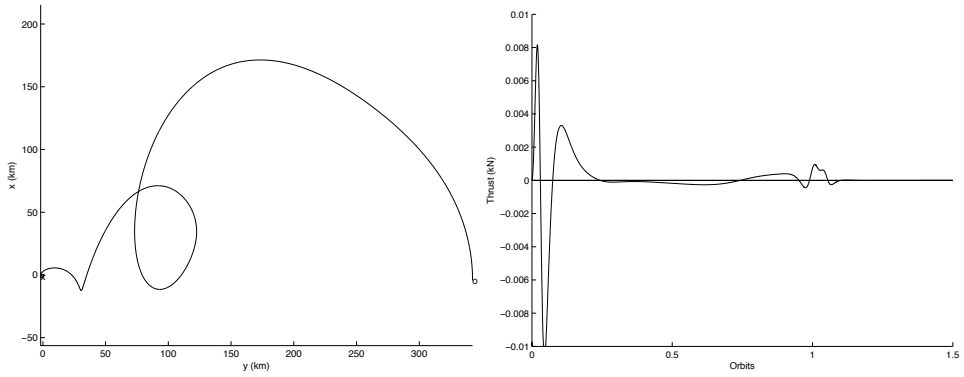

(a) Orbital plane projection (b) Thrust vector components

Figure 5.21: Rendezvous maneuver performed at perigee on a Molniya orbit with 10 N saturated thrust that is aligned with the ram direction. (a) Orbital plane projection; (b) Thrust vector components.

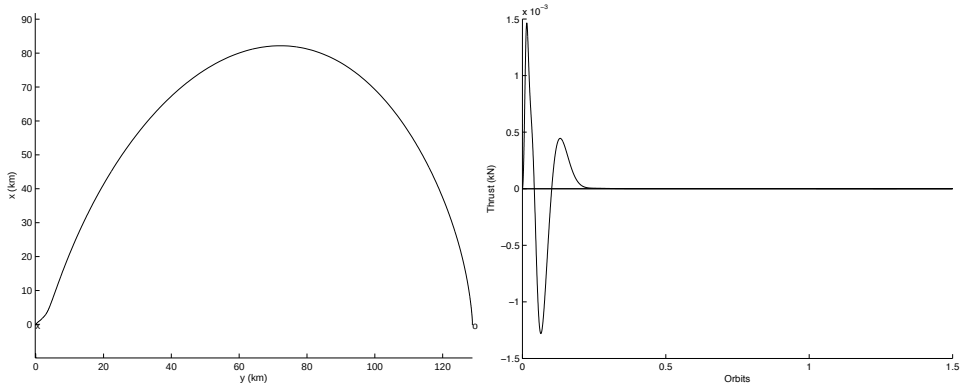

(a) Orbital plane projection (b) Thrust vector components

Figure 5.22: Rendezvous maneuver performed at perigee on a Tundra orbit with 10 N saturated thrust that is aligned with the ram direction. (a) Orbital plane projection; (b) Thrust vector components.

The chaser spacecraft is initially at

$$[\delta x(0) \quad \delta y(0) \quad \delta z(0)] = [50 \quad 50 \quad 50]\,\text{km},$$

with zero initial relative velocity, and the objective is to bring it to rest at the desired final position, $[\delta x \quad \delta y \quad \delta z] = [0 \quad 0 \quad 0]$. Let $u_{\max} = 10$ N.

Fig. 5.23a shows the maneuver projected onto the orbital plane for the Molniya orbit. Fig. 5.23b gives the components of the thrust vector. Note that the thrust is saturated to 10 N and only fires every 30 minutes. The spacecraft rendezvous at the target within 1.5 orbit. Fig. 5.24 shows the same plots for the Tundra orbit.

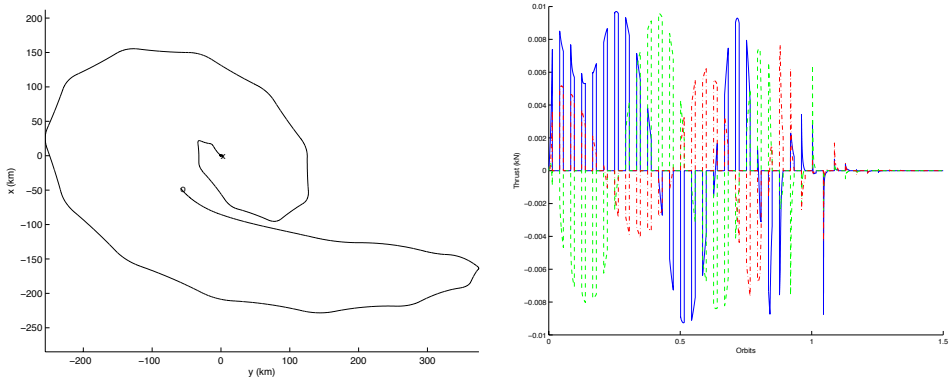

(a) Orbital plane projection (b) Thrust vector components

Figure 5.23: Rendezvous maneuver performed at perigee on a Molniya orbit with 10 N saturated thrust that is only available for 10 minutes every 30 minutes and is rotated by 20 degrees about a random body vector. (a) Orbital plane projection; (b) Thrust vector components.

5.3.6 Output Feedback

We now consider the case where the full-state measurement is not available. In particular, we assume that we do not have measurements of the relative velocity, that is

$$C(t) \in \mathbb{R}^{3\times 6} = \begin{bmatrix} I_3 & 0 \end{bmatrix}.$$

In this case, we use dynamic output feedback (5.27), (5.28) to stabilize the system. We let $V_1 = I_6$, and $V_2^{-1} = 10^{-15}$ in order to slow down the convergence of the estimated states so that they are clearly visible in the simulation.

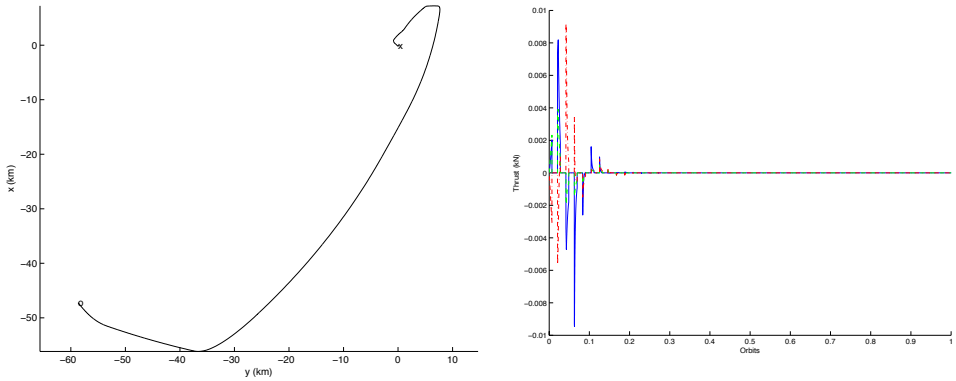

(a) Orbital plane projection (b) Thrust vector components

Figure 5.24: Rendezvous maneuver performed at perigee on a Tundra orbit with 10 N saturated thrust that is only available for 10 minutes every 30 minutes and is rotated by 20 degrees about a random body vector. (a) Orbital plane projection; (b) Thrust vector components.

The chaser spacecraft is initially at

$$[\delta x(0) \quad \delta y(0) \quad \delta z(0)] = [50 \quad 50 \quad 50]\,\text{km},$$

with zero initial relative velocity, and the objective is to bring it to rest at the desired final position, $[\delta x \quad \delta y \quad \delta z] = [0 \quad 0 \quad 0]$. Let $u_{\max} = 10$ N.

Fig. 5.25a shows the maneuver projected onto the orbital plane for the Molniya orbit. Fig. 5.25c gives the components of the thrust vector. Note that the thrust is saturated to 10 N. Fig. 5.25e shows the relative velocity states and estimates. The estimated states converge to the true state values and the spacecraft rendezvous with the target within 1.5 orbits. Fig. 5.25(b),(d),(f) show the same plots for the Tundra orbit.

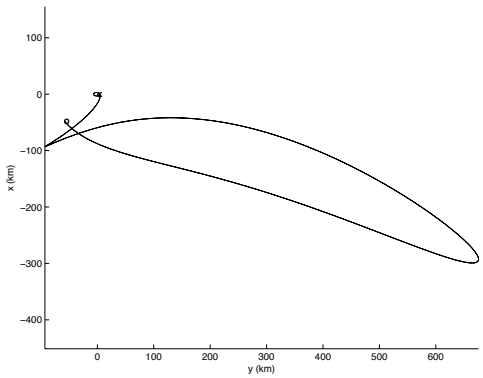

(a) Orbital plane projection

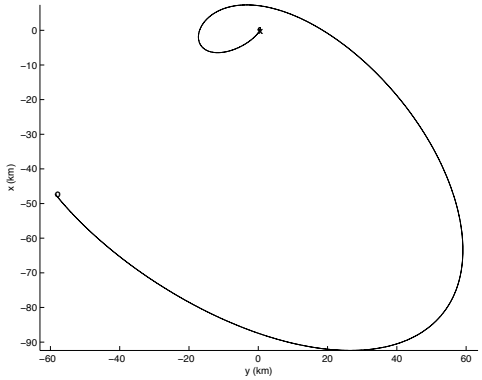

(b) Orbital plane projection

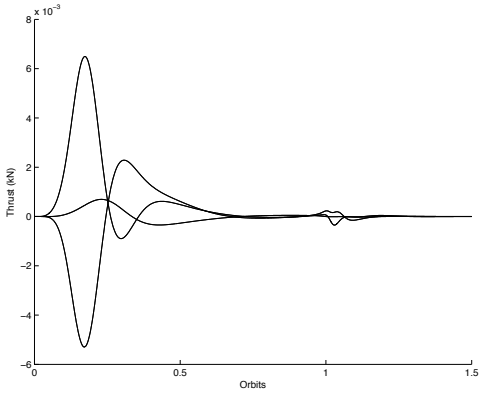

(c) Thrust vector components

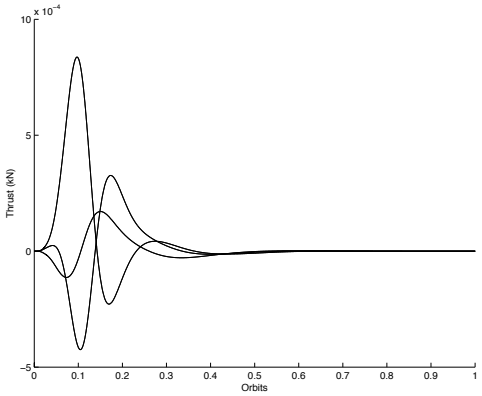

(d) Thrust vector components

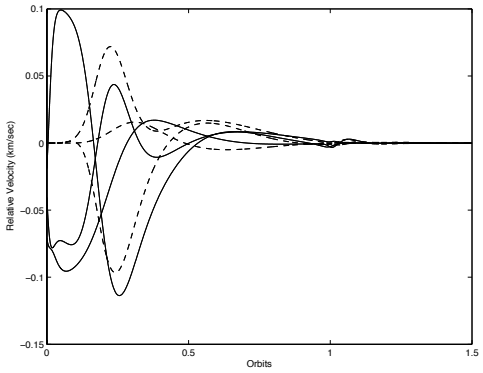

(e) Relative velocity components and estimated states

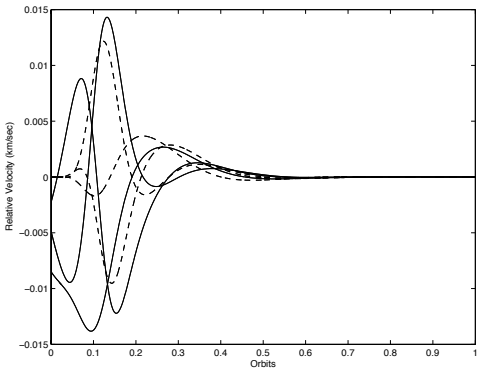

(f) Relative velocity components and estimated states

Figure 5.25: Output feedback rendezvous maneuver performed at perigee on Molniya (left) and Tundra (right) orbits with 10 N saturated thrust. Only relative position data is assumed to be available. (a),(b) Orbital plane projection; (c),(d) Thrust vector components; (e),(f) Relative velocity components and estimated states.

CHAPTER 6

Conclusions

The main conclusions are now summarized for each of the major topics addressed in this dissertation. Directions for future work are discussed.

6.1 MPC

It was demonstrated through simulations on the full nonlinear model that the linear quadratic MPC controller with dynamically reconfigurable constraints can successfully complete three dimensional relative motion maneuvers when coupled to an EKF and while relying only on relative angles and relative range measurements. Path constraints such as obstacle avoidance were handled. The approach presented only requires that a conventional quadratic program with linear inequality constraints be solved numerically. The details of this MPC approach differ from [115] in that this approach is based on a QP (versus linear programming (LP) in [115]), uses a reference governor style formulation of MPC cost for the rendezvous phase, explicitly handles LoS cone and obstacle avoidance constraints, and accounts for the capability of the attitude control system with an attitude penalty in the cost.

6.1.1 Future Work

Stability theory associated with the non-standard constraints, such as the time-varying hyperplane constraint, developed in this work remains a topic for future work.

Future work may consider the extension of MPC to formation control, where multiple spacecraft that fly in a cluster or formation must avoid each other while also avoiding debris. Other applications may include non-cooperative spacecraft docking and capture, and self-assembling spacecraft, where the components of a large space structure such as a telescope may be placed in orbit unassembled.

6.2 Safe Positively Invariant Sets

We described a technique for spacecraft maneuver planning that uses positively-invariant sets in order to avoid collisions with debris, while adhering to specified thrust limits. The approach is based on hopping between neighborhoods of equilibria in a virtual net, and maintaining the spacecraft trajectory within a tube formed by safe positively-invariant sets. For the case where thrust limits can be specified as polyhedral norm bounds, we have shown that the thrust limit on the growth distance can be easily computed; it is, in fact, feasible to perform these computations onboard a spacecraft in order to account for thruster failure or degradation. We described an extension in the presence of moving debris using contractive constraint admissible sets in order to avoid collisions. Lastly, we illustrated that the approach can be extended to include unmeasured bounded disturbances.

6.2.1 Future Work

Developing cost matrices that accurately capture the cost of maneuvers that do not travel through intermediate nodes is a topic for future investigation.

The constraint-admissible positively invariant set method can be extended to attitude control on SO(3) that is capable of handling inequality constraints associated with control authority limits and conical keep-out zones. The controller would use a supervisory strategy with an inner-loop Lyapunov SO(3)-based controller, such as the inertia-free controllers presented in this work, and an outer loop set-point guidance based on positively invariant constraint admissible sets with real-time graph search. The combined methodology would reduce the search space of possible attitude maneuver solutions and effectively handle constraints.

Future work will also consider ways to apply the safe positively invariant set method to non-spacecraft problems, such as ground and other autonomous vehicles.

6.3 Inertia-free Attitude Control Laws

Almost global stabilizability (that is, Lyapunov stability with almost global convergence) of spacecraft tracking is feasible without inertia information and with continuous feedback using magnetic actuation, reaction wheels, and CMGs. In addition, asymptotic rejection of harmonic disturbances (including constant disturbances as a special case) is possible with knowledge of the disturbance spectrum but without knowledge of either the amplitude or phase. Under these assumptions, the inertia-free control laws provide an alternative to

previous controllers that 1) require exact or approximate inertia information or 2) are based on attitude parameterizations such as quaternions that require discontinuous control laws or fail to be physically consistent (that is, specify different control torques for the same physical orientation).

6.3.1 Future Work

Future work may also consider additional effects, including time-varying inertia due, for example, to on-orbit deployment of structural components [116]; non-rigid motion due, for example, to structural modes and fuel slosh; multibody spacecraft involving articulated components; time delays in the feedback path that are possibly unknown and time varying; underactuation and undersensing possibly due to failed actuators and sensors; mixed actuation architectures, such as magnetic torquers and reaction wheels; alternative control devices, such as devices for atmospheric drag modification; and, finally, the interaction between attitude and orbital dynamics.

6.4 FPR Control

We have presented forward-in-time Riccati-based controllers for linear time-varying systems. The controllers do not require advance knowledge of the system dynamics and as such can be implemented in real time applications in which the system matrices are known at the present time but not in advance. Further, we have improved upon the results of [103, 104] in that we do not require a state transformation nor knowledge of the full state and, therefore, can utilize output-feedback. We have shown that if the closed-loop dynamics of the quasi-dual system are symmetric, then the forward-in-time controller is asymptotically stabilizing. We have also shown, using averaging theory, that there exists a sufficiently high frequency for which the dynamics of the closed-loop system become asymptotically stable. Finally, we have proven that there is separation of estimator and FPR regulator dynamics and thus FPR control may be used in an output feedback configuration.

The FPR controller was applied to the problem of spacecraft attitude regulation using only magnetic actuation. The FPR controller seems to be quite robust to many error sources. We have shown that the FPR controller is stabilizing for inertially pointing the spacecraft under actuator saturation, noisy magnetic-field measurements, and without using rate feedback. Additionally, we demonstrated nadir-pointing capabilities by spinning the spacecraft up from rest. The above results have been demonstrated with simulations on a fully nonlinear model.

We have shown that the FPR controller is stabilizing for rendezvous maneuvers on elliptic orbits with large initial conditions and in the presence of thrust limitations, including both saturation and intermittent thrust availability. This has been demonstrated with simulations on a high fidelity nonlinear model with J_2 and air drag perturbations.

6.4.1 Future Work

FPR control shows significant promise as a method for stabilization and robust control of general LTV systems without knowledge of future dynamics. Completing FPR control theory in the general case remains an open problem. Figure 6.1 provides a flow chart of conditions that lead to FPR stabilization.

Initial work has been performed to develop FPR control in discrete time. The discrete time FPR (DTFPR) equation is given by

$$P_{\mathrm{k}+1} = A^{\mathrm{T}} P_{\mathrm{k}} A - A^{\mathrm{T}} P_{\mathrm{k}} B (B^{\mathrm{T}} P_{\mathrm{k}} B + R_2)^{-1} B^{\mathrm{T}} P_{\mathrm{k}} A + R_1. \tag{6.1}$$

As in continuous time, $A_e = A_{c.f}^{\mathrm{T}}$ with appropriate substitutions. Therefore, the same analysis applies here. For example, in discrete time the state transition formula is given by

$$\Phi(k,i) \triangleq \begin{cases} A_{k-1}A_{k-2}...A_{i+1}A_i, & \text{for } k > i, \\ I, & \text{for } k = i, \\ \text{not defined}, & \text{for } k < i. \end{cases}$$

We can easily see that the state transition matrices for A_e and $A_{c,f}$ are not transposes of each other unless the A_i's commute.

Initial work has also been performed on the extension of FPR control to constant setpoint tracking problems. Like linear quadratic integral control, the plant is augmented with integrator states $\bar{x}(t)$, where $\dot{\bar{x}}(t) = y(t) = C(t)x(t)$. The augmented system is given by

$$\begin{bmatrix} \dot{x}(t) \\ \dot{\bar{x}}(t) \end{bmatrix} = \begin{bmatrix} A(t) & 0 \\ C(t) & 0 \end{bmatrix} \begin{bmatrix} x(t) \\ \bar{x}(t) \end{bmatrix} + \begin{bmatrix} B(t) \\ 0 \end{bmatrix} u(t),$$
$$y(t) = \begin{bmatrix} C(t) & 0 \end{bmatrix} \begin{bmatrix} x(t) \\ \bar{x}(t) \end{bmatrix}.$$

Despite FPR control's robustness to nonlinearities, an extension of the theory to a state-dependent formulation so that it may used directly on nonlinear systems without linearization is of interest. It would enable direct treatment of nonlinear applications as time-varying without resorting to the standard frozen time assumption used in traditional state-dependent

Riccati equations (SDRE).

Future work on spacecraft applications may consider nadir pointing on elliptic orbits, uncertain spacecraft inertia, and mixed actuation architectures, such as magnetic torquers and reaction wheels, for concurrent spacecraft attitude control and stored momentum management. Furthermore, FPR control might provide a new method to handle singularity escape for SGCMGs.

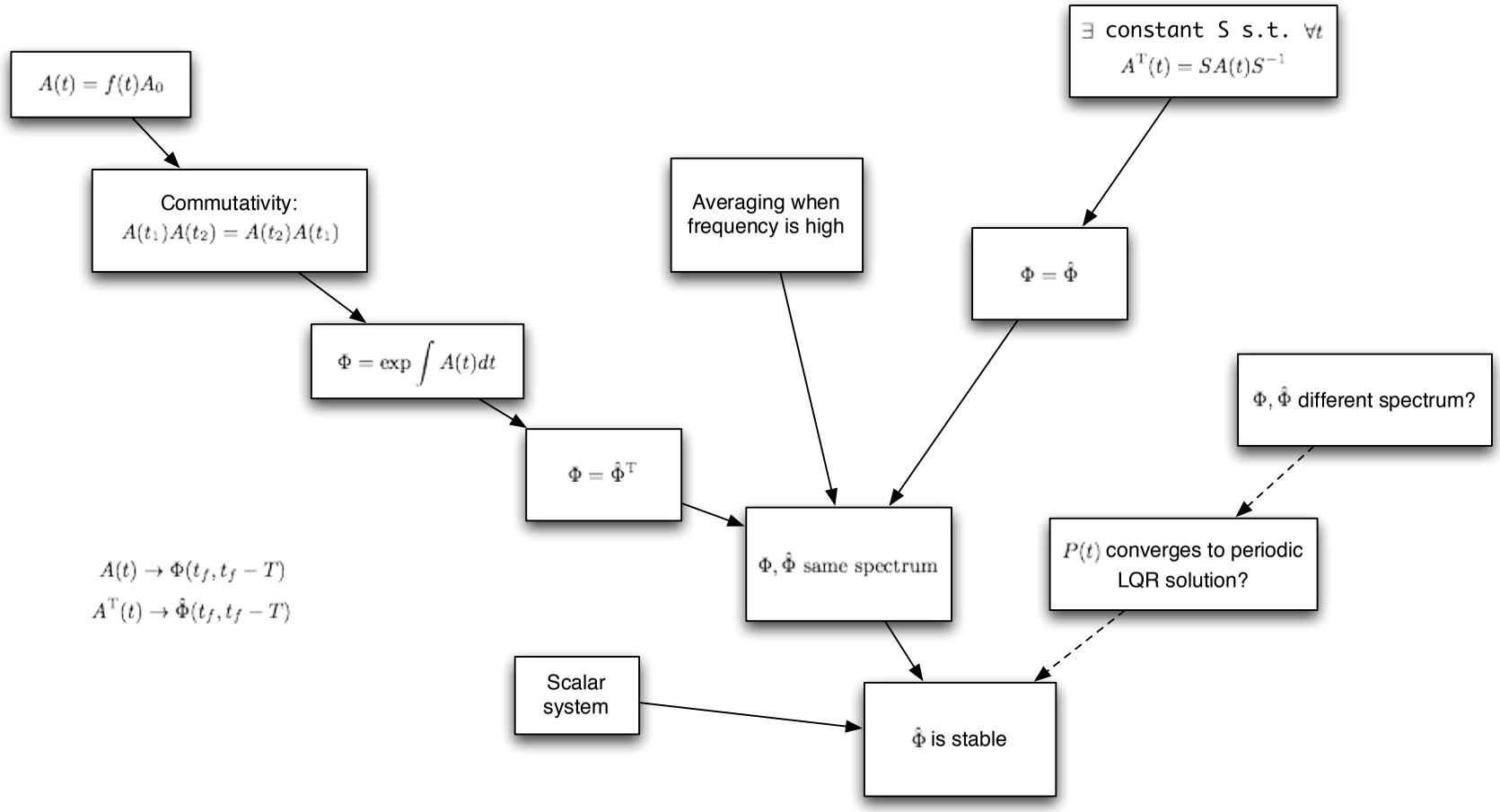

Figure 6.1: Flow chart of conditions that lead to FPR stabilization.

APPENDIX A

Spacecraft Relative Motion Orbital Dynamics

This chapter provides the necessary background on spacecraft relative motion orbital dynamics.

A.1 Relative Motion Model

In traditional relative motion problems, an approaching spacecraft is maneuvered close to a target spacecraft in a nominal orbit. The target spacecraft is assumed to be at the origin of Hill's frame. See Fig A.1.

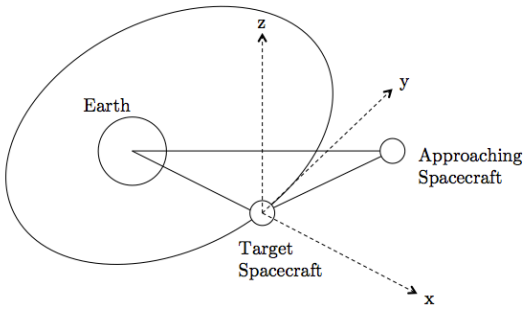

Figure A.1: Hill's frame.

A.1.1 Nonlinear equations of motion

The relative position vector of the spacecraft with respect to a target location on an orbit is expressed as

$$\delta\vec{r} = x\hat{i} + y\hat{j} + z\hat{k},$$

where x, y and z are the components of the position vector of the spacecraft relative to the target location and $\hat{i}$, $\hat{j}$, $\hat{k}$ are the unit vectors of the Hill's frame. The Hill's frame has its x-axis along the orbital radius, y-axis orthogonal to the x-axis and in the orbital plane, and z-axis orthogonal to orbital plane.

The position vector of the spacecraft with respect to the center of the Earth is given by $\vec{R} = \vec{R}_0 + \delta\vec{r}$, where $\vec{R}_0$ is the nominal orbital position vector. The nonlinear equation of motion for the spacecraft (relative to an inertial frame) is given by

$$\ddot{\vec{R}} = -\mu\frac{\vec{R}}{R^3} + \frac{1}{m_c}\vec{F}, \tag{A.1}$$

where $\vec{F}$ is the vector of external forces applied to the spacecraft, $R = |\vec{R}|$, m_c is the mass of the spacecraft, and μ is the gravitational constant.

A.1.2 Linearized equations on circular orbits

For $\delta r << R$, the linearized CWH equations [57] approximate the relative motion of the spacecraft on a circular orbit as

$$\begin{aligned} \ddot{x} - 3n^2x - 2n\dot{y} &= \frac{F_x}{m_c}, \\ \ddot{y} + 2n\dot{x} &= \frac{F_y}{m_c}, \\ \ddot{z} + n^2z &= \frac{F_z}{m_c}, \end{aligned} \tag{A.2}$$

where F_x, F_y, F_z are components of the external force vector (excluding gravity) acting on the spacecraft, and $n = \sqrt{\frac{\mu}{R_0^3}}$ denotes the mean motion of the nominal orbit. The linearized dynamics account for differences in gravity between the spacecraft and nominal orbital location, and for relative motion effects. The spacecraft relative motion dynamics in the orbital plane (x and y) and in the out-of-orbital plane (z) are decoupled. The in-plane dynamics are Lyapunov unstable (2 eigenvalues at the origin and 2 eigenvalues on the imaginary axis at n), while the out-of-plane dynamics are Lyapunov stable (2 eigenvalues on the imaginary axis at n). The in-plane dynamics are completely controllable from F_y input but are not controllable from F_x input. The out-of-plane dynamics are controllable from F_z input.

Assuming a sampling period of ΔT sec, we can convert the model (A.2) to a discrete-time form

$$X_{k+1} = AX_k + BU_k, \tag{A.3}$$

where $X_k = [x_k,\ y_k,\ z_k,\ \dot{x}_k,\ \dot{y}_k, \dot{z}_k]^{\mathrm{T}}$ is the state at time step $k \in Z^+$, $U_k = [F_{x,k},\ F_{y,k},\ F_{z,k}]^{\mathrm{T}}$ is the control vector of thrust forces at the time step $k \in Z^+$, and $A = \exp(A_c \Delta T)$, $B = \int_0^{\Delta T} \exp(A_c(\Delta T - \tau))d\tau B_c$ are the discretized matrices obtained based on the continuous-time system realization (A_c, B_c) in (A.2). Alternatively, the control vector U can represent an instantaneous change in the velocity of the spacecraft, Δv, induced by thrust, with an appropriately re-defined B-matrix,

$$B_{\Delta v} = e^{A_c \Delta T} \begin{bmatrix} 0 & 0 & 0 \\ 0 & 0 & 0 \\ 0 & 0 & 0 \\ 1 & 0 & 0 \\ 0 & 1 & 0 \\ 0 & 0 & 1 \end{bmatrix}.$$

A.1.3 Linearized equations on elliptic orbits

For generic elliptic orbits of arbitrary eccentricity, the linearization of these equations is described by linear time-varying equations [117],

$$\begin{aligned} \frac{F_x}{m_c} &= \delta\ddot{x} - \left(\frac{2\mu}{R_0^3(t)} + \frac{h^2}{R_0^4(t)}\right)\delta x + \frac{2\,(v_0(t)\cdot R_0(t))\,h}{R_0^4(t)}\delta y \\ &\quad - 2\frac{h}{R_0^2(t)}\delta\dot{y}, \\ \frac{F_y}{m_c} &= \delta\ddot{y} + \left(\frac{\mu}{R_0^3(t)} - \frac{h^2}{R_0^4(t)}\right)\delta y - \frac{2\,(v_0(t)\cdot R_0(t))\,h}{R_0^4(t)}\delta x \\ &\quad + 2\frac{h}{R_0^2(t)}\delta\dot{x}, \\ \frac{F_z}{m_c} &= \delta\ddot{z} + \frac{\mu}{R_0^3(t)}\delta z, \end{aligned} \tag{A.4}$$

where δx, δy and δz are (relative) coordinates of the spacecraft in Hill's frame, F_x, F_y, F_z are components of the external force vector (excluding gravity) acting on the spacecraft, h is the orbit angular momentum, $R_0(t)$ is the nominal time-varying orbital radius, and $v_0(t)$ is the nominal time-varying orbital velocity. Equation (A.2) assumes that the target spacecraft motion is in an ideal Keplerian orbit; if its motion is affected by perturbations, F_x, F_y, F_z have to be modified to account for these perturbations [2]. In the subsequent development, we assume that F_x, F_y, F_z are thrust forces that can be realized via on-board thruster on-off time allocation and attitude control system commands [2].

APPENDIX B

Spacecraft Attitude Dynamics

B.1 Spacecraft Model with Reaction Wheels

This section derives the equations of motion for a spacecraft with reaction wheels, while highlighting the underlying assumptions on wheel geometry, inertia, and attachment to the bus. Throughout this chapter, the vector $\vec{r}_{\mathrm{q/p}}$ denotes the position of point q relative to point p, the vector $\vec{v}_{\mathrm{q/p/X}} = \overset{\mathrm{X}\bullet}{\vec{r}}_{\mathrm{q/p}}$ denotes the velocity of point q relative to point p with respect to frame $\mathrm{F_X}$, and the vector $\vec{\omega}_{\mathrm{Y/X}}$ denotes the angular velocity of frame $\mathrm{F_Y}$ relative to frame $\mathrm{F_X}$. Note that $\vec{(\cdot)}$ denotes a coordinate-free (unresolved) vector. All frames are orthogonal and right handed.

Def. 1. Let $\mathrm{F_X}$ be a frame, let $\mathcal{B}$ be a collection of rigid bodies $\mathcal{B}_1, \ldots, \mathcal{B}_l$, and let p be a point. Then, the angular momentum of $\mathcal{B}$ relative to p with respect to $\mathrm{F_X}$ is defined by

$$\vec{H}_{\mathcal{B}/\mathrm{p}/\mathrm{X}} \triangleq \sum_{i=1}^{l} \vec{H}_{\mathcal{B}_i/\mathrm{p}/\mathrm{X}}, \tag{B.1}$$

where, for $i = 1, \ldots, l$, the angular momentum $\vec{H}_{\mathcal{B}_i/\mathrm{p}/\mathrm{X}}$ of $\mathcal{B}_i$ relative to p with respect to $\mathrm{F_X}$ is defined by

$$\vec{H}_{\mathcal{B}_i/\mathrm{p}/\mathrm{X}} \triangleq \int_{\mathcal{B}_i} \vec{r}_{\mathrm{d}m/\mathrm{p}} \times \vec{v}_{\mathrm{d}m/\mathrm{p}/\mathrm{X}} \, \mathrm{d}m. \tag{B.2}$$

The following properties of angular momentum are standard [118].

Lemma 1. Let $\mathcal{B}$ be a rigid body, let $\mathrm{F_X}$ and $\mathrm{F_Y}$ be frames, and let p be a point. Then,

$$\vec{H}_{\mathcal{B}/\mathrm{p}/\mathrm{X}} = \vec{I}_{\mathcal{B}/\mathrm{p}} \vec{\omega}_{\mathrm{Y/X}} + \vec{H}_{\mathcal{B}/\mathrm{p}/\mathrm{Y}}, \tag{B.3}$$

where the positive-definite, coordinate-free inertia tensor $\vec{I}_{\mathcal{B}/\mathrm{p}}$ is defined by

$$\vec{I}_{\mathcal{B}/\mathrm{p}} \triangleq \int_{\mathcal{B}} |\vec{r}_{\mathrm{d}m/\mathrm{p}}|^2 \vec{U} - \vec{r}_{\mathrm{d}m/\mathrm{p}} \vec{r}'_{\mathrm{d}m/\mathrm{p}} \, \mathrm{d}m, \tag{B.4}$$

and where $\vec{U}$ denotes the second-order identity tensor.

Lemma 2. Let $\mathcal{B}$ be a rigid body, let $\mathrm{F_X}$ and $\mathrm{F_Y}$ be frames, let $\mathrm{F_Y}$ be a body-fixed frame, and let p be a point that is fixed in $\mathcal{B}$. Then,

$$\vec{H}_{\mathcal{B}/\mathrm{p}/\mathrm{Y}} = 0 \tag{B.5}$$

and

$$\vec{H}_{\mathcal{B}/\mathrm{p}/\mathrm{X}} = \vec{I}_{\mathcal{B}/\mathrm{p}} \vec{\omega}_{\mathrm{Y}/\mathrm{X}}. \tag{B.6}$$

Lemma 3. Let $\mathrm{F_X}$ be a frame, let p be a point, let $\mathcal{B}$ be a rigid body with mass $m_{\mathcal{B}}$, and let c be the center of mass of $\mathcal{B}$. Then,

$$\vec{H}_{\mathcal{B}/\mathrm{p}/\mathrm{X}} = \vec{H}_{\mathcal{B}/\mathrm{c}/\mathrm{X}} + \vec{r}_{\mathrm{c}/\mathrm{p}} \times m_{\mathcal{B}} \vec{v}_{\mathrm{c}/\mathrm{p}/\mathrm{X}}. \tag{B.7}$$

Consider a spacecraft sc actuated by three axisymmetric wheels $\mathrm{w}_1, \mathrm{w}_2, \mathrm{w}_3$ attached to a rigid bus b in a known and linearly independent, but not necessarily orthogonal, configuration. Although the spacecraft is not a rigid body, the axial symmetry of the wheels implies that the center of mass c of the spacecraft is fixed in both the bus and the spacecraft. Since the inertia properties of the bus are assumed to be unknown, the principal axes of the bus are unknown and thus the wheel configuration has an arbitrary and unknown orientation relative to the principal axes of the bus. Each wheel is mounted so that it rotates about one of its own principal axes passing through its own center of mass. It is not assumed that the axis of rotation of each wheel passes through the center of mass of the bus, nor is it assumed that the wheels are balanced with respect to the bus in order to preserve the location of its center of mass. Thus the center of mass of the spacecraft and the center of mass of the bus may be distinct points, both of which are unknown.

Assume a bus-fixed frame $\mathrm{F_B}$, three wheel-fixed frames $\mathrm{F_{W_1}}, \mathrm{F_{W_2}}, \mathrm{F_{W_3}}$, whose x-axes are aligned with the rotation axes of $\mathrm{w}_1, \mathrm{w}_2, \mathrm{w}_3$, respectively, and an Earth-centered inertial frame $\mathrm{F_E}$. The angular momentum of the spacecraft relative to its center of mass with

respect to the inertial frame is given by

$$\vec{H}_{\mathrm{sc/c/E}} = \vec{H}_{\mathrm{b/c/E}} + \sum_{i=1}^{3} \vec{H}_{\mathrm{w}_i\mathrm{/c/E}}, \qquad \text{(Def. 1)} \tag{B.8}$$

where the angular momentum $\vec{H}_{\mathrm{b/c/E}}$ of the bus relative to c with respect to $\mathrm{F_E}$ is given by

$$\vec{H}_{\mathrm{b/c/E}} = \vec{I}_{\mathrm{b/c}} \vec{\omega}_{\mathrm{B/E}}, \qquad \text{(Lemma 2)} \tag{B.9}$$

where $\vec{I}_{\mathrm{b/c}}$ is the positive-definite inertia tensor of the bus relative to the center of mass of the spacecraft, and $\vec{\omega}_{\mathrm{B/E}}$ is the angular velocity of $\mathrm{F_B}$ with respect to $\mathrm{F_E}$. The angular momentum $\vec{H}_{\mathrm{w}_i\mathrm{/c/E}}$ of wheel i relative to the center of mass of the spacecraft with respect to the inertial frame is given by

$$\begin{aligned}
\vec{H}_{\mathrm{w}_i\mathrm{/c/E}} &= \vec{I}_{\mathrm{w}_i\mathrm{/c}} \vec{\omega}_{\mathrm{B/E}} + \vec{H}_{\mathrm{w}_i\mathrm{/c/B}} && \text{(Lemma 1)} \\
&= \vec{I}_{\mathrm{w}_i\mathrm{/c}} \vec{\omega}_{\mathrm{B/E}} + \vec{H}_{\mathrm{w}_i\mathrm{/c}_i\mathrm{/B}} + \vec{r}_{\mathrm{c}_i\mathrm{/c}} \times m_{\mathrm{w}_i} \vec{v}_{\mathrm{c}_i\mathrm{/c/B}} && \text{(Lemma 3)} \\
&= \vec{I}_{\mathrm{w}_i\mathrm{/c}} \vec{\omega}_{\mathrm{B/E}} + \vec{I}_{\mathrm{w}_i\mathrm{/c}_i} \vec{\omega}_{\mathrm{W}_i\mathrm{/B}}, && \text{(Lemma 2)}
\end{aligned} \tag{B.10}$$

where $\vec{I}_{\mathrm{w}_i\mathrm{/c}}$ is the inertia tensor of wheel i relative to the center of mass of the spacecraft, $\vec{I}_{\mathrm{w}_i\mathrm{/c}_i}$ is the inertia tensor of wheel i relative to the center of mass c_i of the ith wheel, and $\vec{\omega}_{\mathrm{W}_i\mathrm{/B}}$ is the angular velocity of wheel i relative to the bus. Thus (B.8) is given by

$$\vec{H}_{\mathrm{sc/c/E}} = \left(\vec{I}_{\mathrm{b/c}} + \sum_{i=1}^{3} \vec{I}_{\mathrm{w}_i\mathrm{/c}} \right) \vec{\omega}_{\mathrm{B/E}} + \sum_{i=1}^{3} \vec{I}_{\mathrm{w}_i\mathrm{/c}_i} \vec{\omega}_{\mathrm{W}_i\mathrm{/B}}. \tag{B.11}$$

Resolving $\vec{\omega}_{\mathrm{W}_i\mathrm{/B}}$ in $\mathrm{F_{W_i}}$ yields

$$\vec{\omega}_{\mathrm{W}_i\mathrm{/B}}\Big|_{\mathrm{W}_i} = \psi_i e_1, \tag{B.12}$$

where $e_1 = [1 \quad 0 \quad 0]^{\mathrm{T}}$ and ψ_i is the angular rate relative to $\mathrm{F_B}$ of the ith wheel about the x-axis of $\mathrm{F_{W_i}}$. Since $\mathrm{F_{W_i}}$ is aligned with the principal axes of wheel i, it follows that

$$\vec{I}_{\mathrm{w}_i\mathrm{/c}_i}\Big|_{\mathrm{W}_i} = \mathrm{diag}(\alpha_i, \beta_i, \beta_i). \tag{B.13}$$

Note that $\vec{\omega}_{\mathrm{W}_i\mathrm{/B}}$ is an eigenvector of $\vec{I}_{\mathrm{w}_i\mathrm{/c}_i}$ with eigenvalue α_i, that is, $\vec{I}_{\mathrm{w}_i\mathrm{/c}_i} \vec{\omega}_{\mathrm{W}_i\mathrm{/B}} =$

$\alpha_i \vec{\omega}_{\mathrm{W}_i/\mathrm{B}}$.

B.1.1 Spacecraft Equations of Motion

The equations of motion for a spacecraft with reaction wheels as described above are now derived. It follows from Newton's second law for rotation that

$$
\begin{aligned}
\vec{M}_{\mathrm{sc/c}} &= \overset{\mathrm{E}\bullet}{\vec{H}}_{\mathrm{sc/c/E}} \\
&= \overbrace{\left(\vec{I}_{\mathrm{b/c}} + \sum_{i=1}^{3} \vec{I}_{\mathrm{w}_i/\mathrm{c}}\right)\vec{\omega}_{\mathrm{B/E}}}^{\mathrm{E}\bullet} + \overbrace{\sum_{i=1}^{3} \vec{I}_{\mathrm{w}_i/\mathrm{c}_i}\vec{\omega}_{\mathrm{W}_i/\mathrm{B}}}^{\mathrm{E}\bullet} \\
&= \overbrace{\left(\vec{I}_{\mathrm{b/c}} + \sum_{i=1}^{3} \vec{I}_{\mathrm{w}_i/\mathrm{c}}\right)\vec{\omega}_{\mathrm{B/E}}}^{\mathrm{B}\bullet} + \vec{\omega}_{\mathrm{B/E}} \times \left(\vec{I}_{\mathrm{b/c}} + \sum_{i=1}^{3} \vec{I}_{\mathrm{w}_i/\mathrm{c}}\right)\vec{\omega}_{\mathrm{B/E}} \\
&\quad + \overbrace{\sum_{i=1}^{3} \vec{I}_{\mathrm{w}_i/\mathrm{c}_i}\vec{\omega}_{\mathrm{W}_i/\mathrm{B}}}^{\mathrm{B}\bullet} + \vec{\omega}_{\mathrm{B/E}} \times \sum_{i=1}^{3} \vec{I}_{\mathrm{w}_i/\mathrm{c}_i}\vec{\omega}_{\mathrm{W}_i/\mathrm{B}} \\
&= \left(\vec{I}_{\mathrm{b/c}} + \sum_{i=1}^{3} \vec{I}_{\mathrm{w}_i/\mathrm{c}}\right)\overset{\mathrm{B}\bullet}{\vec{\omega}}_{\mathrm{B/E}} + \sum_{i=1}^{3} \alpha_i \overset{\mathrm{B}\bullet}{\vec{\omega}}_{\mathrm{W}_i/\mathrm{B}} \\
&\quad + \vec{\omega}_{\mathrm{B/E}} \times \left(\left(\vec{I}_{\mathrm{b/c}} + \sum_{i=1}^{3} \vec{I}_{\mathrm{w}_i/\mathrm{c}}\right)\vec{\omega}_{\mathrm{B/E}} + \sum_{i=1}^{3} \alpha_i \vec{\omega}_{\mathrm{W}_i/\mathrm{B}}\right).
\end{aligned}
\tag{B.14}
$$

To resolve (B.14) in $\mathrm{F_B}$, the following notation is used:

$$J_\mathrm{b} \triangleq \vec{I}_{\mathrm{b/c}}\Big|_\mathrm{B}, \qquad J_{\mathrm{w}_i} \triangleq \vec{I}_{\mathrm{w}_i/\mathrm{c}}\Big|_\mathrm{B},$$

$$J_\mathrm{w} \triangleq \sum_{i=1}^{3} \vec{I}_{\mathrm{w}_i/\mathrm{c}}\Big|_\mathrm{B}, \qquad J_\mathrm{sc} \triangleq J_\mathrm{b} + J_\mathrm{w},$$

$$\omega \triangleq \vec{\omega}_{\mathrm{B/E}}\Big|_\mathrm{B}, \qquad \dot{\omega} \triangleq \overset{\mathrm{B}\bullet}{\vec{\omega}}_{\mathrm{B/E}}\Big|_\mathrm{B},$$

$$\nu_i \triangleq \vec{\omega}_{\mathrm{W}_i/\mathrm{B}}\Big|_\mathrm{B}, \qquad \dot{\nu}_i \triangleq \overset{\mathrm{B}\bullet}{\vec{\omega}}_{\mathrm{W}_i/\mathrm{B}}\Big|_\mathrm{B},$$

$$\tau_\mathrm{dist} \triangleq \vec{M}_{\mathrm{sc/c}}\Big|_\mathrm{B}.$$

The vector τ_dist represents disturbance torques, that is, all external torques applied to the spacecraft aside from control torques. Disturbance torques may be due to gravity gradients, solar pressure, atmospheric drag, or the ambient magnetic field.

As in (B.12), the angular acceleration $\dot{\nu}_i$ of each wheel has one degree of freedom. In $\mathrm{F_{W}}_i$,

$$\overset{\mathrm{B}\bullet}{\vec{\omega}}_{\mathrm{W}_i/\mathrm{B}}\Big|_{\mathrm{W}_i} = \overset{\mathrm{W}_i\bullet}{\vec{\omega}}_{\mathrm{W}_i/\mathrm{B}}\Big|_{\mathrm{W}_i} = \dot{\psi}_i e_1. \tag{B.15}$$

Thus,

$$\dot{\nu}_i = \overset{\mathrm{B}\bullet}{\vec{\omega}}_{\mathrm{W}_i/\mathrm{B}}\Big|_\mathrm{B} = \mathcal{O}_{\mathrm{B/W}_i}\, \overset{\mathrm{B}\bullet}{\vec{\omega}}_{\mathrm{W}_i/\mathrm{B}}\Big|_{\mathrm{W}_i} = \mathcal{O}_{\mathrm{B/W}_i}\dot{\psi}_i e_1, \tag{B.16}$$

where the proper orthogonal matrix $\mathcal{O}_{\mathrm{B/W}_i} \in \mathbb{R}^{3\times 3}$ is the orientation matrix that transforms components of a vector resolved in $\mathrm{F_{W}}_i$ into the components of the same vector resolved in $\mathrm{F_B}$.

With the above notation, resolving (B.14) in $\mathrm{F_B}$ yields

$$\tau_{\mathrm{dist}} = (J_{\mathrm{b}} + J_{\mathrm{w}})\,\dot{\omega} + \sum_{i=1}^{3} \alpha_i \dot{\nu}_i + \omega \times \left((J_{\mathrm{b}} + J_{\mathrm{w}})\,\omega + \sum_{i=1}^{3} \alpha_i \nu_i \right)$$

$$= J_{\mathrm{sc}}\dot{\omega} + \sum_{i=1}^{3} \alpha_i \mathcal{O}_{\mathrm{B/W_1}} \dot{\psi}_i e_1 + \omega \times \left(J_{\mathrm{sc}}\omega + \sum_{i=1}^{3} \alpha_i \mathcal{O}_{\mathrm{B/W_1}} \psi_i e_1 \right)$$

$$= J_{\mathrm{sc}}\dot{\omega} + J_\alpha \dot{\nu} + \omega \times (J_{\mathrm{sc}}\omega + J_\alpha \nu), \tag{B.17}$$

where

$$J_\alpha \triangleq \begin{bmatrix} \alpha_1 \mathcal{O}_{\mathrm{B/W_1}} e_1 & \alpha_2 \mathcal{O}_{\mathrm{B/W_2}} e_1 & \alpha_3 \mathcal{O}_{\mathrm{B/W_3}} e_1 \end{bmatrix}, \tag{B.18}$$

$\nu \triangleq [\psi_1 \quad \psi_2 \quad \psi_3]^{\mathrm{T}}$, and $\dot{\nu} \triangleq [\dot{\psi}_1 \quad \dot{\psi}_2 \quad \dot{\psi}_3]^{\mathrm{T}}$. Rearranging (B.17) and choosing the control input u to be $\dot{\nu}$ yields the equations of motion for a spacecraft with reaction wheels, which have the form

$$J_{\mathrm{sc}}\dot{\omega} = (J_{\mathrm{sc}}\omega + J_\alpha \nu) \times \omega - J_\alpha u + \tau_{\mathrm{dist}}, \tag{B.19}$$

$$\dot{\nu} = u. \tag{B.20}$$

In practice, a servo loop is closed around each reaction wheel in order to produce the desired wheel angular accelerations given in (B.20).

Instead of commanding wheel angular accelerations by implementing servo loops, motor torque commands can be used. To determine the relationship between the desired angular acceleration and the required motor torque, the dynamic equations for each wheel must

be derived. It follows that

$$\begin{aligned}
\vec{M}_{\mathrm{w}_i/\mathrm{c}_i} &= \overset{\mathrm{E}\bullet}{\vec{H}}_{\mathrm{w}_i/\mathrm{c}_i/\mathrm{E}} \\
&= \overbrace{\vec{I}_{\mathrm{w}_i/\mathrm{c}_i}\vec{\omega}_{\mathrm{W}_i/\mathrm{E}}}^{\mathrm{E}\bullet} \\
&= \vec{I}_{\mathrm{w}_i/\mathrm{c}_i}\,\overset{\mathrm{W}\bullet}{\vec{\omega}}_{\mathrm{W}_i/\mathrm{E}} + \vec{\omega}_{\mathrm{W}_i/\mathrm{E}} \times \vec{I}_{\mathrm{w}_i/\mathrm{c}_i}\vec{\omega}_{\mathrm{W}_i/\mathrm{E}} \\
&= \vec{I}_{\mathrm{w}_i/\mathrm{c}_i}\left(\overset{\mathrm{B}\bullet}{\vec{\omega}}_{\mathrm{B}/\mathrm{E}} + \overset{\mathrm{B}\bullet}{\vec{\omega}}_{\mathrm{W}_i/\mathrm{B}} - \omega_{\mathrm{W}_i/\mathrm{B}} \times \omega_{\mathrm{B}/\mathrm{E}}\right) \\
&\quad + \left(\vec{\omega}_{\mathrm{B}/\mathrm{E}} + \vec{\omega}_{\mathrm{W}_i/\mathrm{B}}\right) \times \vec{I}_{\mathrm{w}_i/\mathrm{c}_i}\left(\vec{\omega}_{\mathrm{B}/\mathrm{E}} + \vec{\omega}_{\mathrm{W}_i/\mathrm{B}}\right).
\end{aligned} \tag{B.21}$$

Resolving (B.21) in F_B and projecting it along each motor axis yields

$$\tau_{\mathrm{motor},i} = e_i^{\mathrm{T}}\left[J_{\mathrm{w}_i/\mathrm{c}_i}(\dot{\omega} + \dot{\nu}_i - \nu_i \times \omega) + (\omega + \nu_i) \times J_{\mathrm{w}_i/\mathrm{c}_i}(\omega + \nu_i)\right], \tag{B.22}$$

where $J_{\mathrm{w}_i/\mathrm{c}_i} \triangleq \vec{I}_{\mathrm{w}_i/\mathrm{c}_i}\Big|_{\mathrm{B}}$. Although (B.22) can be used for torque control, the measurements of $\omega, \dot{\omega}, \nu_i$, and $\dot{\nu}_i$ needed to implement it demonstrate why reaction wheels are typically angular-acceleration commanded and feedback-controlled rather than torque-commanded.

B.1.2 Specialization: principal-axis alignment

As in ref. [119], the equations of motion (B.19), (B.20) are now specialized by assuming that the principal axes of the bus are aligned with the rotational axes of the wheels, that the wheels are mass-balanced relative to the center of mass of the bus so that the center of mass of the spacecraft coincides with the center of mass of the bus, and, finally, that the moments of inertia $\beta_1, \beta_2, \beta_3$ of the wheels are lumped into the bus inertia $J_\mathrm{b} = \mathrm{diag}(J_{\mathrm{b}_1}, J_{\mathrm{b}_2}, J_{\mathrm{b}_3})$, where $J_{\mathrm{b}_1} \triangleq J_{\mathrm{b}_1} + \beta_2 + \beta_3$, $J_{\mathrm{b}_2} \triangleq J_{\mathrm{b}_2} + \beta_1 + \beta_3$, and $J_{\mathrm{b}_3} \triangleq J_{\mathrm{b}_3} + \beta_1 + \beta_2$. In this configuration,

$$\mathcal{O}_{\mathrm{B}/\mathrm{W}_1} e_1 = \begin{bmatrix} 1 \\ 0 \\ 0 \end{bmatrix}, \quad \mathcal{O}_{\mathrm{B}/\mathrm{W}_2} e_1 = \begin{bmatrix} 0 \\ 1 \\ 0 \end{bmatrix}, \quad \mathcal{O}_{\mathrm{B}/\mathrm{W}_3} e_1 = \begin{bmatrix} 0 \\ 0 \\ 1 \end{bmatrix}. \tag{B.23}$$

Therefore, $J_\alpha = J_\mathrm{w} = \mathrm{diag}(\alpha_1, \alpha_2, \alpha_3)$. Rewriting the equations of motion (B.19), (B.20) as

$$J_\mathrm{b}\dot{\omega} = ((J_\mathrm{b} + J_\alpha)\omega + J_\alpha \nu) \times \omega + u + \tau_\mathrm{dist}, \tag{B.24}$$

$$-u = J_\alpha(\dot{\omega} + \dot{\nu}), \tag{B.25}$$

and simplifying, yields

$$J_{\mathrm{b}_1}\dot{\omega}_1 = \left(J_{\mathrm{b}_2} - J_{\mathrm{b}_3}\right)\omega_2\omega_3 + \alpha_2\omega_3(\omega_2 + \nu_2) - \alpha_3\omega_2(\omega_3 + \nu_3) + u_1 + \tau_{\mathrm{dist}_1}, \tag{B.26}$$

$$J_{\mathrm{b}_2}\dot{\omega}_2 = \left(J_{\mathrm{b}_3} - J_{\mathrm{b}_1}\right)\omega_3\omega_1 + \alpha_3\omega_1(\omega_3 + \nu_3) - \alpha_1\omega_3(\omega_1 + \nu_1) + u_2 + \tau_{\mathrm{dist}_2}, \tag{B.27}$$

$$J_{\mathrm{b}_3}\dot{\omega}_3 = \left(J_{\mathrm{b}_1} - J_{\mathrm{b}_2}\right)\omega_1\omega_2 + \alpha_1\omega_2(\omega_1 + \nu_1) - \alpha_2\omega_1(\omega_2 + \nu_2) + u_3 + \tau_{\mathrm{dist}_3}, \tag{B.28}$$

$$-u_1 = \alpha_1(\dot{\omega}_1 + \dot{\nu}_1), \tag{B.29}$$

$$-u_2 = \alpha_2(\dot{\omega}_2 + \dot{\nu}_2), \tag{B.30}$$

$$-u_3 = \alpha_3(\dot{\omega}_3 + \dot{\nu}_3), \tag{B.31}$$

which are equations (7.59) and (7.60) of ref [119].

APPENDIX C

Code

This chapter provides relevant code for the work presented in this dissertation.

C.1 Polyhedral Cone Approximation

The following code generates a polyhedral approximation of a cone.

```
function [Acone,bcone] = generateCone(gamma,N,normal,v)
% ++++++++++++++++++++++++++++++++++++++++++++++++++++++
% Generate a polyhedral approximation for a rotated and
% translated cone aligned with n-vector and vertex at v
% of x-y-z coordinate frame
% ++++++++++++++++++++++++++++++++++++++++++++++++++++++

if norm([0,1,0]'-normal)<1e-6,
    [Acone, bcone] = generateBasicCone(gamma,N);
else,
    axisOfRotation = cross([0,1,0],normal);
    axisOfRotation = axisOfRotation/norm(axisOfRotation);

    angleOfRotation = acos(dot(normal,[0,1,0])/norm(normal));

    e = axisOfRotation;
    S = [0, -e(3), e(2); e(3), 0, -e(1); -e(2), e(1), 0];
    R = expm(-S*angleOfRotation);

    [Acone, bcone] = generateBasicCone(gamma,N);
    Acone = Acone*R;
end;
```

```
bcone = bcone + Acone*v(:);
return

function [Acone,bcone] = generateBasicCone(gamma,N)
% ++++++++++++++++++++++++++++++++++++++++++++++++++++++++
% Generate a polyhedral approximation for a base cone
% aligned with y-axis and vertex at the origin of x-y-z
% coordinate frame
% ++++++++++++++++++++++++++++++++++++++++++++++++++++++++

% ++ generate a list of vectors
x = []; y = []; z = []; n = []; Acone = []; bcone = [];

for (i=1:1:N),
    theta(i)= 2*pi/(N - 1)*(i - 1);
    x(i)    = tan(gamma)*cos(theta(i));
    z(i)    = tan(gamma)*sin(theta(i));
    y(i)    = 1;

    if i>1,
        n(:,i-1)=cross([x(i - 1),y(i - 1),z(i - 1)],
         [x(i),y(i),z(i)])';
        n(:,i-1)=n(:,i - 1)/norm(n(:,i - 1));

        Acone=[Acone; n(:,i - 1)'];
        bcone=[bcone; 0];
    end;
end

return
```

C.2 CVXGEN Code for Rendezvous and Docking QPs

The rendezvous phase CVXGEN code is given by,

```
dimensions
  m = 3  # inputs.
  n = 6  # states.
```

```
  T = 25  # horizon.

end

parameters
  A (n,n)  # dynamics matrix.
  B (n,m)  # transfer matrix.
  Q (n,n) psd diagonal # state cost.
  Q_final (n,n) psd # final state cost.
  R (m,m) psd diagonal # input cost.
  P (n,n) psd diagonal

  x[0] (n)  # initial state.
  u_max nonnegative  # control limit.
  normal[t] (m), t=1..T
  center_of_debris[t] (m), t=1..T
  epsilon nonnegative

end

variables
  x[t] (n), t=1..T+1  # state.
  u[t] (m), t=0..T  # input.
  xs (n)
  us (m)
end

minimize
  sum[t=0..T](quad(x[t]-xs, Q) + quad(u[t]-us, R))
   + quad(x[T+1]-xs, Q_final) + quad(xs, P)

subject to
  x[t+1] == A*x[t] + B*u[t], t=0..T  # dynamics constraints.
  u[t] <= u_max, t=0..T  # maximum input box constraint.
  -u[t] <= u_max, t=0..T  # maximum input box constraint.
  xs == A*xs + B*us
  normal[t][1]*(center_of_debris[t][1]-x[t][1])
   + normal[t][2]*(center_of_debris[t][2]-x[t][2])
```

```
   + normal[t][3]*(center_of_debris[t][3]-x[t][3])
   + epsilon <= 0, t=1..T
end
```

The docking phase CVXGEN code is given by,

```
dimensions
  m = 3  # inputs.
  n = 6  # states.
  T = 29  # horizon.
end

parameters
  A (n,n)  # dynamics matrix.
  Acone1 (10)
  Acone2 (10)
  Acone3 (10)
  B (n,m)  # transfer matrix.
  Q (n,n) psd diagonal # state cost.
  Q_final (n,n) psd diagonal # final state cost.
  R (m,m) psd diagonal # input cost.
  Ra (m,m)  psd diagonal
  bcone (10)
  x[0] (n)  # initial state.
  u_max nonnegative  # control limit.
  eps[t], t=0..T  # input.
  pos
  un1 (m)
end

variables
  x[t] (n), t=1..T+1  # state.
  u[t] (m), t=0..T  # input.
end

minimize
  sum[t=0..T](quad(x[t], Q) + quad(u[t], R))
   + quad(x[T+1],Q_final) +  quad((u[0] - un1), Ra)
   + sum[t=1..T]( 10*sum(pos(Acone1*x[t][1]
```

```
    + Acone2*x[t][2]+Acone3*x[t][3]-bcone))
    + quad((u[t] - u[t-1]), Ra) )
subject to
  x[t+1] == A*x[t] + B*u[t], t=0..T  # dynamics constraints.
  u[t] <= u_max, t=0..T  # maximum input box constraint.
  -u[t] <= u_max, t=0..T  # maximum input box constraint.
  u[t] <= eps[t], t=0..T-1
  x[t+1] >= pos, t=0..T
end
```

BIBLIOGRAPHY

[1] Woffinden, D. C., Geller, D. K., Mosher, T., Kennedy, S., D'Souza, C., Lovell, T. A., and Sauter, L. M., "Navigating the road to autonomous orbital rendezvous," *Journal of Spacecraft and Rockets*, Vol. 44, No. 4, 2007, pp. 898–909.

[2] Fehse, W., *Automated Rendezvous and Docking of Spacecraft*, Cambridge Aerospace Series, 2003.

[3] Breger, L. and How, J., "Safe trajectories for autonomous rendezvous of spacecraft," *Journal of Guidance, Control, and Dynamics*, Vol. 31, No. 5, 2008.

[4] Alfriend, K. T., Vadali, S. R., Gurfil, P., How, J. P., and Breger, L. S., *Spacecraft Formation Flying*, Elsevier Astrodynamics Series, 2010.

[5] Clohessy, W. and Wiltshire, R., "Terminal guidance system for satellite rendezvous," *J. Aerospace Sci*, Vol. 27, No. 9, 1960, pp. 653–658.

[6] Goodman, J., "History of space shuttle rendezvous and proximity operations," *Jounal of Spacecraft and Rockets*, Vol. 43, No. 5, 2006, pp. 944–959.

[7] Luo, Y. and Tang, G., "Spacecraft optimal rendezvous controller design using simulated annealing," *Aerospace Science and Technology*, Vol. 9, 2005, pp. 732–737.

[8] Miele, A., Weeks, M., and Circia, M., "Optimal trajectories for spacecraft rendezvous," *Journal of Optimization Theory and Applications*, Vol. 132, No. 3, 2007, pp. 353–376.

[9] Kong, E., Nolet, S., and Miller, D., "Autonomous docking algorithm development and experimentation using the SPHERES testbed." *Proc. SPIE Defense and Security*, 2004.

[10] Polites, M., "Technology of automated rendezvous and capture in space," *Jounal of Spacecraft and Rockets*, Vol. 36, No. 2, 1999, pp. 280–291.

[11] "XSS-11 micro satellite," http://www.kirtland.af.mil/shared/media/document/AFD-070404-108.pdf.

[12] Park, H., Di Cairano, S., and Kolmanovsky, I. V., "Model Predictive Control of spacecraft docking with a non-rotating platform," *Proceedings of the 18th IFAC World Congress*, 2011.

[13] Park, H., Di Cairano, S., and Kolmanovsky, I. V., "Model Predictive Control for spacecraft rendezvous and docking with a rotating/tumbling platform and for debris avoidance," *Proceedings of American Control Conference*, 2011.

[14] Park, H., Di Cairano, S., and Kolmanovsky, I. V., "Linear quadratic Model Predicitve Control approach to spacecraft rendezvous and docking," *Proceedings of 21st AAS/AAIA Space Flight Mechanics Meeting*, 2011.

[15] Richards, A. and How, J., "Performance evaluation of rendezvous using model predictive control," *AIAA Guidance, Navigation, and Control Conference*, 2003.

[16] Singh, L., Bortolami, S., and Page, L., "Optimal guidance and thruster control in orbital approach and rendezvous for docking using model predictive control," *AIAA Guidance, Navigation, and Control Conference*, 2010.

[17] Holzinger, M., DiMatteo, J., Schwartz, J., and Milam, M., "Passively safe receding horizon control for satellite proximity operations," *47th IEEE Conf. on Decision and Control*, 2008, pp. 3433–3440.

[18] for the Assessment of NASA's Orbital Debris Programs; National Research Council, C., *Limiting Future Collision Risk to Spacecraft:An Assessment of NASA's Meteoroid and Orbital Debris Programs*, The National Academies Press, 2011.

[19] LaValle, S. M., *Planning Algorithms*, Cambridge University Press, 1996.

[20] Maia, M. H. and Galvao, R. K. H., "On the use of mixed-integer linear predictive control with avoidance constraints," *International Journal of Robust and Nonlinear Control*, Vol. 19, 2008, pp. 822–828.

[21] Ranieri, C., "Path-Constrained Trajectory Optimization for Proximity Operations," *AIAA/AAS Astrodynamics Specialist Conference*, Honolulu, HI, August 2008.

[22] Betts, J. T. and Huffman, W. P., "Sparse optimal control software SOCS," *Mathematics and Engineering Analysis Technical Document MEA-LR-085, Boeing Information and Support Services, The Boeing Company, PO Box*, Vol. 3707, 1997, pp. 98124–2207.

[23] Epenoy, R., "Fuel optimization for continuous-thrust orbital rendezvous with collision avoidance constraint," *Journal of Guidance, Control, and Dynamics*, Vol. 34, No. 2, 2011.

[24] Martinson, N., "Obstacle avoidance guidance and control algorithms for spacecraft maneuvers,"," *Proceedings of AIAA Guidance, Navigation, and Control Conference*, Chicago, IL, August 2009.

[25] Sanchez-Ortiz, N., Bello-Mora, M., and Klinkrad, H., "Collision avoidance manoeuvres during spacecraft mission lifetime: Risk reduction and required Δ V," *Advances in Space Research*, Vol. 38, 2006.

[26] Martinson, N., Munoz, J., and Wiens, G., "A new method of guidance control for autonomous rendezvous in a cluttered space environment," *Proceedings of AIAA Guidance, Navigation, and Control Conference*, Hilton Head, SC, August 2007.

[27] Mueller, J. B., Griesemer, P. R., and Thomas, S., "Avoidance maneuver planning incorporating station-keeping constraints and automatic relaxation," *AIAA Infotech@Aerospace 2010*, Atlanta, GA, April 2010.

[28] Ulybyshev, Y., "Trajectory optimization for spacecraft proximity operations with constraints," *AIAA Guidance, Navigation, and Control Conference*, Portland, OR, August 2011.

[29] Richards, A., Schouwenaars, T., How, J., and Feron, E., "Spacecraft trajectory planning with avoidance constraints using mixed-integer linear programming," *AIAA Journal of Guidance, Control, and Dynamics*, Vol. 25, No. 4, August 2002.

[30] Mueller, J. B., "Onboard planning of collision avoidance maneuvers using robust optimization," *AIAA Infotech@ Aerospace Conference, Seattle, AIAA, Washington, DC*, Seattle, WA, April 2009.

[31] Ahmed, J., Coppola, V. T., and Bernstein, D. S., "Asymptotic Tracking of Spacecraft Attitude Motion with Inertia Matrix Identification," *AIAA Journal of Guidance, Control, and Dynamics*, Vol. 21, 1998, pp. 684–691.

[32] Sanyal, A. K., Fosbury, A., Chaturvedi, N., and Bernstein, D. S., "Inertia-Free Spacecraft Attitude Tracking with Disturbance Rejection and Almost Global Stabilization," *AIAA J. Guid. Contr. Dyn*, Vol. 32, 2009, pp. 1167–1178.

[33] Junkins, J. L., Akella, M. R., and Robinett, R., "Nonlinear Adaptive Control of Spacecraft Maneuvers," *AIAA Journal of Guidance, Control, and Dynamics*, Vol. 20, 1997, pp. 1104–1110.

[34] Junkins, J. L., Akella, M. R., and Robinett, R. D., "Nonlinear Adaptive Control of Spacecraft Maneuvers," *AIAA J. Guid. Contr. Dyn.*, Vol. 20, 1997, pp. 1104–1110.

[35] Egeland, O. and Godhavn, J.-M., "Passivity-Based Adaptive Attitude Control of a Rigid Spacecraft," *IEEE Transactions on Automatic Control*, Vol. 39, 1994, pp. 842–846.

[36] Wen, J. T.-Y. and Kreutz-Delgado, K., "The Attitude Control Problem," *IEEE Transactions on Automatic Control*, Vol. 36, 1991, pp. 1148–1162.

[37] Bhat, S. P. and Bernstein, D. S., "A Topological Obstruction to Continuous Global Stabilization of Rotational Motion and the Unwinding Phenomenon," *Sys. Contr. Lett.*, Vol. 39, 2000, pp. 63–70.

[38] Wie, B. and Barba, P. M., "Quaternion Feedback for Spacecraft Large Angle Maneuvers," *AIAA Journal of Guidance, Control, and Dynamics*, Vol. 8, 1985, pp. 360–365.

[39] Joshi, S. M., Kelkar, A. G., and Wen, J. T., "Robust Attitude Stabilization using Nonlinear Quaternion Feedback," *IEEE Transactions on Automatic Control*, Vol. 40, 1995, pp. 1148–1161.

[40] Crassidis, J. L., Vadali, S. R., and Markley, F. L., "Optimal Variable-Structure Control Tracking of Spacecraft Maneuvers," *AIAA Journal of Guidance, Control, and Dynamics*, Vol. 23, 2000, pp. 564–566.

[41] Mayhew, C. G., Sanfelice, R. G., and Teel, A. R., "Quaternion-Based Hybrid Control for Robust Global Attitude Tracking," *IEEE Trans. Autom. Contr.*, Vol. 56, 2011, pp. 2555–2566.

[42] Chaturvedi, N., Sanyal, A., and McClamroch, N. H., "Rigid Body Attitude Control: Using rotation matrices for continuous, singularity-free control laws," *IEEE Control Systems Magazine*, Vol. 31, No. 3, 2011, pp. 30–51.

[43] Chaturvedi, N. A., McClamroch, N. H., and Bernstein, D. S., "Asymptotic Smooth Stabilization of the Inverted 3D Pendulum," *IEEE Transactions on Automatic Control*, Vol. 54, 2009, pp. 1204–1215.

[44] Chaturvedi, N. A., McClamroch, N. H., and Bernstein, D. S., "Stabilization of a 3D Axially Symmetric Pendulum," *Automatica*, Vol. 44, 2008, pp. 2258–2265.

[45] Wertz, J. R., *Spacecraft Attitude Determination and Control*, Vol. 73, Kluwer Academic Pub, 1978.

[46] Sidi, M. J., *Spacecraft Dynamics and Control*, Cambridge University Press, 1997.

[47] Bhat, S., "Controllability of Nonlinear Time-Varying Systems: Applications to Spacecraft Attitude Control Using Magnetic Actuation," *IEEE Transactions on Automatic Control*, Vol. 50, No. 11, 2005, pp. 1725–1735.

[48] Silani, E. and Lovera, M., "Magnetic spacecraft attitude control: a survey and some new results," *Control Engineering Practice*, Vol. 137, 2005, pp. 357–371.

[49] Wisniewski, R., "Linear Time Varying Approach to Satellite Attitude Control Using Only Electromagnetic Actuation," *Proc. of the AIAA Guidance, Navigation, and Control Conf*, August 1997, pp. 243–251.

[50] Lovera, M., Marchi, E. D., and Bittanti, S., "Periodic attitude control techniques for small satellites with magnetic actuators," *IEEE Transactions on Control Systems Technology*, Vol. 10, No. 1, 2002, pp. 90–95.

[51] Psiaki, M., "Magnetic torquer attitude control via asymptotic periodic linear quadratic regulation," *Journal of Guidance, Control and Dynamics*, Vol. 24, No. 2, 2001, pp. 386–394.

[52] Lovera, M. and Astolfi, A., "Global magnetic attitude control of spacecraft," *Proc. Conf. Dec. Contr*, 2004, pp. 267–272.

[53] Finlay, C. C. and et al., "International Geomagnetic Reference Field: the eleventh generation," *Geophysical Journal International*, Vol. 183, No. 3, 2010, pp. 1216–1230.

[54] Lowes, F. J., "The International Geomagnetic Reference Field: A 'Health' Warning," http://www.ngdc.noaa.gov/IAGA/vmod/igrfhw.html.

[55] Ferramosca, A., Limon, D., Alvarado, I., Alamo, T., and Camacho, E., "MPC for tracking with optimal closed-loop performance," *Automatica*, Vol. 45, No. 8, 2009, pp. 1975–1978.

[56] Kolmanovsky, I. and Gilbert, E., "Theory and computation of disturbance invariant sets for discrete-time linear systems," *Mathematical Problems in Engineering*, Vol. 4, No. 4, 1998, pp. 317–367.

[57] Wie, B., *Spacecraft Dynamics and Control*, AIAA, Reston, VA, 2nd ed., 2010.

[58] Fortescue, P., Swinerd, G., and Stark, J., *Spacecraft Systems Engineering*, Wiley, 2011.

[59] Keerthi, S. and Gilbert, E. G., "Optimal infinite-horizon feedback laws for a general class of constrained discrete-time systems: Stability and moving-horizon approximations," *Journal of optimization theory and applications*, Vol. 57, No. 2, 1988, pp. 265–293.

[60] Camacho, E. F., Bordons, C., Camacho, E. F., and Bordons, C., *Model predictive control*, Vol. 303, Springer Berlin, 1999.

[61] Brand, M., Shilpiekandula, V., Yao, C., Bortoff, S. A., Nishiyama, T., Yoshikawa, S., and Iwasaki, T., "A parallel quadratic programming algorithm for model predictive control," *Proc. 18th World Congress of the International Federation of Automatic Control (IFAC)*, Vol. 18, 2011, pp. 1031–1039.

[62] Johansen, T. A., Fossen, T. I., and Tøndel, P., "Efficient optimal constrained control allocation via multiparametric programming," *Journal of guidance, control, and dynamics*, Vol. 28, No. 3, 2005, pp. 506–515.

[63] Tøndel, P., Johansen, T. A., and Bemporad, A., "An algorithm for multi-parametric quadratic programming and explicit MPC solutions," *Automatica*, Vol. 39, No. 3, 2003, pp. 489–497.

[64] Mattingley, J. and Boyd, S., "CVXGEN: a code generator for embedded convex optimization," *Optimization and Engineering*, 2012, pp. 1–27.

[65] Gelb, A., *Applied optimal estimation*, MIT press, 1974.

[66] Kolmanovsky, I. and Gilbert, E., "Multimode regulators for systems with state and control constraints and disturbance inputs," *Proceedings of Workshop Control Using Logic-Based Switching*, edited by M. A.S, Springer-Verlag, Block Island, Rhode Island, 1997, pp. 104–117.

[67] Blanchini, F. and Miani, S., *Set-theoretic methods in control*, Birkhäuser Boston, 2007.

[68] Blanchini, F., "Set invariance in control," *Automatica*, Vol. 35, No. 11, 1999, pp. 1747–1767.

[69] Park, H., Di Cairano, S., and Kolmanovsky, I., "Linear Quadratic Model Predictive Control approach to spacecraft rendezvous and docking," *Proceedings of 21st AAS/AIAA Space Flight Mechanics Meeting*, New Orleans, Louisiana, USA, 2011, pp. Paper AAS–142.

[70] Ong, C. J. and Gilbert, E. G., "Growth distances: New measures for object separation and penetration," *IEEE Transactions on Robotics and Automation*, Vol. 12, No. 6, 1996, pp. 888–903.

[71] Luenberger, D. G. and Ye, Y., *Linear and nonlinear programming*, Vol. 116, Springer, 2008.

[72] Bazaraa, M. S., Sherali, H. D., and Shetty, C. M., *Nonlinear programming: theory and algorithms*, Wiley-interscience, 2006.

[73] Guddat, J., Vazquez, F. G., and Jongen, H. T., *Parametric optimization: singularities, pathfollowing and jumps*, Teubner, 1990.

[74] Quoc, T. D., Savorgnan, C., and Diehl, M., "Adjoint-based predictor-corrector sequential convex programming for parametric nonlinear optimization," *SIAM Journal on Optimization*, Vol. 22, No. 4, 2012, pp. 1258–1284.

[75] Baldwin, M., Weiss, A., Kolmanovsky, I., and Erwin, R. S., "Spacecraft Debris Avoidance using Constraint Admissible Positively Invariant Sets," *Proceedings of AAS Space Flight Mechanics Meeting*, Charleston, South Carolina, 2012, pp. Paper AAS 12–250.

[76] Mahony, R., Hamel, T., and Pflimlin, J., "Nonlinear complementary filters on the special orthogonal group," *IEEE Trans. Autom. Control*, Vol. 53, 2008, pp. 1203–1218.

[77] Markley, F. L., "Attitude filtering on SO(3)," *J. Astronautical Sciences*, Vol. 54, No. 3–4, 2006, pp. 391–413.

[78] Sanyal, A. K., Lee, T., Leok, M., and McClamroch, N. H., "Global Optimal Attitude Estimation Using Uncertainty Ellipsoids," *Systems and Control Letters*, Vol. 57, 2008, pp. 236–245.

[79] Hughes, P. C., *Spacecraft Attitude Dynamics*, John Wiley & Sons Inc, 1986.

[80] Cullity, B. D. and Graham, C. D., *Introduction to magnetic materials*, Wiley-IEEE Press, 2011.

[81] Lee, J., Ng, A., and Jobanputra, R., "On Determining Dipole Moments of a Magnetic Torquer Rod - Experiments and Discussion," *J. Aeronautique et Spatial De Canada*, Vol. 48, No. 1, 2002, pp. 61–67.

[82] Agarwal, K., Weiss, A., Kolmanovsky, I., and Bernstein, D. S., "Inertia-Free Spacecraft Attitude Control with Control-Moment-Gyro Actuation," *Proc. AIAA Guid. Nav. Contr. Conf.*, Minneapolis, MN, August 2012, AIAA-2012-5003-282.

[83] Wie, B., *Space Vehicle Dynamics and Control*, AIAA, 2008.

[84] Lovera, M. and Astolfi, A., "Global magnetic attitude control of inertially pointing spacecraft," *Journal of Guidance Control and Dynamics*, Vol. 28, No. 5, 2005, pp. 1065–1067.

[85] Lovera, M. and Astolfi, A., "Global Magnetic Attitude Control of Spacecraft in the Presence of Gravity Gradient," *Transactions on Aerospace and Electronic Systems*, Vol. 42, No. 3, 2006, pp. 796–805.

[86] Koditschek, D. E., "The Application of Total Energy as a Lyapunov function for Mechanical Control Systems," *Proc. of AMS-IMS-SIAM Joint Summer Research Conf*, Bowdin College, ME, Bowdin College, ME, 1989, pp. 131–157.

[87] Leve, F., Boyarko, G. A., and Fitz-Coy, N. G., *Precise Torque Mapping for Pico-Satellite Single-Gimbal Control Moment Gyroscopes*, Vol. 137, Univelt, Inc., San Diego, CA,, advances in the astronautical sciences ed., 2010.

[88] Meng, T. and Matunaga, S., "Modified Singular-Direction Avoidance Steering for Control Moment Gyros," *Journal of Guidance, Control and Dynamics*, Vol. 34, No. 6, 2011, pp. 1915–1920.

[89] Pechev, A., "Feedback-Based Steering Law for Control Moment Gyros," *Journal of Guidance, Control, and Dynamics*, Vol. 30, No. 3, 2007, pp. 848–855.

[90] Wie, B., "Singularity Analysis and Visualization for Single-Gimbal Control Moment Gyro Systems," *Journal of Guidance, Control, and Dynamics*, Vol. 27, No. 2, 2004, pp. 271–282.

[91] Kurokawa, H., "A Geometry Study of Single Gimbal Control Moment Gyros - Singularity Problem and Steering Law," *TR 175*, Mechanical Engineering Lab., Tsukuba, Ibaraki, Japan 1998.

[92] Takada, K., Kojima, H., and Matsuda, N., "Control Moment Gyro Singularity-Avoidance Steering Control Based on Singular-Surface Cost Function," *Journal of Guidance, Control, and Dynamics*, Vol. 33, No. 5, 2010, pp. 1442–1450.

[93] Wie, B., "Singularity Robust Steering Logic for Redundant Single-Gimbal Control Moment Gyros," *Journal of Guidance, Control, and Dynamics*, Vol. 24, No. 5, 2001, pp. 865–872.

[94] Paradiso, J. A., "Global Steering of Single Gimbaled Control Moment Gyroscopes using a Directed Search," *Journal of Guidance, Control, and Dynamics*, Vol. 15, No. 5, 1992, pp. 1236–1244.

[95] Nakamura, Y. and Hanafusa, H., "Inverse Kinematic Solutions with Singularity Robustness for Robot Manipulator Control," *Journal of Dynamic Systems, Measurement, and Control*, Vol. 108, Sept. 1986, pp. 163–171.

[96] Bedrossian, N. S., *Steering Law Design for Redundant Single Gimbal Control Moment Gyro Systems*, M.s. thesis, Massachusetts Inst. of Technology, Cambridge, MA, Aug. 1987.

[97] Cruz, G., Yang, X., Weiss, A., Kolmanovsky, I., and Bernstein, D. S., "Torque-saturated, Inertia-free Spacecraft Attitude Control," *AIAA Guid. Nav. Contr. Conf.*, Portland, OR, August 2011, pp. AIAA–2011–6507.

[98] Kwakernaak, H. and Sivan, R., *Linear optimal control systems.*, J. Wiley and Sons, New York N.Y., 1972.

[99] Maciejowski, J., *Predictive control with constraints*, Prentice Hall, Harlow, England, 2002.

[100] Camacho, E. and Bordons, C., *Model Predictive Control*, Advanted Textbooks in Control and Signal Processing, Springer, 2nd ed., 2004.

[101] Kwon, W. H. and Han, S. H., *Receding Horizon Control: Model Predictive Control for State Models*, Springer, 1st ed., December 2005.

[102] Kwon, W. and Pearson, A., "A modified quadratic cost problem and feedback stabilization of a linear system," *Automatic Control, IEEE Transactions on*, Vol. 22, No. 5, Oct. 1977, pp. 838 – 842.

[103] Chen, M. S. and Huang, Y. R., "Linear time-varying system control based on the inversion transformation," *Automatica*, Vol. 33, No. 4, 1997, pp. 683 – 688.

[104] Chen, M.-S. and Kao, C.-Y., "Control of Linear Time-Varying Systems Using Forward Riccati Equation," *Journal of Dynamic Systems, Measurement, and Control*, Vol. 119, No. 3, 1997, pp. 536–540.

[105] Afanasiev, V., Kolmanovskii, V., and Nosov, V., *Mathematical theory of control systems design*, Kluwer, 1996.

[106] Rugh, W. J., *Linear system theory*, Prentice-Hall, Inc., Upper Saddle River, NJ, USA, 2nd ed., 1996.

[107] Callier, F., Winkin, J., and Willems, J., "On the exponential convergence of the time-invariant matrix Riccati differential equation," *Decision and Control, 1992., Proceedings of the 31st IEEE Conference on*, 1992, pp. 1536–1537 vol.2.

[108] Khalil, H. K., *Nonlinear Systems*, Prentice Hall, 2nd ed., December 1995.

[109] Loria, A., Chaillet, A., Besancon, G., and Chitour, Y., "On the PE stabilization of time-varying systems: open questions and preliminary answers," *44th IEEE Conference on Decision and Control, 2005 and 2005 European Control Conference, CDC-ECC '05*, December 2005, pp. 6847 – 6852.

[110] Srikant, S. and Akella, M., "Persistence filter-based control for systems with time-varying control gains," *Systems & Control Letters*, Vol. 58, No. 6, 2009, pp. 413 – 420.

[111] Slabaugh, G., "Computing Euler angles from a rotation matrix," http://www.gregslabaugh.name/publications/euler.pdf.

[112] Scholz, A., *Implementation of Advanced Attitude Determination and Control Techniques into a Nanosatellite*, Master's thesis, National Cheng Kung University, Taiwan, 2007.

[113] Alonso, R. and Shuster, M. D., "Attitude-independent magnetometer-bias determination: A survey," *Journal of the Astronautical Sciences*, Vol. 50, No. 4, 2002, pp. 453–476.

[114] Montenbruck, O. and Gill, E., *Satellite orbits: models, methods and applications*, Springer, 2005.

[115] Hartley, E. N., Trodden, P. A., Richards, A. G., and Maciejowski, J. M., "Model predictive control system design and implementation for spacecraft rendezvous," *Control Engineering Practice*, Vol. 20, No. 7, 2012, pp. 695 – 713.

[116] Weiss, A., Kolmanovsky, I., and Bernstein, D. S., "Inertia-Free Attitude Control of Spacecraft with Unknown Time-Varying Mass Distribution," *Proc. 62nd IAC*, Cape Town, South Africa, October 2011, IAC-11-C1.5.9.

[117] Curtis, H. D., *Orbital mechanics for engineering students*, Butterworth-Heinemann, 2005.

[118] Kasdin, N. J. and Paley, D. A., *Engineering Dynamics*, Princeton University Press, Princeton, NJ, USA, 2011.

[119] Levine, W. S., *Control Systems Applications*, CRC Press Inc., Boca Raton, FL, USA, 1999, page 132.